STRUCTURAL INVESTIGATIONS OF COMPOUNDS IN THE XeF_2–MF_4 (M = Mn, Pd, Pt) SYSTEMS

Klemen Motaln

Doctoral Dissertation
Jožef Stefan International Postgraduate School
Ljubljana, Slovenia

Supervisor: Asst. Prof. Dr. Matic Lozinšek, Jožef Stefan Institute and Jožef Stefan International Postgraduate School, Ljubljana, Slovenia

Evaluation Board:
Prof. Dr. Darja Lisjak, Chair, Jožef Stefan Institute and Jožef Stefan International Postgraduate School, Ljubljana, Slovenia
Prof. Dr. Anton Meden, Member, Faculty of Chemistry and Chemical Technology, University of Ljubljana, Ljubljana, Slovenia
Dr. Krešimir Molčanov, Member, Ruđer Bošković Institute, Zagreb, Croatia

MEDNARODNA PODIPLOMSKA ŠOLA JOŽEFA STEFANA
JOŽEF STEFAN INTERNATIONAL POSTGRADUATE SCHOOL



Klemen Motaln

STRUCTURAL INVESTIGATIONS OF COMPOUNDS IN THE XeF_2–MF_4 (M = Mn, Pd, Pt) SYSTEMS

Doctoral Dissertation

STRUKTURNE RAZISKAVE SPOJIN SISTEMOV XeF_2–MF_4 (M = Mn, Pd, Pt)

Doktorska disertacija

Supervisor: Asst. Prof. Dr. Matic Lozinšek

Ljubljana, Slovenia, April 2026

To my family.

Acknowledgments

First, I would like to express my sincere gratitude to my supervisor, Asst. Prof. Dr. Matic Lozinšek, for his invaluable guidance and unwavering support. His infectious passion for science and his high standards of scientific work have profoundly shaped both this dissertation and my personal growth.

I would also like to extend my special thanks to my office mate, Dr. Kristian Radan, for introducing me to the practical aspects of fluorine chemistry and for always being available for insightful discussions and advice.

I am also grateful to all other members of the Extreme Conditions Chemistry Lab, namely Dr. Matic Belak Vivod, Asst. Prof. Dr. Mirela Dragomir, Dr. Valentina Milašinović, Olha Sanko, Dr. Ana Siljanovska Virant, Dr. Kristina Smokrović, Lia Šibav, Dr. Erik Uran, and Dr. Miha Virant, whom I have had the privilege of working with over the years. I thank them both for their direct contributions to my research and for the pleasant and supportive environment they helped create.

I would further like to thank our international collaborators, Dr. Kshitij Gurung, Dr. Petr Brázda, Dr. Lukáš Palatinus, Prof. Dr. Dominik Kurzydłowski, and Sylwia Olszewska, all of whom made significant contributions to the results presented in this dissertation.

I also wish to express my gratitude to the members of my dissertation evaluation committee Prof. Dr. Darja Lisjak, Prof. Dr. Anton Meden, and Dr. Krešimir Molčanov, for their careful review and expert evaluation of this dissertation.

I gratefully acknowledge the European Research Council, the Slovenian Research and Innovation Agency, and the Jožef Stefan Institute for funding the research projects and equipment that made this work possible.

Most importantly, I would like to thank my family, my close friends, and especially Maša for their constant support throughout this journey.

Abstract

The demonstration of noble-gas reactivity by Neil Bartlett's landmark experiment, in which xenon was reacted with PtF_6 to yield a compound of $XePtF_6$ stoichiometry, represents one of the most important milestones in twentieth century inorganic chemistry. Nevertheless, the chemical nature of $XePtF_6$ ($XeF_2 \cdot PtF_4$) remains poorly understood, and its structure has remained enigmatic. To advance the understanding of this substance, previous studies have focused on the related XeF_2–MF_4 systems, which have revealed a rich and diverse structural chemistry within this family of compounds.

This dissertation primarily focuses on the furthering the structural investigations of compounds in the XeF_2–MF_4 systems (M = Mn, Pd, Pt). A longstanding obstacle in this field has been the limited crystallinity of many phases, which have resisted crystallographic characterization by single-crystal X-ray diffraction (SCXRD). To address this challenge, these compounds were examined by 3D electron diffraction (3D ED), which required the development of a new sample transfer protocol that enabled application of the method to highly reactive and air-sensitive samples. Reinvestigation of XeF_2–MnF_4 system revealed three crystalline phases, namely $3XeF_2 \cdot 2MnF_4$, $XeF_2 \cdot MnF_4$, and $XeF_2 \cdot 2MnF_4$, which were characterized by SCXRD, 3D ED, vibrational spectroscopy and periodic density functional theory (DFT) calculations.

The XeF_2–PtF_4 and XeF_2–PdF_4 systems were also reexplored, resulting in the crystal structure determination of $XeF_2 \cdot 2PtF_4$ and $XeF_2 \cdot 2PdF_4$ by 3D ED. Both phases were found to be isostructural with $XeF_2 \cdot 2MnF_4$, establishing a structural link across the three systems. Periodic DFT calculations were employed to assess structural models for $XeF_2 \cdot PtF_4$, derived from experimentally established structures of XeF_2–MF_4 (M = Cr, Mn) analogues, identifying *cis*-bridged motifs, found in the crystal structures of $3XeF_2 \cdot 2MnF_4$ and $XeF_2 \cdot MnF_4$, respectively, as energetically preferred.

Reactions probing the interaction of XeF_2 with both AsF_5 and Lewis acidic tetrafluorides PtF_4 and PdF_4 in anhydrous HF (aHF) yielded amber-colored crystals of the salts $[Xe_2F_3][MF_3(XeF_2)_3][AsF_6]_2$ (M = Pt, Pd) containing the previously unobserved discrete $[MF_3(XeF_2)_3]^+$ cations.

A reinvestigation of the XeF_2–PtF_5 system, which is closely linked to the first preparations of $XePtF_6$ and related studies, was also undertaken and the compounds $[Xe_2F_3][PtF_6] \cdot XeF_2$, $[Xe_2F_3][PtF_6]$, and $[XeF][PtF_6]$ were structurally characterized.

In addition, the role of XeF_2 as a ligand to alkali-metal cations was reevaluated by examining its interactions with alkali metal hexafluoridoplatinates(V) in aHF. XeF_2 was shown to coordinate Li^+, Na^+, and K^+ as the compounds $[Li(XeF_2)_3PtF_6]$, $[Na(XeF_2)PtF_6]$, and $[K(XeF_2)_2PtF_6]$ were characterized by SCXRD and Raman spectroscopy.

Finally, the behavior of $XeF_2 \cdot PtF_4$ under high-pressure and high-temperature conditions generated in a laser-heated diamond anvil cell was investigated. At pressures of 14.5 GPa, $XeF_2 \cdot PtF_4$ crystallizes upon laser heating, enabling determination of its structure for the first time. Laser heating of $XeF_2 \cdot PtF_4$ at lower pressures additionally revealed two previously unobserved polymorphs of $XeF_2 \cdot 2PtF_4$, as well as a new compound, $[PtF_2(XeF_2)_4][Pt_4F_{18}]$.

Povzetek

Demonstracija reaktivnosti žlahtnih plinov, ki jo je v prelomnem poskusu, v katerem je ksenon reagiral s PtF_6 in pridobil spojino s stehiometrijo $XePtF_6$, izvedel Neil Bartlett, predstavlja enega najpomembnejših mejnikov anorganske kemije 20. stoletja. Kljub temu narava spojine $XePtF_6$ ($XeF_2 \cdot PtF_4$) ostaja slabo razumljena, njena struktura pa je še vedno enigmatična. Za poglobitev razumevanja te snovi so se predhodne raziskave osredotočale na sorodne sisteme XeF_2–MF_4 in razkrile bogato in raznoliko strukturno kemijo v tej družini spojin.

Ta disertacija je v prvi vrsti usmerjena v nadaljnje strukturne raziskave spojin sistemov XeF_2–MF_4 (M = Mn, Pd, Pt). Zahtevno oviro na tem področju predstavlja omejena kristaliničnost številnih faz, ki onemogoča njihovo karakterizacijo z rentgensko difrakcijo na monokristalu (SCXRD). Za premagovanje tega izziva smo te spojine preučili s 3D elektronsko difrakcijo (3D ED), kar je zahtevalo razvoj novega protokola za prenos vzorcev, ki je omogočil uporabo te metode pri preučevanju visoko reaktivnih in na zrak občutljivih spojin. Ob ponovni preiskavi sistema XeF_2–MnF_4 smo odkrili tri kristalinične faze, in sicer $3XeF_2 \cdot 2MnF_4$, $XeF_2 \cdot MnF_4$ in $XeF_2 \cdot 2MnF_4$, ter jih karakterizirali s SCXRD, 3D ED, vibracijsko spektroskopijo in izračuni na osnovi teorije gostotnega funkcionala (DFT).

Sistema XeF_2–PtF_4 in XeF_2–PdF_4 smo prav tako ponovno raziskali ter s 3D ED uspešno določili kristalni strukturi faz $XeF_2 \cdot 2PtF_4$ in $XeF_2 \cdot 2PdF_4$. Ugotovili smo, da sta obe fazi izostrukturni s spojino $XeF_2 \cdot 2MnF_4$, s čimer smo vzpostavili povezavo med temi tremi sistemi. Preko uporabe periodičnih DFT izračunov smo ovrednotili strukture modele spojine $XeF_2 \cdot PtF_4$, izpeljane iz eksperimentalno določenih struktur XeF_2–MF_4 (M = Cr, Mn), pri čemer smo kot energijsko najugodnejše prepoznali motive s *cis*-mostovi, prisotne v strukturah $3XeF_2 \cdot 2MnF_4$ in $XeF_2 \cdot MnF_4$.

Preučili smo tudi hkratne interakcije XeF_2 tako z AsF_5 kot z Lewisovo kislima tetrafluoridoma PtF_4 in PdF_4 v brezvodnem HF ter iz teh raztopin izolirali jantarno obarvane kristale soli $[Xe_2F_3][MF_3(XeF_2)_3][AsF_6]_2$ (M = Pt, Pd), ki vsebujejo doslej neopažene diskretne katione $[MF_3(XeF_2)_3]^+$.

Ponovno smo preiskali tudi sistem XeF_2–PtF_5, ki je tesno povezan s prvimi sintezami $XePtF_6$ in sorodnimi študijami, kar je vodilo do strukturne karakterizacije spojin $[Xe_2F_3][PtF_6] \cdot XeF_2$, $[Xe_2F_3][PtF_6]$ in $[XeF][PtF_6]$.

Poleg tega smo ponovno ovrednotili vlogo XeF_2 kot liganda na katione alkalijskih kovin z raziskavo njegovih interakcij s heksafluoridoplatinati(V) alkalijskih kovin v brezvodnem HF. Ob tem smo izolirali spojine $[Li(XeF_2)_3PtF_6]$, $[Na(XeF_2)PtF_6]$ in $[K(XeF_2)_2PtF_6]$ ter jih ovrednotili s SCXRD in Ramansko spektroskopijo.

Raziskali smo tudi obnašanje $XeF_2 \cdot PtF_4$ pri visokem tlaku in temperaturi, doseženih z laserskim segrevanjem vzorca, zaprtega v celici z diamantnimi nakovali. Pri tlaku 14,5 GPa je $XeF_2 \cdot PtF_4$ po laserskem segrevanju kristaliziral, kar je omogočilo, da smo prvič določili kristalno strukturo te spojine. Po laserskem segrevanju $XeF_2 \cdot PtF_4$, izpostavljenega nižjim tlakom, pa smo odkrili obstoj dveh prej neopaženih polimorfov $XeF_2 \cdot 2PtF_4$ ter nove spojine $[PtF_2(XeF_2)_4][Pt_4F_{18}]$.

Contents

List of Figures **xvii**

List of Tables **xix**

Abbreviations **xxi**

Symbols **xxiii**

1 Introduction **1**
1.1 Discovery of Noble Gases and Pursuit of Their Reactivity ... 1
1.2 Binary Fluorides of Noble Gases ... 3
1.3 Chemistry of XeF_2 ... 5
1.3.1 Interactions of XeF_2 with Lewis acidic species ... 6
1.4 Investigations on the Nature of $XePtF_6$ and Related Compounds ... 7
1.5 Structural Chemistry of XeF_2–MF_4 Systems ... 9
1.5.1 XeF_2–TiF_4 system ... 9
1.5.2 XeF_2–CrF_4 system ... 11
1.5.3 XeF_2–MnF_4 system ... 11
1.5.4 XeF_2–PdF_4 system ... 13
1.5.5 XeF_2–SnF_4 system ... 14
1.6 Structural Characterization by 3D Electron Diffraction ... 14
1.7 High-Pressure Chemistry ... 17

2 Aims and Hypotheses **21**
2.1 Aims ... 21
2.2 Hypotheses ... 22

3 Materials and Methods **23**
3.1 Materials ... 23
3.2 Synthesis Methods ... 25
3.2.1 Apparatus ... 25
3.2.2 Reaction vessels ... 26
3.2.3 Thermal syntheses ... 27
3.2.4 UV syntheses ... 27
3.3 High-Pressure Diamond Anvil Cell Experiments ... 28
3.4 Characterization Methods ... 29
3.4.1 Single-crystal X-ray diffraction ... 29
3.4.1.1 Crystal selection and mounting ... 29
3.4.1.2 Data collection and reduction ... 30
3.4.2 Powder X-ray diffraction ... 30
3.4.3 High pressure SCXRD data collection and processing ... 31
3.4.4 3D Electron crystallography ... 31

3.4.5 Vibrational spectroscopy 32
3.4.5.1 Raman spectroscopy 32
3.4.5.2 Attenuated total reflectance-Infrared spectroscopy 33

4 Results and Discussion **35**
4.1 Reactive Noble-Gas Compounds Explored by 3D Electron Diffraction: XeF_2–MnF_4 Adducts and a Facile Sample Handling Procedure 35
4.2 Structures of $XeF_2 \cdot 2PtF_4$ and $XeF_2 \cdot 2PdF_4$ Determined by 3D Electron Diffraction and Structural Models of $XePtF_6$ 47
4.3 Coordination of XeF_2 to Fluoridometal Cations: The Adduct Cations $[PtF_3(XeF_2)_3]^+$ and $[PdF_3(XeF_2)_3]^+$ 59
4.4 Structural Investigations of the XeF_2–PtF_5 System: Crystal Structures of $[Xe_2F_3][PtF_6] \cdot XeF_2$, $[Xe_2F_3][PtF_6]$, and $[XeF][PtF_6]$ 72
4.5 Revisiting the Coordination of XeF_2 to Alkali Metal Cations: Synthesis and Structural Characterization of $[Li(XeF_2)_3PtF_6]$, $[Na(XeF_2)PtF_6]$, and $[K(XeF_2)_2PtF_6]$ 83
4.5.1 Background 83
4.5.2 Results and discussion 83
4.5.2.1 Syntheses 83
4.5.2.2 Crystal structures 85
4.5.2.2.1 Crystal structure of $[Li(XeF_2)_3PtF_6]$ 86
4.5.2.2.2 Crystal structure of $[Na(XeF_2)PtF_6]$ 87
4.5.2.2.3 Crystal structure of $[K(XeF_2)_2PtF_6]$ 88
4.5.2.2.4 Crystal structures of $APtF_6$-type compounds (A = Li, Na, K, Rb) 89
4.5.2.3 Raman spectroscopy 92
4.5.3 Summary 94
4.5.4 Experimental 95
4.5.4.1 Synthesis and crystal growth of $[Li(XeF_2)_3PtF_6]$ 95
4.5.4.2 Synthesis and crystal growth of $[Na(XeF_2)PtF_6]$ 95
4.5.4.3 Synthesis and crystal growth of $[K(XeF_2)_2PtF_6]$ 95
4.5.4.4 Attempted synthesis of $[Rb(XeF_2)_nPtF_6]$ 96
4.6 Structural Investigations of the XeF_2–PtF_4 System Under Extreme Conditions 97
4.6.1 Background 97
4.6.2 Results and discussion 97
4.6.2.1 Crystal structure of $XeF_2 \cdot PtF_4$ 101
4.6.2.2 Crystal structure of $[PtF_2(XeF_2)_4][Pt_4F_{18}]$ 104
4.6.2.3 High-pressure polymorphism of $XeF_2 \cdot 2PtF_4$ 105
4.6.3 Summary 107

5 Conclusions **109**

Appendix A Supporting Information to the Publications Included in this Thesis **111**
A.1 Reactive Noble-Gas Compounds Explored by 3D Electron Diffraction: XeF_2–MnF_4 Adducts and a Facile Sample Handling Procedure 111
A.2 Crystal Structures of $XeF_2 \cdot 2PtF_4$ and $XeF_2 \cdot 2PdF_4$ Determined by 3D Electron Diffraction and Structural Models of $XePtF_6$ 112
A.3 Coordination of XeF_2 to Fluoridometal Cations: The Adduct Cations $[PtF_3(XeF_2)_3]^+$ and $[PdF_3(XeF_2)_3]^+$ 113

A.4 Structural Investigations of the XeF_2–PtF_5 System: Crystal Structures of $[Xe_2F_3][PtF_6] \cdot XeF_2$, $[Xe_2F_3][PtF_6]$, and $[XeF][PtF_6]$ 114

Appendix B Additional Crystallographic Data and Figures **115**

B.1 Revisiting the Coordination of XeF_2 to Alkali Metal Cations: Synthesis and Structural Characterization of $[Li(XeF_2)_3PtF_6]$, $[Na(XeF_2)PtF_6]$, and $[K(XeF_2)_2PtF_6]$ 115

B.2 Structural Investigations of the XeF_2–PtF_4 System Under Extreme Conditions 126

References **139**

Bibliography **157**

Biography **161**

List of Figures

Figure 1.1: Molecular structures of XeF_2 (left), XeF_4 (center), and XeF_6 (right) observed in the solid state. 3
Figure 1.2: Colorless crystals of KrF_2 4
Figure 1.3: Glass bulb ($V \approx 10$ L) containing photochemically prepared XeF_2 6
Figure 1.4: Sections of the crystal structures of $[Xe_2F_3][Ti_8F_{33}]$ (left) and $[XeF]_2[Ti_9F_{38}]$ (right) [104]. 10
Figure 1.5: Section of the crystal structure of $3XeF_2 \cdot 2TiF_4$ [106]. 10
Figure 1.6: Crystal structures of $XeF_2 \cdot CrF_4$ (left) [108] and $XeF_2 \cdot 2CrF_4$ (right) [109]. ..11
Figure 1.7: Crystal structures of $3XeF_2 \cdot 2MnF_4$ (left) and $XeF_2 \cdot MnF_4$ (right) [112]. 12
Figure 1.8: Section of the crystal structure of $[Xe_2F_3][Sn_4F_{17}] \cdot XeF_2 \cdot HF$ [106]. 14
Figure 1.9: TEM adapted for the use as an electron diffractometer installed at the Institute of Physics of the Czech Academy of Sciences in Prague, Czech Republic and micrographs of nano-sized crystallites used for structure determination by 3D ED 16
Figure 1.10: Schematic cross section of a DAC highlighting its components. 18
Figure 3.1: Custom-built vacuum line. 25
Figure 3.2: h-shaped FEP crystallization vessel (left) and nickel reactor (right). 26
Figure 3.3: Experimental setup used for pyrolysis under dynamic vacuum. 27
Figure 3.4: Setup for UV irradiation reactions employing the 600 W LED UV light. 28
Figure 3.5: Merrill–Bassett (left) and SSDAC80 (right) types of DACs. 28
Figure 3.6: Low-temperature crystal mounting apparatus 29
Figure 3.7: Rigaku OD XtaLAB Synergy-S diffractometer used in this work. 30
Figure 3.8: Quartz capillary mounted on the diffractometer for a PXRD measurement. ..31
Figure 3.9: Bruker Senterra II confocal Raman microscope 32
Figure 3.10: Bruker Alpha II FT-IR positioned inside a glovebox. 33
Figure 4.1: Graphical abstract of the publication "Reactive Noble-Gas Compounds Explored by 3D Electron Diffraction: XeF_2–MnF_4 Adducts and a Facile Sample Handling Procedure" [191]. 35
Figure 4.2: Graphical abstract of the publication "Structures of $XeF_2 \cdot 2PtF_4$ and $XeF_2 \cdot 2PdF_4$ Determined by 3D Electron Diffraction and Structural Models of $XePtF_6$" [197]. 47
Figure 4.3: Graphical abstract of the publication "Coordination of XeF_2 to Fluoridometal Cations: The Adduct Cations $[PtF_3(XeF_2)_3]^+$ and $[PdF_3(XeF_2)_3]^+$" [199]. 59
Figure 4.4: Graphical abstract of the publication "Structural investigations of the XeF_2–PtF_5 system: crystal structures of $[Xe_2F_3][PtF_6] \cdot XeF_2$, $[Xe_2F_3][PtF_6]$, and $[XeF][PtF_6]$" [200]. 72
Figure 4.5: Sections of the crystal structure of $[Li(XeF_2)_3PtF_6]$ 86
Figure 4.6: Coordination sphere of Na^+ in $[Na(XeF_2)PtF_6]$ 87
Figure 4.7: Section of the crystal structure of $[K(XeF_2)_2PtF_6]$ displaying the coordination environment of K^+. 88
Figure 4.8: Section of the crystal structure of $LiPtF_6$. 91
Figure 4.9: Section of the crystal structure of $KPtF_6$. 91

Figure 4.10: Low-temperature (100 K) Raman spectra of $[Li(XeF_2)_3PtF_6]$, $[Na(XeF_2)PtF_6]$, and $[K(XeF_2)_2PtF_6]$. 93
Figure 4.11: Ambient temperature Raman spectra of $LiPtF_6$, $NaPtF_6$, $KPtF_6$ and $RbPtF_6$. 94
Figure 4.12: Raman analysis of the DAC loaded with $XeF_2 \cdot PtF_4$ following laser heating at 14.5 GPa. 98
Figure 4.13: Raman analysis of the DAC loaded with $XeF_2 \cdot PtF_4$ following laser heating at 8.0 GPa. 99
Figure 4.14: Raman analysis of the DAC loaded with $XeF_2 \cdot PtF_4$ following decompression to 2 GPa. 99
Figure 4.15 Raman analysis of the SSDAC80 cell loaded with $XeF_2 \cdot PtF_4$ following laser heating at 4.0 GPa. 100
Figure 4.16 Raman analysis of the Merrill-Bassett cell loaded with $XeF_2 \cdot PtF_4$ following laser heating at 8.6 GPa. 101
Figure 4.17: Section of the crystal structure of $XeF_2 \cdot PtF_4$ displaying the *cis*-bridged $^1_\infty[PtF_3F_{2/2}(XeF_2)]$ chains propagating along the *b* crystallographic axis. 102
Figure 4.18: Comparison of the *cis*-bridged chains in the high-pressure structure of $XeF_2 \cdot PtF_4$ (left) and the previously proposed structural model for $XeF_2 \cdot PtF_4$, derived from $3XeF_2 \cdot 2MnF_4$ (right) [197] 103
Figure 4.19: Crystal structure of $[PtF_2(XeF_2)_4][Pt_4F_{18}]$ 104
Figure 4.20: The adduct cation $[PtF_2(XeF_2)_4]^{2+}$. 105
Figure 4.21: Comparison of crystal packing in $XeF_2 \cdot 2PtF_4$(*aP*26)-I (top), $XeF_2 \cdot 2PtF_4$(*aP*26)-II (middle), and $XeF_2 \cdot 2PtF_4$(*mP*52) (bottom) 106
Figure 4.22: View of the double chains in $XeF_2 \cdot 2PtF_4$(*aP*26)-I (top) and $XeF_2 \cdot 2PtF_4$(*aP*26)-II (bottom) along [−111] direction, ... 107

Figure B.1: Crystal packing of $[Li(XeF_2)_3PtF_6]$ viewed along the *a* axis, ... 121
Figure B.2: Sections of the crystal structure of $[Na(XeF_2)PtF_6]$ 122
Figure B.3: Sections of the crystal structure of $[K(XeF_2)_2PtF_6]$ 123
Figure B.4: Coordination environment of the Na^+ cation (top) and the crystal packing of $NaPtF_6$ viewed along the *a* crystallographic axis (bottom). 124
Figure B.5: Coordination environment of the Rb^+ cation (top) and the crystal packing of $RbPtF_6$ viewed along the *c* crystallographic axis (bottom). 125

List of Tables

Table 3.1: Overview of the chemicals used in this work. 23
Table 4.1: Summary of crystal data and refinement results for the structures of $[Li(XeF_2)_3PtF_6]$, $[Na(XeF_2)PtF_6]$, and $[K(XeF_2)_2PtF_6]$, ... 85
Table 4.2: Selected bond lengths (Å) and angles (°) in the crystal structures of $[Li(XeF_2)_3PtF_6]$, $[Na(XeF_2)PtF_6]$, and $[K(XeF_2)_2PtF_6]$. 86
Table 4.3: Crystal data and refinement results for the structures of $LiPtF_6$, $NaPtF_6$, $KPtF_6$, and $RbPtF_6$ 90
Table 4.4: Selected bond lengths (Å) and angles (°) in the crystal structures of $LiPtF_6$, $NaPtF_6$, $KPtF_6$, and $RbPtF_6$. 90
Table 4.5: Selected bond lengths (Å) and angles (°) in the crystal structures of $XeF_2 \cdot PtF_4$ and $[PtF_2(XeF_2)_4][Pt_4F_{18}]$ 102

Table B.1 Crystallographic data and refinement results for $[Li(XeF_2)_3PtF_6]$, $[Na(XeF_2)PtF_6]$, and $[K(XeF_2)_2PtF_6]$. 116
Table B.2 Fractional atomic coordinates and equivalent isotropic displacement parameters (Å^2) for the crystal structure of $[Li(XeF_2)_3PtF_6]$. 117
Table B.3 Fractional atomic coordinates and equivalent isotropic displacement parameters (Å^2) for the crystal structure of $[Na(XeF_2)PtF_6]$ 118
Table B.4 Fractional atomic coordinates and equivalent isotropic displacement parameters (Å^2) for the crystal structure of $[K(XeF_2)_2PtF_6]$. 118
Table B.5 Crystallographic data and refinement results for $LiPtF_6$, $NaPtF_6$, $KPtF_6$, and $RbPtF_6$ 119
Table B.6 Fractional atomic coordinates and equivalent isotropic displacement parameters (Å^2) for the crystal structures of $LiPtF_6$, $NaPtF_6$, $KPtF_6$, and $RbPtF_6$. 120
Table B.7 Summary of phases identified after laser heating. 126
Table B.8 Crystallographic data for $XeF_2 \cdot PtF_4$ collected at different pressure points. 127
Table B.9 Fractional atomic coordinates and equivalent isotropic displacement parameters (Å^2) for the crystal structures of $XeF_2 \cdot PtF_4$. 128
Table B.10 Non-bonded inter- and intramolecular Xe $\cdot \cdot \cdot$ F contacts shorter than the corresponding sum of the van der Waals radii in the crystal structure of $XeF_2 \cdot PtF_4$ determined at 14.5 GPa. 129
Table B.11 Crystallographic data for $[PtF_2(XeF_2)_4][Pt_4F_{18}]$. 130
Table B.12 Fractional atomic coordinates and equivalent isotropic displacement parameters (Å^2) for $[PtF_2(XeF_2)_4][Pt_4F_{18}]$. 131
Table B.13 Non-bonded inter- and intramolecular Xe $\cdot \cdot \cdot$ F contacts shorter than the corresponding sum of the van der Waals radii in the crystal structure of $[PtF_2(XeF_2)_4][Pt_4F_{18}]$. 132
Table B.14 Crystallographic data for $XeF_2 \cdot 2PtF_4(mP52)$ collected at different pressure points. 133
Table B.15 Fractional atomic coordinates and equivalent isotropic displacement parameters (Å^2) for the crystal structures of $XeF_2 \cdot 2PtF_4(mP52)$. 134

Table B.16 Summary of selected bond distances (Å) and angles (°) for $XeF_2 \cdot 2PtF_4$($mP52$) at different pressures. 135
Table B.17 Crystallographic data for $XeF_2 \cdot 2PtF_4$($aP26$)-I and $XeF_2 \cdot 2PtF_4$($aP26$)-II. 136
Table B.18 Fractional atomic coordinates and equivalent isotropic displacement parameters (Å^2) for $XeF_2 \cdot 2PtF_4$($aP26$)-I and $XeF_2 \cdot 2PtF_4$($aP26$)-II. 137
Table B.19 Summary of selected bond distances (Å) and angles (°) for $XeF_2 \cdot 2PtF_4$($aP26$)-I and $XeF_2 \cdot 2PtF_4$($aP26$)-II. 138

Abbreviations

3D ED	3D electron diffraction
aHF	Anhydrous hydrogen fluoride
ATR-IR	Attenuated total reflection infrared spectroscopy
DAC	Diamond anvil cell
DFT	Density functional theory
FEP	Fluorinated ethylene propylene
IR	Infrared
i.d.	Internal diameter
PCTFE	Poly(chlorotrifluoroethylene)
LH	Laser heating
LT	Low-temperature
o.d.	Outer diameter
PTFE	Poly(tetrafluoroethylene)
PXRD	Powder X-ray diffraction
SCXRD	Single-crystal X-ray diffraction
TEM	Transmission electron microscope
UV	Ultraviolet
VSEPR	Valence shell electron pair repulsion model
WCA	Weakly coordinating anion

Symbols

a, b, c, α, β, γ	... Unit cell parameters
λ	... Wavelength
μ	... Absorption coefficient
ρ	... Density
σ	... Standard deviation
F_b	... Bridging fluorine atom
F_c	... Structure factor (calculated)
F_o	... Structure factor (observed)
F_t	... Terminal fluorine atom
F_w	... Formula weight
R_1	... Agreement factor
R_{int}	... Merging R-factor
S	... Goodness of fit
V	... Unit cell volume
wR_2	... Weighted agreement factor
Z	... Formula units per unit cell

Chapter 1

Introduction

1.1 Discovery of Noble Gases and Pursuit of Their Reactivity

The modern history of noble-gas chemistry began in the 1890s with the recognition that the atmosphere contains a family of previously unrecognized elements. Cavendish's experiments in the 18th century had already shown that a small fraction of atmospheric gas resisted conversion to nitric acid, but this anomaly was not pursued further [1]. A century later, Rayleigh's precise density measurements revealed that nitrogen obtained from the atmosphere was denser than chemically prepared nitrogen [2], leading Rayleigh and Ramsay to isolate argon as a new, monatomic constituent of air [3]. Ramsay and co-workers rapidly went on to identify helium released from minerals [4], [5], and separated neon, krypton and xenon from liquefied air, thereby establishing a group of apparently nonreactive gases [6]. Rayleigh and Ramsay placed argon between the halogens and alkali metals in the periodic system [3], a positioning later confirmed by Moseley's work on the X-ray spectra of the elements [7]. Subsequently, the work by Von Antropoff suggested placing the noble gases as the rightmost column of the periodic table in what was then referred to as the Group VIII (now Group 18) [8], [9].

Already in their first report on argon, Rayleigh and Ramsay detailed numerous attempts to induce its chemical reactivity, all of which proved unsuccessful [3]. To further probe its inertness, they sent a sample to Moissan, who was the first to isolate the element fluorine less than a decade earlier. In 1895, Moissan attempted to combine argon with fluorine at ambient temperature and under electric discharge, but observed no sign of chemical reaction [10].

Despite these early failures, reasoning derived from the trends observed in the periodic table encouraged some chemists to predict the existence of genuine noble-gas compounds. In 1902 Oddo wrote to Ramsay, arguing that valence and reactivity should increase with the atomic number of the noble-gas, leading to the expectation that krypton and especially xenon would show some tendency towards chemical bonding [11]. Ramsay agreed in principle, but emphasized the practical difficulty of obtaining sufficient quantities of these gases for experimental studies [12]. In his seminal work on the relationship between atomic structure and molecule formation, Kossel went further and explicitly proposed that fluorides of both krypton and xenon might exist [13]. In parallel, Lewis's model of the chemical bond elevated noble-gas electron configurations as an archetype of stability, reinforcing the expectation of chemical inertness [14]. This classification and unsuccessful early attempts to react these gases reinforced the view that noble gases were fundamentally non-reactive.

Nevertheless, experimental efforts did not cease. In 1932, Von Antropoff and co-workers reported red krypton chlorides and bromides formed by electric discharge reactions of krypton with Cl_2 or Br_2 [15]. Subsequent reinvestigation showed that the isolated material was in fact a known compound of NO and HCl, leading to retraction of the proposed krypton halides [16]. Independent discharge studies by Ruff and Menzel on the reactivity of fluorine toward argon and krypton likewise failed to provide any evidence for stable noble-gas fluorides [17].

The most influential predictions came from Pauling. In 1933, using arguments based on ionic radii and coordination trends together with analogies to hypervalent species such as $Te(OH)_6$, he proposed the existence of xenic acid, H_4XeO_6, which should form salts such as Ag_3XeO_6 and AgH_3XeO_6 [18]. Applying the same reasoning to compounds with fluorine ligands, he further predicted the stability of XeF_6 and KrF_6, and suggested that XeF_8, while unstable, might also be isolable [18]. Pauling subsequently sought to test these ideas experimentally, encouraging his colleague Yost to attempt the synthesis of xenon chlorides and fluorides under strongly oxidizing conditions [19].

Yost and his student Kaye subjected Xe/F_2 and Xe/Cl_2 mixtures to a series of high-voltage discharges and carefully monitored the systems for solid or condensable products. Additionally, they irradiated Xe and Cl_2 mixtures with UV light emitted from mercury and carbon arc lamps. In their 1933 communication, they reported that no definite xenon chloride or fluoride could be identified, and although etching of the quartz side arm was observed in the Xe/F_2 experiments, concluded that xenon appeared not to form halides under the conditions examined [20]. It is especially unfortunate that only Xe/Cl_2 and not Xe/F_2 mixtures were exposed to UV irradiation, since the latter would later prove to be a convenient route to XeF_2 [21]. Later reconstructions, combining Yost and Kaye's published data and recollections with modern chemical reasoning, suggest that xenon fluorides were likely generated transiently but reacted with the apparatus walls or were not efficiently trapped, and thus escaped recognition [12], [19].

These negative results substantially discouraged further efforts to probe noble-gas reactivity, and even Pauling, who had initially been confident that xenon would combine with fluorine, soon ceased actively advocating the chemistry of noble gases. By 1947 he wrote: "The congeners of helium—neon, argon, krypton, xenon, and radon—are also chemically inert. The failure of these inert elements to form chemical compounds is similarly due to the great stability of their electronic structures" [22].

Nonetheless, several key developments in the intervening years helped lay the groundwork for the eventual discovery of noble-gas reactivity. The handling of the strongest oxidizing agents then known, fluorine and high-valent metal fluorides, was significantly improved, driven in large part by their use in well-funded nuclear programs, and the availability of noble gases likewise increased [12], [23]. At the same time, theoretical methods advanced: molecular orbital descriptions of three-center, four-electron bonds in polyhalide species provided a clear bonding framework that could, in principle, accommodate noble-gas–halogen compounds [24].

A major milestone paving the way for the discovery of noble-gas reactivity occurred in 1956, when Neil Bartlett, then at King's College in Newcastle, observed the formation of a deep red, volatile solid while attempting to remove BrF_3 impurities from PtF_4 by heating it in a stream of fluorine diluted with nitrogen [25]. Characterization of this material proved particularly challenging, as although it was established that the compound contained oxygen, introduced by the action of fluorine on the glass apparatus, it was initially misidentified as platinum(VI) oxidetetrafluoride [26]. Only after a careful elemental analysis, which indicated a stoichiometry of PtO_2F_6, and a comparison of its PXRD pattern with that of $NO^+RuF_6^-$, was the correct formulation $O_2^+PtF_6^-$ established [27]. This species was recognized as the first reported salt of the dioxygenyl cation, yet even after its synthesis

was successfully reproduced by oxidizing O_2 with PtF_6, the formulation continued to be viewed with skepticism [25], [28].

Later, in a moment of incisive chemical reasoning, Bartlett recognized that the first ionization potential of O_2 is only slightly lower than that of xenon (12.0 and 12.2 eV, respectively) and immediately devised an experiment to test whether xenon could likewise be oxidized. The apparatus consisted of two quartz bulbs, one containing deep-red PtF_6 and the other colorless xenon gas, connected by a glass tube and a break-seal. Immediately upon breaking the seal, the deep-red color vanished, and a sticky yellow solid was observed to deposit on the reactor walls. Initial analysis indicated a stoichiometry of $XePtF_6$, and the compound was tentatively formulated as $Xe^+PtF_6^-$ [29]. This discovery, which provided the first clear demonstration that noble gases can form genuine chemical compounds, resonated worldwide and marked the birth of a new branch of chemistry, prompting numerous laboratories to join the search for additional stable noble-gas compounds.

1.2 Binary Fluorides of Noble Gases

The synthesis of $XePtF_6$ catalyzed intense interest in this emerging field, and within the same year all binary fluorides of xenon presently known were successfully prepared. The first reported binary noble gas compound was XeF_4, prepared at Argonne National Laboratory by heating a mixture of xenon and fluorine with an approximate molar ratio of 9:1 in a nickel vessel at 400 °C for one hour [30]. At room temperature xenon tetrafluoride forms colorless crystals with a vapor pressure of 400 Pa and a melting point of 114 °C [31]. X-ray and neutron diffraction studies confirmed the structure of XeF_4 to be square planar [32], [33], which is in agreement with the predictions based on molecular orbital theory and valence shell electron pair repulsion (VSEPR) model [34].

The report of the XeF_4 discovery was promptly followed by the reports of other two known binary fluorides of Xenon: XeF_2 and XeF_6. The first syntheses of XeF_2 were reported in 1962 independently by two laboratories who prepared the XeF_2 either by reacting xenon and fluorine in a 1:2 molar ratio with the help of electric discharge or detected it as a by-product of the XeF_4 synthesis [35], [36]. Similar to XeF_4, XeF_2 is solid at room temperature and forms large colorless crystals. The structure of XeF_2 was studied by neutron and X-ray diffraction, establishing that it crystallizes in tetragonal space group $I4/mmm$ with the xenon–fluorine bonds at a distance of 1.999(4) Å [37], [38], [39]. The structure of XeF_2 molecules was found to be linear and centrosymmetric ($D_{\infty h}$), consistent with the prediction from the VSEPR model for a AX_2E_3 species (Figure 1.1).

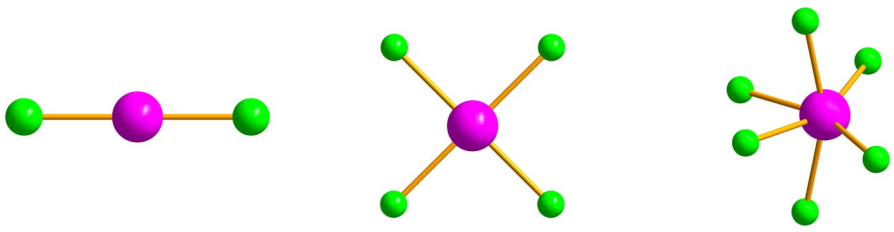


Figure 1.1: Molecular structures of XeF_2 (left), XeF_4 (center), and XeF_6 (right) observed in the solid state. Note that the crystal structures of XeF_6 polymorphs predominantly contain oligomeric units composed of XeF_5^+ cations and bridging F^- anions. Shown here is a rare exception, molecular XeF_6 adopting a slightly distorted C_{2v} geometry found in the crystal structure of XeF_6($mP32$) [40]. By contrast, computational studies predict a C_{3v} structure for the gas-phase XeF_6 [41].

The third known binary fluoride of xenon is xenon hexafluoride. The preparation of XeF_6 was first described by Jože Slivnik's group from Jožef Stefan Institute in 1962 with three more independent reports published in the following year [42], [43], [44], [45]. All early preparations were carried out in metal reactors utilizing high temperatures and pressures. In contrast to other xenon fluorides determination of its structure proved troublesome. Due to a non-bonding valence pair the molecule does not adopt the octahedral structure and forms oligomers in the solid, liquid or dissolved state [40]. This was proven by the early gas-phase electron diffraction analysis which clearly showed that the molecule is not octahedral [46], [47]. XeF_6 also exhibits rich polymorphism, with at least six different modifications structurally characterized [40], [48], [49], [50]. Xenon hexafluoride is much more volatile than the other two xenon fluorides, although much less so than other known hexafluorides [51]. Additionally, XeF_6 is also a much stronger oxidizer and fluorinating agent than XeF_2 and XeF_4. It cannot be stored in glass or quartz as it attacks it and readily exchanges fluorine for oxygen, initially yielding $XeOF_4$ and finally the highly shock sensitive detonator xenon trioxide [52]. The extremely unstable and explosive nature of XeO_3, which is produced upon hydrolysis of both XeF_4 and XeF_6 severely limits their use.

The first synthesis of a krypton fluoride was reported in 1963, using high-voltage glow discharge on Kr/F_2 mixtures at −78 °C [53]. The resulting solid was initially misidentified as krypton tetrafluoride, with subsequent repetitions of the experiment correctly established its composition as krypton difluoride, KrF_2 [54], which had in the meantime already been obtained independently by matrix isolation techniques [55]. In addition to the glow discharge method, KrF_2 can also be synthesized from Kr/F_2 mixtures by generating $F^\bullet$ radicals either via UV photolysis [56] or on a resistively heated Ni wire housed in a liquid-nitrogen-cooled metal reactor [57]. All of these syntheses must be conducted at low temperature, owing to the endothermic heat of formation of KrF_2 ($\Delta H_f = 60.2$ kJ mol^{-1}, gas at 93 °C) [58], which precludes the use of high-temperature, high-pressure routes successfully employed for the xenon fluorides [59]. Like its xenon counterpart, it is a colorless crystalline solid (Figure 1.2), with a molecular structure composed of linear molecules with $D_{\infty h}$ symmetry. It is thermodynamically unstable at room temperature and undergoes slow decomposition, but it can be stored indefinitely at −78 °C. Possessing a vapor pressure of about 13 kPa at ambient temperature [59], KrF_2 is substantially more volatile than the xenon fluorides. Its chemistry parallels that of XeF_2 in many aspects, with the notable exception that it is a considerably stronger oxidizing agent, with the KrF^+ cation being among the strongest chemical oxidants presently known [60], [61].

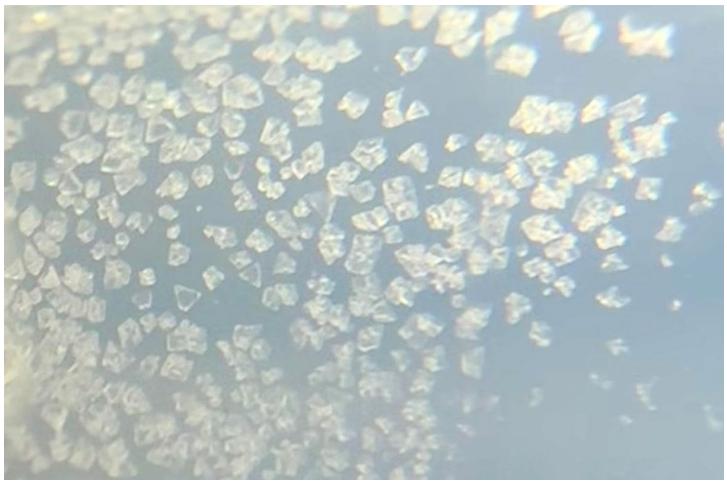


Figure 1.2: Colorless crystals of KrF_2, prepared at JSI, adhering to the inner wall of a 6 mm i.d. fluorinated ethylene propylene (FEP) tube.

The synthesis of compounds of radon, the heaviest noble gas that can be isolated in appreciable quantities, have also been reported [62]. It was later shown that radon reacts with fluorine even at room temperature to form a nonvolatile solid formulated as RnF_2 [63]. Due to the intense radioactivity of radon, which restricts experiments to very small quantities, and the short half-life of its most stable isotope ^{222}Rn (3.8 days), RnF_2 has not been extensively characterized in the solid state.

1.3 Chemistry of XeF_2

Since it is one the easiest xenon compounds to prepare and handle, and even commercially accessible, the chemistry of XeF_2 is the best explored among all binary noble gas fluorides. XeF_2-based precursors also enable the synthesis of compounds featuring xenon bonded to a range of other elements, namely to carbon [64], [65], nitrogen [66], oxygen [67], chlorine [68], or even xenon itself [69]. In addition to the aforementioned synthesis of XeF_2, by subjecting Xe/F_2 mixtures to electric discharge, XeF_2 can also be prepared by heating such mixtures or by exposing them to UV light, γ radiation, or electron irradiation from a Van de Graaff accelerator [70]. Among these routes, the UV-induced synthesis is particularly elegant, as it can proceed simply by exposing a Pyrex flask containing xenon and fluorine to direct sunlight. When carried out using UV light emitted from a mercury lamp and a gaseous mixture of xenon and fluorine in a 2:1 molar ratio, with up to 1 mol % HF serving as a catalyst, this method can be employed to produce XeF_2 on a kilogram scale (Figure 1.3) [52], [71].

The bonding in XeF_2 can be rationalized as a three-center–four-electron system, where a combination of three atomic orbitals provides three molecular orbitals, of which the bonding and non-bonding are occupied, each by two electrons, giving a net bond order of 0.5. It was also shown that the bonding in XeF_2 can be viewed in terms of resonance valence bond model, where its electronic structure is described as a resonating combination of the forms $F–Xe^+\ F^-$, $F^-\ Xe^+–F$, and $F^-\ Xe^{2+}\ F^-$ [72]. Both of the proposed models predict a similar charge distribution of the XeF_2 molecule, which amounts to $^{-0.5}F–Xe^{+1}–F^{-0.5}$. Recently, it was shown that these descriptions fail to fully account for the large stability shown by XeF_2, and that charge-shift bonding plays a pivotal role in stabilizing the molecule. Considerable resonance energy is found both within the $Xe^+–F$ fragments, and from the mixing of the aforementioned ionic and covalently-bound structures, with the resonance energy comparable to the strength of the bonds themselves [73].

Melting point of XeF_2 is 402.18 K and it exhibits vapor pressure of 600 Pa at room temperature, which allows for it to be sublimed under vacuum without decomposition [31]. XeF_2 dissolves without reaction in a variety of inorganic and selected organic solvents, including BrF_3, BrF_5, IF_5, anhydrous HF (aHF), and CH_3CN [74]. Owing to its kinetic stability, it decomposes only slowly in neutral or acidic aqueous solution, from which it can even be recovered by CCl_4 extraction or fractional distillation [52]. The solubility of XeF_2 in aHF is especially high, amounting to 167 g/100 g HF at 29.95 °C making it a very suitable medium for the synthesis of XeF_2-derived compounds [75].

Dissolved in aHF it is able to oxidize elements, lower fluorides, halides and halo complexes, oxides and carbonyls [76]. Its oxidizing power is even greater in the molten state. In aHF solutions, XeF_2 is capable of oxidizing manganese and platinum only up Mn^{III} and Pt^{IV} [76], [77], whereas treatment with molten XeF_2 readily affords complexes of Mn^{IV} and Pt^{V} [78], [79]. Further illustrating its versatility as an oxidant, XeF_2 has been employed for the fluorination of graphene [80] and fullerenes [81], and combinations of XeF_2 with fluoride-ion acceptors have been successfully used as one-electron oxidizers [82]. The utility

of XeF_2 as an oxidative fluorinating reagent is enhanced by the inertness and volatility of its reduction product, xenon, which can be easily separated from the reaction products.



Figure 1.3: Glass bulb ($V \approx 10$ L) containing photochemically prepared XeF_2, later used in the experiments described in this work.

1.3.1 Interactions of XeF_2 with Lewis acidic species

XeF_2 is a moderately strong Lewis base and a medium-strength fluoride-ion donor, placing it between the other two binary xenon fluorides in fluoride-donor ability, which decreases in the order $XeF_6 > XeF_2 >> XeF_4$. This trend is consistent with the enthalpies of ionization, which increase in the same order ($\Delta H_0 = 9.24$ eV, 9.45 eV, 9.66 eV for XeF_6, XeF_2, and XeF_4, respectively) [83]. Depending on the strength of the Lewis acid that interacts with it, XeF_2 forms compounds in which the XeF_2 molecule is at various stages of its ionization pathway $XeF_2 \rightarrow XeF^+ + F^-$ [84]. Ion donor ability of XeF_2 is thermodynamically favored due to the increase of Xe–F bond energy during the formation of the cation (133.9 kJ/mol in XeF_2, 195.9 kJ/mol in XeF^+) [52]. Upon abstraction of fluoride ion from XeF_2, the bond between Xe and the remaining F^- in the XeF^+ cation becomes a two-electron bond [70].

The strongest fluoride ion acceptors have the ability to abstract a fluoride ion from XeF_2, forming tight-ion pairs of XeF^+ cations or salts of the discrete $Xe_2F_3^+$ cation. Typical examples of such reagents are highly Lewis-acidic pentafluorides, e.g., SbF_5, AsF_5 and BiF_5. Generally, reactions of XeF_2 with these pentafluorides afford compounds in three stoichiometries: $2XeF_2 \cdot MF_5$, $XeF_2 \cdot MF_5$ and $XeF_2 \cdot 2MF_5$. The structures of 2:1 compounds consist of well-separated $Xe_2F_3^+$ cations and MF_6^- anions, with single-crystal X-ray diffraction (SCXRD) revealing that $Xe_2F_3^+$ cations are planar V-shaped species [85]. The latter two stoichiometries form compounds with molecular structures, where XeF_2 donates one of its fluorides to MF_5, which leads to the formation of a tight-ion pair salt

with either a mononuclear MF_6^- or dinuclear $M_2F_{11}^-$ anion. Structural investigations of these compounds revealed pronounced distortion of the XeF_2 unit, characterized by significant elongation of the bridging Xe–F_b bond and concurrent shortening of the terminal Xe–F_t bond [39], [86]. In the most extreme case where XeF_2 is reacted with excess of the Lewis superacid SbF_5 to give $[XeF][Sb_2F_{11}]$, its crystal structure exhibits a bridging Xe–F_b distance elongated to 2.343(4) Å and Xe–F_t terminal bond contracted to 1.888(4) Å [39]. Raman spectroscopy has likewise proven to be an effective probe of XeF_2 ionization. Raman spectra of salts containing $Xe_2F_3^+$ display a characteristic doublet at approximately 580 to 600 cm^{-1}, assigned to the symmetric and antisymmetric Xe–F stretching modes, whereas Xe–F stretches of the XeF^+ cations typically appear at Raman shifts above 600 cm^{-1}. In both cases, these values are approximately 100 cm^{-1} higher than the ν_1 band of solid XeF_2 (496 cm^{-1}) [87].

Alternatively, XeF_2 can also interact with comparatively weaker fluoride-ion acceptors, leading to formation of compounds in which the abstraction of the fluoride ion is incomplete and the bonding within the XeF_2 fragment retains a predominantly covalent character. Such behavior is observed, for example, in reactions of XeF_2 with metal tetrafluorides (discussed in detail in Section 1.5), metal(VI) oxidetetrafluorides [88], [89], [90], [91], or vanadium(V) oxidetrifluoride [92]. The crystallographically characterized $XeF_2 \cdot MOF_4$ and $XeF_2 \cdot 2MOF_4$ adducts form molecular species [90], [91], resembling those encountered in XeF_2–MF_5 complexes, whereas the structures of XeF_2–VOF_3 adducts reveal polymeric arrangements of interconnected $[VOF_5]$ octahedra, giving rise to motifs similar to those found in XeF_2–MF_4 adducts [92]. Across these series of compounds, an increase in the $MF_4/MOF_4/MOF_3$:XeF_2 ratio correlates with a pronounced increase of the Lewis acidity of the F-bridged (oxido)fluoridometal fragments. This effect is particularly evident in $[Xe_2F_3][Ti_8F_{33}]$ and $[XeF]_2[Ti_9F_{38}]$ (Section 1.5.1), as well as in $XeF_2 \cdot 4VOF_3$, which exhibits a degree of XeF_2 polarization comparable to that in $[XeF][BiF_6]$ [92].

Another important facet of XeF_2 chemistry is its ability to act as a ligand to metal ions. Reactions of XeF_2 with metal salts containing weakly coordinating anions (WCA) afford compounds of the general formula $[M^{n+}(XeF_2)_p(WCA)_n]$ which constitute a structurally diverse family (see Section 4.5) [93], [94], [95]. The ligand role of XeF_2 is not limited only to metal centers, as it has also been shown to coordinate both halogen centers in the $BrOF_2^+$ [96] and BrO_2^+ [97] cations as well as the xenon center in the XeF_5^+ cation [84].

1.4 Investigations on the Nature of $XePtF_6$ and Related Compounds

Subsequent investigations into $XePtF_6$ revealed that the stoichiometry of the reaction product formed between Xe and PtF_6 is not invariably 1:1. Instead, the product was shown to have a composition of $Xe(PtF_6)_x$, with x between 1 and 2, depending on the initial Xe:PtF_6 ratio. When deposited as thin films, the adduct appeared yellow, whereas in bulk it was deep red and exhibited a plastic-like consistency. Heating Pt-rich material to 165 °C induced its decomposition, yielding XeF_4 and a brick-red solid with composition $XePt_2F_{10}$, which was identified to contain platinum in the +4 oxidation state [98].

Initially, the platinum oxidation state in $XePtF_6$ was proposed to be +5, based on the preparation of alkali metal hexafluoridoplatinates(V) from IF_5 solutions of alkali fluorides and $Xe(PtF_6)_x$. Furthermore, the IR and UV–vis absorption bands recorded for the product with $x = 1.7$ closely resembled those of potassium and dioxygenyl hexafluoridoplatinate(V), lending additional support to the $Xe^+PtF_6^-$ formulation. Nevertheless, the characterization of the adducts was hampered by the absence of powder X-ray diffraction pattern for

compositions approaching $x = 1$, whereas complex patterns were observed in samples richer in platinum [98].

The nature of the platinum-rich phase was later clarified when its diffraction pattern was shown to match that of $[XeF][PtF_6]$, prepared independently from XeF_2 and PtF_5 in BrF_5 solution [99]. On this basis, it was proposed that initially formed $XePtF_6$ spontaneously reacts with excess PtF_6, yielding $[XeF][PtF_6]$ and PtF_5 (Eq. 1.1).

$$XePtF_6 + PtF_6 \rightarrow [XeF][PtF_6] + PtF_5 \tag{1.1}$$

The formation of amorphous PtF_5 is also consistent with the observation that $[XeF][Pt_2F_{11}]$ forms upon warming the sample with the $Xe(PtF_6)_2$ composition to 60 °C [99]. Since the product of the spontaneous reaction at room temperature is known to contain $[XeF][PtF_6]$, the reaction must proceed as (Eq. 1.2):

$$[XeF][PtF_6] + PtF_5 \xrightarrow{60\ °C} [XeF][Pt_2F_{11}] \tag{1.2}$$

In total, the study of the interaction between XeF_2 and PtF_5 in BrF_5 solution yielded adducts in three stoichiometries: 2:1, 1:1, and 1:2. Spectroscopic evidence indicated that the 2:1 compound can be formulated as a salt of the $[Xe_2F_3]^+$ cation $[Xe_2F_3][PtF_6]$, whereas the 1:1 and 1:2 species were proposed to be tight ion-pair salts $[XeF][PtF_6]$ and $[XeF][Pt_2F_{11}]$, respectively, with molecular structures [99].

Subsequently, the XeF_2–PtF_4 system was explored further by investigating the reaction of platinum tetrafluoride with molten XeF_2 [79]. Unexpectedly, PtF_4 was oxidized by the XeF_2 melt and upon removal of excess volatiles $[Xe_2F_3][PtF_6]$ was recovered (Eq. 1.3):

$$5XeF_2 + 2PtF_4 \xrightarrow{140–150\ °C} 2([Xe_2F_3][PtF_6]) + Xe \tag{1.3}$$

This reaction clearly demonstrates both the oxidizing strength and the fluoride donor ability of molten XeF_2. Upon exposure of the salt to dynamic vacuum at 70 °C, its decomposition to $[XeF][PtF_6]$ and XeF_2 was observed (Eq. 1.4).

$$[Xe_2F_3][PtF_6] \xrightarrow{70\ °C,\ \text{dynamic vacuum}} [XeF][PtF_6] + XeF_2 \tag{1.4}$$

Pyrolysis of the 1:1 compound at 160 °C under vacuum led to formation of XeF_4 and $XeF_2 \cdot 2PtF_4$ (Eq. 1.5).

$$2([XeF][PtF_6]) \xrightarrow{160\ °C,\ \text{dynamic vacuum}} XeF_2{\cdot}2PtF_4 + XeF_4 \tag{1.5}$$

The $XeF_2 \cdot 2PtF_4$ obtained in this way was shown to be identical to the $XePt_2F_{10}$ compound of the same composition previously generated by pyrolysis of the Pt-rich product from the Xe/PtF_6 reaction. Furthermore, $XeF_2 \cdot 2PtF_4$ was found to decompose under dynamic vacuum at 460 °C, regenerating XeF_2 and PtF_4 (Eq. 1.6).

$$XeF_2{\cdot}2PtF_4 \xrightarrow{460\ °C,\ \text{dynamic vacuum}} PtF_4 + XeF_2 \tag{1.6}$$

Taken together, all reactions ensuing from the initial XeF_2/PtF_4 interaction have the net effect of converting 2 mol of XeF_2 into 1 mol of Xe and 1 mol of XeF_4. Although $XeF_2 \cdot 2PtF_4$ was shown to be crystalline, it did not yield single crystals suitable for SCXRD, and structural information could therefore only be inferred from its Raman spectrum. A Raman band at 610 cm^{-1} was attributed to the XeF^+ cation, forming a tight

ion-pair salt paired with a fluoridoplatinate(IV) anion, whose structure was proposed to be either oligo- or polymeric [79].

At the turn of the century, Bartlett published one final report on the structure of $XePtF_6$ [100]. A new method for preparing nearly stoichiometric $XePtF_6$ from the Xe/PtF_6 reaction was reported, in which PtF_6 gas was diluted with inert SF_6 and co-condensed with Xe at −196 °C. The reaction was then initiated by slowly warming the mixture, ensuring that all PtF_6 reacted with Xe and minimizing subsequent interaction between $XePtF_6$ and excess PtF_6. This was reflected in the product color, which was yellow rather than the deep red associated with PtF_5 impurities. Structural characterization again proved impossible, as the material yielded neither an X-ray diffraction pattern nor Raman spectra, and magnetic measurements indicated it is only weakly paramagnetic. Since this could be attributed to unavoidable traces of $[XeF][PtF_6]$ and PtF_5, $XePtF_6$ itself likely is diamagnetic and thus a compound of tetravalent platinum, formulated as an adduct $XeF_2 \cdot PtF_4$.

The direct preparation of $XeF_2 \cdot PtF_4$ was also attempted by reacting PtF_4 with XeF_2 in aHF solvent. A large excess of XeF_2 was used to ensure complete dissolution of PtF_4, affording a yellow solution whose ^{19}F NMR spectrum showed the presence of $[PtF_6]^{2-}$ anions. After removal of the solvent and excess XeF_2, a diamagnetic solid of composition $nXeF_2 \cdot PtF_4$ ($0.95 \leq n \leq 1.59$) was obtained (Eq. 1.7) [100].

$$XeF_2 + PtF_4 \xrightarrow{\text{aHF}} nXeF_2{\cdot}PtF_4 \qquad (0.95 \leq n \leq 1.59) \qquad (1.7)$$

Structural characterization again proved impossible, as the solid produced no X-ray diffraction pattern and yielded only broad bands in its Raman spectrum.

1.5 Structural Chemistry of XeF_2–MF_4 Systems

As all attempts to structurally investigate $XeF_2 \cdot PtF_4$ yielded only amorphous material, insight into its structure were instead sought by systematically examining the interactions of XeF_2 with other metal tetrafluorides. XeF_2 was found to combine with the tetrafluorides of Ti, Cr, Mn, Pd, and Sn to form compounds of general formula $aXeF_2 \cdot bMF_4$ with widely varying a:b ratios [52]. Structural investigations again proved difficult, but a number of crystal structures have been reported, showing rich structural diversity. Nevertheless, poor crystallinity is a recurring feature in this family, and the number of reported phases in these systems greatly exceeds the subset that has been structurally characterized.

1.5.1 XeF_2–TiF_4 system

The first compound reported from the XeF_2–TiF_4 system was $2XeF_2 \cdot TiF_4$, obtained from XeF_2/TiF_4 melt [101]. Although another study claimed preparation of $2XeF_2 \cdot TiF_4$ from $TiCl_4$ and XeF_2 [102], a compound with such composition was subsequently not obtained by other laboratories [52]. Investigations of the catalytic effect of TiF_4 on XeF_2 synthesis yielded additional phases in the XeF_2–TiF_4 system, namely $3XeF_2 \cdot 2TiF_4$, $XeF_2 \cdot TiF_4$ and $XeF_2 \cdot 2TiF_4$ [103]. These compounds can also be accessed either by reacting hydrazinium(II) hexafluoridotitanate(IV) with XeF_2 at 120 °C or by reacting XeF_2 with TiF_4 at room temperature, both routes affording $3XeF_2 \cdot 2TiF_4$. Decomposition of 3:2 phase under dynamic vacuum at 60 °C produces $XeF_2 \cdot TiF_4$, which further loses XeF_2 under dynamic vacuum at 75 °C to form $XeF_2 \cdot 2TiF_4$ [103].

Subsequent reexploration of thermal reactions in the XeF_2–TiF_4 system led to two additional crystalline phases, $[Xe_2F_3][Ti_8F_{33}]$ and $[XeF]_2[Ti_9F_{38}]$ (Figure 1.4) [104]. Both were prepared by heating the mixture of XeF_2 with excess TiF_4 at 135 °C, followed by slow cooling to 110 °C to afford colorless crystals with distinct morphologies. Structural

investigation revealed that both compounds contain ionized XeF_2-derived species. The crystal structure of $[Xe_2F_3][Ti_8F_{33}]$ comprises $[TiF_6]$ octahedra linked via F-bridges into octameric cube-like units. These octamers are further connected through six shared fluoride vertices to generate complex anionic layers, with the charge balanced by $Xe_2F_3^+$ cations. In contrast, $[XeF]_2[Ti_9F_{38}]$ consists of trigonal prismatic $[Ti_9F_{38}]$ units, resembling the arrangement in solid TiF_4 [105], which are joined by pairs of bridging fluorine atoms into polymeric chains. Each $[Ti_9F_{38}]$ unit contains two coordinated XeF_2 molecules, whose geometries are sufficiently perturbed to justify a tight-ion pair formulation [Xe–F_t = 1.882(4) Å, 1.890(5) Å; Xe–F_b = 2.219(4) Å, 2.245(4) Å].

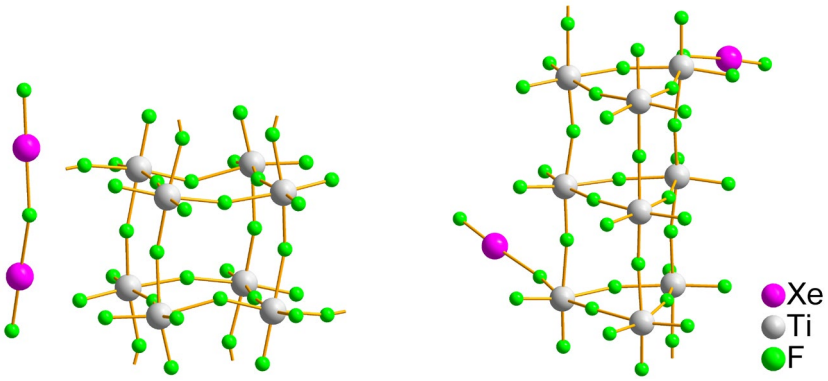


Figure 1.4: Sections of the crystal structures of $[Xe_2F_3][Ti_8F_{33}]$ (left) and $[XeF]_2[Ti_9F_{38}]$ (right) [104].

Additionally, crystalline $3XeF_2 \cdot 2TiF_4$ was prepared from equimolar solution of XeF_2 and TiF_4 in aHF by slow evaporation of the solvent (Eq. 1.8) [106].

$$3XeF_2 + 2TiF_4 \xrightarrow{aHF} 3XeF_2{\cdot}2TiF_4 \tag{1.8}$$

Its structure comprises $[TiF_6]$ octahedra linked through fluorine bridges into infinite zigzag *cis*-chains (Figure 1.5). Each $[TiF_6]$ octahedron also incorporates one F atom donated by a coordinated XeF_2 ligand. The XeF_2 unit is markedly less polarized than in the aforementioned $[XeF]_2[Ti_9F_{38}]$, with Xe–F_t and Xe–F_b distances of 1.922(4) Å and 2.133(3) Å, respectively. In addition, free XeF_2 molecules are co-crystallized in the structure and interact with neighboring atoms solely through electrostatic interactions.

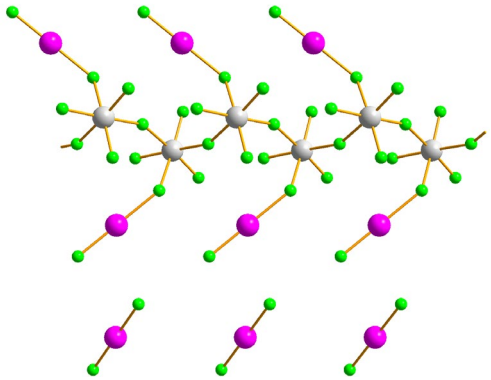


Figure 1.5: Section of the crystal structure of $3XeF_2 \cdot 2TiF_4$ [106].

1.5.2 XeF_2–CrF_4 system

The first report of a compound containing both Xe and Cr was published in 1971 [107]. Study of the reactions of CrF_5 with XeF_2 showed that, when a large excess of XeF_2 was employed, a nonvolatile product with a composition close to $XeCr_2F_{10}$ was obtained, with chromium in the +4 oxidation state. In a subsequent reinvestigation of this system, $XeF_2 \cdot CrF_4$ was prepared by condensing CrF_5 into a FEP ampoule charged with a large excess of XeF_2 and allowing the mixture to react at 50 °C for several hours, followed by removal of volatile components (Eq. 1.9) [108].

$$m\mathrm{CrF_5} + n\mathrm{XeF_2} \xrightarrow{50\ ^\circ\mathrm{C}} m(\mathrm{XeF_2{\cdot}CrF_4}) + 0.5m\mathrm{XeF_4} + (n{-}1.5m)\mathrm{XeF_2} \qquad (1.9)$$

Blue crystals of nonvolatile $XeF_2 \cdot CrF_4$ remaining in the reactor were suitable for single-crystal X-ray diffraction. The crystal structure of $XeF_2 \cdot CrF_4$ was determined to comprise infinite *trans*-chains of $[CrF_6]$ octahedra each bearing a bound XeF_2 molecule (Figure 1.6).

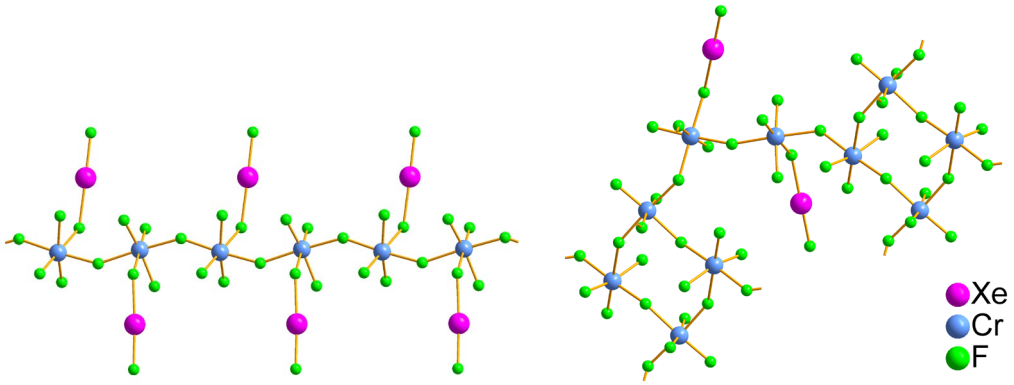


Figure 1.6: Crystal structures of $XeF_2 \cdot CrF_4$ (left) [108] and $XeF_2 \cdot 2CrF_4$ (right) [109].

The Xe—F_t and Xe—F_b bond lengths were determined to measure 1.93(2) Å and 2.13(2) Å, respectively, consistent with only partial ionization of XeF_2 and supporting its description as an adduct. This was the first member of the XeF_2–MF_4 family of compounds whose structure was established by SCXRD, and due to its $XeMF_6$ stoichiometry, it was proposed as a potential structural model for $XePtF_6$ ($XeF_2 \cdot PtF_4$) [100].

The crystal structure of $XeF_2 \cdot 2CrF_4$ was also elucidated [109]. This phase was obtained by solvolysis of $XeF_2 \cdot CrF_4$ in aHF, followed by decantation of the dissolved XeF_2 and aHF, leaving small amount of XeF_2 and excess CrF_4 to react further and form the 1:2 compound. Its basic structural unit consists of four symmetry-independent $[CrF_6]$ octahedra, with XeF_2 bound to two chromium centers. Four $[CrF_6]$ octahedra assemble into tetrameric rings, which are interconnected by linkers consisting of pairs of $[CrF_6]$ octahedra bearing two coordinated XeF_2 molecules, with each ring engaging in six such connections (Figure 1.6). This connectivity extends continuously in two dimensions, giving rise to a complex layered structure. Relative to other tetrafluoride-rich members of the XeF_2–MF_4 family, XeF_2 ionization in this structure is comparably mild, with Xe–F_t distances of 1.903(3) Å and 1.927(3) Å and Xe–F_b bond lengths of 2.186(3) Å and 2.127(3) Å.

1.5.3 XeF_2–MnF_4 system

During studies of the catalytic effect of MnF_3 on the synthesis of XeF_2 from Xe and F_2 at elevated temperatures and pressures, it was observed that xenon forms a compound with manganese [110]. After removal of volatile components, a solid was obtained in which Mn

and Xe were present in a 1:1 ratio, with fluorine content varying between experiments between the values of 5–6. To investigate this material in detail, XeF_2 was subsequently reacted with MnF_2 at 120 °C for 60 hours [78]. After a prolonged evacuation of volatiles, a solid with the composition $XeMnF_6$ was obtained. Magnetic susceptibility measurements indicated that this compound possessed Mn in the +4 oxidation state. It was further shown that $XeF_2 \cdot MnF_4$ decomposes upon heating to 120 °C under dynamic vacuum to give $XeF_2 \cdot 2MnF_4$ and XeF_2 [111]. Both products were examined by PXRD, Raman, and IR spectroscopy, however, the limited availability of reference data for related materials precluded further structural insight.

A later reinvestigation of the XeF_2–MnF_4 system was considerably more successful with respect to crystal structure determination of these compounds [112]. It was discovered, that oxidation of MnF_2 by molten XeF_2 at 120 °C led to the formation of $3XeF_2 \cdot 2MnF_4$ rather than $XeF_2 \cdot MnF_4$ as initially reported (Eq. 1.10).

$$n\mathrm{XeF_2} + 2\mathrm{MnF_2} \xrightarrow{120\text{–}125\ ^\circ\mathrm{C},\quad 96\mathrm{h}} 3\mathrm{XeF_2{\cdot}2MnF_4} + 2\mathrm{Xe} + (n\text{–}5)\mathrm{XeF_2} \tag{1.10}$$

This reaction afforded wine-red single crystals of $3XeF_2 \cdot 2MnF_4$ which were assessed by SCXRD and shown to be isostructural with the titanium analogue, $3XeF_2 \cdot 2TiF_4$. Its structure similarly consists of $[MnF_6]$ octahedra, each bearing a bound XeF_2 molecule, linked by fluoride bridges into infinite zigzag *cis*-chains, with additional XeF_2 molecules co-crystallized in the structure (Figure 1.7). The XeF_2 molecules coordinated to Mn exhibit Xe–F_t and Xe–F_b bond lengths of 1.909(11) Å and 2.16(1) Å, respectively, consistent with an intermediate degree of ionization and supporting an adduct formulation [84].

Solvolysis of the 3:2 phase in aHF, followed by removal of volatiles and recrystallization of the residue, afforded single crystals of $XeF_2 \cdot MnF_4$ (Eq. 1.11), enabling determination of its crystal structure [112].

$$3\mathrm{XeF_2{\cdot}2MnF_4} \xrightarrow{\mathrm{aHF}} 2(\mathrm{XeF_2{\cdot}MnF_4}) + \mathrm{XeF_2} \tag{1.11}$$

The structure of $XeF_2 \cdot MnF_4$ was found to be molecular, comprising octahedrally coordinated Mn centers connected via two fluoride bridges into tetrameric rings (Figure 1.7). Each Mn atom bears one fluoride ligand donated by a coordinated XeF_2 molecule, with two of the XeF_2 molecules positioned above and two below the plane of the ring. As observed in the structure of $3XeF_2 \cdot 2MnF_4$, the Xe—F bond lengths indicate only partial ionization of the bound XeF_2 [Xe–F_t = 1.901(13) Å, 1.903(13) Å; Xe–F_b = 2.170(11) Å, 2.173(12) Å]. Notably, such tetrameric ring motif, similar to the rings found in the crystal structures of some transition metal pentafluorides [113], had been explicitly proposed earlier as a plausible structural model for both $XeF_2 \cdot PdF_4$ and $XeF_2 \cdot PtF_4$ [79].

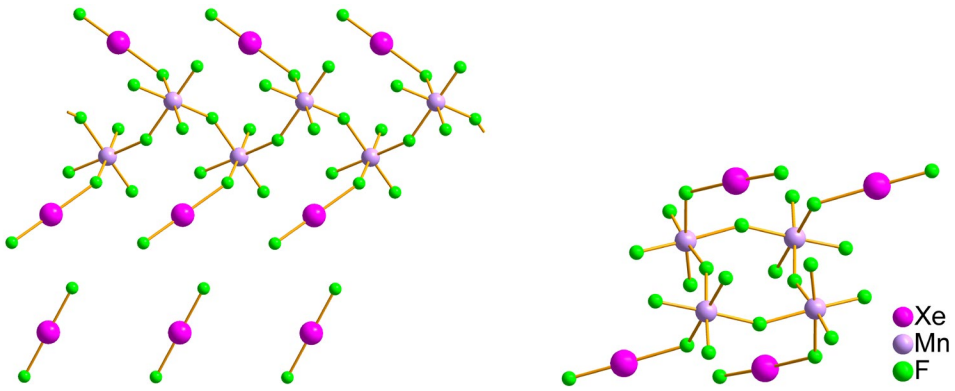


Figure 1.7: Crystal structures of $3XeF_2 \cdot 2MnF_4$ (left) and $XeF_2 \cdot MnF_4$ (right) [112].

1.5.4 XeF_2–PdF_4 system

The study of xenon difluoride–palladium tetrafluoride system established it as one of the closest relatives to the XeF_2–PtF_4 family of compounds. Stemming from the interaction of PdF_4 with molten XeF_2, adducts with XeF_2:PdF_4 stoichiometric ratios of 4:1, 3:1, 2:1, 1:1 and 1:2 were reported to form [79]. All XeF_2-rich phases loose XeF_2 at or below room temperature when exposed to dynamic vacuum, ultimately affording $XeF_2 \cdot PdF_4$ (Eq. 1.12).

$$n\mathrm{XeF_2{\cdot}PdF_4} \xrightarrow{\text{RT, dynamic vacuum}} \mathrm{XeF_2{\cdot}PdF_4} + (n{-}1)\mathrm{XeF_2} \tag{1.12}$$

Upon exposing $XeF_2 \cdot PdF_4$ to dynamic vacuum at 140–150 °C it decomposed to yield $XeF_2 \cdot 2PdF_4$ and XeF_2 (Eq. 1.13).

$$2(\mathrm{XeF_2{\cdot}PdF_4}) \xrightarrow{\text{140–150 °C, dynamic vacuum}} \mathrm{XeF_2{\cdot}2PdF_4} + \mathrm{XeF_2} \tag{1.13}$$

Pyrolysis of this Pd-rich compound could be achieved at 280 °C when notably, Pd_2F_6 and XeF_4 were isolated (Eq. 1.14).

$$\mathrm{XeF_2{\cdot}2PdF_4} \xrightarrow{\text{280 °C, dynamic vacuum}} \mathrm{Pd_2F_6} + \mathrm{XeF_2} \tag{1.14}$$

It was also revealed that Pd_2F_6 can, in turn, be oxidized by excess liquid XeF_2, releasing xenon and producing the same XeF_2-derived phases as those obtained from reactions between XeF_2 and PdF_4. This demonstrated that the overall sequence of reactions results in disproportionation of XeF_2 to Xe and XeF_4, analogous to the behavior observed in the platinum system [79]. Because $XeF_2 \cdot PdF_4$ proved to be amorphous, no structural information could be obtained by X-ray diffraction techniques. However, on the basis of vibrational spectroscopy, it was proposed that 2:1 and 1:1 phases are both salts of the XeF^+ cation [79], [85]. The structure of $XeF_2 \cdot PdF_4$ was further suggested to contain either polymeric or discrete anions, with the simplest discrete motif being a tetrameric ring, analogous to those observed in the crystal structures of Rh, Ir, and Pt pentafluorides [79]. The amorphous nature of $XeF_2 \cdot PdF_4$ was also taken to indicate a broader structural relationship with the similarly amorphous $XeF_2 \cdot PtF_4$. Likewise, $XeF_2 \cdot 2PdF_4$ was found to be closely related to its platinum analogue on the basis of both Raman spectroscopy and its powder X-ray diffraction pattern. Raman data further indicated that both compounds are XeF^+ salts, featuring Xe–F_t stretching modes at Raman shifts above 600 cm^{-1}.

When the interaction of excess XeF_2 with PdF_4 in aHF solvent was examined, partial reduction of PdF_4 to Pd_2F_6 was observed, accompanied by oxidation of XeF_2 to XeF_4 [100]. This contrasts with reactions in molten XeF_2, where the oxidation of Pd_2F_6 was observed, further underscoring the greater oxidizing power of XeF_2 melt relative to the solution of XeF_2 in aHF at room temperature. Analysis of the amorphous orange solid obtained after the removal of volatiles, formed under conditions that produced the smallest amount of Pd_2F_6, showed it to be diamagnetic, with the combining ratio of XeF_2 and PdF_4 likely equal to 1.36:1 (Eq. 1.15)

$$n\mathrm{XeF_2} + \mathrm{PdF_4} \xrightarrow{\text{aHF}} n\mathrm{XeF_2{\cdot}PdF_4} \qquad (n = 1.36) \tag{1.15}$$

1.5.5 XeF_2–SnF_4 system

As in the XeF_2–TiF_4 system, the first reported compound from the XeF_2–SnF_4 system was $2XeF_2 \cdot SnF_4$, supposedly formed upon interaction of XeF_2 with $SnCl_4$ [102]. Subsequent attempts to reproduce this adduct were unsuccessful, and only the phases $3XeF_2 \cdot 4SnF_4$ and $XeF_2 \cdot 2SnF_4$ were obtained [114]. $XeF_2 \cdot 2SnF_4$ was prepared by treating SnF_2 with excess of molten XeF_2 at 140 °C and removing the excess volatiles. The same compound could also be prepared by reacting hydrazinium(II) tetrafluoridostannate(II) with XeF_2 at 60 °C. During the course of the removal of volatiles from the reaction mixture, a distinct change in the slope of the weight-loss curve was observed at a composition corresponding to $3XeF_2 \cdot 4SnF_4$. This compound is not stable at room temperature, readily loosing XeF_2, but could be isolated at 0 °C. Because the Raman spectra of the two phases were very similar, differing primarily by a single band at 509 cm^{-1}, the 3:4 phase was proposed to be a cocrystal of XeF_2 and the 1:2 compound, with the formula $(XeF_2 \cdot 2SnF_4)_2 \cdot XeF_2$.

The XeF_2–SnF_4 system was reinvestigated recently with an emphasis on reactions in aHF. Dissolution of SnF_4 in aHF in the presence of excess XeF_2, followed by slow cooling of the solution to −20 °C, afforded thin, colorless crystals of $[Xe_2F_3][Sn_4F_{17}] \cdot XeF_2 \cdot HF$ [106]. This compound exhibits a highly complex crystal structure, featuring an anionic layer built from six- and seven-coordinated tin centers interconnected via four or five equatorial vertices. Notably, the anionic layer is nonplanar and adopts an unusual sinusoidal topology (Figure 1.8). Sandwiched between such layers are the $[Xe_2F_3]^+$ cations, together with co-crystallized XeF_2 and HF molecules. The presence of $[Xe_2F_3]^+$ cations attests to the pronounced Lewis acidity of the parent Sn_4F_{16} unit.

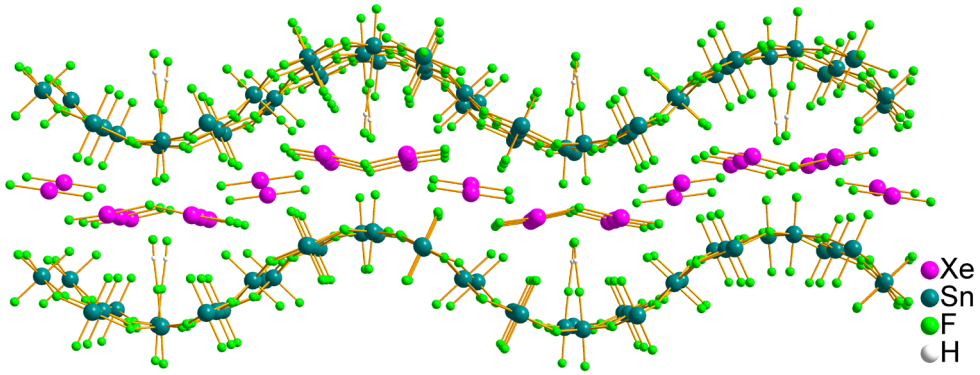


Figure 1.8: Section of the crystal structure of $[Xe_2F_3][Sn_4F_{17}] \cdot XeF_2 \cdot HF$ [106].

1.6 Structural Characterization by 3D Electron Diffraction

As noted above, a recurrent challenge in studies of XeF_2–MF_4 adducts is their limited propensity to form single crystals of sufficient size for SCXRD, with several phases obtained only as crystalline powders. Despite substantial recent advancements in laboratory single-crystal diffractometers, reliable structure determination typically still requires crystals on the order of 50 µm in all three dimensions. This requirement can be relaxed by employing high-flux synchrotron X-ray radiation, which enables structural analysis of crystals only a few micrometers across. However, even this remains inadequate for many materials conventionally described as powders, whose particle sizes are commonly on the nanometer scale. In recent years, detailed structural investigation of such nanosized crystallites has become increasingly feasible owing to rapid development of 3D electron diffraction (3D ED), which probes crystal structures using electrons rather than X-rays. This enables the collection of meaningful diffraction data from much smaller crystal volumes (Figure 1.9),

primarily because electrons interact with matter far more strongly than X-rays. This difference arises from the fundamentally distinct scattering mechanisms, with electrons elastically scattered by the electrostatic potential of the crystal, rather than by its electron density as in X-ray diffraction [115].

Usage of electrons as probes for the observation of diffraction phenomena on crystalline materials is by no means a new idea, as it has emerged directly from the early experimental validation of wave–particle duality. In 1927, Davisson and Germer observed discrete diffraction maxima for electrons scattered from a single-crystal Ni target and by invoking Bragg's law showed that their derived wavelength is in good agreement with the one predicted using de Broglie's wavelength relation [116], [117]. Within months, Thomson and Reid reported powder-like ring patterns from thin polycrystalline films irradiated by high-energy electrons, with the experimentally derived electron wavelength again showing excellent agreement with de Broglie relation and further establishing electron diffraction as an analogue of X-ray diffraction [118]. By the 1930s, electron diffraction was already being used as a standalone crystallographic technique, for example to solve the structures of NH_4Cl and anthracene [119], [120]. Despite this promising start, electron diffraction did not become a routine method for structure determination and, by the mid-20th century, was rapidly eclipsed by SCXRD. This was largely due to the aforementioned strong interaction of electrons with matter, which also results in the electron beam undergoing multiple elastic scattering events while passing through a crystal (dynamical effects). This can scramble the observed intensities away from the kinematical regime, where the observed reflection intensity is proportional to the squared structure factor amplitudes, and are required by standard crystallographic phasing and refinement strategies [121]. In subsequent years, there were sporadic reports of successful *ab initio* structure determinations by electron diffraction [122], however, the method did not develop into a widely adopted approach for routine structure solution. Such work relied on collecting electron diffraction data in a transmission electron microscope (TEM) by orienting the crystals along a low-index zone axis orientation, which facilitates indexing of the reflections but exacerbates dynamical scattering effects and misses a great number of reflections during data collection [115].

In 2007, Kolb and co-workers proposed and implemented automated diffraction tomography method in which a randomly oriented crystal is tilted in discrete goniometer steps and diffraction patterns are collected largely off-zone, thereby deliberately avoiding the most significant dynamical effects associated with zone-axis measurements [123], [124]. This acquisition strategy mirrors established X-ray crystallographic workflows and, because the angular relationships between successive patterns are known, enables reconstruction of a reciprocal space volume from which unit cell parameters, extinction conditions, and reflection intensities can be extracted [125].

Nevertheless, a simple stepwise tilt series can leave angular gaps between adjacent orientations, which can lead to incorrect intensity integration. To minimize these gaps, data collection strategies were extended to incorporate, at each step, either beam precession about a conical surface [126] or a fine beam tilt [127]. More recently, the advent of hybrid pixel detectors with negligible readout times has enabled data acquisition during continuous goniometer rotation, further improving correct diffraction spot intensity sampling [128]. Although modern 3D ED data acquisition protocols markedly mitigate multiple-scattering artefacts, residual dynamical effects often remain sufficiently strong that conventional kinematical refinement, in programs developed for X-ray data, yields relatively high agreement factors, less accurate structural models, and reduced sensitivity to subtle structural features such as displacement parameters, partial occupancies, and light-atom coordinates [125].

To account explicitly for multiple scattering during refinement, Palatinus and co-workers developed a dynamical refinement approach in which the kinematical approximation is replaced by structure factors calculated from dynamical diffraction theory using Bloch-wave formalism [129], [130]. In this procedure, the observed intensities from each recorded frame are treated independently, and crystal thickness is included among the refined parameters. Structures refined dynamically from 3D ED data typically provide substantially improved atomic positions and structural parameters relative to kinematical refinements, approaching the accuracy of models obtained from SCXRD. A key implication is that the positions of light atoms and even hydrogen atoms can be determined reliably in both organic and inorganic structures [131]. Moreover, high-quality dynamical refinements can support modelling of charge transfer between atoms by performing kappa refinement [132] and enable reliable assignment of the absolute configuration of chiral compounds [133].

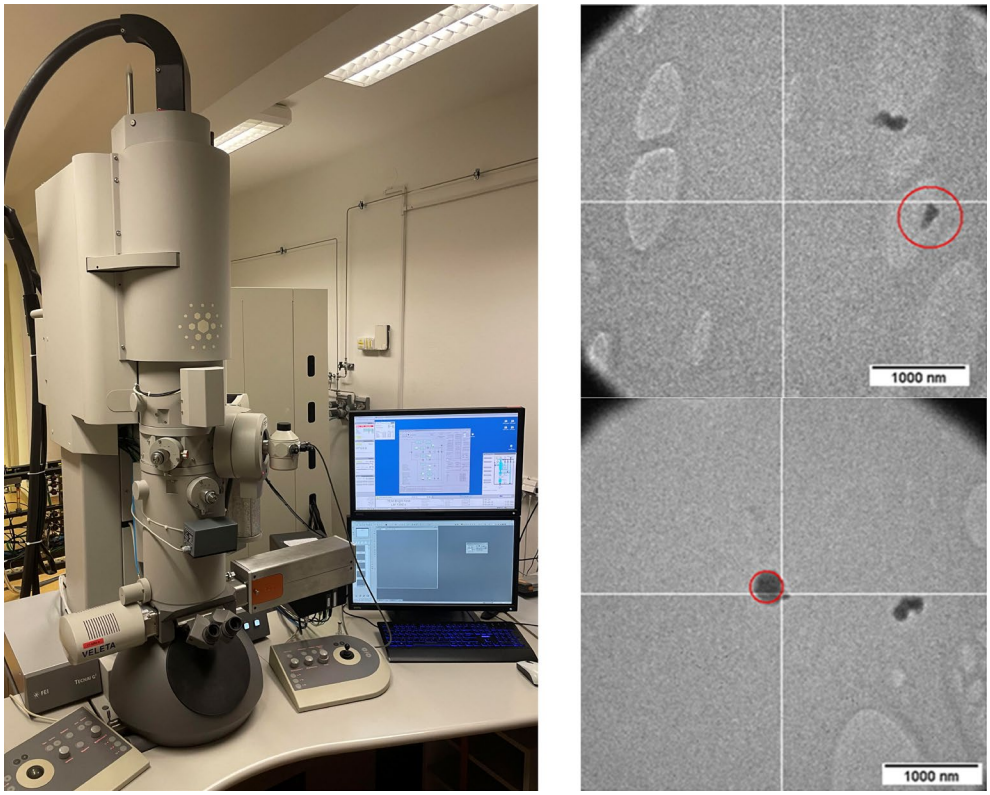


Figure 1.9: TEM adapted for the use as an electron diffractometer installed at the Institute of Physics of the Czech Academy of Sciences in Prague, Czech Republic (left) and micrographs of nano-sized crystallites used for structure determination by 3D ED (right).

Despite the substantial progress and recent successes of 3D ED, the method retains several inherent limitations compared to X-ray diffraction techniques. Although these do not represent unsurmountable obstacles, specific practical considerations are often required to ensure successful 3D ED data acquisition. Firstly, because measurements are performed under high vacuum in a TEM (or a similarly configured dedicated electron diffractometer), volatile compounds or materials prone to solvent loss must be protected during sample insertion, which is commonly achieved by cryogenic handling and maintaining the sample at low temperature during the measurement [134]. Performing the measurements at low temperatures also helps mitigating radiation damage in strongly beam-sensitive specimens [115]. In addition, TEM goniometers are typically limited to rotation about a single axis

and offer a restricted tilt range, often not exceeding about 120° in total. This constraint introduces a missing wedge in the reconstructed reciprocal space and reduces the completeness of captured reflections. When a single tilt series does not provide sufficiently complete data, or when beam damage limits the number of usable frames, diffraction datasets collected from multiple crystallites can be merged into one dataset, which can then be used for structure elucidation [135].

Taken together, these methodological advances have established 3D ED as a mature technique that has been applied to a broad range of materials, including minerals, ceramics, metal-organic frameworks, small molecule pharmaceuticals, and proteins [125]. In spite of the successful application of 3D ED to a wide array of compounds, a class of materials comparatively underexplored by 3D ED are reactive or air-sensitive species, with only a limited number of reports describing structural characterization of air-sensitive organometallic species [136], [137].

1.7 High-Pressure Chemistry

Pressure and temperature are fundamental thermodynamic variables and therefore play central roles in governing both the equilibrium state of a system and the kinetics of its transformations. High-pressure and high-temperature studies are most naturally associated with geoscience and planetary science, because many minerals and phases relevant to planetary interiors exist under such conditions, motivating laboratory investigations of their synthesis and properties under compression. At pressures of tens to hundreds of gigapascals, however, the contribution of pressure to the Gibbs free energy via the PV term becomes comparable to chemical bond energies [138], driving condensed matter into regimes where familiar trends in bonding, structure, and reactivity can change profoundly. This renders high-pressure research attractive not only for planetary contexts, but also for advancing fundamental chemical understanding. Under such conditions, a range of fascinating phenomena has been documented, including the formation of a quartz-like phase from compressed CO_2 [139], polymerization of nitrogen [140] and rich structural chemistry of its anionic derivatives [141], [142], and observation of superconductivity at temperatures as high as 250 K in lanthanum hydride with a clathrate-like structure [143]. Collectively, these examples illustrate a broader principle: high pressure can stabilize bonding and coordination environments that are inaccessible at ambient conditions, thereby expanding accessible chemical space in both stoichiometry and structure.

In the field of high-pressure chemistry, the term “high pressure” generally refers to pressures in the gigapascal range (1 GPa = 10,000 bar). Two principal experimental approaches are used to reach such conditions: dynamic compression (shock waves) and static compression (sustained load). Dynamic compression methods can, at the extreme, access pressures in the terapascal range [144], but are typically generated in very short time scales and impose strong concomitant heating, which severely limits their applicability [145]. By contrast, static techniques maintain elevated pressures over extended periods (from hours to years), enabling systematic investigations of compressed materials using a wide range of analytical methods and providing precise control over the applied pressure. Within the static regime, large-volume presses are particularly valuable for high-pressure synthesis because they can combine pressures of several tens of gigapascals with temperatures exceeding 2000 K using internal heaters and thermocouples [146], producing appreciable sample quantities suitable for *ex situ* characterization and property measurements [147]. The most versatile and commonly used tool for generation of high static pressures is the diamond anvil cell (DAC), which is routinely used to achieve

pressures up to 100 GPa, with specialized designs and configurations allowing access into the terapascal range [148].

The first concepts of devices employing opposed diamond anvils to generate high pressures were demonstrated in 1959 [149], [150], establishing diamond as an especially attractive anvil material for static high-pressure work owing to its exceptional hardness and optical transparency. Although many DAC designs are in use today, they all share the same basic operating principles (Figure 1.10) [151]. A DAC consists of a metal body holding two well-aligned opposing diamond anvils, which are mounted on seats that transfer the applied load from the cell body to the anvils. A gasket containing a central hole is positioned between the small, flat anvil tips (culets), and together these components define the sample chamber that is subsequently compressed. The achievable pressure follows directly from $P = F/A$, and therefore reducing the culet area is a key strategy for extending the accessible pressure range. The gasket is typically a metal (e.g., stainless steel or rhenium) that is pre-indented and then drilled to form the sample chamber, with both the indentation thickness and the hole diameter influencing the maximum attainable pressure [145]. The sample may be loaded into the chamber together with a pressure-transmitting medium, thus ensuring uniform pressure distribution within the sample chamber. Numerous materials including soft solids, chemically inert fluids, and noble gases have been evaluated as pressure-transmitting media, [152], [153], [154], and their selection is generally dictated by the targeted pressure range and chemical compatibility with the sample.

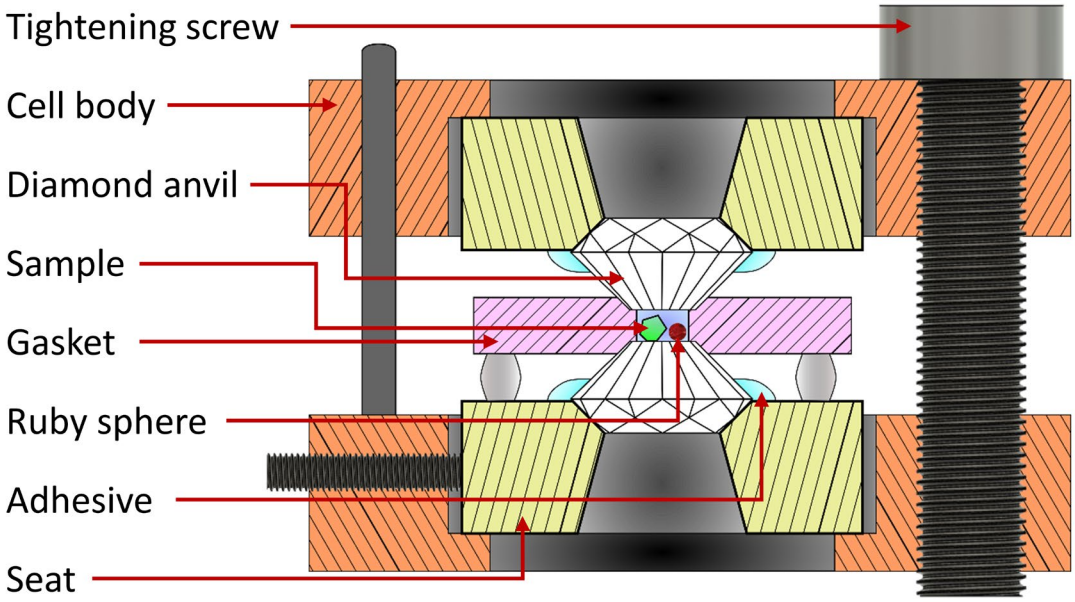


Figure 1.10: Schematic cross section of a DAC highlighting its components. Graphic is courtesy of Dr. Miha Virant [155].

Determination of pressure within a DAC is most commonly performed by ruby fluorescence method. One or more small ruby chips or balls are loaded into the sample chamber and excited with laser light, producing a characteristic fluorescence spectrum dominated by two sharp lines [156]. The pressure is obtained from the shift of the R_1 line using an established calibration scale, with the most recent calibrations reported to provide an accuracy of 2.5% up to the pressure of 150 GPa [157]. Alternatively, pressure may be determined by X-ray diffraction through measurement of unit-cell parameters of a standard material with a well-characterized equation of state [158], or by monitoring the Raman

signal of the diamond anvils [159]. The latter approach is particularly advantageous when the introduction of an internal pressure marker into the sample chamber is undesirable.

A central strength of DAC methods is the ability to combine the generation of extreme pressures with a broad suite of in situ probes, enabled largely by diamond's optical transparency and relatively low X-ray absorption. Accordingly, DAC experiments can be coupled to numerous analytical techniques including X-ray diffraction (single-crystal and powder), Raman and infrared spectroscopy, X-ray absorption spectroscopy, and by using specialized experiment or cell designs even magnetic and electrical conductivity measurements [160]. Synchrotron sources play a key role in modern high-pressure diffraction measurements. Microfocused high-flux beams together with large-area detectors permit data collection from micron-sized and multigrain samples, whereas shorter X-ray wavelengths (< 0.5 Å) and DAC designs offering larger opening angles provide access to a broader region of reciprocal space [151].

Samples enclosed in DACs can also easily be heated, enabling studies of thermally activated transformations at high pressure. Moderate temperatures can be achieved by resistive heating, with reported operation above 1500 K, although the rapid graphitization of diamond above 1900 K presents an intrinsic limit [151]. To reach substantially higher temperatures, laser heating is widely employed. Here, the optical transparency of diamond is again crucial, as it allows infrared lasers (commonly CO_2 or Nd:YAG) to be transmitted and focused onto the sample, producing localized temperatures of several thousand kelvins [161]. Laser-heating systems are now routinely available at synchrotron facilities, and heating can even be performed concurrently with data collection, providing direct insight into pressure and temperature conditions comparable to those in deep planetary interiors [162].

Chapter 2

Aims and Hypotheses

This dissertation focuses on the structural characterization of noble-gas compounds in the XeF_2–MF_4 family. Expanding the structural landscape in these systems will improve our understanding of the Lewis acid-base interactions therein, with a particular emphasis on the structures of $XeF_2 \cdot MF_4$ phases which include first noble-gas compound $XePtF_6$ ($XeF_2 \cdot PtF_4$). Determining the structure of this landmark compound is a central objective, for which high-pressure methods will also be employed. Because crystals of adequate size for SCXRD are challenging to obtain in these systems, 3D ED will likewise be used for structure elucidation. Demonstrating that 3D ED can be applied to structural studies of noble-gas compounds would constitute a significant advance, and the sample-handling procedures developed here are expected to be transferable to a broad range of other reactive or sensitive materials. In addition, this work seeks to enrich the chemistry of xenon difluoride by probing its behavior in aHF solutions in the presence of both Lewis-acidic tetra- and pentafluorides, and by reexploring the coordination chemistry of XeF_2 as a ligand toward alkali metal cations.

2.1 Aims

- Develop and test a sample handling protocol that enables the transfer of moisture-sensitive noble-gas compounds into a TEM for structural analysis by 3D ED.
- Structurally characterize the noble-gas compounds of interest by 3D ED and benchmark the results against SCXRD determinations.
- Reinvestigate the XeF_2–MF_4 (M = Mn, Pd, Pt) systems and attempt to fully characterize all the observed compounds, with particular emphasis on $XeF_2 \cdot MF_4$ stoichiometries that may provide key insights into the structure of $XePtF_6$.
- Probe the chemistry of XeF_2 in systems where both Lewis-acidic tetra- and pentafluorides are present.
- Reexplore the XeF_2–PtF_5 system and pursue structural characterization of its members, which include some of the earliest reported noble-gas compounds.
- Prepare novel examples of coordination compounds with XeF_2 as a ligand to alkali metal cations, with a particular focus on alkali metals heavier than Na, for which no examples have been reported to date.
- Investigate the behavior of $XeF_2 \cdot PtF_4$ under high-pressure and high-temperature conditions and attempt to structurally characterize the resulting crystalline phases by synchrotron-radiation-based SCXRD and Raman spectroscopy.

2.2 Hypotheses

- The structural characterization of noble-gas compounds by 3D ED should be feasible, provided that appropriate care is taken during the transfer of the samples into the TEM.
- Structures of noble-gas compounds elucidated by 3D ED are expected to be comparable to the SCXRD results. Due to recent innovations regarding 3D ED data acquisition and processing, the resulting crystal structures are of increasingly high quality, offering not only insight into the molecular connectivity but yielding precise geometrical parameters. Nevertheless, beam sensitivity and radiation damage could be problematic.
- Reinvestigation of the XeF_2–MF_4 systems should result in successful structural elucidation of several of its members. This is expected due to prior reports of microcrystalline phases $XeF_2 \cdot 2MF_4$ (M = Pt, Pd), identifying them as promising candidates for structural elucidation by 3D ED even if larger single crystals cannot be prepared. These compounds would enrich the structural diversity of the XeF_2–MF_4 family of noble-gas compounds.
- Reacting XeF_2 with both Lewis acidic tetra- and pentafluorides in aHF solvent might result in formation of novel species, as there are currently no reports of such investigations.
- In view of the numerous crystal structures that have already been reported for the related XeF_2–AF_5 systems (A = As, Ru, Sb, Ir, Bi), it is anticipated that the preparation of single crystals of phases belonging to the XeF_2–PtF_5 family will prove feasible, thereby enabling their crystallographic characterization by SCXRD.
- Exploration of the interaction of XeF_2 with $AM^{V}F_6$-type compounds (A = alkali metal; M = transition metal) in aHF for hitherto unexplored transition metal anions, as well as the variation of the crystallization conditions, could result in the isolation of novel examples of coordination compounds where XeF_2 acts as a ligand to alkali metal centers.
- Laser heating of $XeF_2 \cdot PtF_4$ enclosed in a DAC to temperatures above 2000 K and pressurized in the gigapascal range may allow for its crystallization or result in the formation of novel exotic species. LH-DAC experiments with xenon compounds have thus far focused on its binary compounds, presenting a significant opportunity for new discoveries.

Chapter 3

Materials and Methods

3.1 Materials

Table 3.1: Overview of the chemicals used in this work.

Chemical	Source
Anhydrous HF	Linde, 99.995 %
$APtF_6$ (A = Li, Na, K, Rb)	Synthesis (see below)
AsF_5	Synthesis (see below)
F_2	Solvay Fluor, 98–99 %
K_2NiF_6	Advance Research Chemicals, 99.9 %
K_2PdF_6	Synthesis (see below)
K_2PtF_6	Synthesis (see below)
KF	Acros Organics, 99.99%
Li_2PdF_6	Synthesis (see below)
LiF	Aldrich, ≥99.98%
MnF_2	Alfa Aesar, 99%
MnF_4	Synthesis (see below)
NaF	Alfa Aesar 99.99%
Pd	Sigma-Aldrich, 99.9%
PdF_4	Synthesis (see below)
Pt	Thermo Scientific, 99.98%
PtF_4	Synthesis (see below)
PtF_5	Synthesis (see below)
RbF	Alfa Aesar, 99.975%
Xenon	Messer, 99.99 %
XeF_2	Synthesis (see below)
$[XeF][AsF_6]$	Synthesis (see below)

Commercial anhydrous HF was dried and kept dry by storage over the solid K_2NiF_6 in an FEP vessel equipped with PTFE valve.

Alkali metal hexafluoridoplatinates(V) were prepared by adapting a literature procedure, previously applied to the synthesis of $CsPtF_6$ [163]. The selected alkali fluoride and Pt powder were weighed into an FEP reactor in a 1:1 molar ratio, after which aHF solvent

and approximately a 2 to 3-fold excess of F_2 were introduced. The reactor was then placed on a shaker and exposed to UV irradiation. After 24 h, the reactors were recharged with F_2 and irradiated for an additional day. This procedure afforded bright yellow–orange solutions from which yellow solids were isolated. The resulting products were characterized by Raman spectroscopy.

AsF_5 was prepared by static fluorination of As_2O_3 in a nickel pressure vessel [164].

K_2PdF_6, K_2PtF_6, and Li_2PdF_6 were prepared by oxidizing either Pd or Pt metal with excess F_2 in aHF in the presence of two equivalents of the appropriate alkali metal fluoride [165]. In the case of K_2PtF_6, the FEP reactor was wrapped in aluminum foil, to prevent further oxidation to platinum(V), induced by sunlight [166]. Product identities were confirmed by Raman spectroscopy and PXRD.

Synthesis of MnF_4 was conducted following a previously described procedure [167], beginning by reacting MnF_2 suspended in aHF with excess fluorine to form MnF_3, which was then converted to MnF_4 by further reaction with excess fluorine under UV irradiation. The amorphous dark blue-purple product was analyzed by Raman spectroscopy.

PdF_4 was prepared by the addition of AsF_5 to Li_2PdF_6, which was partially dissolved in aHF, following the previously outlined synthesis [100], [168]. However, this reaction consistently produced Pd_2F_6 as a byproduct, which dominated the Raman spectrum of the isolated solid. To obtain high-purity PdF_4, aHF and F_2 were condensed in the reaction vessel containing the Pd_2F_6/PdF_4 mixture, and the suspension was irradiated under UV light with continuous agitation [169]. After 39 hours of UV irradiation, the Raman spectrum of the product showed that the 566 cm^{-1} band attributable to Pd_2F_6, persisted, albeit with a significantly weaker intensity. Additionally, a weak band at 1819 cm^{-1} appeared, indicative of the formation of an O_2^+ cation salt. A further 22-hour round of UV-aided fluorination did not alter the Raman spectrum of the product. Nevertheless, the PXRD of the brick-red solid revealed only the lines attributable to PdF_4.

The synthesis of PtF_4 was conducted in accordance with the literature procedure, commencing with the oxidation of Pt powder by XeF_2 in aHF [77]. The orange-red initial product ($n XeF_2 \cdot PtF_4$) was decomposed by heating it to 430 °C *in vacuo*, yielding brown PtF_4 and collecting the released XeF_2 in a U-shaped FEP trap cooled by liquid nitrogen.

PtF_5 was synthesized by static fluorination of Pt powder enclosed in a nickel pressure vessel [170]. Approximately 4 bar of F_2 was introduced into a reactor containing Pt powder at ambient temperature, corresponding to an F_2:Pt molar ratio of 3.5–2.8:1, and the mixture was then maintained at 350 °C for 8 hours. The reactor was subsequently recharged with F_2 and heated again to the same temperature. This procedure also generated some volatile PtF_6, which was readily removed under dynamic vacuum, leaving the non-volatile, deep-red PtF_5 adhering to the reactor walls.

XeF_2 was synthesized by a photochemical reaction between xenon and fluorine in a thoroughly dried glass apparatus at room temperature, aided by UV light emitted from a medium-pressure Hg lamp as previously described (Figure 1.3) [71]. Its purity was assessed by Raman spectroscopy.

$[XeF][AsF_6]$ was synthesized by condensing an equimolar amount of AsF_5 to a frozen solution of XeF_2 in aHF [39]. The product was subsequently isolated by removing the

volatiles at −45 °C, thus preventing its decomposition to $[Xe_2F_3][AsF_6]$ and AsF_5 [99]. The purity of the product was checked by Raman spectroscopy and PXRD.

3.2 Synthesis Methods

3.2.1 Apparatus

The majority of compounds described herein are pronouncedly air and moisture sensitive, thus requiring their manipulation and study under rigorous anhydrous conditions. The work involving dispensing volatile materials into reactors was conducted on a custom-built fluorine-resistant vacuum line (Figure 3.1).



Figure 3.1: Custom-built vacuum line.

The vacuum line is constructed of nickel, copper, and brass-encased PTFE parts. It is equipped with FEP manifolds, a Monel Helicoid pressure gauge, a soda lime scrubber, two traps cooled with liquid nitrogen, and a two-stage rotary vane pump (Edwards RV3). Reaction vessels were connected to the vacuum line via the FEP manifolds. The vacuum level at the manifolds was periodically monitored using a vacuum gauge (Pfeiffer TPG 201 or Vacuubrand VACUU · VIEW) to detect potential leaks. Under typical operational conditions, a 20-minute exposure to dynamic vacuum produced pressures in the range of 1.9×10^{-1} to 9.1×10^{-2} mbar.

Volatile reagents were introduced into the reactors by immersing the vessels in liquid N_2 and condensing the gases under static vacuum. Before adding volatiles or exposing the reactor contents to the line, the section enclosed by the manifolds, PTFE components, and Helicoid gauge was evacuated under dynamic vacuum for at least 20 minutes. Since the volume of this section (≈22.5 mL, remeasured periodically) was known, this procedure enabled dosing of defined quantities of volatiles into the reaction vessels.

All handling of solid materials and their loading into reaction vessels or capillaries was carried out in an inert-atmosphere glovebox assembly (Vigor SG1200/750E–SG1500/750E), where the H_2O content was maintained below 1 ppm. Prior to transfer into the glovebox, glass weighing vessels, metal spatulas, and agate mortars were thoroughly cleaned (demineralized water, ethanol, acetone) and dried overnight in an oven at 120 °C. Before loading the solids into capillaries, samples were gently ground in an agate mortar. Quartz capillaries (400–600 µm diameter; WJM-Glas Müller) were dried under dynamic vacuum and passivated with F_2. After filling, the capillaries were temporarily sealed with 25-5S halocarbon grease (Halocarbon Corporation), removed from the glovebox, and permanently sealed in an H_2/O_2 flame.

3.2.2 Reaction vessels

Two main types of reaction vessels were employed in this work, either constructed of fluoropolymer parts or nickel metal (Figure 3.2). Prior to their use, all vessels were passivated with 300–700 Torr of F_2 overnight.



Figure 3.2: h-shaped FEP crystallization vessel (left) and nickel reactor (right).

Syntheses involving liquid solvents employed reaction vessels fabricated from cylindrical FEP tubing with i.d. of 4.78, 6, or 16 mm. Each tube was heat-sealed at one end and heat-flared at the other, then joined to the conical end of a PTFE or PCTFE valve to provide a pressure-tight seal. Modified h-shaped vessels, used primarily for crystallization, consisted of two FEP tubes: a straight “main” arm and a “side” arm angled at 90°. Both arms were connected perpendicularly to a PTFE T-section via male–male PTFE connectors such that the angled side arm terminated in parallel to the wider main arm (Figure 3.2). The vessels were closed with a PTFE or PCTFE valve mounted in parallel with the main arm. All PTFE components, including the valves, were enclosed in brass housings to prevent stress-induced deformation, whereas PCTFE valves were mounted in aluminum bodies.

Reactions requiring elevated temperatures or high fluorine pressures were carried out in all-metal reactors. These reactors consist of an argon-arc-welded nickel vessel equipped with a PTFE-gasketed nickel or stainless-steel valve. Prior to use, each reactor was leak-tested by pressurizing it with at least 10 bar of dry N_2.

3.2.3 Thermal syntheses

Thermal reactions carried out at temperatures not exceeding 150 °C were performed by placing the reactors, either all-metal vessels or heat-sealed FEP ampoules, into a preheated oven (Heraeus T12) set to the desired temperature. When crystal growth was targeted, the oven temperature was gradually lowered using one of the preset cooling programs.

Syntheses requiring higher temperatures were conducted in metal reactors positioned in a furnace regulated by a temperature controller (Digi-Sense TC9100). To prevent damage to the PTFE gaskets, the upper part of each reactor was water-cooled via a cooling ring welded onto the vessel, with the circulating water maintained at 20 °C using a cooling-bath thermostat (Huber KISS K6).

A similar heating setup was employed for vacuum pyrolysis, with the distinction that the nickel reactor was additionally connected to the vacuum line through FEP connectors (i.d. 3 mm, o.d. 6 mm) and a U-shaped FEP trap (i.d. 6 mm, o.d. 8 mm) fitted with brass-encased PTFE valves (Figure 3.3). The trap was immersed in liquid nitrogen to condense and collect the evolved volatile products.



Figure 3.3: Experimental setup used for pyrolysis under dynamic vacuum.

3.2.4 UV syntheses

The experimental setup for UV-irradiation syntheses is shown in Figure 3.4. Inside a fume hood, the reactors set for irradiation were secured to a laboratory shaker using elastic bands, with the UV light source positioned above the assembly. UV radiation was supplied either by a 1 kW air-cooled Hg lamp or by an LED source with a nominal optical power of 600 W and emission centered at 365 nm. The shaker was wrapped in aluminum foil to prevent photodegradation of plastic components. Because the reactors heated under UV exposure, particularly when the mercury lamp was used, the temperature at the surface of the FEP reactor was monitored continuously. To facilitate cooling, 12 V DC fans were installed adjacent to the shaker to direct airflow over the reactors.



Figure 3.4: Setup for UV irradiation reactions employing the 600 W LED UV light.

3.3 High-Pressure Diamond Anvil Cell Experiments

For the high-pressure experiments described in Chapter 4.6, Merrill–Bassett and SSDAC80-type cells were used (Figure 3.5). Merrill–Bassett DACs, especially when equipped with larger-diameter culets (>500 µm), enable the generation of pressures up to 10 GPa, whereas the more robust SSDAC80 cells can be configured to reach pressures well in excess of 50 GPa. In all experiments described in this thesis, powdered samples were loaded into the cells without employing a pressure-transmitting medium.

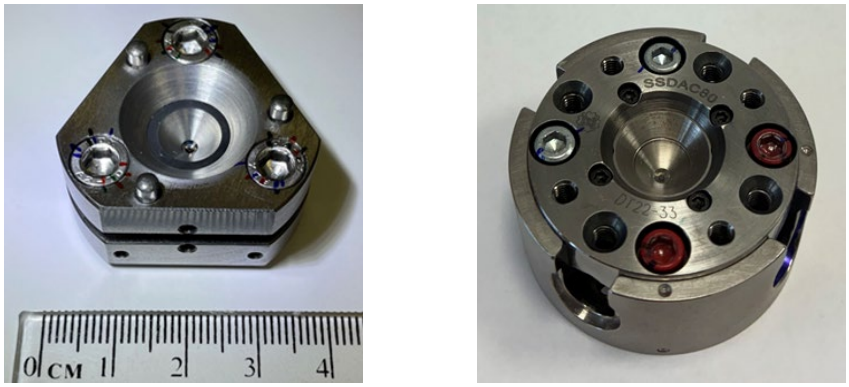


Figure 3.5: Merrill–Bassett (left) and SSDAC80 (right) types of DACs.

Merrill–Bassett DAC [171] was prepared by pairing the cell body with Boehler–Almax design type IIas diamonds [172] with 700 µm diameter culets and tungsten carbide seats (Almax easyLab) [173]. Inconel X750 (Goodfellow, Ni74/Cr15/Fe7/Ti/Al/Nb, annealed) with a starting thickness of 250 µm and pre-indented to 110 µm was employed as gasket material. Gasket hole with a 250 µm diameter was drilled using a spark eroder (LOTO-eng SEC-400). To aid with pressure determination in this experiment, the cell was loaded with 2 ruby balls (BETSA, Al_2O_3:Cr^{3+}, 3600 p.p.m. Cr^{3+}, 3–50 µm mean diameter) [174], and

the pressure generated within the cell was calculated using the Ruby2020 gauge equation [157], implemented in *CrimsonCalc* software [175].

SSDAC80 cells were prepared and loaded by Prof. Dominik Kurzydłowski and Sylwia Olszewska at the Faculty of Mathematics and Natural Sciences, Cardinal Stefan Wyszynski University in Warsaw, Poland. Samples were loaded into SSDAC80-type cells (DAC Tools) equipped with type IIa synthetic diamond anvils with culet sizes of 300 μm (SD1) and 200 μm (SD2). Inconel alloy served as the gasket material, with the gaskets preindented to a thickness of 25 μm (SD1) and 23 μm (SD2), and the hole drilled into the gasked by spark erosion. Pressure in the cell was probed using the Raman diamond edge method [159].

3.4 Characterization Methods

3.4.1 Single-crystal X-ray diffraction

3.4.1.1 Crystal selection and mounting

Two approaches were employed to protect air-sensitive crystals during selection and mounting, one using an inert oil layer and the other relying on a stream of cold, dry N_2.

For the former, crystals were placed on a watch glass and covered by perfluorodecalin (*cis* and *trans*, ABCR, AB102850, 98%) in a glovebox. Suitable crystals were then selected under a stereomicroscope and mounted on the tip of a MiTeGen dual-thickness polymer loop. As soon as the pin assembly was lifted above the oil surface, it was grasped with cryo tongs precooled in liquid nitrogen (−196 °C) and rapidly transferred to the magnetic holder on the goniometer head, where the crystal was maintained in a stream of cold N_2.

Alternatively, crystals were first placed in a capsule assembled from two heat-sealed FEP tubes of different internal diameters (i.d. of 4.78 mm and 6 mm) inside an inert-atmosphere glovebox. The crystals were then quickly transferred from the capsule onto the aluminum trough of a low-temperature crystal-mounting apparatus [176], [177], cooled to at least −50 °C and protected by a flow of cold, dry N_2 gas (Figure 3.6). Suitable crystals were selected under a stereomicroscope and affixed to the tip of a MiTeGen loop using Fomblin Z25 oil (Solvay). The loop assembly was then picked up with cryo tongs cooled to −196 °C and promptly transferred to the goniometer head.

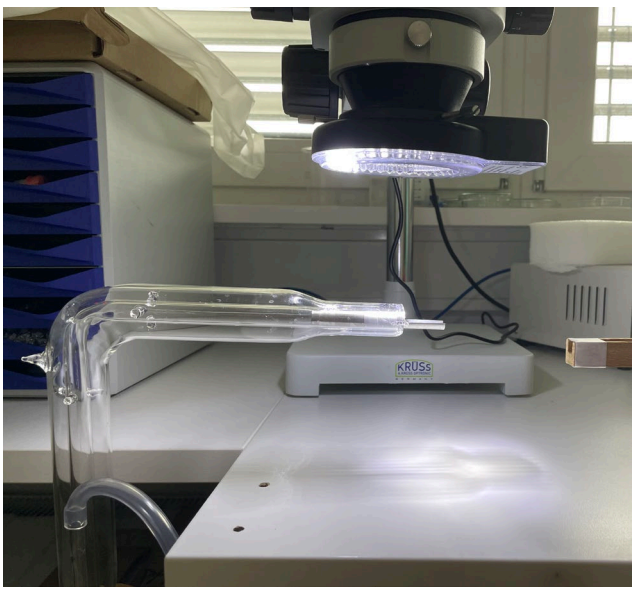


Figure 3.6: Low-temperature crystal mounting apparatus positioned under a microscope.

3.4.1.2 Data collection and reduction

SCXRD data were collected on a Rigaku OD XtaLAB Synergy-S diffractometer equipped with a Dectris EIGER2 R CdTe 1M hybrid pixel array detector using either microfocused Ag Kα (λ = 0.56087 Å) or Cu Kα (λ = 1.54184 Å) radiation (Figure 3.7).

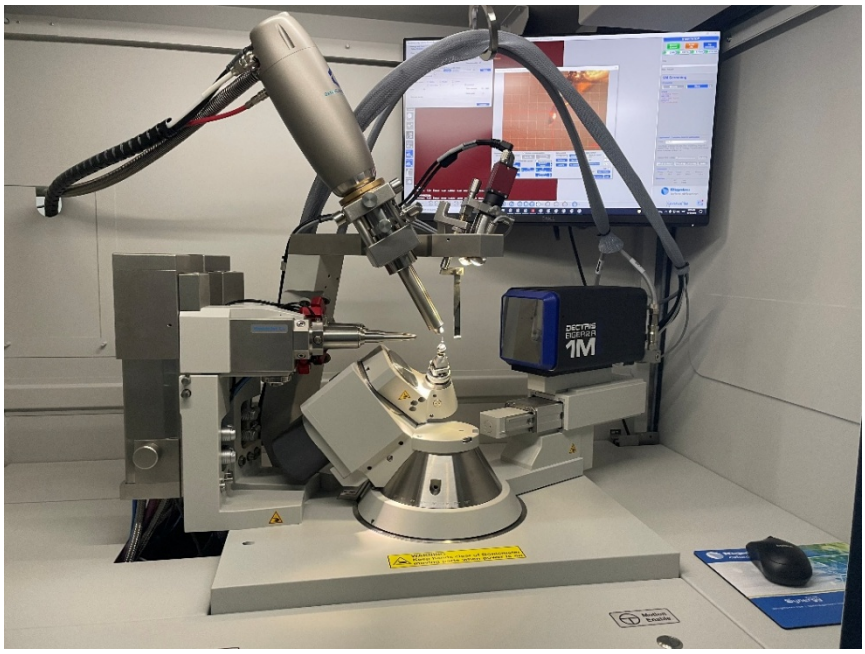


Figure 3.7: Rigaku OD XtaLAB Synergy-S diffractometer used in this work.

Data collection was performed at a temperature of −173 °C, with the cold N_2 stream provided by an Oxford Cryosystems 800 Series Cryostream. All datasets were processed with empirical and numerical absorption correction and corrections for Lorentz and polarization effects using *CrysAlisPro* software [178]. Crystal structures were solved either with the dual-space method implemented in *SHELXT* [179], the charge flipping method using *SUPERFLIP* [180], or the Patterson method implemented in *SHELXS* [181], [182], and refined with *SHELXL* [183] within *Olex2* software [184]. Figures were drawn using the program *Diamond* [185].

3.4.2 Powder X-ray diffraction

Powder X-ray diffraction data were obtained on a Rigaku OD XtaLAB Synergy-S diffractometer with Dectris EIGER2 R CdTe 1M detector using Ag Kα radiation (λ = 0.56087 Å). Gandolfi movement was used to enhance the random orientation of the crystallites. In a typical measurement, 6 frames were recorded with an exposure time of 300 s per frame with the detector positioned 90 mm away from the sample. The data were collected either at room temperature or at −173 °C, achieved by the use of an Oxford Cryosystems 800 Series Cryostream. Two-dimensional powder diffraction frames were reduced to standard profiles using *CrysAlisPro* [178] software and analyzed using *Match!* Software [186].

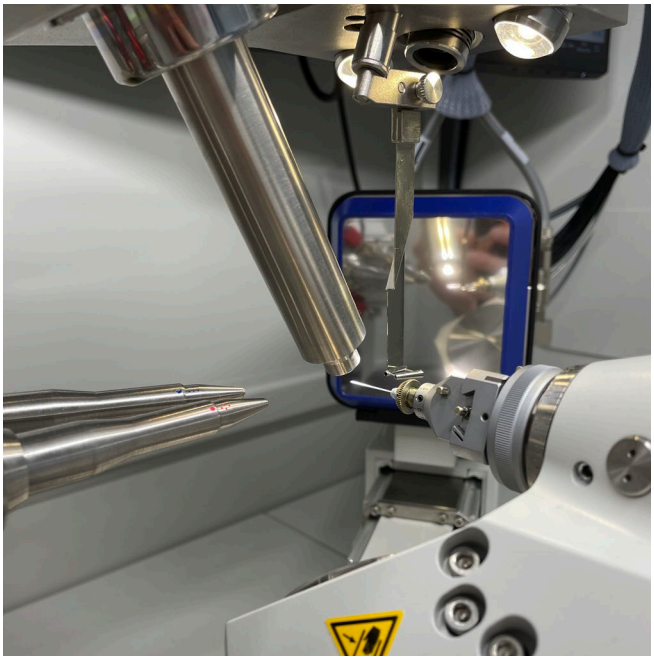


Figure 3.8: Quartz capillary mounted on the diffractometer for a PXRD measurement.

3.4.3 High pressure SCXRD data collection and processing

Synchrotron SCXRD measurements were conducted at ID27 beamline at the European Synchrotron Radiation Facility (ESRF) [187] and at P02.2 beamline at the Deutsches Elektronen-Synchrotron (DESY PETRA III) [188], [189]. The data collection at ID27 was performed using radiation with a wavelength of 0.3738 Å (33.2 keV) and the beam size on the sample focused to 0.7×0.7 μm^2, with the diffraction patterns collected on a Dectris EIGER2 X CdTe 9M detector. At P02.2 X-ray beam focused on the sample to a 2×2 μm^2 spot size with wavelengths of 0.2898 Å (42.8 keV) and 0.2906 Å (42.7 keV) and the data were collected on a Perkin Elmer XRD1621 detector. Diffraction patterns were acquired by rotating the DAC from −35 to +35° about the vertical axis, perpendicular to the direction of the beam, with the step size of 0.5°. *DAFi* [190] was used to index reflections to individual domains and the resulting single-crystal diffraction data were then integrated using the *CrysAlisPro* software suite [178]. Crystal structures were solved using *SHELXT* [179] and refined with *SHELXL* [183] within the *Olex2* software [184].

3.4.4 3D Electron crystallography

Electron crystallography work included in the Chapters 4.1 and 4.2 was performed by Dr. Kshitij Gurung, Dr. Petr Brázda, and Dr.rer.nat. Lukáš Palatinus from the Group of electron crystallography, Institute of Physics of the Czech Academy of Sciences, Prague, Czech Republic. 3D ED data were collected on a Tecnai G^2 TEM (Figure 1.9). Data sets were obtained at a temperature of 100 K using a continuous rotation electron diffraction (cRED) method with a tilt step of 0.30° per diffraction frame. The electron beam was generated using a LaB_6 source at 200 kV ($\lambda = 0.02508$ Å), and a Medipix 3 hybrid pixel detector ASI CheeTah (512×512 pixels, 24-bit dynamic range) was used to collect the diffraction patterns. Air-sensitive crystalline samples were transferred into the TEM using a newly developed low-temperature, inert-atmosphere sample-handling protocol [191], [192]. The data reduction and processing were done in *PETS2* [193], and the structure

solution (performed using *SIR2014* [194]) and refinements were done in *JANA2020* [195] software.

3.4.5 Vibrational spectroscopy

3.4.5.1 Raman spectroscopy

Raman spectra were obtained on a Bruker Senterra II confocal Raman microscope. using either a 532 or 785 nm emission line, with the power output ranging from 0.5 mW to 50 mW for the former and between 1 mW and 100 mW for the latter. The spectra were measured in the 50–1410 cm^{-1} range with a resolution of 1.5 cm^{-1}. Low-temperature measurements were performed using a Linkam LTS420 low-temperature stage (Figure 3.9), enabling data acquisition at temperatures down to −173 °C. Samples for analysis were loaded in quartz capillaries as described above (Section 3.2.1).

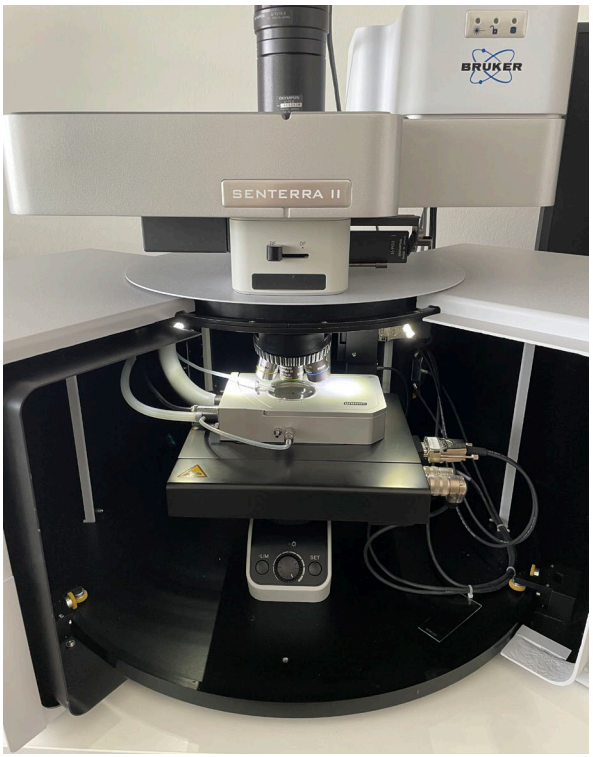


Figure 3.9: Bruker Senterra II confocal Raman microscope, equipped with the Linkam LTS420 low-temperature stage.

Raman spectra of DACs loaded with compressed and laser-heated $XeF_2 \cdot PtF_4$, discussed in Chapter 4.5, were collected by Prof. Dr. Dominik Kurzydłowski and Sylwia Olszewska at the Faculty of Mathematics and Natural Sciences, Cardinal Stefan Wyszynski University in Warsaw, Poland. Raman spectra were collected at room temperature using a WITec Alpha300M+ confocal Raman microscope. Excitation was provided by a 532 nm laser operated at 10 mW. Area scans were acquired by recording spectra at multiple points arranged on a grid, yielding pixel sizes between 3 × 3 µm and 2 × 2 µm. The spectral range of the measurements was 70–1260 cm^{-1}. An analogous scan was taken in the spectral range corresponding to the first order Raman signal of diamond (1300–1500 cm^{-1}) in order to determine the pressure gradient with the sample. The data were processed using WITec *Project Six* software for cosmic-ray removal and background subtraction. Raman band

positions were determined by fitting the spectra with pseudo-Voigt profiles in *Fityk* software [196].

3.4.5.2 Attenuated total reflectance-Infrared spectroscopy

Absorbance infrared spectra were measured on a Bruker Alpha II FT-IR spectrometer located inside an N_2 atmosphere glovebox and equipped with a Platinum Diamond-ATR sampling module (Figure 3.10). Prior to measurement, the samples of solid compounds were homogenized in an agate mortar and then placed on the diamond. Spectra were recorded in the range of 400–4000 cm^{-1} with a resolution of 4 cm^{-1} and 24 scans were taken per measurement.

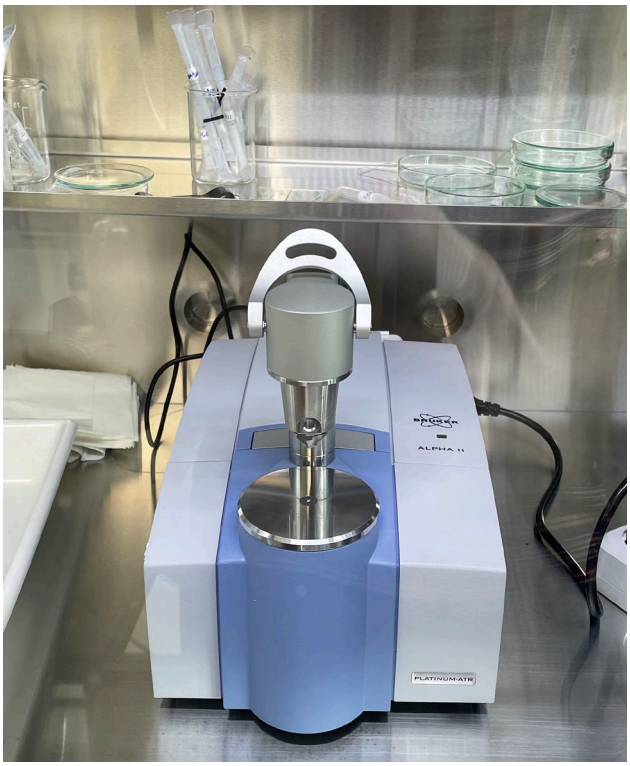


Figure 3.10: Bruker Alpha II FT-IR positioned inside a glovebox.

Chapter 4

Results and Discussion

4.1 Reactive Noble-Gas Compounds Explored by 3D Electron Diffraction: XeF_2–MnF_4 Adducts and a Facile Sample Handling Procedure

K. Motaln, K. Gurung, P. Brázda, A. Kokalj, K. Radan, M. Dragomir, B. Žemva, L. Palatinus, and M. Lozinšek

Published in: *ACS Central Science*, 2024, 10, 9, 1733–1741

DOI: 10.1021/acscentsci.4c00815

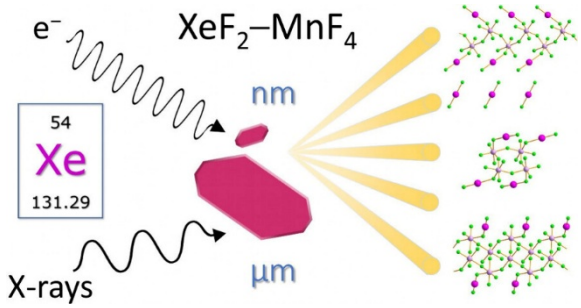


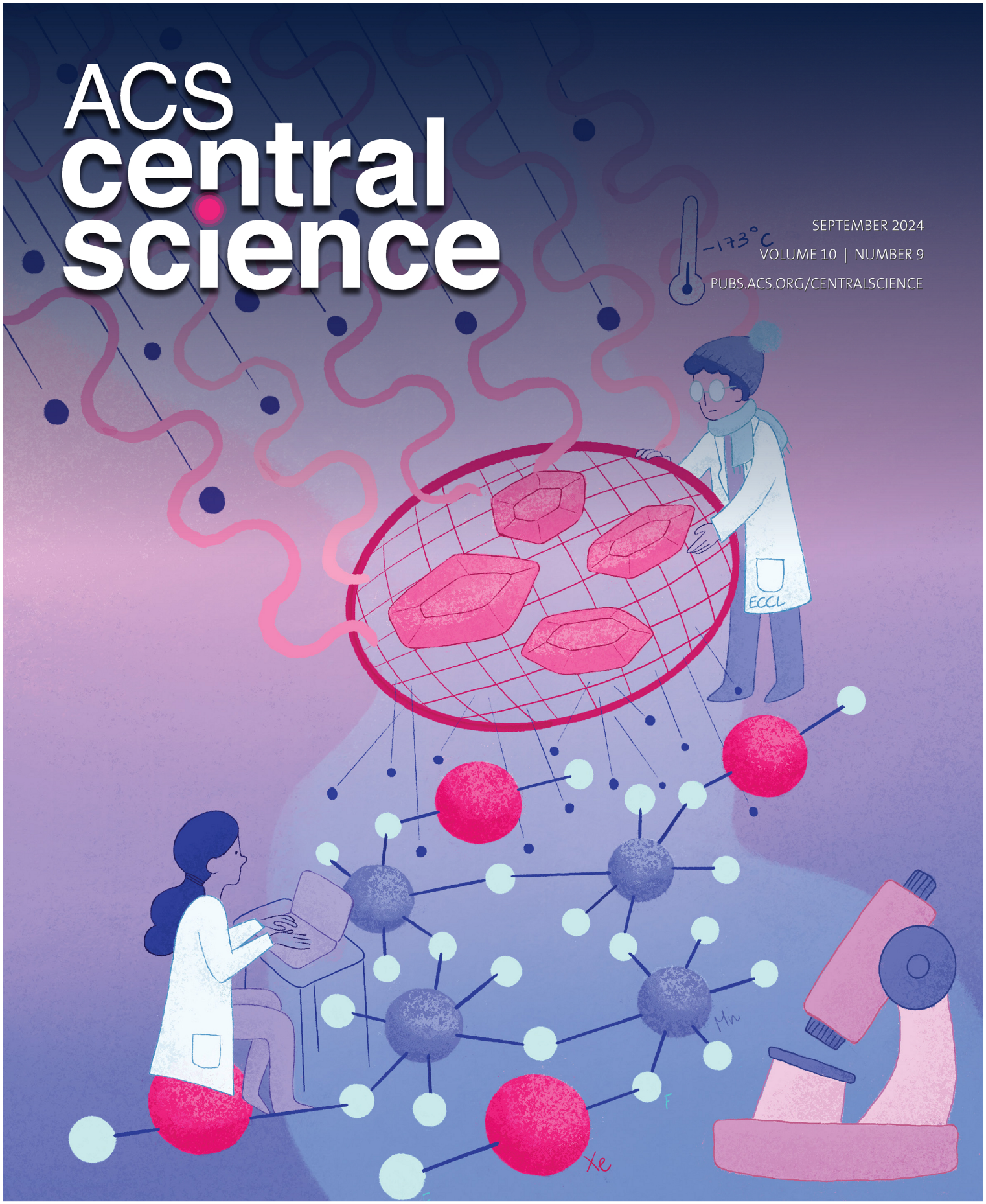
Figure 4.1: Graphical abstract of the publication "Reactive Noble-Gas Compounds Explored by 3D Electron Diffraction: XeF_2–MnF_4 Adducts and a Facile Sample Handling Procedure" [191].

The structural analysis of xenon(II) compounds continues to prove a challenging prospect as many phases are highly oxidizing, exquisitely air-sensitive, and reluctant to form crystals suitable for SCXRD. Motivated by the longstanding ambiguity surrounding the nature of $XePtF_6$ [100] and by the broader need for reliable structure determination from sub-micron crystallites of reactive compounds, this study reexamines the related XeF_2–MnF_4 system [78], [111], [112] as a testbed for applying 3D ED to structural study of reactive noble-gas fluorides. To preserve sample integrity and crystallinity, a novel low-temperature and inert-atmosphere workflow for loading and transferring nanocrystalline specimens was developed [192]. Using this procedure on XeF_2–MnF_4 adducts allowed for their transfer into the TEM without significant sample degradation. Structures solved from 3D ED data were refined with dynamical refinement to account for multiple scattering and were benchmarked directly against SCXRD results.

The investigations of the XeF_2–MnF_4 system yielded three compounds which were fully characterized: $3XeF_2 \cdot 2MnF_4$, $XeF_2 \cdot MnF_4$, and $XeF_2 \cdot 2MnF_4$. Despite the pronounced reactivity of these materials, the crystal structures derived from nanosized crystallites using 3D ED were in agreement, within experimental uncertainty, with the structural models obtained by SCXRD. The three phases exhibit distinct structural motifs arising from different connectivities of XeF_2-coordinated $[MnF_6]$ units: $3XeF_2 \cdot 2MnF_4$ features infinite zig-zag *cis*-bridged chains with cocrystallized XeF_2 in the interchain space, $XeF_2 \cdot MnF_4$ forms discrete F-bridged cyclic tetramers, and $XeF_2 \cdot 2MnF_4$ assembles into corrugated ladder-like double chains. Across the series, a progressive ionization of XeF_2 with increasing MnF_4 content is observed, culminating in $XeF_2 \cdot 2MnF_4$ where the degree of polarization of XeF_2 is sufficient to justify a tight ion pair formulation $[XeF]^+[Mn_2F_9]^-$. The conclusions drawn from diffraction studies were corroborated by vibrational spectroscopy and periodic DFT calculations, which support the inferred extent of XeF_2 ionization and the calculations assigning antiferromagnetically ordered spin states for Mn^{IV} in these materials.

By demonstrating that 3D ED, when combined with a sample transfer method that can preserve the integrity of the studied compound, can yield reliable crystal structures for strongly oxidizing, air-sensitive noble-gas adducts, this study broadens the scope of electron crystallography in main-group chemistry. The three XeF_2–MnF_4 structures significantly enrich the still limited set of structurally characterized XeF_2–MF_4 adducts [104], [106], [108], [109]. Moreover, the polymeric *cis* chains and tetrameric ring motif present in $3XeF_2 \cdot 2MnF_4$ and $XeF_2 \cdot MnF_4$, respectively, satisfy the overall $XeMF_6$ stoichiometry and are therefore highly pertinent as structural models for $XePtF_6$. More generally, the newly developed sample-handling and transfer methodology provides a route to elucidate the structures of compounds that have historically resisted crystallographic study due to their small crystallite size or extreme reactivity, positioning 3D ED as a complementary technique to SCXRD for the structural characterization of highly reactive or unstable inorganic solids.

K. Motaln, the author of this dissertation, carried out the syntheses of the XeF_2–MnF_4 adducts, determined their structures by SCXRD, recorded their PXRD patterns and vibrational spectra, and contributed to the preparation of the initial draft of the manuscript and the review, editing, and revision of the final manuscript.



ACS Publications
Most Trusted. Most Cited. Most Read.
www.acs.org

ACS central science

Open Access

This article is licensed under CC-BY 4.0

http://pubs.acs.org/journal/acscii

Article

Reactive Noble-Gas Compounds Explored by 3D Electron Diffraction: XeF_2–MnF_4 Adducts and a Facile Sample Handling Procedure

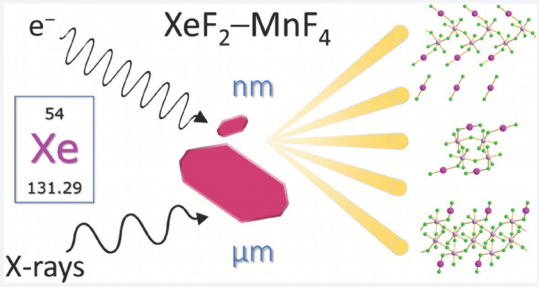
Klemen Motaln, Kshitij Gurung, Petr Brázda, Anton Kokalj, Kristian Radan, Mirela Dragomir, Boris Žemva, Lukáš Palatinus,* and Matic Lozinšek*

Cite This: *ACS Cent. Sci.* 2024, 10, 1733–1741

Read Online

ACCESS | Metrics & More | Article Recommendations | Supporting Information

ABSTRACT: Recent advances in 3D electron diffraction (3D ED) have succeeded in matching the capabilities of single-crystal X-ray diffraction (SCXRD), while requiring only submicron crystals for successful structural investigations. One of the many diverse areas to benefit from the 3D ED structural analysis is main-group chemistry, where compounds are often poorly crystalline or single-crystal growth is challenging. A facile method for loading and transferring highly air-sensitive and strongly oxidizing samples at low temperatures to a transmission electron microscope (TEM) for 3D ED analysis was successfully developed and tested on xenon(II) compounds from the XeF_2–MnF_4 system. The crystal structures determined on nanometer-sized crystallites by dynamical refinement of the 3D ED data are in complete agreement with the results obtained by SCXRD on micrometer-sized crystals and by periodic density-functional theory (DFT) calculations, demonstrating the applicability of this approach for structural studies of noble-gas compounds and highly reactive species in general. The compounds $3XeF_2{\cdot}2MnF_4$, $XeF_2{\cdot}MnF_4$, and $XeF_2{\cdot}2MnF_4$ are rare examples of structurally fully characterized xenon difluoride–metal tetrafluoride adducts and thus advance our knowledge of the diverse structural chemistry of these systems, which also includes the hitherto poorly characterized first noble-gas compound, "$XePtF_6$".



■ INTRODUCTION

Methods for structural characterization have played a pivotal role in the development of chemistry, materials science, and related fields. X-ray crystallography, particularly single-crystal X-ray diffraction (SCXRD), has assumed a central role in structural elucidation due to the wealth of information it provides about a sample.[1,2] However, the main obstacle for the characterization by SCXRD is predominantly the unavailability of single crystals of suitable size and quality. Recently, 3D electron diffraction (3D ED) has emerged as an attractive alternative technique, which enables the crystal structure determination on nanometer-sized crystallites.[3−5] However, the fine powdered form of the sample with a large surface area also possesses a higher risk for inadvertent reactions with both air and the grid materials. While the 3D ED analysis of air-stable and nonreactive samples is gaining prominence, only scarce attention was devoted to the study of reactive species.[6] In this work, a facile low-temperature method for loading and transferring highly air-sensitive and strongly oxidizing samples into the TEM for 3D ED analysis was developed and tested on xenon compounds.

At present, the chemistry of xenon is the most explored and the richest of all the noble gases, with more than 150 reported crystal structures of xenon-containing compounds. However, the first noble-gas compound, "$XePtF_6$", remains a notable exception. It was first synthesized in 1962 in a landmark experiment by Neil Bartlett that finally disproved the dogmatic assumption that noble gases cannot form true chemical compounds.[7,8] Although discovered more than 60 years ago, the first noble-gas compound remains poorly structurally characterized, and in the reinvestigation of the reaction of Xe with PtF_6, it has been proposed that the product formed is a mixture of $Xe^{II}Pt^{IV}F_6$, $[Xe^{II}F][Pt^{V}F_6]$, and PtF_5, the ratio depending on the reactant stoichiometry.[9−13] Although the crystal structure of "$XePtF_6$" was not elucidated, it has been suggested that it may be $XeF_2{\cdot}PtF_4$ adduct containing the $[PtF_5]^-$ anion, which might take the form of either an infinite polymer or a discrete cyclic oligomer.[10,11]

To gain insight into the structural characteristics of "$XePtF_6$", investigations of analogous systems were carried out, revealing

Received: May 22, 2024
Revised: July 8, 2024
Accepted: July 17, 2024
Published: August 14, 2024



ACS Publications

© 2024 The Authors. Published by American Chemical Society

https://doi.org/10.1021/acscentsci.4c00815
ACS Cent. Sci. 2024, 10, 1733−1741

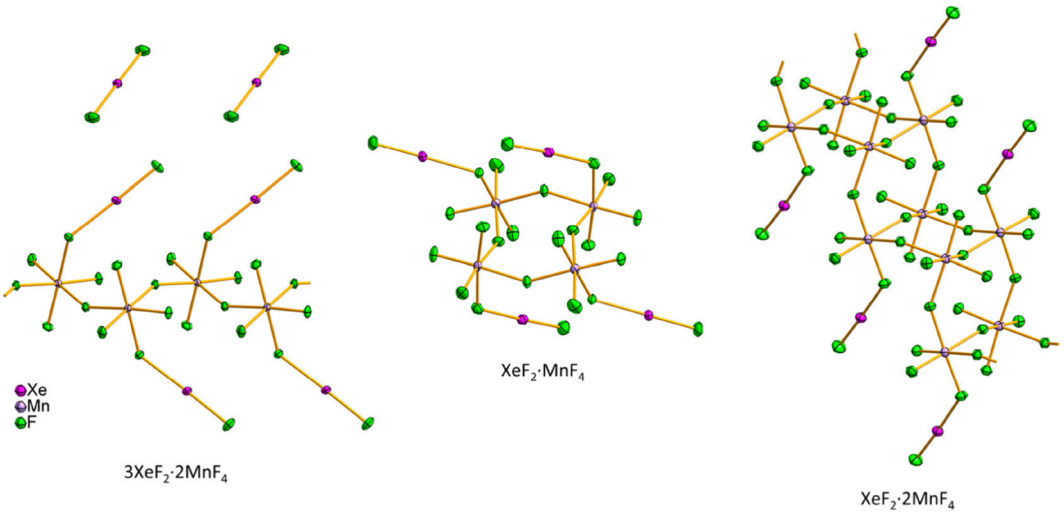


Figure 1. X-ray crystal structures of $3XeF_2{\cdot}2MnF_4$ (left), $XeF_2{\cdot}MnF_4$ (center), and $XeF_2{\cdot}2MnF_4$ (right). Thermal ellipsoids are drawn at the 50% probability level.

Table 1. Crystal Data and Refinement Results for $3XeF_2{\cdot}2MnF_4$, $XeF_2{\cdot}MnF_4$, and $XeF_2{\cdot}2MnF_4$[a]

Compound	$3XeF_2{\cdot}2MnF_4$			$XeF_2{\cdot}MnF_4$			$XeF_2{\cdot}2MnF_4$		
Method	SCXRD	3D ED	DFT/PBE-D	SCXRD	3D ED	DFT/PBE-D	SCXRD	3D ED	DFT/PBE-D
Space group		$P2_1/n$			$P2_1/n$			$P2_1/n$	
a (Å)	10.24504(11)	10.2668(19)	10.134	9.6430(5)	9.6505(9)	9.635	5.18640(8)	5.2046(4)	5.213
b (Å)	4.99654(5)	5.0036(3)	4.982	10.9859(4)	11.108(2)	10.976	9.88546(13)	9.9679(8)	9.715
c (Å)	12.44149(14)	12.4668(9)	12.439	9.7927(3)	9.7900(11)	9.570	14.6809(2)	14.6946(18)	14.534
β (deg)	96.5287(10)	96.551(11)	95.8	96.979(4)	96.858(8)	96.28	96.8660(14)	96.789(6)	96.47
V (Å^3)	632.747(12)	636.25(13)	624.76	1029.72(7)	1042.0(3)	1006.05	747.292(19)	756.99(13)	731.44
Z		2			8			4	
M_r (g mol^{-1})		769.78			300.24			431.18	
D_{calcd} (g cm^{-3})	4.040	4.017		3.873	3.827		3.832	3.783	
T (K)	100	100		100	100		100	100	
R_1	0.0226	0.1320		0.0378	0.1180		0.0350	0.0770	
wR_2/wR_{all}	0.0600	0.1480		0.0864	0.1326		0.0775	0.0848	
$\Delta\rho_{max}$, $\Delta\rho_{min}$ (e Å^{-3}) /ΔV_{max}, ΔV_{min} (e Å^{-1})	1.577, −1.956	1.96, −1.94		6.666, −1.608	0.91, −0.83		2.015, −1.399	0.68, −0.63	

[a]Experimental determinations were performed at a temperature of 100 K.

the existence of several other $aXeF_2{-}bMF_4$ adducts[14] with M = Ti,[15−17] Cr,[15,18−20] Mn,[15,21−23] Rh,[9] Pd,[10] Sn,[24] and Pt.[9−11] In particular, a close structural relation of $XeF_2{\cdot}PtF_4$ ("$XePtF_6$") and $XeF_2{\cdot}2PtF_4$ adducts to the corresponding palladium analogs was established.[10,11] However, structural characterization of the majority of these compounds was again hampered by their amorphous or poorly crystalline nature and the challenges associated with crystal growth, so that only four crystal structures have been reported to date, namely $XeF_2{\cdot}CrF_4$,[19] $XeF_2{\cdot}2CrF_4$,[20] $[Xe_2F_3][Ti_8F_{33}]$ $(2XeF_2{\cdot}8TiF_4)$, and $[XeF]_2[Ti_9F_{38}]$ $(2XeF_2{\cdot}9TiF_4)$.[17] Particularly noteworthy is the structure of $XeF_2{\cdot}CrF_4$, which consists of $[CrF_6]$ octahedra, each with coordinated XeF_2 unit and connected by *trans*-vertices to form polymeric chains, and thus represents a structural model for "$XePtF_6$".[11] The crystallographically characterized $XeF_2{-}MF_4$ compounds are structurally diverse and exhibit different degrees of XeF_2 ionization.[25] Previous published work on the $XeF_2{-}MnF_4$ system reported the syntheses of $XeF_2{\cdot}MnF_4$ and $XeF_2{\cdot}2MnF_4$ and the measurements of their infrared spectra and magnetic susceptibility.[21,22] Despite the incomplete structural characterization, $XeF_2{\cdot}MnF_4$ was clearly established as a Mn^{IV} compound by the magnetic susceptibility measurements, thus marking it as a potential analog of "$XePtF_6$".

In this work, the $XeF_2{-}MnF_4$ system was re-examined. The adducts $3XeF_2{\cdot}2MnF_4$, $XeF_2{\cdot}MnF_4$, and $XeF_2{\cdot}2MnF_4$ have been synthesized and fully characterized. The structural determination of these strongly oxidizing and highly air-sensitive compounds was performed by 3D ED, and the results were benchmarked against SCXRD data and periodic DFT calculations. This work represents the first case of structural elucidation of noble-gas compounds by 3D ED. The successful transfer of the highly reactive and air-sensitive noble-gas compounds into a transmission electron microscope (TEM) and 3D ED analysis demonstrates the feasibility and broad applicability of structural determination of reactive species using 3D ED. This procedure opens the path to characterizing other challenging compounds that have evaded crystal structure determination.

https://doi.org/10.1021/acscentsci.4c00815
ACS Cent. Sci. 2024, 10, 1733−1741

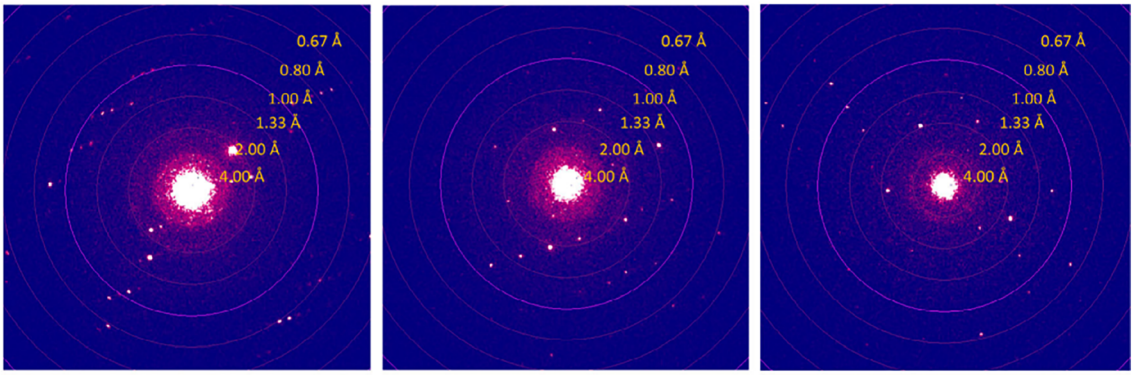


Figure 2. Frames at the beginning of the 3D ED data collection containing reflections to the highest resolution. For $3XeF_2{\cdot}2MnF_4$ and $XeF_2{\cdot}2MnF_4$, the maximum resolution was consistently high (d_{min} = 0.71 Å) throughout the data collection.

Table 2. Selected Bond Lengths (Å) and Angles (deg) in the Crystal Structures of $3XeF_2{\cdot}2MnF_4$, $XeF_2{\cdot}MnF_4$, and $XeF_2{\cdot}2MnF_4$[a]

	$3XeF_2{\cdot}2MnF_4$			$XeF_2{\cdot}MnF_4$			$XeF_2{\cdot}2MnF_4$		
	SCXRD	3D ED	DFT/PBE-D	SCXRD	3D ED	DFT/PBE-D	SCXRD	3D ED	DFT/PBE-D
Xe−F_t	1.9204(7), 1.9933(7)[b]	1.900(8), 1.985(8)[b]	1.981, 2.042[b]	1.906(3), 1.910(3)	1.917(18), 1.922(13)	1.973, 1.976	1.8946(18)	1.877(9)	1.950
Xe−F_b	2.1695(6)	2.176(6)	2.181	2.176(3), 2.180(3)	2.189(15), 2.200(14)	2.193, 2.198	2.2829(16)	2.286(7)	2.266
Mn−F_b(Xe)	1.9133(6)	1.896(9)	1.953	1.902(3), 1.928(3)	1.887(17), 1.960(17)	1.940, 1.984	1.8181(16)	1.823(5)	1.865
Mn−F_b(Mn)	1.9011(6), 1.9058(6)	1.893(6), 1.908(5)	1.915, 1.920	1.887(3) −1.903(3)	1.862(12) −1.929(12)	1.910−1.925	1.8499(15) −1.9330(16)	1.872(5) −1.921(6)	1.891−1.948
Mn−F_t	1.7264(6) −1.7358(8)	1.686(9) −1.728(6)	1.745−1.752	1.720(3) −1.741(3)	1.65(2) −1.79(2)	1.744−1.753	1.7253(17) −1.7340(16)	1.713(5) −1.752(6)	1.742−1.749
Mn−F−Mn	149.60(4)	150.4(4)	146.0	147.93(17), 149.24(17)	146.0(9), 147.7(9)	143.4, 143.9	138.81(9) −147.19(9)	138.7(4) −148.1(3)	133.5−142.6
cis-F−Mn−F	85.08(3) −94.31(4)	85.6(3) −94.4(3)	83.4−95.3	82.96(13) −94.42(15)	82.7(6) −98.0(9)	82.8−95.4	86.47(7) −93.39(8)	85.9(2) −93.4(3)	86.6−94.5
trans-F−Mn−F	174.13(3) −176.14(3)	174.3(3) −176.4(3)	172.6−175.2	172.62(15) −175.23(15)	168.9(9) −175.3(7)	171.6−174.3	173.99(8) −177.71(8)	174.1(3) −177.0(3)	172.9−178.4
F−Xe−F	177.47(3), 180.00(5)[b]	177.0(3), 180[b]	176.7, 180.0[b]	177.48(14), 178.52(14)	178.2(7), 179.2(6)	176.9, 177.6	176.84(8)	176.8(2)	177.6

[a]F_t and F_b denote the terminal and bridging fluorine atoms, respectively. [b]Cocrystallized centrosymmetric XeF_2 molecule in $3XeF_2{\cdot}2MnF_4$.

RESULTS AND DISCUSSION

Crystal Structure Determination by 3D ED, SCXRD, and Periodic DFT Calculations. The crystal structures of all three XeF_2−MnF_4 adducts were determined using 3D ED data and SCXRD (Figures 1, S1−S3; Tables 1, S1−S4). Despite the strongly oxidizing nature of Xe^{II} and Mn^{IV} (MnF_4 is the highest binary fluoride of manganese),[26] the compounds $3XeF_2{\cdot}2MnF_4$ and $XeF_2{\cdot}2MnF_4$ proved to be surprisingly stable under the electron beam and produced high-resolution diffraction patterns (d_{min} = 0.71 Å) throughout the entire tilt range (Figure 2, Tables S1, S3). However, this was not the case for $XeF_2{\cdot}MnF_4$, as its crystals decomposed after only a few seconds of electron beam irradiation, resulting in a significant decrease in the diffraction resolution. To address this issue, diffraction patterns from different crystals were collected at various tilt angles (Table S2) and merged to obtain complete information for the structure solution. The same merging process was performed for the $3XeF_2{\cdot}2MnF_4$ to obtain more complete data (Table S1). The structures were initially refined kinematically (Tables S1−S3), ignoring the contribution of dynamical effects to the diffracted intensities. Further refinement of the structures by accounting for multiple scattering using dynamical refinement theory[27,28] led to much lower figures of merit and more precise lattice parameters and bond lengths (Tables 1 and 2).

The values of the agreement parameter R_1 for the 3D ED structures are considerably higher than their SCXRD counterparts (Table 1), but these values are nevertheless good for 3D ED.[29] The lattice parameters determined from 3D ED are generally believed to be of very low accuracy, and compared to the unit cell parameters obtained from SCXRD, there is a deviation of up to −1.1%, with a maximum difference amounting to −0.122 Å/0.12° and an average difference of −0.03 Å/0.06° (Figure 3a). These discrepancies are comparable to differences observed when comparing lattice parameters from SCXRD and values calculated by DFT. The PBE-D functional slightly underestimates lattice parameters and volumes, with deviations ranging from −0.5% to +2.3%. Moreover, comparing the unit cell parameters, which were obtained in several independent SCXRD structure determinations, differences of up to −0.4% are observed (Table S4). This indicates that the systematic differences in the values of the unit cell parameters obtained by 3D ED when compared to SCXRD and DFT/PBE-D are reasonably small. Such a good agreement could be obtained owing to the careful determination of the lattice parameters from 3D ED using the program *PETS2*,[30] and employing the

https://doi.org/10.1021/acscentsci.4c00815
ACS Cent. Sci. 2024, 10, 1733−1741

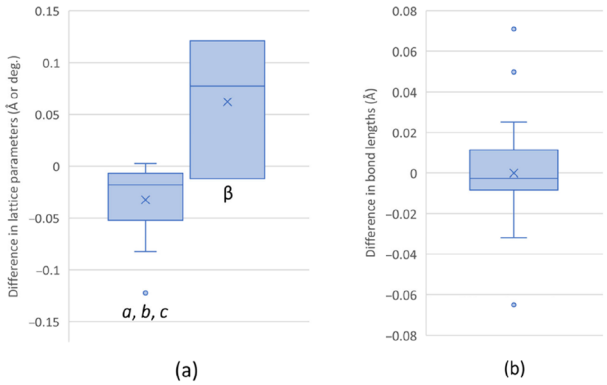


Figure 3. Box and whisker plots showing the difference in (a) lattice parameters and (b) bond lengths of the three XeF_2–MnF_4 compounds between SCXRD and 3D ED refinement results. The differences were calculated as the value of the parameter obtained from SCXRD minus the value of the parameter determined by 3D ED. The average difference is marked with a symbol × and the outliers are shown as circles.

refinement of the optical distortions along with the refinement of the lattice parameters.[31] It is also evident that 3D ED lattice parameters are, on average, slightly larger than their counterparts derived from SCXRD (Table 1). This difference, and consequently, the higher unit cell volumes of all structures determined by 3D ED compared to SCXRD results suggest that the deviation of the 3D ED results might be due to the radiation damage of the samples exerted by the electron beam. The unit-cell volume expansion is a frequently observed global radiation damage effect.[32,33]

A comparison of bond lengths and angles of the elucidated crystal structures and DFT calculations (Table 2, Figure 3b) gives a better understanding of the accuracy of the results. The bond parameters derived from the two methods are in very good agreement. Typically, the differences are not significant (88.4% of all bond distances and angles are within the "3σ rule"; Tables S5–S7) and are within the range of ±0.08 Å and ±5°. The terminal Mn–F_t bond lengths showed the largest discrepancies (exceeding the 3σ threshold) between the bond lengths determined by SCXRD and 3D ED. In the crystal structures of $3XeF_2{\cdot}2MnF_4$ and $XeF_2{\cdot}MnF_4$ determined by 3D ED, one of the Mn–F_t bonds was significantly shorter than the corresponding bonds in structures determined by SCXRD (1.686(9) Å vs 1.7358(8) Å in $3XeF_2{\cdot}2MnF_4$; 1.65(2) Å vs 1.721(3) Å in $XeF_2{\cdot}MnF_4$). Similarly, in the 3D ED structures of $XeF_2{\cdot}MnF_4$ and $XeF_2{\cdot}2MnF_4$, one of the Mn–F_t bonds is elongated compared to the SCXRD results (1.79(2) Å vs 1.725(3) Å in $XeF_2{\cdot}MnF_4$; 1.752(6) Å vs 1.7282(16) Å in $XeF_2{\cdot}2MnF_4$). Significant discrepancies between the 3D ED and SCXRD results are also observed in the Mn–F_b(Mn) bond lengths in the crystal structure of $XeF_2{\cdot}2MnF_4$, where a shift in the position of the fluorine atom F5 leads to the elongation of one bond (1.872(5) Å vs 1.8499(15) Å) and shortening of the other Mn–F_b(Mn) bond (1.909(6) Å vs 1.9330(16) Å). Similar to the observed increase in lattice parameters and unit cell volume, the most likely reason for the differences in bond distances is the effect of site-specific radiation damage, which is typically manifested in particular fragments or sensitive functional groups.[32,33] In spite of these small differences, the overall results are in good agreement and validate each other. As the results from X-ray diffraction have better figures of merit and, in general, smaller standard uncertainties, the structure parameters from SCXRD are discussed in the subsequent description of the structures, with the note that the same overall picture and conclusions are obtained also on the basis of the 3D ED data.

Crystal structures were modeled with DFT as antiferromagnetic, resulting in zero total magnetization (the antiferromagnetic arrangements of the Mn ions within the unit cell of the three considered crystal structures are depicted in Figure 4). However, the absolute magnetization is about 3 μ_B/Mn-ion for all three crystal structures (Table 3), in fair agreement with experimental magnetic measurements.[21,22] These values are consistent with a $3d^3$ valence electronic configuration, confirming the +4 oxidation state of Mn. In contrast, the calculated Bader charges of Mn ions are considerably smaller than +4, being around +2.1 (Table 3 and Figure 4). This finding is not surprising because atomic charge is not synonymous with the formal oxidation state. It is known that even ions that are formally without valence electrons, such as V^V, display a substantial valence electron density.[34] Bader charges of Xe are about +1.3 and those of F atoms range from about −0.5 to −0.6, consistent with the formal oxidation states of +2 and −1 for xenon and fluorine, respectively. These values are similar to the calculated Bader charges of Xe and F atoms in the XeF_2 crystal, +1.21 and −0.61, respectively.

Description of the Crystal Structures. *$3XeF_2{\cdot}2MnF_4$.* The crystal structure of $3XeF_2{\cdot}2MnF_4$ consists of polymeric chains of *cis*-F-bridged [MnF_6] octahedra with the apically coordinated XeF_2 molecules (Figure 1) alternating above and below the chain, which can be described by the crystal coordination formula[35] $^1_\infty[MnF_3F_{2/2}(XeF_2)]$. The manganese bridging F atoms lie alternating above and below the plane of metal atoms, thus the chain could also be described as Mn–F–Mn–F–Mn helix, which propagates parallel to the *b*-crystallographic axis (Figure S4). The bond lengths of the terminal F atoms (Mn–F_t 1.7264(6)–1.7358(8) Å) are considerably shorter than the bond lengths of the bridging F atoms (Mn–F_b(Mn) 1.9011(6), 1.9058(6) Å), with the longest bond involving the XeF_2 ligand (Mn–F_b(Xe) 1.9133(6) Å). The voids between adjacent chains are occupied by cocrystallized XeF_2 molecules. The molecular geometry of the cocrystallized XeF_2 (1.9933(7) Å, 180.00(5)°) is essentially the same as that observed in the crystal structure of pure XeF_2.[36] On the other hand, the XeF_2 ligand coordinated to the Mn center is significantly distorted, with shortened Xe–F_t (1.9204(7) Å) and elongated Xe–F_b (2.1695(6) Å) bonds. A similar helical polymeric *cis*-chain was observed in the crystal structure of $H_3O^+[TiF_5]^-$.[37]

$XeF_2{\cdot}MnF_4$. In contrast to the polymeric structure of $3XeF_2{\cdot}2MnF_4$, the building unit of $XeF_2{\cdot}MnF_4$ crystal structure is a discrete F-bridged cyclic tetramer, $^0_\infty[\langle MnF_3F_{2/2}(XeF_2)\rangle^r_4]$ (Figure 1). The three bridging F atoms of [MnF_6] octahedron form a *fac* geometry, with XeF_2 ligand coordinated apically. A pair of ligands is situated above a centrosymmetric ring, and the other pair is below it (Figure S5). The Mn–F_t (1.720(3)–1.741(3) Å), Mn–F_b(Mn) (1.887(3)–1.903(3) Å), and Mn–F_b(Xe) (1.902(3), 1.928(3) Å) bond distances are comparable to those observed in $3XeF_2{\cdot}2MnF_4$, as is the distortion of the XeF_2 ligand (Xe–F_t 1.906(3), 1.910(3) Å; Xe–F_b 2.176(3), 2.180(3) Å). Interestingly, such a tetrameric ring motif, based on the RhF_5 tetramer,[38] has been proposed earlier for the crystal structures of both "$XePtF_6$" ($XeF_2{\cdot}PtF_4$) and $XeF_2{\cdot}PdF_4$.[10] The other rare crystallographically characterized examples of anionic M_4F_{20} rings known to date include the $Ti_4F_{20}^{4-}$ and $Ge_4F_{20}^{4-}$ anions.[39,40]

https://doi.org/10.1021/acscentsci.4c00815
ACS Cent. Sci. 2024, 10, 1733−1741

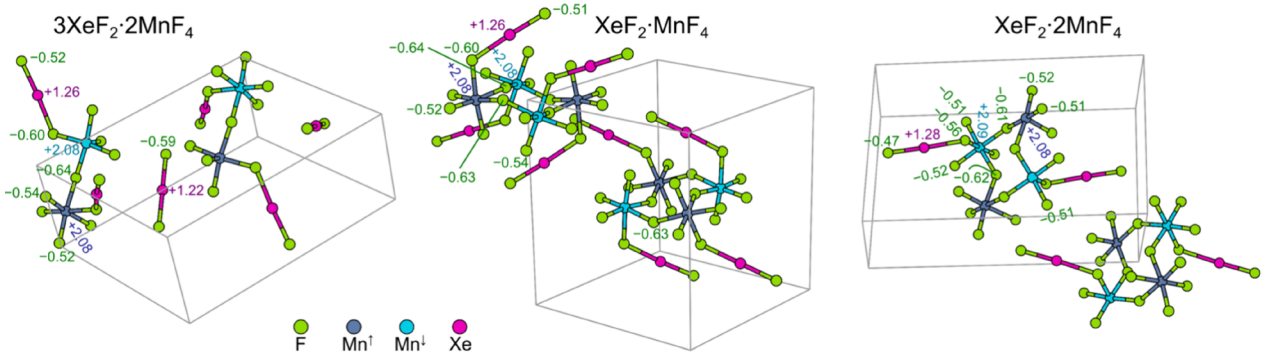


Figure 4. DFT-modeled crystal structures of $3XeF_2{\cdot}2MnF_4$, $XeF_2{\cdot}MnF_4$, and $XeF_2{\cdot}2MnF_4$, with the utilized antiferromagnetic arrangements shown by using different colors for the spin-up ($Mn^{\uparrow}$) and spin-down ($Mn^{\downarrow}$) polarized Mn ions. Calculated atomic Bader charges are also stated (for comparison, the Bader charges of Xe and F ions in the XeF_2 crystal are +1.21 and −0.61, respectively).

Table 3. PBE-D Calculated Absolute Magnetizations (Normalized Per Mn Ion) and Atomic Bader Charges of $3XeF_2{\cdot}2MnF_4$, $XeF_2{\cdot}MnF_4$, and $XeF_2{\cdot}2MnF_4$[a]

Compound	Abs. mag.[b] (μ_B/Mn-ion)	Bader charge of $Mn^{\uparrow}$, $Mn^{\downarrow}$	Bader charge of Xe	Bader charge of F(Mn)	Bader charge of F_t(Xe), F_b(Xe), F(Xe)[d]	Charge on XeF_2
XeF_2	-	-	1.21	-	−0.605	0
$3XeF_2{\cdot}2MnF_4$	3.15	2.08, 2.08	1.26,[c] 1.22[d]	from −0.52 to −0.64	−0.52, −0.60, −0.59	0.14,[c] 0.04[d]
$XeF_2{\cdot}MnF_4$	3.15	2.08, 2.08	1.26	from −0.52 to −0.64	−0.51, −0.60	0.15
$XeF_2{\cdot}2MnF_4$	3.12	2.08, 2.09	1.28	from −0.51 to −0.62	−0.47, −0.56	0.25

[a]Note that all structures have zero total magnetization, i.e., the modeled structures are perfectly antiferromagnetic. For the illustration of the antiferromagnetic arrangement of the Mn ions within the unit cell and atomic Bader charges, see Figure 4. [b]Calculated as $M_{abs} = 1/N_{Mn} \int_{cell} |n^{\uparrow}(r) - n^{\downarrow}(r)|\, dr$, where N_{Mn} is the number of Mn ions in the unit cell and $n^{\uparrow}(r)$ and $n^{\downarrow}(r)$ are the spin-up and spin-down electron number densities. [c]XeF_2 coordinated to Mn as F−Xe−F−Mn. [d]Cocrystallized XeF_2.

$XeF_2{\cdot}2MnF_4$. The asymmetric unit of $XeF_2{\cdot}2MnF_4$ consists of two crystallographically independent $[MnF_6]$ units, one of which is apically coordinated by XeF_2. Each $[MnF_6]$ unit is connected to three neighboring units into a polymeric double chain, $^1_\infty[\langle MnF_2F_{3/1+1}(XeF_2)\rangle\langle MnF_3F_{3/1+1}\rangle]$, so that each XeF_2-bearing octahedron is connected to three regular $[MnF_6]$ units and vice versa. The double chain has the form of a corrugated ladder or a staircase-like shape (Figure S6). The Mn−F_t bond lengths (1.7253(17)−1.7340(16) Å) are comparable to those observed in the two aforementioned adducts, whereas Mn−F_b(Mn) distances (1.8499(15)−1.9330(16) Å) span a larger range, and Mn−F_b(Xe) (1.8181(16) Å) is the shortest bridging bond. The latter is in stark contrast with the structures of $3XeF_2{\cdot}2MnF_4$ and $XeF_2{\cdot}MnF_4$, where the Mn−F bonds involving the XeF_2 ligand are the longest. Similarly, the distortion of XeF_2 ligand (Xe−F_t 1.8946(18) Å; Xe−F_b 2.2829(16) Å) is much larger and comparable to the XeF^+ salts (e.g., $[XeF]_2[Ti_9F_{38}]$,[17] $[XeF][AF_6]$, A = As, Sb, Bi).[36] Therefore, the $XeF_2{\cdot}2MnF_4$ compound could be considered a XeF^+ salt or tight ion pair, $[XeF]^+[Mn_2F_9]^-$. An anion with a similar staircase-like double chain structure is $[Ti_2F_9]^-$,[39,41] whereas the geometry of the double chain anion in the crystal structure of $[O_2]^+[Mn_2F_9]^-$ is different.[42]

Xenon atoms in all three crystal structures exhibit a number of nonbonded Xe···F contacts shorter than the sum of van der Waals radii (Figures S7−S9; Tables S8−S10).

Ionization of XeF_2. Raman spectroscopy is an effective tool for compound identification and monitoring the ionization of the bound XeF_2, along the ionization pathway $XeF_2 \rightarrow XeF^+ + F^-$,[25] in its Lewis acid−base adducts. As observed for fluoridotitanates(IV),[17,43] the dimensionality of the anion affects the position of the strong symmetric in-phase M−F_t stretching mode. For $3XeF_2{\cdot}2MnF_4$ and $XeF_2{\cdot}MnF_4$, this band is located at 719 and 721 cm^{-1}, respectively, whereas for $XeF_2{\cdot}2MnF_4$ the mode is observed at 728 cm^{-1} (Figures 5, S10; Table S11). The symmetric stretching vibration of cocrystallized XeF_2 at 508 cm^{-1} observed in the Raman spectrum of $3XeF_2{\cdot}2MnF_4$ is only slightly shifted from the position of the band at 497 cm^{-1} in pure XeF_2.[44] The strong Xe−F_t stretching band of coordinated XeF_2 shifts to higher wavenumbers with increasing stoichiometry of MnF_4 and thus increasing Lewis-acid strength, with observed positions of 574 cm^{-1} in $3XeF_2{\cdot}2MnF_4$, 581, 588 cm^{-1} in $XeF_2{\cdot}MnF_4$ and 612 cm^{-1} in $XeF_2{\cdot}2MnF_4$. In the reported Raman spectra of $XeF_2{\cdot}PdF_4$ and $XeF_2{\cdot}PtF_4$, bands that could be attributed to the Xe−F_t stretch are observed at 585 and 591 cm^{-1}, respectively,[10,11] suggesting that these compounds exhibit a similar degree of XeF_2 ionization as $XeF_2{\cdot}MnF_4$. The position of the Xe−F_t band at 612 cm^{-1} in $XeF_2{\cdot}2MnF_4$ is comparable to other XeF^+ salts (e.g., 607, 611 cm^{-1} in $[XeF][AsF_6]$;[36] 605, 610, 614 cm^{-1} in $[XeF][Ta_2F_{11}]$;[45] 612 cm^{-1} in $[XeF]_2[Ti_9F_{38}]$).[17] The Raman spectroscopy thus corroborates the high degree of XeF_2 ionization, as inferred from the observed shortening and elongation of the Xe−F_t and Xe−F_b bonds, respectively, in the crystal structure of $XeF_2{\cdot}2MnF_4$. Moreover, the trend in ionization is also confirmed by periodic DFT calculations, which show that Bader charges (Table 3, Figure 4) on Xe atom and XeF_2 moiety are larger in $XeF_2{\cdot}2MnF_4$ (+1.28, +0.25) than in $3XeF_2{\cdot}2MnF_4$ (+1.26, +0.14) and $XeF_2{\cdot}MnF_4$ (+1.26, +0.15). The $[XeF][Mn_2F_9]$ tight ion pair formulation is therefore justified. For the formation of XeF^+, the strongest fluoride-ion abstracting Lewis acids, such as pentafluorides AsF_5 and SbF_5, are typically required. The $[XeF][Mn_2F_9]$ is a rare structurally confirmed example of a highly ionized Xe^{II} species, which formed in interaction with a weaker Lewis acid and

https://doi.org/10.1021/acscentsci.4c00815
ACS Cent. Sci. 2024, 10, 1733−1741

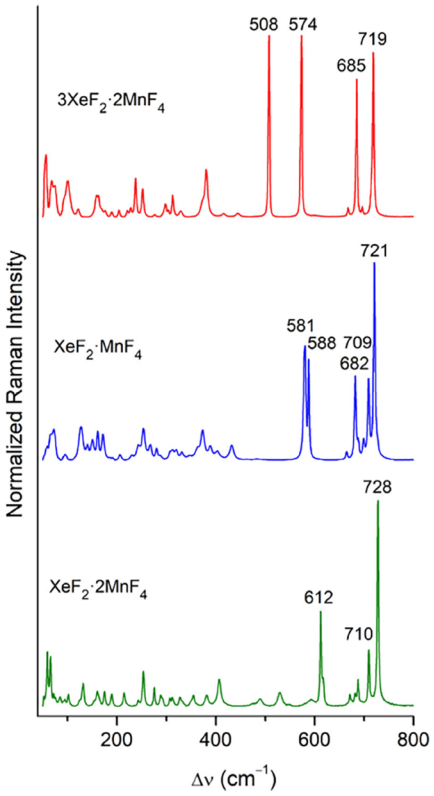


Figure 5. Raman spectra of powdered samples of $3XeF_2{\cdot}2MnF_4$, $XeF_2{\cdot}MnF_4$, and $XeF_2{\cdot}2MnF_4$ recorded at −150 °C using 785 nm excitation.

exhibits a polymeric anion. The only other examples of this kind are from the XeF_2–TiF_4 system: $[Xe_2F_3][Ti_8F_{33}]$ and $[XeF]_2[Ti_9F_{38}]$.[17]

CONCLUSIONS

Despite considerable interest in the structural characteristics of XeF_2–MF_4 adducts due to their relationship with the first noble-gas compound, "$XePtF_6$", only four such compounds were crystallographically characterized and reported prior to this study.[17,19,20] These compounds not only pose a synthetic challenge due to their air sensitivity and oxidizing nature but also present considerable difficulties in the growth of single crystals large enough for SCXRD. In limited aforementioned cases, this could be resolved only by lengthy screening for optimal crystallization conditions[17] or recrystallization of the powdered products by prolonged exposure to a temperature gradient or the use of supercritical SF_6.[20] In this work, the XeF_2–MnF_4 system was reinvestigated, leading to the synthesis of $3XeF_2{\cdot}2MnF_4$, $XeF_2{\cdot}MnF_4$, and $XeF_2{\cdot}2MnF_4$, which were characterized by 3D ED, SCXRD, powder X-ray diffraction (PXRD), vibrational spectroscopy, and periodic DFT calculations. The crystal structures of $3XeF_2{\cdot}2MnF_4$ and $XeF_2{\cdot}2MnF_4$ consist of infinite zigzag chains and staircase-like double chains, respectively, formed by F-bridged $[MnF_6]$ octahedra (Figure 1). In contrast, the crystal structure of $XeF_2{\cdot}MnF_4$ consists of discrete tetrameric units and is only the second crystallographically characterized example of a $Xe^{II}M^{IV}F_6$ compound. The structures of $3XeF_2{\cdot}2MnF_4$ and $XeF_2{\cdot}MnF_4$ provide new possible structural models for the currently unknown structure of "$XePtF_6$" (Figure 6). In this series of compounds, a progressive increase in the Lewis acidity of the fluoridomanganate(IV) with increasing MnF_4 content leads to the observed progressive ionization of XeF_2. The $XeF_2{\cdot}2MnF_4$ adduct could thus be formulated as a tight ion pair $[XeF]^+[Mn_2F_9]^-$—a rare example of $[XeF]^+$ salt with polymeric anion.

By developing a novel method for sample loading and transfer under low temperatures and inert conditions, the highly reactive noble-gas compounds could be successfully introduced into a TEM, enabling their structural determination by 3D ED. Despite comparatively poorer agreement parameters and less precise bond distances and angles, the crystal structures obtained by 3D ED are in full agreement with the SCXRD results. This study therefore demonstrates that the crystal structures of reactive, strongly oxidizing, and air-sensitive compounds can be elucidated by 3D ED analysis of nanosized crystallites, sidestepping the time-consuming single-crystal growth attempts. In conjunction with the inert sample transfer method described herein, this renders 3D ED an attractive option in the analytical toolbox for the determination of hitherto unknown structures of noble-gas compounds and other highly reactive or unstable species.

METHODS

Syntheses. The oxidizing power of XeF_2 near its melting point is sufficient to oxidize Mn^{II} to Mn^{IV}.[21] In the present study, MnF_2 was treated with excess XeF_2 in a nickel reaction vessel heated to 120 °C for 2–3 days, followed by slow cooling and removal of volatiles under dynamic vacuum at room temperature. This procedure resulted in the formation of $3XeF_2{\cdot}2MnF_4$ in the form of red needle-shaped single crystals and pink crystalline powder (Figure S11). This result contradicts the earlier reports, where a similar procedure was claimed to result in the formation of $XeF_2{\cdot}MnF_4$.[21] The single crystals obtained with this preparation proved suitable for SCXRD, while the powder was used for 3D ED. Attempts to prepare $XeF_2{\cdot}MnF_4$ or $XeF_2{\cdot}2MnF_4$ by oxidation of MnF_2 with a stoichiometric amount of XeF_2 were unsuccessful, and the Raman spectra of the obtained products indicated that $3XeF_2{\cdot}2MnF_4$ and MnF_3 formed instead. Therefore, thermal reactions between XeF_2 and MnF_4 were investigated by heating the reactants in heat-sealed

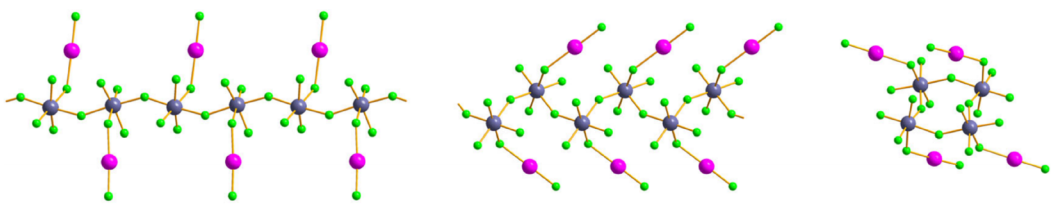


Figure 6. Structural models for "$XePtF_6$" ($XeF_2{\cdot}PtF_4$): *trans*-chain from $XeF_2{\cdot}CrF_4$ (left),[19] *cis*-chain from $3XeF_2{\cdot}2MnF_4$ (center), and tetrameric ring from $XeF_2{\cdot}MnF_4$ (right).

https://doi.org/10.1021/acscentsci.4c00815
ACS Cent. Sci. 2024, 10, 1733−1741

fluorinated ethylene-propylene (FEP) ampules, with XeF_2 always present in a slight stoichiometric excess to compensate for the loss through the ampule walls. This procedure resulted in the formation of wine-red crystals of $XeF_2{\cdot}MnF_4$ and $XeF_2{\cdot}2MnF_4$, which were always covered by a large amount of a purple amorphous solid (Figure S11). The use of FEP ampules for the reactions proved advantageous, since the material that formed in the nickel reactor under the same reaction conditions contained even more of the amorphous phase. The crystals of $XeF_2{\cdot}MnF_4$ and $XeF_2{\cdot}2MnF_4$ prepared in FEP ampules always formed agglomerates that could not be completely separated, although some multiple crystals were found to be suitable for structural analysis by SCXRD. Another synthetic path to $XeF_2{\cdot}MnF_4$ is the solvolysis of $3XeF_2{\cdot}2MnF_4$ in anhydrous HF (aHF). Upon prolonged stirring of the initially formed pink solution over the insoluble purple precipitate, pink powdery material began to deposit, replacing the dark precipitate, while the color of the solution changed to a light pink. Such preparation yielded pure microcrystalline $XeF_2{\cdot}MnF_4$, however, its low solubility in aHF prevented the preparation of single crystals by recrystallization. In one of the experiments, it was found that after two cycles of adding aHF, stirring, and removing the volatiles under a dynamic vacuum, $XeF_2{\cdot}2MnF_4$ also began to form, as shown by powder X-ray diffraction and Raman spectroscopy (Figure S12). The sample containing both $XeF_2{\cdot}MnF_4$ and $XeF_2{\cdot}2MnF_4$ was used in 3D ED studies.

Sample Loading and Transfer for Observation in TEM. A copper TEM grid with lacey carbon was loaded onto a cryogenic TEM sample holder, which was cooled with liquid N_2 inside a nitrogen-filled glovebox (Figures S13–S15). After the holder had cooled for about 15 min, a small amount of powdered sample was transferred onto the grid. The excess sample was removed by gently tapping the holder. The cover protecting the grid was moved over the sample, and the holder was then covered with a sleeve to protect it from the atmosphere. Sealed and cooled, the holder was then removed from the glovebox and very quickly transferred into the transmission electron microscope for data acquisition (Table S12). The sleeve was removed only immediately before inserting the holder in the TEM, while the protective cover remained in place during the whole procedure. Throughout the entire process, the maximum temperature of the holder did not exceed ~125 K, and the exposure to air did not exceed 2 s. Despite all these measures, a significant amount of ice was usually found on the grid. However, due to low temperatures the ice did not react with the sample and did not prevent TEM observation and 3D ED data collection. Ice can be removed by briefly warming the sample to 173 K in the microscope. Detailed information on the setup for the sample loading process in the glovebox is provided in the Supporting Information.

3D ED, SCXRD, PXRD, Vibrational Spectroscopy, and Periodic DFT Calculations. Technical details about 3D ED, SCXRD and PXRD measurements, vibrational spectroscopy, and periodic DFT calculations are provided in the Supporting Information.

■ ASSOCIATED CONTENT

Supporting Information

The Supporting Information is available free of charge at https://pubs.acs.org/doi/10.1021/acscentsci.4c00815.

Detailed descriptions of experimental and computational procedures, PXRD data, additional crystallographic data (Table S13) and figures, IR spectra (Figures S16, S17; Table S14) and visualizations of the calculated vibrational modes (Figure S18–S20), and the DFT-optimized structure coordinates (PDF)

Crystallographic information files (CIF) for $3XeF_2{\cdot}2MnF_4$, $XeF_2{\cdot}MnF_4$, and $XeF_2{\cdot}2MnF_4$, determined by both 3D ED and SCXRD (CSD 2368882–2368887) (ZIP-1 and ZIP-2).

■ AUTHOR INFORMATION

Corresponding Authors

Lukáš Palatinus – *Department of Structure Analysis, Institute of Physics of the Czech Academy of Sciences, Prague 8 18221, Czech Republic*; orcid.org/0000-0002-8987-8164; Email: palat@fzu.cz

Matic Lozinšek – *Jožef Stefan Institute, 1000 Ljubljana, Slovenia; Jožef Stefan International Postgraduate School, 1000 Ljubljana, Slovenia*; orcid.org/0000-0002-1864-4248; Email: matic.lozinsek@ijs.si

Authors

Klemen Motaln – *Jožef Stefan Institute, 1000 Ljubljana, Slovenia; Jožef Stefan International Postgraduate School, 1000 Ljubljana, Slovenia*

Kshitij Gurung – *Department of Structure Analysis, Institute of Physics of the Czech Academy of Sciences, Prague 8 18221, Czech Republic*

Petr Brázda – *Department of Structure Analysis, Institute of Physics of the Czech Academy of Sciences, Prague 8 18221, Czech Republic*

Anton Kokalj – *Jožef Stefan Institute, 1000 Ljubljana, Slovenia; Jožef Stefan International Postgraduate School, 1000 Ljubljana, Slovenia*; orcid.org/0000-0001-7237-0041

Kristian Radan – *Jožef Stefan Institute, 1000 Ljubljana, Slovenia*

Mirela Dragomir – *Jožef Stefan Institute, 1000 Ljubljana, Slovenia; Jožef Stefan International Postgraduate School, 1000 Ljubljana, Slovenia*; orcid.org/0000-0002-4910-253X

Boris Žemva – *Jožef Stefan Institute, 1000 Ljubljana, Slovenia; Jožef Stefan International Postgraduate School, 1000 Ljubljana, Slovenia*

Complete contact information is available at: https://pubs.acs.org/10.1021/acscentsci.4c00815

Notes

The authors declare no competing financial interest.
Prof. B. Žemva sadly passed away on November 2, 2023.

■ ACKNOWLEDGMENTS

The support from the Czech Science Foundation (GACR) (21-06744K) and Slovenian Research and Innovation Agency (ARIS) (N1-089, J2-2496) in the form of a joint project within the Central European Science Partnership (CEUS); the European Research Council (ERC) under the European Union's Horizon 2020 research and innovation programme (Starting Grant 950625); the Jožef Stefan Institute Director's Fund; and the CzechNanoLab Research Infrastructure supported by MEYS CR (LM2023051), is gratefully acknowledged. The authors also thank Dr. Felix Hennersdorf and Dr. Jakub M. Wojciechowski, Rigaku Europe SE, Neu-Isenburg, Germany, for the measurement time on the Rigaku OD XtaLAB Synergy-DW VHF Flow diffractometer.

https://doi.org/10.1021/acscentsci.4c00815
ACS Cent. Sci. 2024, 10, 1733–1741

REFERENCES

(1) Blake, A. J.; Clegg, W.; Cole, J. M.; Evans, J. S. O.; Main, P.; Parsons, S.; Watkin, D. J. *Crystal Structure Analysis: Principles and Practice*, 2nd ed.; Clegg, W., Ed.; Oxford University Press: New York, 2009.

(2) Howard, J. A. K.; Probert, M. R. Cutting-Edge Techniques Used for the Structural Investigation of Single Crystals. *Science* **2014**, *343* (6175), 1098−1102.

(3) Gemmi, M.; Mugnaioli, E.; Gorelik, T. E.; Kolb, U.; Palatinus, L.; Boullay, P.; Hovmöller, S.; Abrahams, J. P. 3D Electron Diffraction: The Nanocrystallography Revolution. *ACS Cent. Sci.* **2019**, *5* (8), 1315−1329.

(4) Gruene, T.; Holstein, J. J.; Clever, G. H.; Keppler, B. Establishing Electron Diffraction in Chemical Crystallography. *Nat. Rev. Chem.* **2021**, *5* (9), 660−668.

(5) Gruene, T.; Mugnaioli, E. 3D Electron Diffraction for Chemical Analysis: Instrumentation Developments and Innovative Applications. *Chem. Rev.* **2021**, *121* (19), 11823−11834.

(6) Jones, C. G.; Asay, M.; Kim, L. J.; Kleinsasser, J. F.; Saha, A.; Fulton, T. J.; Berkley, K. R.; Cascio, D.; Malyutin, A. G.; Conley, M. P.; Stoltz, B. M.; Lavallo, V.; Rodríguez, J. A.; Nelson, H. M. Characterization of Reactive Organometallic Species via MicroED. *ACS Cent. Sci.* **2019**, *5* (9), 1507−1513.

(7) Bartlett, N. Xenon Hexafluoroplatinate(V) $Xe^{+}[PtF_6]^{-}$. *Proc. Chem. Soc.* **1962**, 218.

(8) Hargittai, I. Neil Bartlett and the First Noble-Gas Compound. *Struct. Chem.* **2009**, *20* (6), 953−959.

(9) Bartlett, N.; Jha, N. K. The Xenon-Platinum Hexafluoride Reaction and Related Reactions. In *Noble-Gas Compounds*; Hyman, H. H., Ed.; The University of Chicago Press: Chicago, 1963; pp 23−30.

(10) Bartlett, N.; Žemva, B.; Graham, L. Redox Reactions in the XeF_2/Platinum Fluoride and XeF_2/Palladium Fluoride Systems and the Conversion of XeF_2 to XeF_4 and Xe. *J. Fluorine Chem.* **1976**, *7* (1), 301−320.

(11) Graham, L.; Graudejus, O.; Jha, N. K.; Bartlett, N. Concerning the Nature of $XePtF_6$. *Coord. Chem. Rev.* **2000**, *197* (1), 321−334.

(12) Craciun, R.; Picone, D.; Long, R. T.; Li, S.; Dixon, D. A.; Peterson, K. A.; Christe, K. O. Third Row Transition Metal Hexafluorides, Extraordinary Oxidizers, and Lewis Acids: Electron Affinities, Fluoride Affinities, and Heats of Formation of WF_6, ReF_6, OsF_6, IrF_6, PtF_6, and AuF_6. *Inorg. Chem.* **2010**, *49* (3), 1056−1070.

(13) Christe, K. O. Bartlett's Discovery of Noble Gas Fluorides, a Milestone in Chemical History. *Chem. Commun.* **2013**, *49* (41), 4588−4590.

(14) Žemva, B. Binary Fluorides of Noble-Gases and Their Compounds. *Croat. Chem. Acta* **1988**, *61* (1), 163−187.

(15) Žemva, B.; Slivnik, J. On the Xenon-Fluorine Reactions. *J. Inorg. Nucl. Chem.* **1976**, *28* (Supplement 1), 173−178.

(16) Žemva, B.; Slivnik, J.; Bohinc, M. On the Syntheses of Xenon Fluorotitanates(IV). *J. Inorg. Nucl. Chem.* **1976**, *38* (1), 73−74.

(17) Radan, K.; Goreshnik, E.; Žemva, B. Xenon(II) Polyfluoridotitanates(IV): Synthesis and Structural Characterization of $[Xe_2F_3]^{+}$ and $[XeF]^{+}$ Salts. *Angew. Chem. Int. Ed.* **2014**, *53* (50), 13715−13719.

(18) Slivnik, J.; Žemva, B. Reaktionen von Chrom(V)-fluorid mit Xenon und Xenondifluorid. *Z. Anorg. Allg. Chem.* **1971**, *385* (1−2), 137−141.

(19) Lutar, K.; Leban, I.; Ogrin, T.; Žemva, B. $XeF_2{\cdot}CrF_4$ and $(XeF_5^{+}CrF_5^{-})_4{\cdot}XeF_4$: Syntheses, Crystal Structures and Some Properties. *Eur. J. Solid State Inorg. Chem.* **1992**, *29* (4−5), 713−727.

(20) Lutar, K.; Borrmann, H.; Žemva, B. $XeF_2{\cdot}2CrF_4$ and $XeF_5^{+}CrF_5^{-}$: Syntheses, Crystal Structures, and Some Properties. *Inorg. Chem.* **1998**, *37* (12), 3002−3006.

(21) Žemva, B.; Zupan, J.; Slivnik, J. On the $XeMnF_6$ Synthesis. *J. Inorg. Nucl. Chem.* **1971**, *33* (11), 3953−3955.

(22) Bohinc, M.; Grannec, J.; Slivnik, J.; Žemva, B. On the Syntheses of Xenon Fluoromanganates(IV). *J. Inorg. Nucl. Chem.* **1976**, *38* (1), 75−76.

(23) Lozinšek, M. Synthesis and Characterization of Xenon(II) Hexafluoromanganates(IV). Diploma thesis, University of Ljubljana, 2008.

(24) Družina, B.; Žemva, B. On the Synthesis of Xenon(II) Fluorostannates(IV). *J. Fluorine Chem.* **1986**, *34* (2), 233−239.

(25) Žemva, B.; Jesih, A.; Templeton, D. H.; Zalkin, A.; Cheetham, A. K.; Bartlett, N. Phases in the System XeF_2/XeF_5AsF_6 and Structural and Vibrational Evidence for the Following Ionization Pathway: $XeF_2 \rightarrow XeF^{+} + F^{-}$. *J. Am. Chem. Soc.* **1987**, *109* (24), 7420−7427.

(26) Higelin, A.; Riedel, S. High Oxidation States in Transition Metal Fluorides. In *Modern Synthesis Processes and Reactivity of Fluorinated Compounds*; Groult, H., Leroux, F. R., Tressaud, A., Eds.; Progress in Fluorine Science; Elsevier: Amsterdam, 2017; pp 561−586.

(27) Palatinus, L.; Petříček, V.; Corrêa, C. A. Structure Refinement Using Precession Electron Diffraction Tomography and Dynamical Diffraction: Theory and Implementation. *Acta Crystallogr. A* **2015**, *71* (2), 235−244.

(28) Palatinus, L.; Corrêa, C. A.; Steciuk, G.; Jacob, D.; Roussel, P.; Boullay, P.; Klementová, M.; Gemmi, M.; Kopeček, J.; Domeneghetti, M. C.; Cámara, F.; Petříček, V. Structure Refinement Using Precession Electron Diffraction Tomography and Dynamical Diffraction: Tests on Experimental Data. *Acta Crystallogr. B* **2015**, *71* (6), 740−751.

(29) Wang, Y.; Yang, T.; Xu, H.; Zou, X.; Wan, W. On the Quality of the Continuous Rotation Electron Diffraction Data for Accurate Atomic Structure Determination of Inorganic Compounds. *J. Appl. Crystallogr.* **2018**, *51* (4), 1094−1101.

(30) Palatinus, L.; Brázda, P.; Jelínek, M.; Hrdá, J.; Steciuk, G.; Klementová, M. Specifics of the Data Processing of Precession Electron Diffraction Tomography Data and Their Implementation in the Program *PETS2.0*. *Acta Crystallogr. B* **2019**, *75* (4), 512−522.

(31) Brázda, P.; Klementová, M.; Krysiak, Y.; Palatinus, L. Accurate Lattice Parameters from 3D Electron Diffraction Data. I. Optical Distortions. *IUCrJ* **2022**, *9* (6), 735−755.

(32) Hattne, J.; Shi, D.; Glynn, C.; Zee, C.-T.; Gallagher-Jones, M.; Martynowycz, M. W.; Rodriguez, J. A.; Gonen, T. Analysis of Global and Site-Specific Radiation Damage in Cryo-EM. *Structure* **2018**, *26* (5), 759−766.

(33) Saha, A.; Nia, S. S.; Rodríguez, J. A. Electron Diffraction of 3D Molecular Crystals. *Chem. Rev.* **2022**, *122* (17), 13883−13914.

(34) Zupanek, Ž.; Tramšek, M.; Kokalj, A.; Tavčar, G. Reactivity of VOF_3 with N-Heterocyclic Carbene and Imidazolium Fluoride: Analysis of Ligand−VOF_3 Bonding with Evidence of a Minute π Back-Donation of Fluoride. *Inorg. Chem.* **2018**, *57* (21), 13866−13879.

(35) Jensen, W. B. Crystal Coordination Formulas: A Flexible Notation for the Interpretation of Solid-State Structures. In *The Structures of Binary Compounds*; Hafner, J., Hulliger, F., Jensen, W. B., Majewski, J. A., Mathis, K., Villars, P., Vogl, P., Eds.; *Cohesion and Structure*; de Boer, F. R., Pettifor, D. G., Eds.; North-Holland: Amsterdam, 1989; Vol. 2, pp 105−146.

(36) Elliott, H. St. A.; Lehmann, J. F.; Mercier, H. P. A.; Jenkins, H. D. B.; Schrobilgen, G. J. X-Ray Crystal Structures of $[XeF][MF_6]$ (M = As, Sb, Bi), $[XeF][M_2F_{11}]$ (M = Sb, Bi) and Estimated Thermochemical Data and Predicted Stabilities for Noble-Gas Fluorocation Salts Using Volume-Based Thermodynamics. *Inorg. Chem.* **2010**, *49* (18), 8504−8523.

(37) Cohen, S.; Selig, H.; Gut, R. The Structure of $H_3O^{+}TiF_5^{-}$. *J. Fluorine Chem.* **1982**, *20* (3), 349−356.

(38) Morrell, B. K.; Zalkin, A.; Tressaud, A.; Bartlett, N. Crystal Structure of Rhodium Pentafluoride. *Inorg. Chem.* **1973**, *12* (11), 2640−2644.

(39) Shlyapnikov, I. M.; Mercier, H. P. A.; Goreshnik, E. A.; Schrobilgen, G. J.; Mazej, Z. Crystal Structures and Raman Spectra of Imidazolium Poly[Perfluorotitanate(IV)] Salts Containing the $[TiF_6]^{2-}$, $([Ti_2F_9]^{-})_\infty$, and $[Ti_2F_{11}]^{3-}$ and the New $[Ti_4F_{20}]^{4-}$ and $[Ti_5F_{23}]^{3-}$ Anions. *Inorg. Chem.* **2013**, *52* (15), 8315−8326.

(40) Leitz, D.; Nitzer, A.; Morgenstern, Y.; Zischka, F.; Kornath, A. J. Structural Investigation of Thiourea Dioxide in Superacids. *Eur. J. Inorg. Chem.* **2019**, No. 6, 808−812.

https://doi.org/10.1021/acscentsci.4c00815
ACS Cent. Sci. 2024, 10, 1733−1741

(41) Scheibe, B.; Karttunen, A. J.; Kraus, F. Reactions of ClF_3 with Main Group and Transition Metal Oxides: Access to Dioxychloronium-(V) Fluoridometallates and Oxidofluoridometallates. *Eur. J. Inorg. Chem.* **2021**, No. 4, 405−421.
(42) Müller, B. G. Zur kenntnis von $[O_2]^+[Mn_2F_9]^-$. *J. Fluorine Chem.* **1981**, *17* (5), 409−421.
(43) Christe, K. O.; Schack, C. J. Synthesis and Characterization of Bis(Perfluoroammonium) Hexafluorotitanate and of Higher Perfluoroammonium(1+) and Cesium(1+) Poly(Perfluorotitanate-(IV)) Salts. *Inorg. Chem.* **1977**, *16* (2), 353−359.
(44) Agron, P. A.; Begun, G. M.; Levy, H. A.; Mason, A. A.; Jones, C. G.; Smith, D. F. Xenon Difluoride and the Nature of the Xenon-Fluorine Bond. *Science* **1963**, *139* (3557), 842−844.
(45) Frlec, B.; Holloway, J. H. The XeF_2−MF_5 (M = Sb, Ta, or Nb) Systems: Vibrational Spectra of Solid Xenon Difluoride Adducts. *J. Chem. Soc., Dalton Trans.* **1975**, No. 6, 535−540.

https://doi.org/10.1021/acscentsci.4c00815
ACS Cent. Sci. 2024, 10, 1733−1741

4.2 Structures of $XeF_2 \cdot 2PtF_4$ and $XeF_2 \cdot 2PdF_4$ Determined by 3D Electron Diffraction and Structural Models of $XePtF_6$

K. Motaln, K. Gurung, M. Dragomir, D. Kurzydłowski, L. Palatinus, and M. Lozinšek

Published in: *Inorganic Chemistry*, 2025, 64, 29, 14968−14976

DOI: 10.1021/acs.inorgchem.5c01740

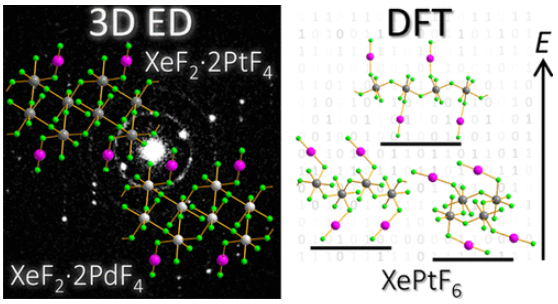


Figure 4.2: Graphical abstract of the publication "Structures of $XeF_2 \cdot 2PtF_4$ and $XeF_2 \cdot 2PdF_4$ Determined by 3D Electron Diffraction and Structural Models of $XePtF_6$" [197].

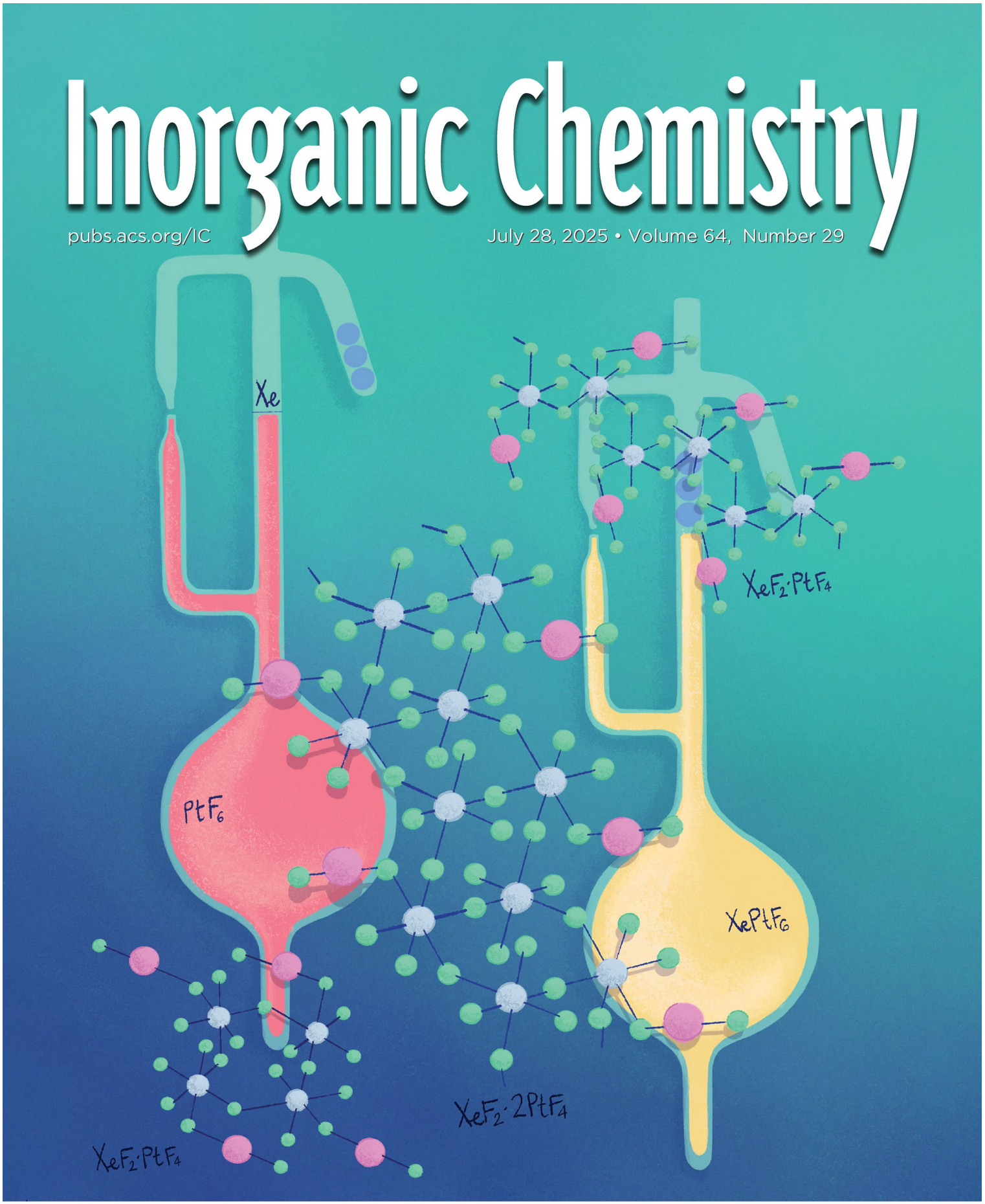
Building on the successful application of 3D ED to reactive XeF_2–MnF_4 compounds, which proved that reliable crystal structures for these compounds could be obtained from nanosized crystals [191], investigations of other compounds belonging to the XeF_2–MF_4 family was pursued. Previous studies into the XeF_2–PtF_4 system, which includes the first noble-gas compound $XePtF_6$ ($XeF_2 \cdot PtF_4$), have established strong parallels with the related XeF_2–PdF_4 system and showed that all air- and moisture-sensitive phases isolated from these families are either microcrystalline or amorphous, thereby precluding structure determination by SCXRD [79], [100]. This work aimed at reinvestigating both systems, applying 3D ED to enable crystallographic characterization of the previously observed microcrystalline $XeF_2 \cdot 2MF_4$ (M = Pd, Pt) phases, and attempt to gain further insight into viable structural models for $XeF_2 \cdot PtF_4$ with the aid of quantum chemical calculations.

Raman spectroscopic investigation of the amorphous bright orange solid obtained from the reaction of XeF_2 with Pt powder in aHF supported its formulation as $n XeF_2 \cdot PtF_4$, containing weakly bound XeF_2 molecules in its structure. The co-crystallized XeF_2 could be removed by pyrolysis under dynamic vacuum at 100 °C, affording $XeF_2 \cdot PtF_4$, which again proved amorphous to X-rays. Further pyrolysis of $XeF_2 \cdot PtF_4$ and of the related $XeF_2 \cdot PdF_4$ (the latter prepared by thermal reaction of PdF_4 and XeF_2) under dynamic vacuum at temperatures above 150 °C yielded phase-pure microcrystalline $XeF_2 \cdot 2PtF_4$ and $XeF_2 \cdot 2PdF_4$, as confirmed by PXRD.

Samples of these crystalline materials were loaded into the TEM under inert conditions using a cryogenic transfer protocol that preserved sample integrity and enabled collection of 3D ED data suitable for *ab initio* structure solution and dynamical refinement [192]. Both $XeF_2 \cdot 2PtF_4$ and $XeF_2 \cdot 2PdF_4$ were found to be isostructural with the previously characterized $XeF_2 \cdot 2MnF_4$, providing a direct structural link between the Pt/Pd adducts and the well-studied Mn analogues. Their structures comprise corrugated zigzag double chains constructed from corner-sharing [MF_6] octahedra. The XeF_2 ligands attached to this backbone are strongly polarized, exhibiting Xe–F_t bond distances comparable to those observed when XeF_2 is treated with excess Lewis superacid SbF_5 [198], consistent with describing these solids as tight-ion-pair salts $[XeF]^+[M_2F_9]^-$. The pronounced polarization of XeF_2 is further corroborated by low-temperature Raman spectra, which display Xe–F_t stretching bands above 600 cm^{-1}, characteristic of highly ionized XeF_2 ligands [39].

Guided by the experimentally determined structures possessing $XeMF_6$ stoichiometry from the XeF_2–CrF_4 and XeF_2–MF_4 systems [108], [191], periodic DFT was used to assess candidate structural models for $XeF_2 \cdot PtF_4$. The analysis revealed clear preference for *cis*-bridged connectivities, exemplified by a *cis*-chain and tetrameric ring motifs derived from the $3XeF_2 \cdot 2MnF_4$ and $XeF_2 \cdot MnF_4$ structures, respectively, over the *trans*-chain alternative stemming from the structure of $XeF_2 \cdot CrF_4$. In aggregate, the study revisited the XeF_2–MF_4 (M = Pt, Pd) systems, fully characterized the two crystalline phases using 3D ED in combination with PXRD, vibrational spectroscopy, and periodic DFT calculations, and narrowed the plausible structural space of the elusive $XePtF_6$ to *cis*-bridged structural motifs.

K. Motaln, the author of this dissertation, performed all synthetic work on the XeF_2–MF_4 compounds, measured their PXRD patterns and vibrational spectra, prepared the initial draft of the manuscript, and contributed to the review, editing, and revision of the final manuscript.



ACS Publications
Most Trusted. Most Cited. Most Read.
www.acs.org

Inorganic Chemistry

Open Access
This article is licensed under CC-BY 4.0

pubs.acs.org/IC Article

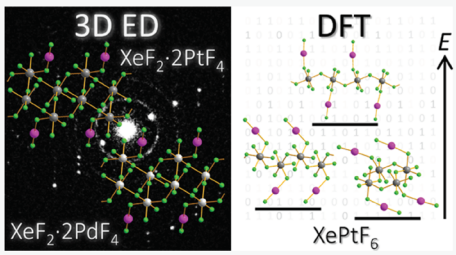
Crystal Structures of $XeF_2{\cdot}2PtF_4$ and $XeF_2{\cdot}2PdF_4$ Determined by 3D Electron Diffraction and Structural Models of $XePtF_6$

Klemen Motaln, Kshitij Gurung, Mirela Dragomir, Dominik Kurzydłowski,* Lukáš Palatinus,* and Matic Lozinšek*

Cite This: *Inorg. Chem.* 2025, 64, 14968−14976 Read Online

ACCESS | Metrics & More | Article Recommendations | Supporting Information

ABSTRACT: Although the demonstration of noble-gas reactivity represents one of the most significant breakthroughs of 20th-century inorganic chemistry, the first noble-gas compound, $XePtF_6$ ($XeF_2{\cdot}PtF_4$), lacks comprehensive structural characterization, and its structure remains to be elucidated. In this study, the XeF_2−PtF_4 and XeF_2−PdF_4 systems were reexplored, resulting in the crystal structure determination of $XeF_2{\cdot}2PtF_4$ and $XeF_2{\cdot}2PdF_4$ by 3D electron diffraction, marking the first successful structural characterization of compounds from these systems. Both compounds are isostructural with the previously characterized $XeF_2{\cdot}2MnF_4$, featuring corrugated zigzag double-chain motifs formed by interconnected octahedral fluoridometallate(IV) units. Periodic density functional theory calculations were employed to evaluate the structural models of $XeF_2{\cdot}PtF_4$, which were derived from experimentally determined crystal structures of XeF_2−MF_4 (M = Cr, Mn) analogues. The results reveal a preference for *cis*-bridging between adjacent platinum(IV) centers and show that a tetrameric ring structure and *cis*-chain polymorph, modeled after the crystal structure of $XeF_2{\cdot}MnF_4$ and XeF_2-deficient $3XeF_2{\cdot}2MnF_4$, respectively, emerge as energetically favored. The results of this study thus provide a direct structural link between platinum, palladium, and manganese analogues in the XeF_2−MF_4 systems and highlight the tetrameric ring structure and *cis*-chain as likely structural models of $XeF_2{\cdot}PtF_4$.



1. INTRODUCTION

The dogma of the chemical inertness of noble gases was dispelled in 1962 by a landmark experiment carried out by Neil Bartlett, where he oxidized and fluorinated gaseous xenon by PtF_6.[1] This daring experiment was inspired[2] by his earlier observation that PtF_6 oxidizes O_2 gas,[3] identifying PtF_6 as an extremely powerful oxidizing agent. The analysis of the yellow solid deposited in the reaction of red PtF_6 vapors with colorless Xe gas revealed that the stoichiometry of the product was $XePtF_6$.[1,4] A subsequent reinvestigation of this reaction indicated that the compound is likely diamagnetic, thus corresponding to oxidation states of +4 for platinum and +2 for xenon, and can therefore be represented as a Lewis acid−base adduct, $XeF_2{\cdot}PtF_4$.[4] It has been conjectured that the structure of this compound may consist of a F-bridged fluoridoplatinate backbone, which could adopt the form of either a chain polymer or a discrete ring, coordinated by XeF_2 molecules.[4] However, due to its inherently amorphous nature, no definitive structural information on this fascinating compound could ever be obtained, despite its great historical significance.[4,5] To complicate matters further, compounds of pentavalent platinum are also formed when Xe gas is oxidized by PtF_6, especially when an excess of the latter is used, as evidenced by the observation of the powder X-ray diffraction pattern[6] of $[XeF][PtF_6]$ during various preparations of $XePtF_6$.[4,5,7] Both PtF_5 and PtF_4 can form adducts with XeF_2, and in addition to the aforementioned $XeF_2{\cdot}PtF_4$ and $[XeF][PtF_6]$; $[Xe_2F_3][PtF_6]$, $[XeF][Pt_2F_{11}]$,[4,6−8] and $XeF_2{\cdot}2PtF_4$[4,5,7] have also been synthesized and vibrationally characterized. Unfortunately, no crystal structures of any of the aforementioned compounds have been reported to date.

The structures of platinum(V) compounds are expected to be analogous to the well-characterized pnictogen(V) analogues, namely ionic $[Xe_2F_3]^+[PnF_6]^-$ (Pn = As, Sb),[8,9] and molecular species $[XeF]^+[PnF_6]^-$ and $[XeF]^+[Pn_2F_{11}]^-$ (Pn = As, Sb, Bi),[10] which are better described as tight ion pairs with the anion F-coordinated to the strongly Lewis acidic XeF^+ cation. On the other hand, the investigations of XeF_2−MF_4 adducts as chemical analogues to $XeF_2{\cdot}PtF_4$, where M = Ti,[11−13] Cr,[14−16] Mn,[17−19] Rh,[5] Pd,[7] and Sn,[20] have established the existence of products with a wide range of stoichiometries.[21] Despite the fact that only a handful of crystal structures have been reported, these adducts display a remarkable structural diversity (Figure 1). A *trans*-chain of $[CrF_6]$ octahedra, each coordinated by a XeF_2 ligand, is

Received: April 18, 2025
Revised: June 4, 2025
Accepted: June 13, 2025
Published: July 14, 2025



ACS Publications
© 2025 The Authors. Published by American Chemical Society

https://doi.org/10.1021/acs.inorgchem.5c01740
Inorg. Chem. 2025, 64, 14968−14976

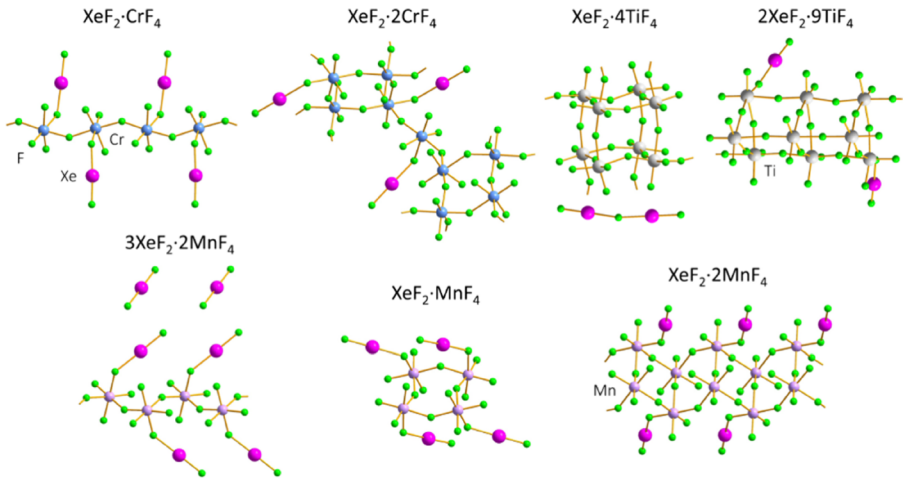


Figure 1. Rich structural diversity exhibited by crystallographically characterized XeF_2−MF_4 compounds.[13,15,16,19]

observed in $XeF_2 \cdot CrF_4$, whereas in the $XeF_2 \cdot 2CrF_4$ adduct, tetrameric rings are interconnected into a layered structure. The metal-rich adducts from the XeF_2−TiF_4 system display a high degree of XeF_2 ionization[22] and are therefore better described as salts of $Xe_2F_3^+$ and XeF^+. Octameric cube-like units are connected into a layer in $[Xe_2F_3][Ti_8F_{33}]$ ($XeF_2 \cdot 4TiF_4$), whereas the structure of $[XeF]_2[Ti_9F_{38}]$ ($2XeF_2 \cdot 9TiF_4$) features nonameric trigonal prismatic units connected by fluoride bridges into chains.[13] In a recent reinvestigation of the XeF_2−MnF_4 system, the crystal structures of $3XeF_2 \cdot 2MnF_4$, $XeF_2 \cdot MnF_4$, and $XeF_2 \cdot 2MnF_4$ were determined by both single-crystal X-ray diffraction (SCXRD) and 3D electron diffraction (3D ED).[19] The successful application of 3D ED to the study of these reactive compounds is of particular importance, as the previous structural investigations of the XeF_2−MF_4 family of compounds were often impeded by the inability to prepare single crystals of sufficient size and quality for SCXRD. The crystal structures of $3XeF_2 \cdot 2MnF_4$ and $XeF_2 \cdot 2MnF_4$ were found to consist of infinite polymeric chains and double chains, respectively, whereas discrete tetrameric rings were observed in the structure of $XeF_2 \cdot MnF_4$. Among the structurally characterized XeF_2−MF_4 compounds, only $XeF_2 \cdot CrF_4$ and $XeF_2 \cdot MnF_4$ represent the $XeMF_6$ stoichiometry observed in the first noble-gas compound $XePtF_6$, which renders them potential structural models for the structure of $XeF_2 \cdot PtF_4$, although various other structural types are also possible.

In this work, the XeF_2−PdF_4 and XeF_2−PtF_4 systems were reinvestigated, leading to the first successful structural characterization of compounds from these systems, with the crystal structures of $XeF_2 \cdot 2PdF_4$ and $XeF_2 \cdot 2PtF_4$ elucidated by 3D ED. The two compounds were revealed to be isostructural with $XeF_2 \cdot 2MnF_4$, thus establishing a direct structural link between the well-characterized XeF_2−MnF_4 system and its platinum and palladium analogues. Moreover, structural models for the crystal structure of the first discovered noble-gas compound $XePtF_6$ ($XeF_2 \cdot PtF_4$) are proposed based on DFT calculations augmented by evolutionary structure searches.

2. RESULTS AND DISCUSSION

2.1. Syntheses. The reaction of XeF_2 with platinum powder in aHF media (Figure 2) was previously reported as

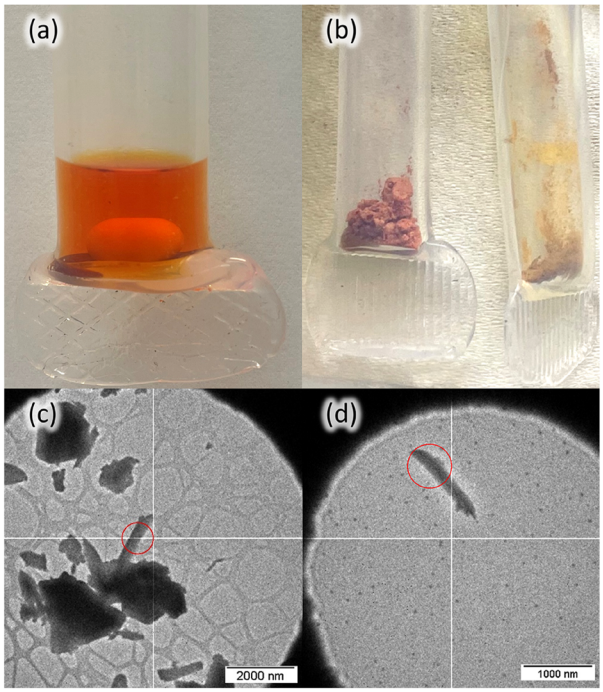


Figure 2. (a) Bright orange-colored solution formed when XeF_2 oxidizes Pt powder in aHF (19 mm o.d. FEP vessel). (b) Isolated $XeF_2 \cdot 2PtF_4$ (left) and $XeF_2 \cdot 2PdF_4$ (right) powder samples stored in FEP containers (8 mm o.d.), showing their vivid peach and orange-brown colors, respectively. (c,d) Crystallites of $XeF_2 \cdot 2PtF_4$ and $XeF_2 \cdot 2PdF_4$, respectively, used for structural determination by 3D ED, as observed in the TEM.

the first step of a convenient method for synthesizing PtF_4. The initially formed orange solid could be pyrolyzed at 300 °C to yield pure PtF_4, although the nature of the intermediate orange product was not investigated.[23] During the course of this study, the orange-red solid that forms after the removal of the solvent was isolated at temperatures between −40 and −60 °C. The material obtained was found to be a mixture of XeF_2 and an amorphous orange-red solid, which exhibited only broad bands in its Raman spectrum (Figure 3). Nevertheless, the positions of the strongest bands, located at 655 and 588 cm^{-1}, were

https://doi.org/10.1021/acs.inorgchem.5c01740
Inorg. Chem. 2025, 64, 14968−14976

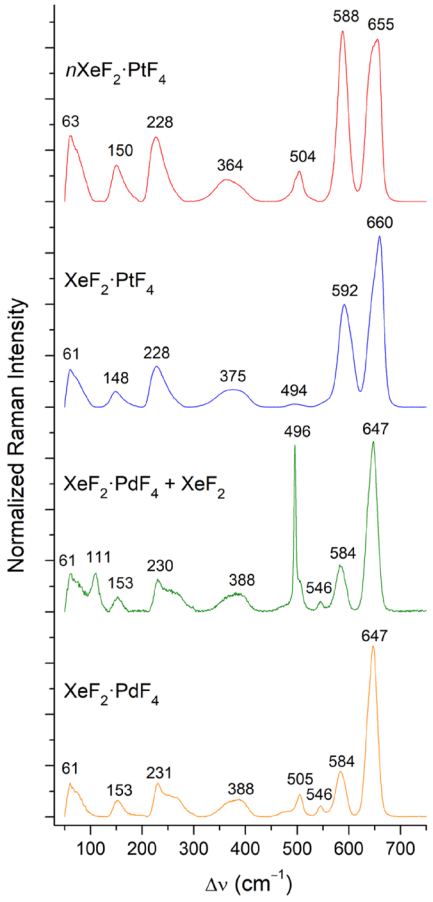


Figure 3. Ambient-temperature Raman spectra of the product of Pt oxidation by XeF_2 in aHF, $nXeF_2{\cdot}PtF_4$, $n > 1$ (red), the product of its pyrolysis under dynamic vacuum at 100 °C, $XeF_2{\cdot}PtF_4$ (blue), mixture of $XeF_2{\cdot}PdF_4$ and unreacted XeF_2 (green), and $XeF_2{\cdot}PdF_4$ (orange).

found to agree reasonably well with the reported Raman spectrum of the $XePtF_6$ prepared by the reaction of excess XeF_2 with PtF_4 in anhydrous HF, which exhibited three lines: 657 cm^{-1} (very strong), 591 cm^{-1} (strong), and 480 cm^{-1} (weak).[4] When the orange-red product investigated in this study was heated to a temperature of 100 °C under dynamic vacuum, the release of XeF_2 was observed, which was accumulated in an FEP trap held at −196 °C. The orange pyrolysis product was again found to be amorphous (Figure S1) and exhibited a Raman spectrum that was highly similar to that of the initial orange-red phase, with the exception of the band at 504 cm^{-1}, which was no longer present (Figure 3). Furthermore, a slight change in the position of some of the bands is evident. As it was observed by Bartlett et al. that reactions of excess XeF_2 with PtF_4 in aHF produced orange-colored adducts, with the molar ratio of XeF_2:PtF_4 as high as 1.6:1,[4] it can be assumed, that the initially formed orange-red solid is likely a XeF_2 "rich" phase with a stoichiometry of $nXeF_2{\cdot}PtF_4$ where $1 < n < 1.6$ (eq 1), which loses the weakly bound XeF_2 at elevated temperatures under dynamic vacuum, yielding a phase with composition $\sim XeF_2{\cdot}PtF_4$ (eq 2).

$$Pt + (n+2)XeF_2 \xrightarrow{aHF} nXeF_2{\cdot}PtF_4 + 2Xe \quad (1 < n < 1.6) \tag{1}$$

$$nXeF_2{\cdot}PtF_4 \xrightarrow[\text{dynamic vacuum}]{100\ ^\circ C} XeF_2{\cdot}PtF_4 + (n-1)XeF_2 \quad (1 < n < 1.6) \tag{2}$$

It is probable that the XeF_2 "rich" phase $nXeF_2{\cdot}PtF_4$ comprises cocrystallized XeF_2 molecules, a structural feature analogous to what is observed in the crystal structure of $3XeF_2{\cdot}2MnF_4$.[19] This is corroborated by a comparison of the Raman spectra of the compounds, as the ambient-temperature Raman spectrum of $3XeF_2{\cdot}2MnF_4$ exhibits a strong band at 506 cm^{-1} that has been assigned to cocrystallized XeF_2 and thus corresponds well to the position of the band observed at 504 cm^{-1} in the Raman spectrum of $nXeF_2{\cdot}PtF_4$ ($n > 1$) (Figure 3).

Previously, it was reported that the changes in the slope in a weight-loss curve indicated that the action of molten XeF_2 on either PdF_4 or Pd_2F_6 results in the formation of adducts $nXeF_2{\cdot}PdF_4$ (n = 4, 3, 2, 1) all of which lose XeF_2 under dynamic vacuum at room temperature except for $XeF_2{\cdot}PdF_4$.[7] The reinvestigation of the products of this reaction by Raman spectroscopy revealed that amorphous $XeF_2{\cdot}PdF_4$, along with unreacted XeF_2 (111, 496 cm^{-1}), is the sole identifiable product (Figure 3), although the reaction product was not exposed to dynamic vacuum (eq 3). $XeF_2{\cdot}PdF_4$ could be isolated from the product mixture by removing the excess XeF_2 under dynamic vacuum at room temperature.

$$XeF_2 + PdF_4 \xrightarrow{130\ ^\circ C} XeF_2{\cdot}PdF_4 \tag{3}$$

The Raman spectrum of $XeF_2{\cdot}PdF_4$ obtained during this study is in good agreement with the previously reported spectrum for this compound, which consisted of a strong band at 649 cm^{-1}, accompanied by weaker lines at 585, 505, 385, and 230 cm^{-1},[7] and shows a high degree of similarity to the Raman spectra of the platinum phases (Figure 3). The strong lines located at 588 and 592 cm^{-1} in the Raman spectra of the two platinum phases and the medium-strong line at 584 cm^{-1} in the spectrum of $XeF_2{\cdot}PdF_4$ can be readily assigned to the Xe−F_t (t: terminal) stretching modes. The observed position of these bands is comparable to that observed in the ambient-temperature Raman spectrum of $XeF_2{\cdot}MnF_4$, where two lines attributable to the Xe−F_t stretch are located at 580 and 587 cm^{-1},[19] thereby indicating that a similar degree of XeF_2 ionization is exhibited across this series of compounds. In comparison, the band attributable to the Xe−F_t stretch is located at 574 cm^{-1} in the Raman spectrum of $XeF_2{\cdot}CrF_4$.[24]

Heating the $XeF_2{\cdot}PtF_4$ and $XeF_2{\cdot}PdF_4$ adducts above 150 °C under dynamic vacuum resulted in the release of XeF_2 (eq 4). Powder X-ray diffraction (PXRD) patterns recorded on the resulting microcrystalline solids revealed them to be pure $XeF_2{\cdot}2PtF_4$ and $XeF_2{\cdot}2PdF_4$, respectively (Figures S1 and S2).

$$2(XeF_2{\cdot}MF_4) \xrightarrow[\text{dynamic vacuum}]{\geq 150\ ^\circ C} XeF_2{\cdot}2MF_4 + XeF_2 \quad (M = Pd, Pt) \tag{4}$$

Raman spectra of $XeF_2{\cdot}2PtF_4$ and $XeF_2{\cdot}2PdF_4$ were measured at a temperature of −173 °C (Figure 4 and Table S1) and exhibit excellent agreement with the previously reported ambient temperature spectra.[7] In both spectra, the strongest band expected for the Xe−F_t stretching mode is observed at 609 cm^{-1}. This value is comparable to the mode observed in other $[XeF]^+$ compounds, such as $[XeF][AsF_6]$ (607, 611 cm^{-1})[10] $[XeF][BiF_6]$ (602, 608 cm^{-1}),[10] and $XeF_2{\cdot}2MnF_4$ (612 cm^{-1}),[19] and thus attests that the XeF_2 ligand is highly ionized[22] due to the substantial Lewis acidity of the

https://doi.org/10.1021/acs.inorgchem.5c01740
Inorg. Chem. 2025, 64, 14968−14976

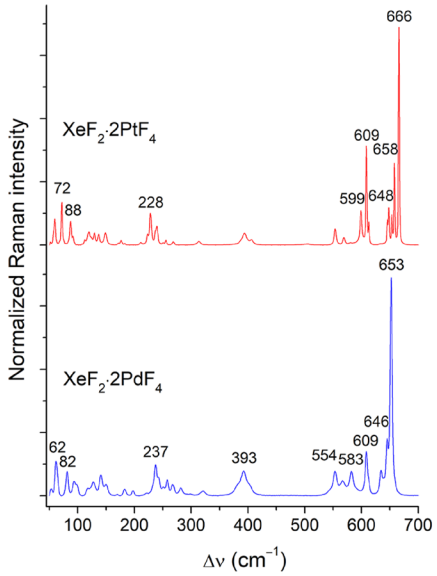


Figure 4. Low-temperature (−173 °C) Raman spectra of powdered $XeF_2 \cdot 2PtF_4$ (top) and $XeF_2 \cdot 2PdF_4$ (bottom).

$2MF_4$ unit or the low Lewis basicity of the $[(M_2F_9)^-]_\infty$ backbone.

2.2. Crystal Structures. The obtained powder samples of $XeF_2 \cdot 2PtF_4$ and $XeF_2 \cdot 2PdF_4$ were crystalline (Figures S1 and S2), however, the crystal sizes were too small for SCXRD analysis (Figure 2). Structural investigation by 3D ED revealed that $XeF_2 \cdot 2PtF_4$ and $XeF_2 \cdot 2PdF_4$ are isostructural and that this relationship extends also to the previously characterized $XeF_2 \cdot 2MnF_4$.[19] All compounds crystallize in the $P2_1/n$ space group with a slight increase in unit cell volume from 756.99(13) Å^3 for $XeF_2 \cdot 2MnF_4$ to 799.5(9) Å^3 for $XeF_2 \cdot 2PtF_4$ as the atomic number of the metal increases from Mn to Pt (Table 1).

In both structures, the asymmetric unit comprises two crystallographically independent metal(IV) centers, octahedrally coordinated by F atoms, with one of the centers coordinated by the XeF_2 ligand. Both crystallographically independent $[MF_6]$ octahedra exhibit slightly distorted geometry, with the *cis*-F−M−F angles spanning a range of 86.2(4)−92.2(4)° in the structure of $XeF_2 \cdot 2PtF_4$ and 87.0(3)−92.3(2)° in the case of $XeF_2 \cdot 2PdF_4$ (Tables 1, S2 and S3). Each $[MF_6]$ unit shares three *fac*-F-vertices with three different neighboring octahedra, establishing a linkage whereby each XeF_2-bearing octahedron is connected to three non-XeF_2-carrying octahedra, and vice versa (Figures 5, S3 and S4). The bridging M−F_b(M) bonds in $XeF_2 \cdot 2PtF_4$ measure between 1.957(7) and 2.032(7) Å, whereas in $XeF_2 \cdot 2PdF_4$ they range from 1.946(4) to 2.020(4) Å. The shorter M−F_t terminal bonds range from 1.863(7) to 1.905(11) Å in the case of $XeF_2 \cdot 2PtF_4$ and from 1.844(4) to 1.866(4) Å in the $XeF_2 \cdot 2PdF_4$ structure (Tables 1, S2 and S3).

This connectivity gives rise to infinite zigzag double chains propagating along the *a*-crystallographic axis, which can be formulated[25] as $^1_\infty[\langle MF_2F_{3/1+1}(XeF_2)\rangle\langle MF_3F_{3/1+1}\rangle]$ (Figure 5). In addition to the isostructural $XeF_2 \cdot 2MnF_4$, analogous corrugated double-chain motifs have been previously observed in the $[Ti_2F_9]^-$ anions, as evidenced in the crystal structures of, for example, $Cs[Ti_2F_9]$ and $[ClO_2][Ti_2F_9]$.[26,27] Although oligo- or polymeric anions, which arise from interconnected

Table 1. Summary of Crystal Data, Refinement Results, and Selected Bond Distances and Angles for the Structures of $XeF_2 \cdot 2PtF_4$ and $XeF_2 \cdot 2PdF_4$ Determined by 3D ED

	$XeF_2 \cdot 2PtF_4$	$XeF_2 \cdot 2PdF_4$
space group	$P2_1/n$	$P2_1/n$
a (Å)	5.4189(3)	5.3722(5)
b (Å)	9.8998(8)	9.959(3)
c (Å)	14.9993(9)	14.9091(8)
β (°)	96.506(5)	96.842(6)
V (Å^3)	799.5(9)	792.0(2)
Z	4	4
M_w (g mol^{-1})	711.4	534
D_{calcd} (g cm^{-3})	5.9195	4.4788
T (K)	100	100
R_1	0.0952	0.0657
wR_{all}	0.1120	0.0685
ΔV_{min}, ΔV_{max} (e Å^{-1})	−0.27, 0.29	−0.09, 0.10
Bond Lengths (Å) and Angles (°)		
Xe−F_t	1.909(10)	1.892(5)
Xe−F_b	2.316(8)	2.320(4)
M−F_b(Xe)	1.932(8)	1.894(4)
M−F_b(M)	1.957(7)−2.032(7)	1.946(4)−2.020(4)
M−F_t	1.863(7)−1.905(11)	1.844(4)−1.866(4)
M−F−M	131.9(5)−133.0(4)	132.0(3)−134.4(3)
cis-F−M−F	86.2(4)−92.2(4)	87.0(3)−92.3(2)
trans-F−M−F	177.2(4)−179.5(4)	176.7(3)−179.3(2)
F−Xe−F	176.0(5)	178.0(3)

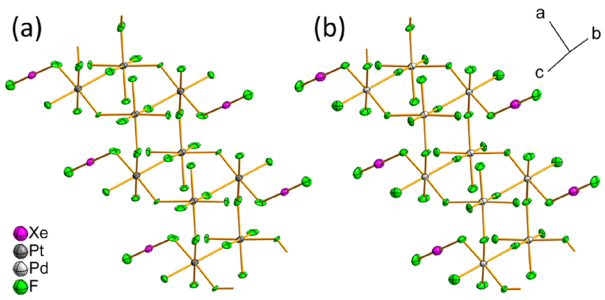


Figure 5. Sections of the crystal structures of (a) $XeF_2 \cdot 2PtF_4$ and (b) $XeF_2 \cdot 2PdF_4$ displaying the infinite corrugated zigzag double-chain motif. All atoms were refined anisotropically and are drawn as ellipsoids set at the 50% probability level.

$[MF_6]$ octahedra, have been observed to form with various tetravalent metals,[28] $XeF_2 \cdot 2PtF_4$ and $XeF_2 \cdot 2PdF_4$ represent the first crystal structures featuring polymeric F-bridged fluoridoplatinates(IV) and fluoridopalladates(IV), respectively.

As previously established in the XeF_2−TiF_4 and XeF_2−MnF_4 systems,[13,19] the increased dimensionality of the polyfluoridometallate backbone also leads to an increase in Lewis acidity, which is evidenced by the substantial ionization of the coordinated XeF_2 molecule. The bridging Xe−F_b bonds are highly elongated, measuring 2.316(8) and 2.320(4) Å in the structures of $XeF_2 \cdot 2PtF_4$ and $XeF_2 \cdot 2PdF_4$, respectively, whereas the Xe−F_t terminal bonds are contracted, measuring 1.909(10) and 1.892(5) Å, respectively. In the crystal structure of XeF_2 ($D_{\infty h}$), the Xe−F bond distance was determined to be 1.999(4) Å by SCXRD[10] and 1.992(8) Å by 3D ED.[29] The Xe−F_b bond length exceeding 2.3 Å has been hitherto observed exclusively in the crystal structure of $[XeF]^+[Sb_2F_{11}]^-$, which forms if XeF_2 is reacted with an

https://doi.org/10.1021/acs.inorgchem.5c01740
Inorg. Chem. 2025, 64, 14968−14976

Inorganic Chemistry pubs.acs.org/IC Article

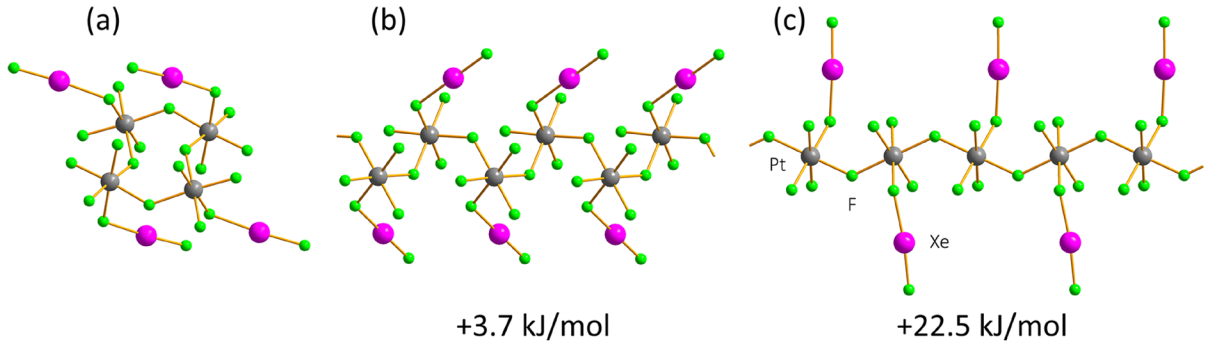


Figure 6. Periodic DFT-optimized structural models of $XeF_2{\cdot}PtF_4$ ($XePtF_6$) and the differences in their relative stabilities: (a) tetrameric ring, (b) *cis*-chain, and (c) *trans*-chain.

excess of Lewis superacid SbF_5.[10,30] This attests to the unprecedented Lewis acidity exhibited by the chains and confirms that the two $XeF_2{\cdot}2MF_4$ compounds can be regarded as a tight-ion pair salts, $[XeF]^+[M_2F_9]^-$.

Additionally, the crystal structures are stabilized by 8 Xe···F contacts, shorter than the corresponding sum of the van der Waals radii (3.52 Å),[31] with 3 of the contacts formed by F atoms, which are part of the same chain as the coordinated XeF_2 moiety and 5 belonging to the neighboring chains (Figures S5 and S6). The Xe···F contacts measure between 3.019(10) and 3.421(10) Å in the case of $XeF_2{\cdot}2PtF_4$ and between 3.049(6) and 3.427(7) Å in the case of $XeF_2{\cdot}2PdF_4$ (Tables S4 and S5).

2.3. Structural Models of $XePtF_6$. Computational evaluation of the structural models of $XeF_2{\cdot}PtF_4$ was performed using periodic density functional theory calculations, utilizing r^{2}SCAN meta-GGA functional supplemented with the D3 van der Waals corrections. The computational approach was initially benchmarked by performing geometry optimization calculations for $XeF_2{\cdot}CrF_4$ and $XeF_2{\cdot}MnF_4$ in the three considered structure types: $XeF_2{\cdot}CrF_4$,[15] $XeF_2{\cdot}MnF_4$,[19] and $3XeF_2{\cdot}2MnF_4$ with cocrystallized XeF_2 removed. For the sake of clarity, each of these structures will henceforth be labeled with respect to the connectivity of the $[MF_6]$ units: *trans*-chains (= $XeF_2{\cdot}CrF_4$), *cis*-chains (= $3XeF_2{\cdot}2MnF_4$; cocrystallized XeF_2 removed), and tetramers (= $XeF_2{\cdot}MnF_4$).

For $XeF_2{\cdot}CrF_4$, the results show that the *trans*-chain geometry has the lowest energy, in accordance with the experimentally observed structure (Figure 1).[15] The tetrameric ring polymorph is higher in energy (+9.8 kJ/mol per formula unit), whereas the *cis*-chain structure is even more destabilized (+11.6 kJ/mol). Calculations suggest that the lowest magnetic state for *trans*-chain $XeF_2{\cdot}CrF_4$ is an antiferromagnetic (AFM) arrangement of the unpaired electrons along the chains, which is in agreement with the previously reported magnetic measurements.[32] For $XeF_2{\cdot}MnF_4$, the experimental tetrameric structure has the lowest energy with *cis*- and *trans*-chains higher in energy (+3.2 and +16.3 kJ/mol, respectively). An AFM coupling of the magnetic moments within the tetramers is found as the lowest magnetic configuration. For both $XeF_2{\cdot}CrF_4$ and $XeF_2{\cdot}MnF_4$, the DFT-derived geometries of the lowest-energy structures are in close agreement with the experimental ones (Tables S6 and S7). In addition, geometry optimization calculations were also performed for $XeF_2{\cdot}2PtF_4$ and $XeF_2{\cdot}2PdF_4$, with the resulting bond lengths and angles showing good agreement with the experimentally determined structures (Tables S2 and S3).

Calculations performed for $XeF_2{\cdot}PtF_4$ (Figure 6 and Table 2) yield the same structure preferences as in the case of $XeF_2{\cdot}MnF_4$: the tetrameric ring ($XeF_2{\cdot}MnF_4$-type) structure has the lowest energy, with the *cis*-chain polymorph ($3XeF_2{\cdot}2MnF_4$-type; cocrystallized XeF_2 removed) slightly higher in energy (+3.7 kJ/mol), and the *trans*-chain structure ($XeF_2{\cdot}CrF_4$-type) much less stable by a significant value (+22.5 kJ/mol). These results indicate that the hypothesized *trans*-bridged chain structure based on $XeF_2{\cdot}CrF_4$,[15] which has been previously proposed as a model for the structure of $XeF_2{\cdot}PtF_4$,[4] is improbable, with *cis*-bridging among the neighboring octahedra, either in the form of tetramers or infinite chains, evidently preferred. Similar trend was observed in calculations performed for $XeF_2{\cdot}PdF_4$, with the tetrameric structure proving to be the most energetically favorable, followed by *cis*-chain (+4.6 kJ/mol) and *trans*-chain (+22.7 kJ/mol) structures. Additional probing of the potential energy surface of solid $XeF_2{\cdot}PtF_4$ was performed using an evolutionary algorithm search, which yielded 400 structures whose energy and geometry were optimized by DFT calculations. None of the generated structures had a lower energy than the tetrameric ring model, corroborating the notion that this is a likely ground-

Table 2. DFT-Calculated Unit-Cell Parameters and Selected Bond Distances and Angles for the Three Candidate Structures of $XeF_2{\cdot}PtF_4$

	$XeF_2{\cdot}PtF_4$ (tetrameric rings)	$XeF_2{\cdot}PtF_4$ (*cis*-chains)	$XeF_2{\cdot}PtF_4$ (*trans*-chains)
Space group	$P2_1/n$	$P2_1/n$	$P2_1/n$
a (Å)	9.630	9.794	7.425
b (Å)	11.151	5.038	7.215
c (Å)	9.872	11.457	10.032
β (°)	93.76	94.91	92.78
V (Å^3)	1057.75	563.32	536.78
Z	8	4	4
Bond Lengths (Å), Angles (°)			
Xe−F_t	1.981, 1.988	1.989	1.983
Xe−F_b	2.241, 2.259	2.230	2.242
M−F_b(Xe)	2.004, 2.022	2.009	2.004
M−F_b(M)	2.018−2.032	2.019, 2.019	1.977, 1.980
M−F_t	1.897−1.907	1.890−1.904	1.897−1.940
M−F−M	130.89, 131.78	134.04	131.47
cis-F−M−F	87.12−94.08	83.85−95.90	84.33−95.80
trans-F−M−F	175.58−179.84	175.71−177.22	178.30−178.90
F−Xe−F	174.83, 175.24	174.95	173.33

https://doi.org/10.1021/acs.inorgchem.5c01740
Inorg. Chem. 2025, 64, 14968−14976

state structure of $XeF_2 \cdot PtF_4$, at least at ambient pressure (P = 1 atm).

These results testify to the similarity in the structural landscape of the studied XeF_2-PtF_4 and XeF_2-MnF_4 compounds, in particular the preference for the formation of *cis*-bridges between adjacent metal centers. The calculations predict that in all of the investigated $XeF_2 \cdot PtF_4$ polymorphs the Pt^{IV} (d^6 electron count) adopt a low-spin configuration resulting in no net magnetic moment. This is in accordance with previous suggestions that pure $XePtF_6$ is diamagnetic, as the weak paramagnetic response of samples of this compound were the result of contamination with Pt^V compounds.[4]

3. CONCLUSIONS

In the present work, the chemistry of the XeF_2-PtF_4 and XeF_2-PdF_4 systems was revisited. The interaction of XeF_2 with metallic Pt in aHF solvent yielded an orange-red solution from which $n XeF_2 \cdot PtF_4$ ($1 < n < 1.6$) was isolated, and its Raman spectrum indicated that it contains cocrystallized XeF_2. The pyrolysis of this compound at 100 °C under dynamic vacuum resulted in the release of the cocrystallized XeF_2 giving rise to an orange solid, whose composition is likely $XeF_2 \cdot PtF_4$. The Raman spectra of both solids also exhibited a high degree of similarity to the Raman spectrum of $XeF_2 \cdot PdF_4$, which was prepared by the interaction of Pd_2F_6/PdF_4 mixture with molten XeF_2. However, the detailed structural investigation of these compounds was precluded due to their invariably amorphous nature. When exposed to dynamic vacuum at temperatures of 160 and 150 °C, respectively, $XeF_2 \cdot PtF_4$ and $XeF_2 \cdot PdF_4$ undergo pyrolysis, releasing XeF_2 and resulting in the formation of microcrystalline $XeF_2 \cdot 2PtF_4$ and $XeF_2 \cdot 2PdF_4$. Their structures were successfully elucidated by 3D ED, making them the first structurally characterized XeF_2-MF_4 (M = Pd, Pt) compounds and revealing them to be isostructural with the previously investigated $XeF_2 \cdot 2MnF_4$.[19] This observation provides the first evidence that directly links the XeF_2-PtF_4 system with the structurally well-characterized XeF_2-MnF_4 compounds. Moreover, $XeF_2 \cdot 2PtF_4$ and $XeF_2 \cdot 2PdF_4$ exhibit nearly identical PXRD patterns, corroborating their isostructural nature and the full profile fits using the Rietveld method also confirmed the structures derived from 3D ED.

In addition, quantum chemical calculations were utilized to assess the relative stabilities of $XeF_2 \cdot PtF_4$ in three distinct structural types, which were derived from the experimentally determined structures. The results indicated that the tetrameric-ring structure, based on $XeF_2 \cdot MnF_4$, is the most stable and that *cis*-bridging among the adjacent $[PtF_6]$ units is favored. The computational approach was benchmarked by performing the optimizations also for $XeF_2 \cdot CrF_4$ and $XeF_2 \cdot MnF_4$ in all three evaluated structural types, yielding the experimentally observed structure as the lowest in energy in both cases. The combined identification of isostructural relationships across the XeF_2-PtF_4 and XeF_2-MnF_4 systems, with the observed highest relative stability of the tetrameric ring-based structure closely followed by a *cis*-chain, establishes the $XeF_2 \cdot MnF_4$-type structures as the leading candidates for the structure of the first noble-gas compound $XeF_2 \cdot PtF_4$ ($XePtF_6$).

4. EXPERIMENTAL SECTION

Caution: The handling of anhydrous HF, F_2, and high-valent fluorides requires great care and should be conducted only by appropriately trained experimentalists in a well-ventilated fume hood. It is imperative that protective equipment is worn at all times, and that access to proper treatment procedures is available in case of exposure.[33,34]

4.1. Materials and Methods. *4.1.1. Reagents and Apparatus.* F_2 (Solvay Fluor, 98–99%), LiF (Aldrich, ≥99.98%), Pd (Sigma-Aldrich, 99.9%), and Pt powder (Thermo Scientific, 99.98%) were used as supplied without further purification. Prior to its use, commercial anhydrous HF (aHF; Linde, 99.995%) was condensed in a FEP reactor vessel loaded with K_2NiF_6 (Advance Research Chemicals, 99.9%) and left to stir overnight, thus eliminating the residual traces of moisture.[4,35] XeF_2 was synthesized via a gas-phase UV-photochemical reaction of F_2 and Xe, as previously described.[36] AsF_5 was prepared by the static fluorination of As_2O_3 in a nickel reaction vessel.[37]

All xenon(II) compounds examined in this study are highly moisture sensitive and require that all experimental procedures be conducted under strictly anhydrous conditions. The dispensing of volatiles and the work with aHF solvent were conducted on a custom-built vacuum line constructed from nickel, copper, polytetrafluoroethylene (PTFE) and fluorinated ethylene propylene (FEP). The handling of solids was conducted in a glovebox (Vigor SG1200/750E–SG1500/750E) containing an inert nitrogen atmosphere, with moisture levels maintained below 1 ppm at all times.

Thermal syntheses were conducted in PTFE-gasketed nickel reactors. Reactions in aHF were performed in reactors constructed of 16 mm i.d. × 19 mm o.d. FEP tubing, capped with brass-encased PTFE valves. Prior to use, all reactors were passivated with 300–700 Torr of F_2 overnight.

4.1.2. Synthesis of $nXeF_2 \cdot PtF_4$ ($n > 1$), $XeF_2 \cdot PtF_4$, and $XeF_2 \cdot 2PtF_4$. The first step of the synthesis involved the oxidation of Pt powder by an excess of XeF_2 in aHF solvent, following the previously outlined approach.[23] In an inert atmosphere glovebox, 327 mg (1.68 mmol) of platinum powder and 1020 mg (6.03 mmol) of XeF_2 were loaded into a reactor constructed from a 16 mm i.d. FEP tubing ($V \approx 32$ mL). The reactor was connected to the vacuum line and 2.4 mL of aHF was condensed on the solid reagents at the temperature of −196 °C. After the reactor contents were warmed to room temperature and the resulting mixture agitated, a gradual change in the color of the solution from colorless to orange-red was observed. Following an additional 16 h of agitation, an orange-red solution above a viscous dark-red liquid phase was observed in the reactor (Figure 2). The products were isolated by removing the volatiles under a dynamic vacuum at temperatures between −40 and −60 °C, resulting in the formation of an orange-red solid together with colorless crystals. The residual material was homogenized in a mortar and filled into a quartz capillary for analysis by PXRD and Raman spectroscopy. PXRD measurements revealed predominantly diffuse scattering, accompanied by very weak lines that could be attributed to XeF_2, whereas the Raman spectrum (Figure 3, top) resembled those previously reported for $XeF_2 \cdot PtF_4$ and $XeF_2 \cdot PdF_4$,[4,7] with a peak at 504 cm^{-1} and a shoulder at approximately 496 cm^{-1} likely corresponding to the cocrystallized and admixed XeF_2, respectively. Subsequently, 486 mg of the resulting product mixture was transferred to a nickel reaction vessel ($V \approx 7.4$ mL) which was then connected to the vacuum line via a U-shaped trap constructed of 6 mm i.d. FEP tubing (Figure S7). The reactor was heated to a temperature of 100 °C while held under dynamic vacuum and the released XeF_2 was collected in the FEP trap, which was cooled by liquid nitrogen. After 5 h, the accumulation of XeF_2 in the trap ceased. The orange material $XeF_2 \cdot PtF_4$ remaining in the reactor was loaded into a quartz capillary for analysis, which revealed no lines in the PXRD pattern (Figure S1) and yielded a Raman spectrum that was very similar to that of the initially formed orange-red product, albeit without the signals at 496/504 cm^{-1} (Figure 3, middle). A further round of pyrolysis under a dynamic vacuum was conducted at 160 °C. After 3.5 h, the accumulation of XeF_2 ceased. The PXRD pattern (Figures S1 and S2) and Raman spectrum (Figure 4) of the resulting peach-colored crystalline material (Figure 2) indicated that pure $XeF_2 \cdot 2PtF_4$ had formed.[7]

4.1.3. Synthesis of $XeF_2 \cdot PdF_4$ and $XeF_2 \cdot 2PdF_4$. An attempt was made to synthesize PdF_4 following the previously described route by

https://doi.org/10.1021/acs.inorgchem.5c01740
Inorg. Chem. 2025, 64, 14968−14976

displacing it from Li_2PdF_6 dissolved in aHF through the use of AsF_5.[4] Li_2PdF_6 was prepared by oxidizing Pd powder with F_2 in the presence of LiF in aHF solvent.[38] In all attempts to synthesize PdF_4 using this procedure, the resulting PdF_4 was partially reduced, forming a mixture of Pd_2F_6 and PdF_4.

In a typical experiment, a nickel reaction vessel ($V \approx 7.4$ mL) was loaded with XeF_2 (522 mg, 3.08 mmol) and the Pd_2F_6/PdF_4 mixture (61 mg) inside an inert atmosphere glovebox. The sealed reactor was transferred to an oven, which had been preheated to 130 °C, where it was left for 16 h. This resulted in a mixture of yellow solid $XeF_2{\cdot}PdF_4$ and colorless XeF_2 crystals as revealed by Raman spectroscopy (Figure 3). Unreacted XeF_2 can be removed from the product by sublimation under dynamic vacuum at room temperature. The produced pure $XeF_2{\cdot}PdF_4$ is amorphous and exhibits broad Raman bands that are in accordance with the previously reported results (Figure 3).[7] The pyrolysis of $XeF_2{\cdot}PdF_4$ was conducted under dynamic vacuum at a temperature of 150 °C,[7] resulting in the release of XeF_2, which was collected in a U-trap cooled with liquid nitrogen. The decomposition was complete after 5 h, yielding an orange-brown crystalline agglomerated powder (Figure 2) of pure $XeF_2{\cdot}2PdF_4$, as revealed by PXRD (Figure S2) and Raman spectroscopy (Figure 4).[7]

4.2. Characterization. *4.2.1. Powder X-ray Diffraction (PXRD).* Powder X-ray diffraction patterns were obtained on a Rigaku OD XtaLAB Synergy-S diffractometer equipped with a Dectris EIGER2 R CdTe 1M detector using microfocused Ag Kα radiation (λ = 0.56087 Å). PXRD profiles were extracted and processed using *CrysAlisPro* software.[39] The measurements were conducted at 100 K, using an Oxford Cryosystems 800 Series Cryostream. The measurement parameters employed in this study were consistent with those previously reported.[19,40] The samples were pulverized in an agate mortar within a glovebox and loaded into quartz capillaries, which were subsequently flame-sealed in a hydrogen−oxygen flame. Prior to use, quartz capillaries (500 μm diameter) were thoroughly dried under dynamic vacuum and passivated with F_2. *GSAS-II* program[41] was used for the structural refinements and quantitative phase analyses with the Rietveld refinement method.[42] Crystal structures determined by 3D ED were used to fit the PXRD data (Figure S2).

4.2.2. Vibrational Spectroscopy. Ambient and low-temperature Raman spectra were measured on a Bruker Senterra II confocal Raman microscope using a 785 nm emission line. The spectra were measured in the 50−1410 cm^{-1} range with a resolution of 1.5 cm^{-1}. An aperture of 50 × 1000 μm was used to acquire the spectra of $XeF_2{\cdot}PdF_4$, $XeF_2{\cdot}PdF_4$ with admixed XeF_2, $XeF_2{\cdot}PtF_4$ and $nXeF_2{\cdot}PtF_4$, whereas the spectra of $XeF_2{\cdot}2PtF_4$ and $XeF_2{\cdot}2PdF_4$ were obtained using an aperture of 15 × 1000 μm. The nominal power of the laser used was varied between 100 mW ($XeF_2{\cdot}2PtF_4$), 25 mW ($XeF_2{\cdot}2PdF_4$ $XeF_2{\cdot}PtF_4$, $nXeF_2{\cdot}PtF_4$), and 10 mW ($XeF_2{\cdot}PdF_4$, $XeF_2{\cdot}PdF_4$ with admixed XeF_2). Low-temperature spectra were measured at −173 °C employing a Linkam LTS420 low-temperature stage. Sample preparation involved loading the materials into quartz capillaries, as described in Section 4.2.1. Background subtraction from the spectra was performed using the Bruker *OPUS* 8.7 software suite, with 3 iterations of concave rubber band correction and 64 baseline points.

Infrared spectra (Figures S8 and S9) were measured inside an N_2 atmosphere glovebox on a Bruker Alpha II FT-IR spectrometer equipped with a Platinum Diamond-ATR sampling module. Prior to analysis, the compounds were finely ground in an agate mortar. Spectra were recorded in the range of 400−4000 cm^{-1} with a resolution of 4 cm^{-1} and 24 scans were taken per measurement.

4.2.3. 3D Electron Diffraction. 3D ED data collection was performed on an FEI Tecnai G^2 transmission electron microscope (TEM). Data sets were collected at a temperature of 100 K using a continuous rotation electron diffraction (cRED) method with a tilt step of 0.30° per diffraction frame. The electron beam was generated using a LaB_6 source at 200 kV (λ = 0.02508 Å), and a Medipix 3 hybrid pixel detector ASI CheeTah (512 × 512 pixels, 24-bit dynamic range) was used to collect the diffraction patterns.

Recently, a novel cryotransfer protocol was developed and successfully applied for the study of several air-sensitive and highly oxidizing xenon compounds, including $XeF_2{\cdot}2MnF_4$.[19] Following this procedure,[29] the samples were transferred directly from the FEP vessels in an N_2-filled glovebox to the cooled (< −150 °C) cryo-holder (Gatan Model 914), ensuring an air- and moisture-free environment. Then, the cooled cryo-holder was quickly transferred into the TEM.

The crystallites of $XeF_2{\cdot}2PtF_4$ and $XeF_2{\cdot}2PdF_4$, from which the 3D ED data were collected, are shown in Figures 2, S10 and S11. In the case of $XeF_2{\cdot}2PtF_4$, the data were collected on two crystals and subsequently merged. The diffraction data were processed in *PETS2* software[43] for indexation, lattice parameter determination, and data reduction. The optical distortions of the diffraction patterns were taken into account to ensure accurate lattice parameter determinations.[44] Then the processed data were imported into *JANA2020*[45] for crystal structure determination ab initio using *SIR2014*.[46] The structures were first refined kinematically and then, without further optimization of kinematical refinement, they were refined dynamically.[47] For the dynamical calculation of the diffracted intensities, an incoherent mosaicity model was used, which assumes the crystals to be composed of large mosaic blocks that span the entire crystal thickness.[48] Including this model significantly improved the *R*-factors by about 3.8−4.8%. Further information on the experimental setup for 3D ED can be found in the SI (Tables S8−S10). Molecular graphics were prepared using the *Diamond* 5.0 software.[49]

4.3. Periodic DFT Calculations. Periodic plane-wave density functional theory (DFT) calculations were performed within the projector-augmented-wave (PAW) method as implemented in *VASP* 6.4.3.[50,51] r^2SCAN meta-GGA functional[52,53] supplemented with the D3 van der Waals corrections[54,55] was employed, which has proven to yield more accurate results for the modeling of palladium fluorides than the GGA-based PBE functional.[56] The calculations were performed using a plane-wave basis set with a cutoff energy of 700 eV, and the convergence criterion for electronic minimization was 10^{-6} eV. Brillouin zone sampling was performed using the Monkhorst−Pack mesh with a *k*-point spacing of $2\pi \times 0.033$ $Å^{-1}$.[57] Geometry optimization of the crystal structures was conducted with all free parameters (i.e., those not constrained by space group symmetry) allowed to vary. The optimization was conducted until the forces acting on atoms were smaller than 5 meV/Å and stresses were below 100 bar. Calculations were conducted assuming spin-polarization of the Kohn−Sham orbitals, and for each structure and stoichiometry, several spin states were tested—the geometry optimization was performed for the one exhibiting the lowest energy.

The optimization was conducted for $XeF_2{\cdot}2PtF_4$, $XeF_2{\cdot}2PdF_4$, and $XeF_2{\cdot}MF_4$ (M = Cr, Mn, Pd, Pt) compounds. For the latter, three possible structure types were considered: $XeF_2{\cdot}CrF_4$,[15] $XeF_2{\cdot}MnF_4$,[19] and a structure derived from $3XeF_2{\cdot}2MnF_4$[19] by removing the cocrystallized XeF_2 molecules (yielding a $XeF_2{\cdot}MF_4$ stoichiometry). The energies (per formula unit) of the optimized structures were compared as a proxy for their relative stability. Atom coordinates of the DFT-calculated crystal structures are reported in the SI (Table S11).

Evolutionary structure searches for structure candidates for $XeF_2{\cdot}PtF_4$ were conducted in the *XtalOpt* program (version r12).[58] The searches for crystal structures containing up to 4 $XePtF_6$ formula units in the primitive unit cell were carried out at ambient pressure at the same level of theory as described above.

■ ASSOCIATED CONTENT

Data Availability Statement

The data supporting the findings of this study are available on the Zenodo open repository https://zenodo.org/ under the DOI number: 10.5281/zenodo.15594028.

Supporting Information

The Supporting Information is available free of charge at https://pubs.acs.org/doi/10.1021/acs.inorgchem.5c01740.

PXRD data and Rietveld refinement results, tabulated Raman data, additional crystallographic data and figures displaying crystal packing and nonbonded Xe···F

https://doi.org/10.1021/acs.inorgchem.5c01740
Inorg. Chem. 2025, 64, 14968−14976

contacts, comparison of the experimental and DFT-calculated structural parameters, ATR-IR spectra, and the coordinates of the DFT-calculated structures (PDF)

Accession Codes

Deposition Numbers 2438371 and 2438372 contain the supplementary crystallographic data for this paper. These data can be obtained free of charge via the joint Cambridge Crystallographic Data Centre (CCDC) and Fachinformationszentrum Karlsruhe Access Structures service.

AUTHOR INFORMATION

Corresponding Authors

Dominik Kurzydłowski − *Faculty of Mathematics and Natural Sciences, Cardinal Stefan Wyszyński University in Warsaw, 01-938 Warsaw, Poland;* orcid.org/0000-0003-2862-0538; Email: d.kurzydlowski@uksw.edu.pl

Lukáš Palatinus − *Department of Structure Analysis, Institute of Physics of the Czech Academy of Sciences, Prague 8 18221, Czech Republic;* orcid.org/0000-0002-8987-8164; Email: palat@fzu.cz

Matic Lozinšek − *Jožef Stefan Institute, 1000 Ljubljana, Slovenia; Jožef Stefan International Postgraduate School, 1000 Ljubljana, Slovenia;* orcid.org/0000-0002-1864-4248; Email: matic.lozinsek@ijs.si

Authors

Klemen Motaln − *Jožef Stefan Institute, 1000 Ljubljana, Slovenia; Jožef Stefan International Postgraduate School, 1000 Ljubljana, Slovenia;* orcid.org/0000-0003-0051-8611

Kshitij Gurung − *Department of Structure Analysis, Institute of Physics of the Czech Academy of Sciences, Prague 8 18221, Czech Republic*

Mirela Dragomir − *Jožef Stefan Institute, 1000 Ljubljana, Slovenia; Jožef Stefan International Postgraduate School, 1000 Ljubljana, Slovenia;* orcid.org/0000-0002-4910-253X

Complete contact information is available at: https://pubs.acs.org/10.1021/acs.inorgchem.5c01740

Notes

The authors declare no competing financial interest.

ACKNOWLEDGMENTS

The support from the Slovenian Research and Innovation Agency (ARIS) (N1-0189, N1-0225, N1-0397, P2-0105), the Czech Science Foundation (GACR) (21-06744K), and the National Science Centre, Poland (NCN) (OPUS Grant UMO-2020/39/I/ST4/03442) in the form of joint projects (GACR−ARIS, NCN−ARIS) within the Central European Science Partnership (CEUS); the European Research Council (ERC) under the European Union's Horizon 2020 Research and Innovation Programme (Starting Grant 950625); the Jožef Stefan Institute Director's Fund; and the CzechNanoLab Research Infrastructure supported by MEYS CR (LM2023051) is gratefully acknowledged. DFT modeling was carried out with the support of the Poznań Supercomputing and Networking Center (PSNC) (allocation pl0091-02). Evolutionary structural searches were conducted with the computing resources of the Interdisciplinary Centre for Mathematical and Computational Modelling (ICM), University of Warsaw (allocation g97-1918).

REFERENCES

(1) Bartlett, N. Xenon Hexafluoroplatinate(V) $Xe^+[PtF_6]^-$. *Proc. Chem. Soc.* **1962**, No. 6, 197−236.

(2) Hargittai, I. Neil Bartlett and the First Noble-Gas Compound. *Struct. Chem.* **2009**, *20* (6), 953−959.

(3) Bartlett, N.; Lohmann, D. H. 1005. Fluorides of the noble metals. Part II. Dioxygenyl Hexafluoroplatinate(V) $O_2^+[PtF_6]^-$. *J. Chem. Soc.* **1962**, 5253.

(4) Graham, L.; Graudejus, O.; Jha, N. K.; Bartlett, N. Concerning the Nature of $XePtF_6$. *Coord. Chem. Rev.* **2000**, *197* (1), 321−334.

(5) Bartlett, N.; Jha, N. K. The Xenon−Platinum Hexafluoride Reaction and Related Reactions. In *Noble-gas compounds*; Hyman, H. H., Ed.; The University of Chicago Press: Chicago, 1963; pp 23−30.

(6) Sladky, F. O.; Bulliner, P. A.; Bartlett, N. Xenon Difluoride as a Fluoride Ion Donor. Evidence for the Salts $[Xe_2F_3]^+[MF_6]^-$, $[XeF]^+[MF_6]^-$ and $[XeF]^+[M_2F_{11}]^-$. *J. Chem. Soc. A* **1969**, 2179−2188.

(7) Bartlett, N.; Žemva, B.; Graham, L. Redox Reactions in the XeF_2/Platinum Fluoride and XeF_2/Palladium Fluoride Systems and the Conversion of XeF_2 to XeF_4 and Xe. *J. Fluorine Chem.* **1976**, *7* (1), 301−320.

(8) Sladkey, F. O.; Bulliner, P. A.; Bartlett, N.; DeBoer, B. G.; Zalkin, A. Xenon Difluoride as a Fluoride Ion Donor and the Crystal Structure of $[Xe_2F_3]^+[AsF_6]^-$. *Chem. Commun. (London)* **1968**, No. 17, 1048−1049.

(9) Fir, B. A.; Gerken, M.; Pointner, B. E.; Mercier, H. P. A.; Dixon, D. A.; Schrobilgen, G. J. An X-Ray Crystallographic Study of $[Xe_2F_3][SbF_6]$ and Dimorphism in $[Xe_2F_3][AsF_6]$; and a Density Functional Theory Study of the $Xe_2F_3^+$ Cation. *J. Fluorine Chem.* **2000**, *105* (1), 159−167.

(10) Elliott, H. St. A.; Lehmann, J. F.; Mercier, H. P. A.; Jenkins, H. D. B.; Schrobilgen, G. J. X-Ray Crystal Structures of $[XeF][MF_6]$ (M = As, Sb, Bi), $[XeF][M_2F_{11}]$ (M = Sb, Bi) and Estimated Thermochemical Data and Predicted Stabilities for Noble-Gas Fluorocation Salts Using Volume-Based Thermodynamics. *Inorg. Chem.* **2010**, *49* (18), 8504−8523.

(11) Žemva, B.; Slivnik, J. On the Xenon−Fluorine Reactions. *J. Inorg. Nucl. Chem.* **1976**, *28* (Suppl 1), 173−178.

(12) Žemva, B.; Slivnik, J.; Bohinc, M. On the Syntheses of Xenon Fluorotitanates(IV). *J. Inorg. Nucl. Chem.* **1976**, *38* (1), 73−74.

(13) Radan, K.; Goreshnik, E.; Žemva, B. Xenon(II) Polyfluoridotitanates(IV): Synthesis and Structural Characterization of $[Xe_2F_3]^+$ and $[XeF]^+$ Salts. *Angew. Chem. Int. Ed.* **2014**, *53* (50), 13715−13719.

(14) Slivnik, J.; Žemva, B. Reaktionen von Chrom(V)−fluorid mit Xenon und Xenondifluorid. *Z. Anorg. Allg. Chem.* **1971**, *385* (1−2), 137−141.

(15) Lutar, K.; Leban, I.; Ogrin, T.; Žemva, B. $XeF_2 \cdot CrF_4$ and $(XeF_5^+CrF_5^-)_4 \cdot XeF_4$: Syntheses, Crystal Structures and Some Properties. *Eur. J. Solid State Inorg. Chem.* **1992**, *29*, 713−727.

(16) Lutar, K.; Borrmann, H.; Žemva, B. $XeF_2 \cdot 2CrF_4$ and $XeF_5^+CrF_5^-$: Syntheses, Crystal Structures, and Some Properties. *Inorg. Chem.* **1998**, *37* (12), 3002−3006.

(17) Žemva, B.; Zupan, J.; Slivnik, J. On the $XeMnF_6$ Synthesis. *J. Inorg. Nucl. Chem.* **1971**, *33* (11), 3953−3955.

(18) Bohinc, M.; Grannec, J.; Slivnik, J.; Žemva, B. On the Syntheses of Xenon Fluoromanganates(IV). *J. Inorg. Nucl. Chem.* **1976**, *38* (1), 75−76.

(19) Motaln, K.; Gurung, K.; Brázda, P.; Kokalj, A.; Radan, K.; Dragomir, M.; Žemva, B.; Palatinus, L.; Lozinšek, M. Reactive Noble-Gas Compounds Explored by 3D Electron Diffraction: XeF_2−MnF_4 Adducts and a Facile Sample Handling Procedure. *ACS Cent. Sci.* **2024**, *10* (9), 1733−1741.

(20) Družina, B.; Žemva, B. On the Synthesis of Xenon(II) Fluorostannates(IV). *J. Fluorine Chem.* **1986**, *34* (2), 233−239.

(21) Žemva, B. Binary Fluorides of Noble-Gases and Their Compounds. *Croat. Chem. Acta* **1988**, *61* (1), 163−187.

(22) Žemva, B.; Jesih, A.; Templeton, D. H.; Zalkin, A.; Cheetham, A. K.; Bartlett, N. Phases in the System XeF_2/XeF_5AsF_6 and Structural

https://doi.org/10.1021/acs.inorgchem.5c01740
Inorg. Chem. 2025, 64, 14968−14976

and Vibrational Evidence for the Following Ionization Pathway: $XeF_2 \rightarrow XeF^+ + F^-$. *J. Am. Chem. Soc.* **1987**, *109* (24), 7420−7427.
(23) Drews, T.; Rusch, D.; Seidel, S.; Willemsen, S.; Seppelt, K. Systematic Reactions of $[Pt(PF_3)_4]$. *Chem. − Eur. J.* **2008**, *14* (14), 4280−4286.
(24) Milićev, S.; Lutar, K.; Žemva, B.; Ogrin, T. Vibrational Spectra of Solid CrF_4 and of Three New Fluorochromate(IV) Complexes with Xe Fluorides, $XeF_2{\cdot}CrF_4$, $(XeF_5^+CrF_5^-)_4{\cdot}XeF_4$ and $XeF_5^+CrF_5^-$. *J. Mol. Struct.* **1994**, *323*, 1−6.
(25) Jensen, W. B. Crystal Coordination Formulas: A Flexible Notation for the Interpretation of Solid-State Structures. In *The Structures of Binary Compounds*; de Boer, F. R.; Pettifor, D. G., Eds.; Cohesion and Structure; Elsevier: North-Holland, Amsterdam, 1989; Vol. 2, pp 105−146.
(26) Mazej, Z.; Goreshnik, E. Poly[Perfluorotitanate(IV)] Salts of $[H_3O]^+$, Cs^+, $[Me_4N]^+$, and $[Ph_4P]^+$ and about the Existence of an Isolated $[Ti_2F_9]^-$ Anion in the Solid State. *Inorg. Chem.* **2009**, *48* (14), 6918−6923.
(27) Scheibe, B.; Karttunen, A. J.; Kraus, F. Reactions of ClF_3 with Main Group and Transition Metal Oxides: Access to Dioxychloronium(V) Fluoridometallates and Oxidofluoridometallates. *Eur. J. Inorg. Chem.* **2021**, *2021* (4), 405−421.
(28) Mazej, Z. Polyanion Condensation in Inorganic and Hybrid Fluoridometallates (IV) of Octahedrally Coordinated Ti, Zr, Hf, V, Cr, W, Mn, Ge, Sn, and Pb. *Molecules* **2024**, *29* (6), No. 1361.
(29) Gurung, K.; Uran, E.; Motaln, K.; Brázda, P.; Radan, K.; Lozinšek, M.; Palatinus, L. A Simple Cryo-Transfer Method for 3D Electron Diffraction Measurements of Highly Sensitive Samples. *J. Appl. Crystallogr.* **2025**, *58* (3), 1079−1084.
(30) Burgess, J.; Fraser, C. J. W.; McRae, V. M.; Peacock, R. D.; Russell, D. R. The Adduct $XeF_2{\cdot}2SbF_5$: Its Crystal Structure and Thermochemistry. *J. Inorg. Nucl. Chem.* **1976**, *28*, 183−188.
(31) Alvarez, S. A Cartography of the van Der Waals Territories. *Dalton Trans.* **2013**, *42* (24), 8617−8636.
(32) Mazej, Z.; Darriet, J.; Grannec, J.; Lutar, K.; Tressaud, A.; Žemva, B. Magnetic Properties of CrF_4 and Two Fluorochromate(IV) Complexes with Xenon Fluorides, $XeF_2{\cdot}CrF_4$ and $(XeF_5^+CrF_5^-)_4{\cdot}XeF_4$. *J. Fluorine Chem.* **1999**, *99* (1), 25−28.
(33) Peters, D.; Miethchen, R. Symptoms and Treatment of Hydrogen Fluoride Injuries. *J. Fluorine Chem.* **1996**, *79* (2), 161−165.
(34) Segal, E. B. First Aid for a Unique Acid, HF: A Sequel. *Chem. Health Saf.* **2000**, *7* (1), 18−23.
(35) Möbs, M.; Karttunen, A. J.; Christe, K. O.; Kraus, F. Further Insights into the Chemical Synthesis of F_2 and on Drying Moist HF. *Inorg. Chem.* **2024**, *63* (16), 7105−7112.
(36) Šmalc, A.; Lutar, K. Xenon Difluoride (Modification). In *Inorganic Syntheses*; Grimes, R. N., Ed.; John Wiley & Sons: 1992; Vol. *29*, pp 1−4.
(37) Mazej, Z.; Žemva, B. Synthesis of Arsenic Pentafluoride by Static Fluorination of As_2O_3 in a Closed System. *J. Fluorine Chem.* **2005**, *126* (9), 1432−1434.
(38) Lucier, G. M.; Elder, S. H.; Chacon, L.; Bartlett, N. The Room Temperature Oxidation of Gold, Ruthenium, Osmium, Iridium, Platinum, or Palladium with Fluorine in Anhydrous Hydrogen Fluoride. *Eur. J. Solid State Inorg. Chem.* **1996**, *33*, 809−820.
(39) Rigaku, O. D. *CrysAlisPro*; Rigaku Corporation: Wroclaw, Poland, 2024.
(40) Belak Vivod, M.; Jagličić, Z.; King, G.; Hansen, T. C.; Lozinšek, M.; Dragomir, M. Mechanochemical Synthesis and Magnetic Properties of the Mixed-Valent Binary Silver(I,II) Fluorides, $Ag^I{}_2Ag^{II}F_4$ and $Ag^IAg^{II}F_3$. *J. Am. Chem. Soc.* **2024**, *146* (44), 30510−30517.
(41) Toby, B. H.; Von Dreele, R. B. *GSAS-II*: The Genesis of a Modern Open-Source All Purpose Crystallography Software Package. *J. Appl. Crystallogr.* **2013**, *46* (2), 544−549.
(42) Rietveld, H. M. A Profile Refinement Method for Nuclear and Magnetic Structures. *J. Appl. Crystallogr.* **1969**, *2* (2), 65−71.
(43) Palatinus, L.; Brázda, P.; Jelínek, M.; Hrdá, J.; Steciuk, G.; Klementová, M. Specifics of the Data Processing of Precession Electron Diffraction Tomography Data and Their Implementation in the Program *PETS2.0*. *Acta Crystallogr. B* **2019**, *75* (4), 512−522.
(44) Brázda, P.; Klementová, M.; Krysiak, Y.; Palatinus, L. Accurate Lattice Parameters from 3D Electron Diffraction Data. *I. Optical Distortions*. *IUCrJ*. **2022**, *9* (6), 735−755.
(45) Petříček, V.; Dušek, M.; Palatinus, L. Crystallographic Computing System *JANA2006*: General features. *Z. Kristallogr. Cryst. Mater.* **2014**, *229* (5), 345−352.
(46) Burla, M. C.; Caliandro, R.; Carrozzini, B.; Cascarano, G. L.; Cuocci, C.; Giacovazzo, C.; Mallamo, M.; Mazzone, A.; Polidori, G. Crystal Structure Determination and Refinement via *SIR2014*. *J. Appl. Crystallogr.* **2015**, *48* (1), 306−309.
(47) Palatinus, L.; Petříček, V.; Corrêa, C. A. Structure Refinement Using Precession Electron Diffraction Tomography and Dynamical Diffraction: Theory and Implementation. *Acta Crystallogr. A* **2015**, *71* (2), 235−244.
(48) Palatinus, L. Including Mosaicity Effects in the Dynamical Refinement against 3D ED Data. *Acta Crystallogr. A* **2024**, *80*, No. e225.
(49) Putz, H.; Brandenburg, K. *Diamond − Crystal and Molecular Structure Visualization*; Crystal Impact: Bonn, Germany, 2024.
(50) Kresse, G.; Furthmüller, J. Efficient Iterative Schemes for *Ab Initio* Total-Energy Calculations Using a Plane-Wave Basis Set. *Phys. Rev. B* **1996**, *54* (16), 11169−11186.
(51) Kresse, G.; Joubert, D. From Ultrasoft Pseudopotentials to the Projector Augmented-Wave Method. *Phys. Rev. B* **1999**, *59* (3), 1758−1775.
(52) Sun, J.; Ruzsinszky, A.; Perdew, J. P. Strongly Constrained and Appropriately Normed Semilocal Density Functional. *Phys. Rev. Lett.* **2015**, *115* (3), No. 036402.
(53) Furness, J. W.; Kaplan, A. D.; Ning, J.; Perdew, J. P.; Sun, J. Accurate and Numerically Efficient r^2SCAN Meta-Generalized Gradient Approximation. *J. Phys. Chem. Lett.* **2020**, *11* (19), 8208−8215.
(54) Grimme, S.; Antony, J.; Ehrlich, S.; Krieg, H. A Consistent and Accurate *Ab Initio* Parametrization of Density Functional Dispersion Correction (DFT-D) for the 94 Elements H-Pu. *J. Chem. Phys.* **2010**, *132* (15), No. 154104.
(55) Ehlert, S.; Huniar, U.; Ning, J.; Furness, J. W.; Sun, J.; Kaplan, A. D.; Perdew, J. P.; Brandenburg, J. G. r^2SCAN-D4: Dispersion Corrected Meta-Generalized Gradient Approximation for General Chemical Applications. *J. Chem. Phys.* **2021**, *154* (6), No. 061101.
(56) Olszewska, S.; Pillai, S. B.; Upadhyay, D.; Zdun, K.; Drapała, J.; Motaln, K.; Dragomir, M.; Lozinšek, M.; Kurzydłowski, D. Pressure-Induced Comproportionation in Palladium Trifluoride. *Inorg. Chem.* **2025**, *64* (18), 9026−9034.
(57) Monkhorst, H. J.; Pack, J. D. Special Points for Brillouin-Zone Integrations. *Phys. Rev. B* **1976**, *13* (12), 5188−5192.
(58) Falls, Z.; Avery, P.; Wang, X.; Hilleke, K. P.; Zurek, E. The *XtalOpt* Evolutionary Algorithm for Crystal Structure Prediction. *J. Phys. Chem. C* **2021**, *125* (3), 1601−1620.

NOTE ADDED AFTER ASAP PUBLICATION

Additional corrections were made after this paper published ASAP on July 14, 2025. The corrected version reposted on July 27, 2025.

https://doi.org/10.1021/acs.inorgchem.5c01740
Inorg. Chem. 2025, 64, 14968−14976

4.3 Coordination of XeF_2 to Fluoridometal Cations: The Adduct Cations $[PtF_3(XeF_2)_3]^+$ and $[PdF_3(XeF_2)_3]^+$

K. Motaln, M. Virant, and M. Lozinšek

Published in: *Inorganic Chemistry*, 2026, 65, 10, 5668−5677

DOI: 10.1021/acs.inorgchem.5c05940

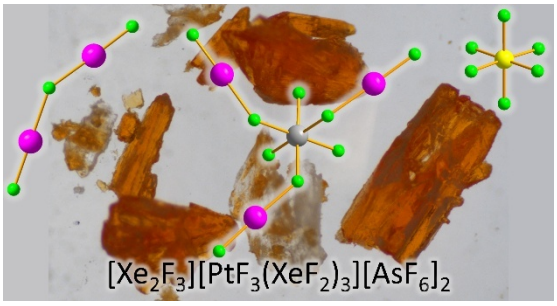


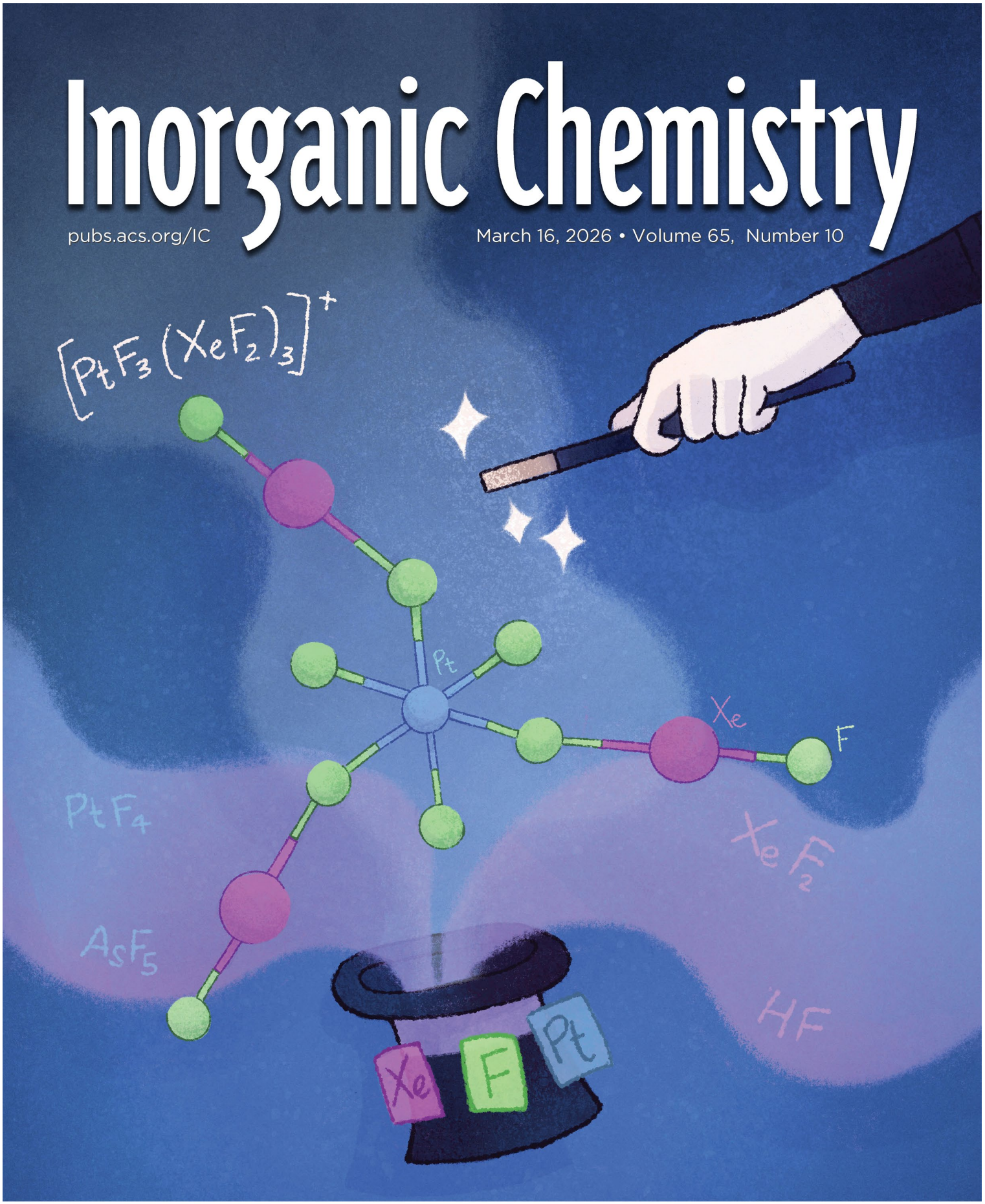
Figure 4.3: Graphical abstract of the publication "Coordination of XeF_2 to Fluoridometal Cations: The Adduct Cations $[PtF_3(XeF_2)_3]^+$ and $[PdF_3(XeF_2)_3]^+$" [199].

The structural chemistry of XeF_2 coordinated to tetravalent transition metals remains underexplored, despite its relevance to the long-debated structure of $XePtF_6$ [100]. This work aims to bridge that gap by probing the reactivity of XeF_2 in the presence of both Lewis-acidic tetra- and pentafluorides. Salts formulated as $[Xe_2F_3][MF_3(XeF_2)_3][AsF_6]_2$ (M = Pd, Pt) were obtained from aHF solutions and were isolated as bright amber-colored, air-sensitive crystals. The products were characterized by low-temperature SCXRD and low-temperature Raman spectroscopy, supported by quantum-chemical calculations.

Single-crystal structure determinations show that these salts comprise previously unobserved mononuclear *fac*-$[MF_3(XeF_2)_3]^+$ adduct cations, accompanied by discrete $[Xe_2F_3]^+$ and $[AsF_6]^-$ ions. Each M^{IV} center adopts a slightly distorted octahedral coordination environment in which three XeF_2 molecules serve as ligands, establishing the highest known coordination number of XeF_2 ligands bonded to a single metal(IV) site. The coordinated XeF_2 units are moderately polarized relative to free XeF_2, consistent with partial ionization along the $XeF_2 \rightarrow XeF^+ + F^-$ pathway [84]. The platinum salt crystallizes in two polymorphic forms with distinct packing arrangements and conformation of the cations, whereas the palladium analogue is not isotypic with either polymorph. Calculations on the isolated cations reproduce the essential geometric parameters and vibrational features, and further elucidate the distribution of electron density within the XeF_2 ligands upon coordination.

These results markedly enrich the XeF_2–MF_4 chemistry by establishing a new class of XeF_2 compounds in which it ligates a discrete fluoridometal(IV) cation rather than a oligo- or polymeric unit, complementing the previously characterized compounds from XeF_2–MF_4 (M = Cr, Ti, Pd, Pt, Sn) systems [104], [106], [108], [109], [191], [197]. More broadly, the synthetic strategy of probing XeF_2 reactivity in the presence of multiple oxidatively resistant Lewis acidic species, emerges as a prospective strategy for discovering additional members of this compound family and to diversify the structural landscape of noble-gas fluoride coordination complexes.

K. Motaln, the author of this dissertation, synthesized all of the salts of $[MF_3(XeF_2)_3]^+$ cations, determined their crystal structures from SCXRD data, collected their vibrational spectra, performed preliminary DFT geometry optimizations and vibrational frequency calculations of the cations, prepared the initial draft of the manuscript, and was involved in the review, editing, and revision of the final manuscript.



ACS Publications
Most Trusted. Most Cited. Most Read.
www.acs.org

Inorganic Chemistry

Open Access
This article is licensed under CC-BY 4.0

pubs.acs.org/IC Article

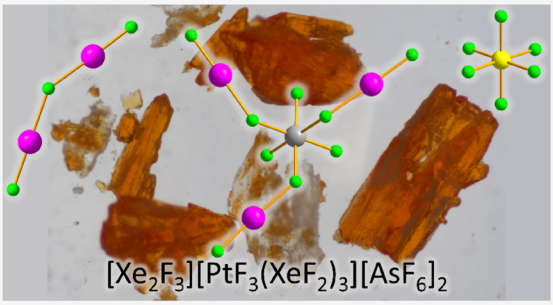
Coordination of XeF_2 to Fluoridometal Cations: The Adduct Cations $[PtF_3(XeF_2)_3]^+$ and $[PdF_3(XeF_2)_3]^+$

Klemen Motaln, Miha Virant, and Matic Lozinšek*

Cite This: *Inorg. Chem.* 2026, 65, 5668−5677 Read Online

ACCESS | Metrics & More | Article Recommendations | Supporting Information

ABSTRACT: Crystals of the double salts $[Xe_2F_3][MF_3(XeF_2)_3][AsF_6]_2$ (M = Pd, Pt), prepared from anhydrous HF solutions, were characterized by low-temperature single-crystal X-ray diffraction and Raman spectroscopy. The crystal structures reveal that the compounds contain the hitherto unobserved $[MF_3(XeF_2)_3]^+$ adduct cations, which differ from all previously identified examples of XeF_2 coordination to a metal(IV) center in their mononuclear and cationic nature, as well as in the coordination of multiple XeF_2 ligands to a single metal(IV) center. Quantum-chemical calculations were performed to gain insight into the bonding and electronic structure of the $[MF_3(XeF_2)_3]^+$ adduct cations, with the optimized gas-phase geometries showing good agreement with the experimental solid-state structures. The characterized $[MF_3(XeF_2)_3]^+$ adduct cations markedly extend the chemistry of XeF_2−MF_4 systems and represent rare, crystallographically characterized examples of XeF_2 coordination to Pt^{IV} and Pd^{IV}, a feature also believed to occur in the structure of the first discovered noble-gas compound, $XePtF_6$. Moreover, the $[MF_3(XeF_2)_3]^+$ cations constitute the first examples of a new class of XeF_2 coordination compounds, which are characterized by XeF_2 ligation to a fluoridometal $[MF_x]^{n+}$ cation, thereby enabling further expansion of the coordination chemistry of noble-gas fluorides.



INTRODUCTION

Xenon difluoride, XeF_2, is arguably the most well-known noble-gas compound and, owing to its commercial availability, one of the most important synthetic precursors for xenon chemistry.[1] The reactivity of XeF_2 is typically governed by its pronounced Lewis basicity and fluoride-ion donor abilities.[2,3] Upon interaction with Lewis acids or fluoride-ion acceptors, XeF_2 forms a variety of complexes, adducts, and tight ion-pair salts (Figure 1),[4] exhibiting varying degrees of ionization along the following pathway: $XeF_2 \rightarrow XeF^+ + F^-$.[5] Compounds derived from metal-based Lewis acids can be qualitatively divided into three classes:

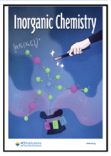
i) $[M^{n+}(XeF_2)_m(AF_x^-)_n]$ **complexes**, formed by coordination of XeF_2 to a "naked" metal cation M^{n+} derived from an $M(AF_x)_n$ salt with a weakly coordinating anion, for example homoleptic $[Cu(XeF_2)_6](RuF_6)_2$, anion-bridged $[Ni(XeF_2)_2(RuF_6)_2]$,[6] and anion- and XeF_2-bridged $[Ba(XeF_2)_4(AsF_6)_2]\cdot XeF_2$ (Figure 1a).[7]

ii) $mXeF_2{\cdot}nMF_x$ **and** $mXeF_2{\cdot}nMO_xF_y$ **Lewis acid−base adducts**, formed by interaction of XeF_2 with moderately strong Lewis acids such as metal tetrafluorides and oxyfluorides, for example: $XeF_2\cdot CrF_4$,[8] $3XeF_2\cdot 2MnF_4$, $XeF_2\cdot MnF_4$,[9] $XeF_2\cdot CrOF_4$, $XeF_2\cdot 2CrOF_4$,[10] $XeF_2\cdot MoOF_4$, $XeF_2\cdot WOF_4$, $XeF_2\cdot 2WOF_4$ (Figure 1b).[11]

iii) $[XeF]^+$ **tight ion-pair salts and** $[Xe_2F_3]^+$ **salts**, produced in reactions with strongly Lewis acidic metal or metalloid pentafluorides, for example: $[XeF][AF_6]$ (A = As, Nb, Ru, Sb, Ta, Pt, Bi), $[XeF][A_2F_{11}]$ (A = Ru, Sb, Ta, Pt, Bi), and $[Xe_2F_3][AF_6]$ (A = As, Ru, Sb, Ta, Pt, Au, Bi) (Figure 1c).[1,4,12−15]

However, there are borderline cases that may be classified as either class (ii) or class (iii). For example, $2XeF_2\cdot 9TiF_4$ and $XeF_2\cdot 2MF_4$ (M = Mn, Pd, Pt) exhibit sufficient ionization of XeF_2 coordinated to the metal(IV) center to justify ionic formulations of $[XeF]^+_2[Ti_9F_{38}]^{2-}$ and $[XeF]^+[M_2F_9]^-$ (M = Mn, Pd, Pt), respectively (Figure 1d).[9,16,17] In contrast, crossover species between classes (i) and (ii), such as $[M^{n+}F_p(XeF_2)_m]^{(n-p)+}(AF_x^-)_{n-p}$, in which the metal center is coordinated by both XeF_2 and F^- ligands, have not been reported. Comparable linkages have been observed in the coordination chemistry of the related KrF_2, as the crystal structures of $[\mu\text{-}FHg(\mu_3\text{-}FKrF)_{1.5}(FKrF)_{0.5}AsF_6]_2$ and $[\mu_3\text{-}FHg(\mu_3\text{-}FKrF)_{0.5}(FKrF)_{1.5}AsF_6]_2$ were shown to consist of extended three-dimensional networks incorporating bridging F^- and KrF_2 units which ligate Hg^{2+} centers.[18]

Received: December 19, 2025
Revised: February 5, 2026
Accepted: February 10, 2026
Published: February 26, 2026



ACS Publications
© 2026 The Authors. Published by American Chemical Society

https://doi.org/10.1021/acs.inorgchem.5c05940
Inorg. Chem. 2026, 65, 5668−5677

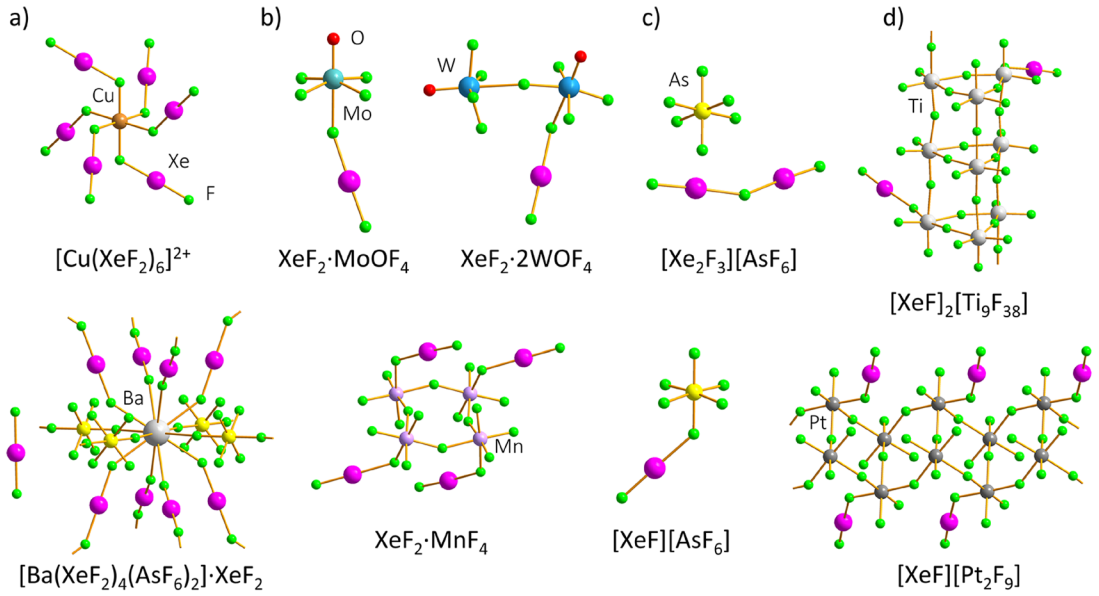


Figure 1. Structural diversity of compounds stemming from the interaction of XeF_2 with metal-based (and metalloid-based) Lewis acids.[6,7,9,11,13,15−17]

In this work, the first examples of discrete $[M^{n+}F_p(XeF_2)_m]^{(n-p)+}$ species are reported, represented by the unique $[MF_3(XeF_2)_3]^+$ (M = Pt, Pd) adduct cations, which were isolated as brightly colored crystals of the corresponding $[Xe_2F_3][MF_3(XeF_2)_3][AsF_6]_2$ double salts. Despite the fact that XeF_2 coordination to platinum constitutes a defining structural feature of the first discovered noble-gas compound, $XePtF_6$ ($XeF_2{\cdot}PtF_4$),[19,20] the structural chemistry of the XeF_2−PtF_4 system and the related[21] XeF_2−PdF_4 system remains poorly explored. The *fac*-$[M^{IV}F_3(XeF_2)_3]^+$ adduct cations described herein represent only the second instance of crystallographically characterized species featuring XeF_2 coordination to platinum and palladium, following the recently structurally characterized $XeF_2{\cdot}2PtF_4$ and $XeF_2{\cdot}2PdF_4$ adducts, whose structures were elucidated by 3D electron diffraction.[17] The newly discovered $[MF_3(XeF_2)_3]^+$ (M = Pt, Pd) adduct cations thus offer additional insights into these historically important systems.

■ RESULTS AND DISCUSSION

Synthesis

The title compounds were synthesized in anhydrous HF (aHF) by reactions of the appropriate binary fluorides in the molar ratios observed in the final products ($XeF_2/MF_4/AsF_5$ = 5:1:2) (eqs 1, 2).

$$5XeF_2 + PtF_4 + 2AsF_5 \xrightarrow{aHF} x[Xe_2F_3][PtF_3(XeF_2)_3][AsF_6]_2(oP256) + y[Xe_2F_3][AsF_6] \quad (1)$$

$$5XeF_2 + PdF_4 + 2AsF_5 \xrightarrow{aHF} x[Xe_2F_3][PdF_3(XeF_2)_3][AsF_6]_2 + y[Xe_2F_3][AsF_6] + z(XeF_2{\cdot}2PdF_4) \quad (2)$$

To the best of our knowledge, this approach represents a rare targeted investigation of XeF_2 reactivity in a system containing both Lewis-acidic tetra- and pentafluorides. The fluorobasic conditions established by the excess of XeF_2 ensured partial dissolution of the otherwise aHF-insoluble metal tetrafluorides, resulting in yellow-colored solutions, into which AsF_5 was subsequently dosed. Slow crystallization induced by solvent evaporation afforded amber-colored crystals (Figure S1), which were isolated and characterized by low-temperature (LT) single-crystal X-ray diffraction (SCXRD) and LT Raman spectroscopy. The formation of $[Xe_2F_3][MF_3(XeF_2)_3][AsF_6]_2$ single crystals was invariably accompanied by the formation of colorless crystals of $[Xe_2F_3][AsF_6]$, which were identified by Raman spectroscopy and SCXRD. Additional reaction pathways were explored by reacting a 2-fold molar excess of $[XeF][AsF_6]$ with K_2PtF_6, or by combining $[XeF][AsF_6]$, $XeF_2{\cdot}PdF_4$, and XeF_2 while maintaining a $XeF_2/MF_4/AsF_5$ ratio of 5:1:2 (see the Experimental Section). In both cases, the title compounds were again obtained; however, in the former reaction, a triclinic polymorph of $[Xe_2F_3][PtF_3(XeF_2)_3][AsF_6]_2$ was isolated (eq 3).

$$2[XeF][AsF_6] + K_2PtF_6 \xrightarrow{aHF} x[Xe_2F_3][PtF_3(XeF_2)_3][AsF_6]_2(aP256) + yKAsF_6 + z(nXeF_2{\cdot}PtF_4) \quad (3)$$

Crystal Structures

Structural analysis revealed that $[Xe_2F_3][PtF_3(XeF_2)_3][AsF_6]_2$, synthesized from the binary fluorides XeF_2, PtF_4, and AsF_5, crystallizes in the orthorhombic $P2_12_12_1$ space group, whereas the polymorph prepared by the reaction of $[XeF][AsF_6]$ with K_2PtF_6 crystallizes in the lower-symmetry triclinic $P\bar{1}$ space group. The two polymorphic forms are henceforth referred to by their Pearson symbols as *oP*256 and *aP*256, respectively. In contrast, crystal structure determination of $[Xe_2F_3]$-$[PdF_3(XeF_2)_3][AsF_6]_2$ revealed that it is not isotypic with

https://doi.org/10.1021/acs.inorgchem.5c05940
Inorg. Chem. 2026, 65, 5668−5677

either of the $[Xe_2F_3][PtF_3(XeF_2)_3][AsF_6]_2$ polymorphs and instead crystallizes in the monoclinic $P2_1$ space group (Tables 1 and S1). Tables 1 and 2 contain the summary of crystal data

Table 1. Summary of Crystal Data and Refinement Results for $[Xe_2F_3][PtF_3(XeF_2)_3][AsF_6]_2$(*oP*256) $[Xe_2F_3][PtF_3(XeF_2)_3][AsF_6]_2$(*aP*256), and $[Xe_2F_3][PdF_3(XeF_2)_3][AsF_6]_2$

	$[Xe_2F_3][PtF_3(XeF_2)_3][AsF_6]_2$(*oP*256)	$[Xe_2F_3][PtF_3(XeF_2)_3][AsF_6]_2$(*aP*256)	$[Xe_2F_3][PdF_3(XeF_2)_3][AsF_6]_2$
space group	$P2_12_12_1$	$P\bar{1}$	$P2_1$
a (Å)	11.86164(10)	12.92922(7)	6.53000(4)
b (Å)	16.48399(13)	13.07591(6)	11.83284(6)
c (Å)	23.8108(2)	27.91602(13)	14.93053(9)
α (°)	90	83.6237(4)	90
β (°)	90	79.6369(4)	90.0233(5)
γ (°)	90	75.7149(5)	90
V (Å^3)	4655.66(7)	4487.97(4)	1153.658(11)
Z	8	8	2
M_w (g mol^{-1})	1457.43	1457.43	1368.74
D_{calcd} (g cm^{-3})	4.159	4.314	3.940
μ (mm^{-1})	8.639	8.962	5.838
R_1	0.0389	0.0319	0.0320
wR_2	0.1001	0.0811	0.0797
$\Delta\rho_{min,\ max}$ (e Å^{-3})	−1.958, 5.733	−2.818, 4.386	−1.959, 1.990

and refinement results, and the selected bond lengths and angles observed in the crystal structures, respectively, whereas complete crystallographic tables are provided in the Supporting Information (Tables S1−S4).

In all structures, the asymmetric unit is comprised of isolated $[Xe_2F_3]^+$, $[MF_3(XeF_2)_3]^+$, and $[AsF_6]^-$ ions, with all atoms occupying general positions (Figures 2,3 and S2−S6). The $M^{IV}F_3^+$ fragment is coordinated by three XeF_2 ligands in a *fac* arrangement, resulting in a slightly distorted octahedral coordination environment around the M^{IV} center. These compounds, which feature three XeF_2 ligands coordinated to a single metal(IV) center, currently represent the highest number of XeF_2 ligands observed for any metal(IV) species. They also constitute a unique case in which XeF_2 coordination

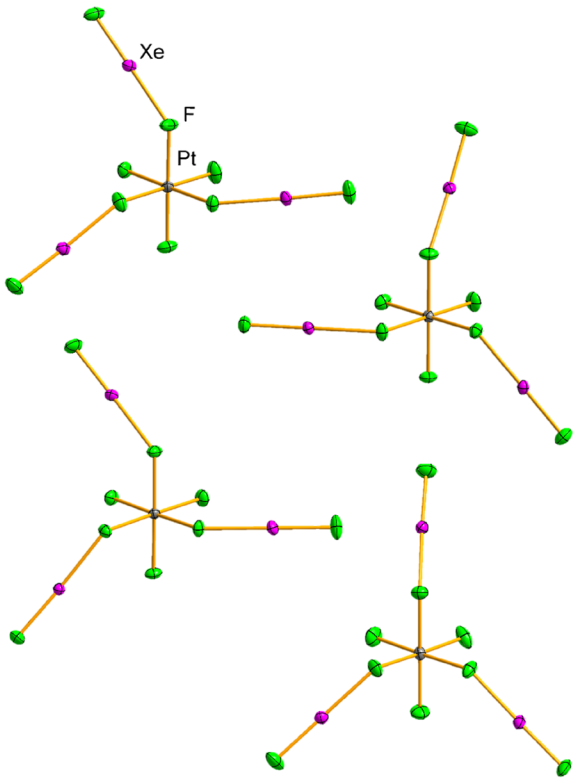


Figure 2. Four crystallographically independent $[PtF_3(XeF_2)_3]^+$ cations in the crystal structure of $[Xe_2F_3][PtF_3(XeF_2)_3][AsF_6]_2$(*aP*256). Displacement ellipsoids are drawn at the 50% probability level.

to a metal(IV) center results in a mononuclear complex. In contrast, the other known compounds exhibiting XeF_2 coordination to metal(IV) centers predominantly adopt polymeric structures composed of interconnected $[MF_6]$ octahedra, forming chains ($XeF_2{\cdot}CrF_4$ and $3XeF_2{\cdot}2MnF_4$),[8,9] double chains ($XeF_2{\cdot}2MnF_4$, $XeF_2{\cdot}2PdF_4$, and $XeF_2{\cdot}2PtF_4$)[9,17] (Figure 1d), columnar motifs ($[XeF]_2[Ti_9F_{38}]$)[16] (Figure 1d), or layers ($XeF_2{\cdot}2CrF_4$).[22] The sole exception within this family of compounds is $XeF_2{\cdot}MnF_4$, whose structure comprises

Table 2. Selected Bond Lengths (Å) and Angles (°) for the Crystal Structures of $[Xe_2F_3][PtF_3(XeF_2)_3][AsF_6]_2$ and $[Xe_2F_3][PdF_3(XeF_2)_3][AsF_6]_2$

	$[Xe_2F_3][PtF_3(XeF_2)_3][AsF_6]_2$(*oP*256)	$[Xe_2F_3][PtF_3(XeF_2)_3][AsF_6]_2$(*aP*256)	$[Xe_2F_3][PdF_3(XeF_2)_3][AsF_6]_2$
Xe−F_t	1.888(6)−1.921(6)	1.898(3)−1.918(3)	1.918(4)−1.923(4)
Xe−F_b(M)	2.182(5)−2.211(5)	2.179(3)−2.214(2)	2.143(4)−2.178(4)
Xe−F_t[a]	1.906(5)−1.929(5)	1.908(3)−1.923(3)	1.915(4), 1.916(4)
Xe−F_b(Xe)	2.125(5)−2.174(5)	2.157(3)−2.188(3)	2.142(4), 2.162(4)
M−F_t	1.881(5)−1.898(5)	1.882(3)−1.897(2)	1.842(5)−1.860(4)
M−F_b(Xe)	1.978(5)−1.996(5)	1.981(3)−2.002(2)	1.975(4)−1.990(4)
As−F	1.657(13)−1.786(13)	1.704(3)−1.737(3)	1.714(4)−1.740(4)
F−Xe−F	175.9(2)−176.8(2)	173.35(14)−179.40(12)	177.2(2)−178.2(2)
F−Xe−F[a]	177.1(3)−178.9(3)	178.11(15)−179.36(14)	178.1(2), 179.36(19)
Xe−F_b−Xe[a]	139.9(3), 140.3(3)	127.10(13)−134.65(15)	133.11(19)
cis-F−M−F	87.0(2)−93.3(2)	85.56(12)−92.53(12)	87.9(2)−92.6(3)
trans-F−M−F	178.3(2)−179.6(2)	177.12(12)−179.00(12)	178.16(19)−179.5(2)
cis-F−As−F	79.7(8)−98.3(8)	88.11(17)−91.72(15)	87.5(2)−91.2(3)
trans-F−As−F	169.0(11)−179.3(4)	177.69(17)−179.73(17)	177.4(2)−179.7(3)

[a]Pertaining to the bonds in the $[Xe_2F_3]^+$ cations.

https://doi.org/10.1021/acs.inorgchem.5c05940
Inorg. Chem. 2026, 65, 5668−5677

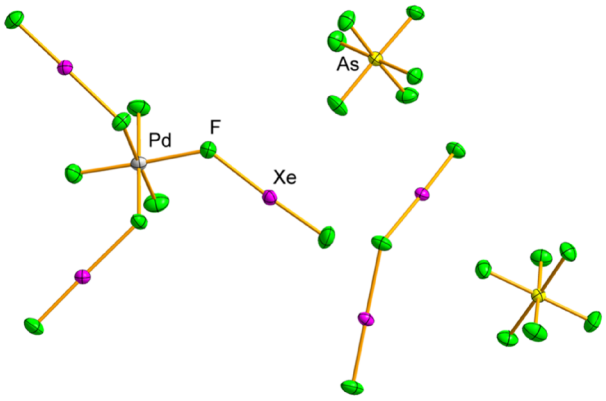


Figure 3. Asymmetric unit of the $[Xe_2F_3][PdF_3(XeF_2)_3][AsF_6]_2$ crystal structure. Displacement ellipsoids are drawn at the 50% probability level.

discrete tetrameric ring units (Figure 1b). Across all of these structures, each metal(IV) center is coordinated by no more than one XeF_2 ligand.

The geometry of the coordinated XeF_2 ligands in the $[PtF_3(XeF_2)_3]^+$ and $[PdF_3(XeF_2)_3]^+$ adduct cations is perturbed, showing slight deviations of the F−Xe−F angles from linearity [175.9(2)−176.8(2)° in *oP*256, 173.35(14)−179.35(12)° in *aP*256, and 177.2(2)−178.2(2)° in the Pd compound] and a pronounced elongation of the bridging Xe−F_b bonds, accompanied by shortening of the terminal Xe−F_t bonds. The Xe−F_t and Xe−F_b bond lengths in the $[PdF_3(XeF_2)_3]^+$ cation span the ranges of 1.918(4)−1.923(4) Å and 2.143(4)−2.178(4) Å, respectively, with average values of 1.920 and 2.159 Å. These distances indicate that the XeF_2 moiety displays an intermediate degree of ionization, comparable to that observed in some XeF_2−MF_4 adducts, namely $3XeF_2 \cdot 2MnF_4$, $XeF_2 \cdot MnF_4$,[9] and $XeF_2 \cdot CrF_4$.[8] For comparison, the Xe−F bond length of the centrosymmetric XeF_2 molecule ($D_{\infty h}$) in the solid state is 1.999(4) Å.[13] In the case of the $[PtF_3(XeF_2)_3]^+$ cations, a greater variability in the Xe−F bond lengths is observed. The Xe−F_t bonds measure 1.888(6)−1.921(6) Å and 1.898(3)−1.918(3) Å, whereas the Xe−F_b bonds measure 2.182(5)−2.211(5) Å and 2.179(3)−2.214(2) Å in the *oP*256 and *aP*256 polymorphs, respectively. Examination of the average values of the Xe−F_t and Xe−F_b bond lengths, which amount to 1.908 Å and 2.196 Å in the *oP*256 polymorph, and 1.908 Å and 2.200 Å in the *aP*256 polymorph, reveals a pronounced distortion of the geometry of the coordinated XeF_2 ligands. The mean values are comparable to the bond lengths observed in the $[XeF][BiF_6]$ tight ion-pair salt [Xe−F_t: 1.913(7) Å; Xe−F_b: 2.204(7) Å],[13] providing evidence for the substantial fluoride-ion affinity of the $[PtF_3]^+$ cation. Nevertheless, the fluoride-ion affinity of these cations is

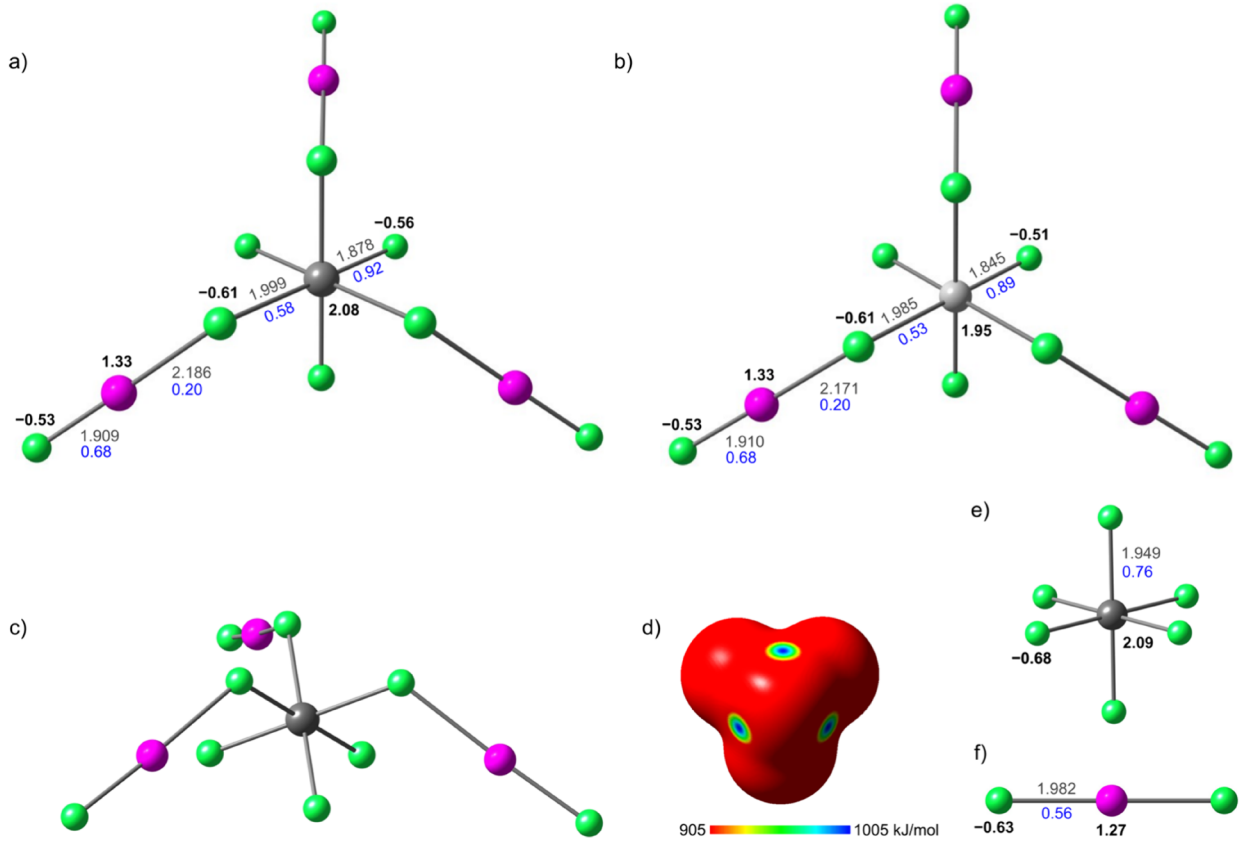


Figure 4. Calculated gas-phase geometries of (a) $[PtF_3(XeF_2)_3]^+$ and (b) $[PdF_3(XeF_2)_3]^+$ cations; (c) an alternative view of $[PtF_3(XeF_2)_3]^+$ cation; (d) molecular electrostatic potential surface (MEPS) of $[PtF_3]^+$ fragment (top 10% of the positive electrostatic potential range); and optimized gas-phase geometries of (e) $[PtF_6]^{2-}$ anion and (f) free XeF_2, included for comparison. Bond distances (Å) are indicated in gray, AIM charges are listed in black, and Mayer bond orders are given in blue.

https://doi.org/10.1021/acs.inorgchem.5c05940
Inorg. Chem. 2026, 65, 5668−5677

less pronounced than that exhibited by the polymeric fluoridoplatinate(IV) and fluoridopalladate(IV) units present in the crystal structures of $XeF_2{\cdot}2MF_4$ (M = Pt, Pd), where Xe−F_b bond lengths exceeding 2.3 Å are observed.[17] The Pt−F_t [*oP*256: 1.881(5)−1.898(5) Å; *aP*256: 1.882(3)−1.897(2) Å] and Pd−F_t bond lengths [1.842(5)−1.860(5) Å] show good agreement with the values observed in the crystal structures of $XeF_2{\cdot}2PtF_4$ [1.863(7)−1.905(11) Å] and $XeF_2{\cdot}2PdF_4$ [1.844(4)−1.866(4) Å], respectively. Conversely, the bridging Pt−F_b(Xe) bond distances [*oP*256: 1.978(5)−1.996(5) Å; *aP*256: 1.981(3)−2.002(2) Å] and Pd−F_b(Xe) [1.975(4)−1.990(4) Å] are notably elongated in comparison to their counterparts observed in the crystal structures of $XeF_2{\cdot}2PtF_4$ [1.932(8) Å] and $XeF_2{\cdot}2PdF_4$ [1.894(4) Å], respectively.[17] In all three crystal structures, a number of inter- and intramolecular Xe···F contacts are formed, with distances shorter than the corresponding sum of the van der Waals radii 3.74 Å (Tables S5−S7).[23,24] These contacts contribute to stabilization of the crystal packing and influence the marked conformational differences observed among the crystallographically independent $[PtF_3(XeF_2)_3]^+$ and $[PdF_3(XeF_2)_3]^+$ adduct cations (Figure S7). In the crystal structures, the adduct cations possess C_1 point-group symmetry and are therefore chiral. As $[Xe_2F_3][PtF_3(XeF_2)_3][AsF_6]_2$(*oP*256) and $[Xe_2F_3][PdF_3(XeF_2)_3][AsF_6]_2$ crystallize in Sohncke space groups, only one enantiomeric form of each cation is present in each crystal structure. Conversely, both enantiomers of the cation are present in the centrosymmetric $P\bar{1}$ crystal structure of $[Xe_2F_3][PtF_3(XeF_2)_3][AsF_6]_2$(*aP*256).

The second cationic species present in these double salts are the planar, V-shaped $[Xe_2F_3]^+$ cations. Interestingly, the Xe−F_b−Xe angles determined in the crystal structures of $[Xe_2F_3][PtF_3(XeF_2)_3][AsF_6]_2$(*aP*256) [127.10(13)−134.65(15)°] and $[Xe_2F_3][PdF_3(XeF_2)_3][AsF_6]_2$ [133.11(19)°] (Figures S3 and 3) are the least obtuse angles observed for $[Xe_2F_3]^+$ cations to date. Previously reported fluoride-bridge angles span the range from 139.8(8)° in trigonal $[Xe_2F_3][AsF_6]$[15] to 164.3(3)° observed in the crystal structure of $[Xe_2F_3][Ti_8F_{33}]$.[16] On the other hand, the Xe−F_b−Xe angles observed in the crystal structure of $[Xe_2F_3][PtF_3(XeF_2)_3][AsF_6]_2$(*oP*256) are noticeably more open [139.9(3)° and 140.3(3)°]. As quantum-chemical calculations have previously shown that the vibrational mode corresponding to the bending deformation of the Xe−F_b−Xe angle is very low in frequency, the large variability of these angles has been ascribed to crystal-packing effects.[15]

Computational Results

To investigate the electronic structures of the isolated $[MF_3(XeF_2)_3]^+$ cations, their geometries were optimized using the DFT method PBE0-D3/aug-cc-pVQZ(-PP) as implemented in the *ORCA* software (version 6.0.0).[25] The resulting stationary points were confirmed to be true minima on the potential energy surface with no imaginary frequencies (Table S8). In the absence of additional interactions, the isolated cations examined in the computational analysis converged to a slightly distorted C_{3v} symmetry (Figure 4, Tables S9 and S10). A comparison of the experimentally determined and calculated bond lengths demonstrates good agreement, with deviations not exceeding 0.6% (Table S11 and S12). However, greater discrepancies between the experimental and calculated structures are observed in the conformation of the cations. In particular, the Xe−F_b−M angles are, on average, more acute in the calculated geometries than in the experimental structures (Tables S11 and S12). Moreover, although the Xe−F_b−M−F_t' (where F_t' denotes the terminal F atom nearest to Xe) torsion angles observed in the crystal structures span a wide range of values (Tables S2−S4), the calculated geometries converge to torsion angles that correspond to staggered conformations (Tables S11 and S12).[13]

The studied $[MF_3(XeF_2)_3]^+$ adduct cations can be described in terms of two limiting structures: one featuring neutral XeF_2 ligands coordinated to a $[MF_3]^+$ cation, and the other corresponding to complete ionization into $[XeF]^+$ cations coordinated to a $[MF_6]^{2-}$ anion.

Unbound, centrosymmetric XeF_2 is characterized by negative atoms-in-molecules (AIM) charges on the fluorine atoms (−0.63), a positive charge on the xenon atom (+1.27), and equal Mayer bond orders (0.56) for both Xe−F bonds (1.982 Å; Figure 4, Table S13). Upon coordination, XeF_2 becomes polarized, developing a net positive charge (+0.20). The terminal fluorine atom (−0.53) becomes less negative and the xenon atom (+1.33) becomes more positive, accompanied by shortening of the terminal Xe−F_t bond (1.909 Å) and an increase in the corresponding Mayer bond order (0.68). In contrast, the charge on the bridging fluorine atoms remains nearly unchanged (−0.61), while the bridging Xe−F_b bonds are significantly elongated (Pt: 2.186 Å; Pd: 2.171 Å), resulting in a decrease in the corresponding Mayer bond orders (0.20). These changes are attributed to the transfer of electron density from XeF_2 toward regions of positive electrostatic potential on the $[MF_3]^+$ fragments, which display pronounced σ-holes along the extensions of the M−F bonds (Figures 4, S8, S9 and Table S14). The coordination of XeF_2 ligands to the MF_3^+ cation can therefore be described as a regium-bonding interaction.[26]

The AIM charges of the metal centers in the adduct cations (Pt: +2.08; Pd: +1.95) are nearly identical to those calculated for the isolated $[PtF_6]^{2-}$ (+2.09) and $[PdF_6]^{2-}$ (+1.97) anions, whereas the fluorine atoms of the anions carry more negative charge (Pt: −0.68; Pd: −0.66) than either the bridging (−0.61) or terminal F atoms (Pt: −0.56; Pd: −0.51) in the adduct cations (Figure 4, Tables S15, S16). The total charge of the $[MF_6]$ fragments (−1.41) is less negative than that of the isolated $[MF_6]^{2-}$ anions (−2.00), consistent with the positive charge developed on the coordinated XeF_2 ligands (+0.59). The Mayer bond orders of the M−F_t bonds in the adduct cations (Pt: 0.92; Pd: 0.89) are significantly higher than those calculated for the M−F bonds in the $[MF_6]^{2-}$ anions (Pt: 0.76; Pd: 0.70), whereas the M−F_b bond orders in the adduct cations are smaller (Pt: 0.58; Pd: 0.53).

The topological parameters obtained from the quantum theory of atoms in molecules (QTAIM) analysis[27] (Table S17) further corroborate the polarization of XeF_2. Specifically, the Xe−F_b bond exhibits a reduced covalent character relative to uncoordinated XeF_2, as indicated by a lower electron density at the bond critical point ($\rho(r)$), a smaller Laplacian of electron density ($\nabla^2\rho(r)$), and a less negative local energy density ($H(r)$). In contrast, the Xe−F_t bond shows an enhanced covalent character, reflected in higher $\rho(r)$ values, a larger $\nabla^2\rho(r)$, and a more negative $H(r)$. The M−F_b interactions, characterized by low $\rho(r)$ values, small positive $\nabla^2\rho(r)$, and slightly negative $H(r)$ values, are consistent with predominantly electrostatic σ-hole−type interactions.[11]

https://doi.org/10.1021/acs.inorgchem.5c05940
Inorg. Chem. 2026, 65, 5668−5677

Vibrational Spectroscopy

Low-temperature Raman spectra of the compounds, recorded at 100 K, exhibit the strongest bands in the Xe−F_t stretching region (580−620 cm^{-1}; Figure 5, Table S18). Given that

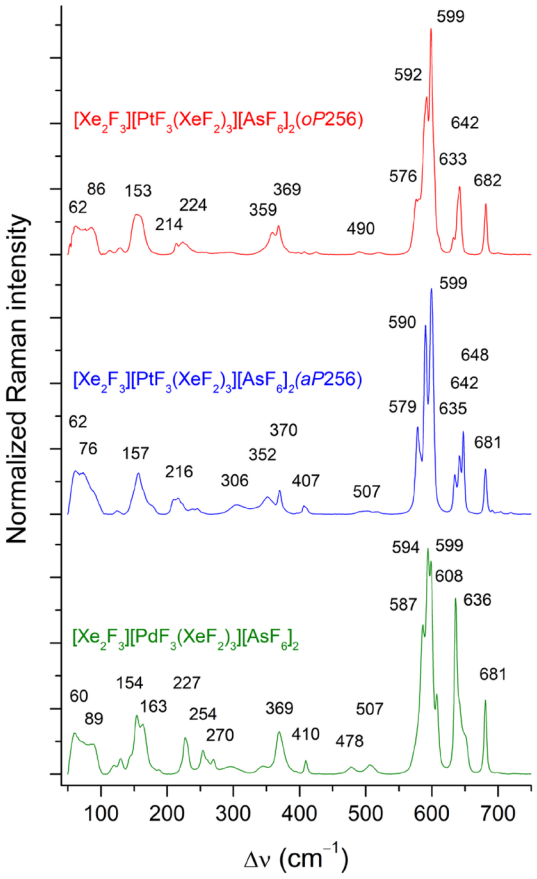


Figure 5. Raman spectra of the two polymorphs of $[Xe_2F_3][PtF_3(XeF_2)_3][AsF_6]_2$ and $[Xe_2F_3][PdF_3(XeF_2)_3][AsF_6]_2$ recorded at 100 K using 785 nm excitation.

stretching modes of both $[Xe_2F_3]^+$ and coordinated, partially ionized XeF_2 species are expected to occur in this region,[9,15,28,29] assignment of the observed bands to the respective vibrational modes is challenging. The spectra of $[Xe_2F_3][MF_3(XeF_2)_3][AsF_6]_2$ exhibit similarities to the Raman spectrum of $[Xe_2F_3][AsF_6]$, as evidenced by the nearly unchanged positions of the ν_1 (681, 682 cm^{-1}) and ν_5 bands (369, 370 cm^{-1}) of the $[AsF_6]^-$ anion in comparison to the Raman spectrum of $[Xe_2F_3][AsF_6]$, in which these bands are located at 681 and 367 cm^{-1}, respectively (Figures S10 and S11).[28] Another prominent feature of the spectra is the presence of medium-strong bands in the 630−650 cm^{-1} region. These bands correspond reasonably well to the calculated in-phase and out-of-phase M−F_t stretching modes of the $[MF_3(XeF_2)_3]^+$ cations (Table S8, Figure S10, S11). The ATR-IR spectra of samples containing $[Xe_2F_3][MF_3(XeF_2)_3][AsF_6]_2$ double salts and the spectra of pure $[Xe_2F_3][AsF_6]$ and $KAsF_6$, are provided in the Supporting Information (Figures S12 and S13).

CONCLUSIONS

In summary, two polymorphic forms of $[Xe_2F_3][PtF_3(XeF_2)_3][AsF_6]_2$, as well as $[Xe_2F_3][PdF_3(XeF_2)_3][AsF_6]_2$, were synthesized and characterized by SCXRD, vibrational spectroscopy, and quantum-chemical calculations. The novel $[MF_3(XeF_2)_3]^+$ adduct cations present in the crystal structures of these double salts provide rare, structurally characterized examples of XeF_2 coordination to platinum(IV) and palladium(IV) centers and represent the highest number of XeF_2 ligands bound to a single metal(IV) center observed to date. These findings highlight the substantial structural diversity exhibited by species in which XeF_2 ligates a tetravalent metal center.

The adduct cations identified in this study define a new class of coordination complexes in which XeF_2 serves as a ligand to a fluoridometal cation, thereby broadening the scope of XeF_2 coordination chemistry. Moreover, the results indicate that probing the reactivity of XeF_2 in systems containing multiple high-valent, Lewis-acidic fluorides can lead to the formation of novel species. This observation underscores the potential for systematic exploration across the broad landscape of mixed MF_4/AF_5−XeF_2 systems, a largely unexplored domain with a strong potential for advancing this emerging class of compounds.

EXPERIMENTAL SECTION

CAUTION: *Anhydrous HF, F_2, and AsF_5 are highly toxic volatile substances and must be handled with great care in a well-ventilated fume hood while wearing appropriate personal protective equipment at all times. XeF_2 and its derivatives are potent oxidizing fluorinating agents and release HF upon hydrolysis. Work with such chemicals should be undertaken only by properly trained experimentalists and the access to proper treatment procedures in the event of exposure must be ensured.*[30−32]

General

All experimental work on the compounds described herein was conducted under strictly anhydrous conditions. Manipulation of volatile materials was performed on a custom-built, fluorine-resistant vacuum line constructed from nickel, copper, poly(tetrafluoroethylene) (PTFE), and fluorinated ethylene propylene (FEP). Solid materials were handled in a glovebox (Vigor SG1200/750E−SG1500/750E) under an inert nitrogen atmosphere, with moisture levels maintained below 1 ppm at all times.

The syntheses of $[Xe_2F_3][MF_3(XeF_2)_3][AsF_6]_2$ compounds were carried out in h-shaped reaction vessels, constructed from two FEP tubes (6 mm i.d. × 8 mm o.d.) and equipped with either a brass-encased PTFE valve or an aluminum-encased poly(chlorotrifluoroethylene) (PCTFE) valve. The FEP tubes were heat-sealed at one end and heat-flared at the other, with one tube bent at 90° angle. The two tubes were connected to a PTFE T-section via two male-to-male PTFE connectors, with the angled side arm positioned perpendicular to the main arm. Prior to use, the reaction vessels and PTFE-coated magnetic stirring bars were passivated with 300−500 Torr of F_2 for a minimum of 8 h.

Starting Materials

Fluorine gas (Solvay Fluor, 98−99%) was used as supplied. Residual moisture was removed from commercial anhydrous HF (Linde, 99.995%) by condensing it into an FEP vessel containing K_2NiF_6 (Advance Research Chemicals, 99.9%). XeF_2 was synthesized by UV irradiation of a xenon (Messer, 99.99%) and fluorine mixture in a thoroughly dried glass bulb, employing a medium-pressure Hg lamp, as previously described.[33] AsF_5 was prepared by static fluorination of As_2O_3 in a nickel pressure vessel.[34]

Li_2PdF_6 and K_2PtF_6 were prepared by oxidation of Pd (Sigma-Aldrich, 99.9%) and Pt (Thermo Scientific, 99.98%) metals with F_2 in

https://doi.org/10.1021/acs.inorgchem.5c05940
Inorg. Chem. 2026, 65, 5668−5677

aHF in the presence of LiF (Aldrich, ≥99.98%) and KF (Acros Organics, 99.99%), respectively.[35]

The synthesis of PtF_4 was conducted in accordance with the previously published procedure, commencing with the oxidation of Pt powder by XeF_2 in aHF.[36] The resulting orange-red product[17] was subsequently decomposed by heating to 430 °C in vacuo, yielding brown PtF_4, while the released XeF_2 was collected in a U-shaped FEP trap cooled with liquid nitrogen.[17]

PdF_4 was prepared by addition of AsF_5 to Li_2PdF_6 partially dissolved in aHF, following a previously reported procedure.[20,37] However, this reaction was consistently observed to yield Pd_2F_6 as a byproduct, which dominated the Raman spectrum of the isolated solid. In an attempt to synthesize high-purity PdF_4, aHF (2.0 mL) and F_2 (2.303 mmol) were condensed into a reaction vessel containing a Pd_2F_6/PdF_4 mixture (prepared from 2.293 mmol of Pd), and the vessel was placed, with agitation, under a UV light,[38] emitted from an air-cooled 1 kW Hg lamp. Following a 39-h period of UV irradiation, the product was isolated and analyzed by Raman spectroscopy. The Raman spectra revealed that the band at 566 cm^{-1}, attributable to Pd_2F_6, persisted, albeit with markedly reduced intensity. In addition, a very weak band at 1819 cm^{-1} was observed, which is likely indicative of the formation of a fluoridopalladate(IV) salt containing O_2^+ cation. A further 22-h round of UV-aided fluorination was conducted using aHF (2.0 mL) and F_2 (2.065 mmol), yet the Raman spectrum of the product remained unaltered. Nevertheless, the PXRD of the product revealed only reflections attributable to PdF_4. This material was subsequently used in the following syntheses.

$[XeF][AsF_6]$ was synthesized by condensing an equimolar amount of AsF_5 onto a frozen solution of XeF_2 in aHF.[13] The product was subsequently isolated by removal of volatiles at −45 °C using a cooled EtOH bath.

$XeF_2{\cdot}PdF_4$ was synthesized by treatment of PdF_4 with an excess of molten XeF_2, followed by removal of the excess XeF_2 under vacuum at room temperature.[17,21]

Syntheses

Synthesis of $[Xe_2F_3][PtF_3(XeF_2)_3][AsF_6]_2$(*oP*256). XeF_2 (52 mg, 0.307 mmol) and PtF_4 (14 mg, 0.052 mmol) were loaded into an h-shaped FEP vessel, and aHF (1.0 mL) was condensed onto the solids. The mixture was stirred for 20 h using a PTFE-coated magnetic stir bar, yielding a pale-yellow solution above a light-brown powder precipitate. Subsequently, AsF_5 (0.115 mmol) was condensed into the vessel, resulting in a more intense yellow coloration of the solution, while the light-brown precipitate persisted. Following an additional 2 h of stirring, the solution was decanted into the side arm, and the vessel was placed in a cooling-bath thermostat (Julabo F25-MD or Huber CC2-K6). The main arm was submerged in cooled ethanol, while the side arm containing the solution remained at room temperature. Over the subsequent 13 days, the temperature gradient between the two arms was gradually increased from 2 to 37 °C by lowering the temperature of the cooling bath, causing all aHF to evaporate from the side arm into the main arm and leaving a dark-orange solid material in the side arm. The solvent was then removed from the vessel at room temperature. Upon gentle crushing of the material isolated from the side arm, it was revealed that it consists of colorless and amber-colored crystalline chunks. SCXRD and Raman spectroscopy showed that the amber-colored and colorless crystals corresponded to $[Xe_2F_3][PtF_3(XeF_2)_3][AsF_6]_2$(*oP*256) and $[Xe_2F_3][AsF_6]$, respectively. The light-brown material remaining in the main arm exhibited PXRD pattern and Raman spectrum consistent with a mixture of PtF_4 and $[Xe_2F_3][PtF_3(XeF_2)_3][AsF_6]_2$(*oP*256).

Synthesis of $[Xe_2F_3][PtF_3(XeF_2)_3][AsF_6]_2$(*aP*256). In a typical experiment, $[XeF][AsF_6]$ (49 mg, 0.144 mmol) and K_2PtF_6 (21 mg, 0.054 mmol) were loaded into an h-shaped FEP vessel, and aHF (0.8 mL) was dispensed onto the reactants under static vacuum. Initially, a pale-orange solution formed above an orange−red solid. Upon overnight stirring, the orange-red solid converted into a tan-colored, powdered precipitate. The solution was then decanted into the side arm, and the main arm was placed in a cooling bath thermostat. The temperature gradient between the two arms was gradually increased from 4 to 46 °C over a period of 12 days, resulting in the growth of a large colorless crystal of $KAsF_6$ surrounded by orange crystalline material of $[Xe_2F_3][PtF_3(XeF_2)_3][AsF_6]_2$(*aP*256), which were analyzed by SCXRD and Raman spectroscopy. The residual tan-colored material in the main arm exhibited no powder diffraction lines and displayed a Raman spectrum matching that reported for $n XeF_2{\cdot}PtF_4$ ($1 < n < 1.6$).[17]

Synthesis of $[Xe_2F_3][PdF_3(XeF_2)_3][AsF_6]_2$ from XeF_2, PdF_4, and AsF_5 in aHF. XeF_2 (73 mg, 0.431 mmol) and PdF_4 (14 mg, 0.077 mmol) were loaded into an FEP reaction vessel, followed by the addition of aHF (1.0 mL). After stirring for 24 h, most of the brick-red PdF_4 had dissolved, affording a pale-yellow solution above a small amount of insoluble brown material. Subsequent addition of AsF_5 (0.189 mmol) produced a solution with a more intense yellow coloration, although some insoluble residue remained at the bottom of the vessel. The clear yellow supernatant was transferred to the side arm, and the main arm of the h-shaped vessel was immersed in a cooling-bath thermostat. The temperature difference between the two arms was increased from 6 to 39 °C over a period of 8 days. The resulting solid orange material in the side arm consisted of colorless crystals of $[Xe_2F_3][AsF_6]$ and amber-colored crystals of $[Xe_2F_3][PdF_3(XeF_2)_3][AsF_6]_2$, whereas Raman spectra of the brown solid remaining in the main arm indicated a mixture of $XeF_2{\cdot}2PdF_4$, $[Xe_2F_3][AsF_6]$, PdF_4, and Pd_2F_6.

Synthesis of $[Xe_2F_3][PdF_3(XeF_2)_3][AsF_6]_2$ from $[XeF][AsF_6]$, $XeF_2{\cdot}PdF_4$, and XeF_2 in aHF. The main arm of an h-shaped FEP vessel was loaded with $[XeF][AsF_6]$ (35 mg, 0.103 mmol), $XeF_2{\cdot}PdF_4$ (18 mg, 0.051 mmol), XeF_2 (19 mg, 0.112 mmol), and aHF (1 mL). The mixture was stirred for 90 min, producing a yellow solution and a dark-brown solid precipitate that adhered to the magnetic stirring bar. The solution was decanted into the side arm of the FEP vessel, and the main arm was placed in a cooling-bath thermostat. As the temperature gradient between the arms increased from 5 to 34 °C over the course of 8 days, the solvent gradually evaporated back into the main arm, leaving a solid amber-colored material in the side arm. SCXRD and Raman spectroscopy demonstrated that the amber-colored solid was composed of $[Xe_2F_3][PdF_3(XeF_2)_3][AsF_6]_2$ and $[Xe_2F_3][AsF_6]$, whereas Raman spectra of the aHF-insoluble brown material remaining in the main arm indicated that it consisted of $XeF_2{\cdot}2PdF_4$ and Pd_2F_6. The crystal of $[Xe_2F_3][PdF_3(XeF_2)_3][AsF_6]_2$ used for structural characterization by SCXRD was obtained from this preparation.

Single-Crystal X-Ray Diffraction

Crystal Mounting. Crystalline samples were placed on a watch glass and submerged in inert perfluorodecalin oil (ABCR, AB102850, 98%, *cis* and *trans*) inside an inert-atmosphere glovebox. Suitable crystals were selected under polarized light using a stereomicroscope outside the glovebox and attached to a MiTeGen dual-thickness polymer loop. Immediately after the pin was lifted above the surface of the perfluorodecalin, it was grasped with cryo-pin tongs cooled to −196 °C and rapidly transferred to the goniometer head of the diffractometer, where the crystal was protected by a stream of cold nitrogen gas (Oxford Cryosystems 800 Series Cryostream).

X-Ray Data Collection, Data Reduction, and Structure Solution. Single-crystal X-ray diffraction data was collected at low temperature (100 K) on a Rigaku OD XtaLAB Synergy-S diffractometer equipped with a Dectris EIGER2 R CdTe 1M hybrid pixel array detector using microfocused Ag *Kα* radiation (λ = 0.56087 Å). *CrysAlisPro* software was employed for data processing, utilizing empirical and numerical absorption correction.[39] The crystal structure of $[Xe_2F_3][PtF_3(XeF_2)_3][AsF_6]_2$(*oP*256) was solved using *SUPERFLIP*,[40] whereas the crystal structures of $[Xe_2F_3][PtF_3(XeF_2)_3][AsF_6]_2$(*aP*256) and $[Xe_2F_3][PdF_3(XeF_2)_3][AsF_6]_2$ were solved using *SHELXT*.[41] All three structures were refined with *SHELXL*[42] within the *Olex2* software.[43] Tabulated distances of the nonbonded Xe···F contacts were calculated using the *PLATON* program.[44] Figures were generated using the *DIAMOND* software.[45]

Because the $[Xe_2F_3][PtF_3(XeF_2)_3][AsF_6]_2$(*oP*256) crystals were always found attached to the colorless byproduct $[Xe_2F_3][AsF_6]$,

https://doi.org/10.1021/acs.inorgchem.5c05940
Inorg. Chem. 2026, 65, 5668−5677

some reflections attributable to the unit cell of the latter were observed after data collection. However, application of a multicrystal data treatment resulted in a structure with inferior agreement parameters. Crystals of $[Xe_2F_3][PtF_3(XeF_2)_3][AsF_6]_2$(*oP*256) and $[Xe_2F_3][PdF_3(XeF_2)_3][AsF_6]_2$ were also found to be twinned. Furthermore, crystals of the *oP*256 and *aP*256 polymorphs of $[Xe_2F_3][PtF_3(XeF_2)_3][AsF_6]_2$ diffracted weakly at high theta angles. Accordingly, the data sets were truncated at resolutions of 0.55 Å and 0.60 Å, respectively.

One symmetry-inequivalent $[AsF_6]^-$ anion in the crystal structure of $[Xe_2F_3][PtF_3(XeF_2)_3][AsF_6]_2$(*oP*256) exhibited disorder, which was treated by splitting four axial atoms and applying SADI and RIGU restraints during refinement.

Vibrational Spectroscopy

Raman Spectroscopy. Raman spectra were measured at 100 K using a Bruker Senterra II confocal Raman microscope equipped with a Linkam LTS420 low-temperature stage. The samples were excited using a 785 nm laser at either 25 mW in the case of $[Xe_2F_3][PtF_3(XeF_2)_3][AsF_6]_2$(*oP*256) or 50 mW in the case of $[Xe_2F_3][PtF_3(XeF_2)_3][AsF_6]_2$(*aP*256) and $[Xe_2F_3][PdF_3(XeF_2)_3][AsF_6]_2$. Spectra were measured over the 50−1410 cm^{-1} range with a spectral resolution of 1.5 cm^{-1} using a 50 μm aperture. Samples were prepared by coarsely homogenizing the reaction products in an agate mortar inside a glovebox and loading the material into quartz capillaries, which had been thoroughly dried and passivated with elemental F_2 beforehand. Crystals of the $[MF_3(XeF_2)_3]^+$ salts invariably formed in the presence of $[Xe_2F_3][AsF_6]$ and $KAsF_6$ byproducts and could not be readily separated. Consequently, Raman spectra of the target compounds were obtained from isolated, brightly colored crystalline particulates that could be visually distinguished from the colorless $[Xe_2F_3][AsF_6]$ or $KAsF_6$ crystals. The plotted spectra (Figure 5) were obtained by averaging spectra from multiple, distinct, randomly oriented crystallites. The number of averaged spectra was 7 for both the *oP*256 and *aP*256 polymorphs of $[Xe_2F_3][PtF_3(XeF_2)_3][AsF_6]_2$ and 13 for $[Xe_2F_3][PdF_3(XeF_2)_3][AsF_6]_2$.

Infrared Spectroscopy. ATR-IR spectra were measured on a Bruker Alpha II FT-IR spectrometer equipped with a Platinum Diamond-ATR sampling module, operated inside an N_2-atmosphere glovebox. Spectra were measured by accumulation of 24 scans over the 400−4000 cm^{-1} range at a resolution of 4 cm^{-1}. The spectra were obtained from finely pulverized materials, which consisted of mixtures of the $[MF_3(XeF_2)_3]^+$ salts and $[Xe_2F_3][AsF_6]$ or $KAsF_6$ byproducts (Figure S12). For comparison, ATR-IR spectra of pure $[Xe_2F_3][AsF_6]$ and $KAsF_6$ were also recorded under identical conditions (Figure S13).

Computational Details

Quantum-chemical calculations were carried out using density functional theory (DFT) as implemented in the *ORCA* software package (version 6.0.0).[25,46,47] The electronic structures of the $[MF_3(XeF_2)_3]^+$ cations were calculated starting from the crystallographic coordinates and converged to stationary points with all vibrational frequencies real. The calculations were performed using the PBE0-D3 functional,[48−51] aug-cc-pVQZ for F, and aug-cc-pVQZ-PP basis sets with SK-MCDHF-RSC effective core potentials for the heavy atoms Pd,[52] Pt,[53] and Xe.[54]

Raman spectra were calculated using numerical frequency calculations (!NumFreq) together with polarizability calculations (%elprop Polar 1 end).[55] Raman intensities were calculated using the *ChemCraft*[56] Raman spectra utility with a temperature of 298.15 K and incident laser frequency of 10,000 cm^{-1}. Gaussian broadening with a full width at half-maximum of 2 cm^{-1} was applied.

Computational results were processed using the *Multiwfn* software[57,58] (version 3.8(dev)) to perform Mayer bond order analysis,[59,60] and quantitative molecular surface analyses.[27,61,62] *GaussView*[63] was used to visualize the MEPS.

■ ASSOCIATED CONTENT

Data Availability Statement

The data supporting the findings of this study are available in the Zenodo open repository (https://zenodo.org/) under the DOI number: 10.5281/zenodo.17787891.

Supporting Information

The Supporting Information is available free of charge at https://pubs.acs.org/doi/10.1021/acs.inorgchem.5c05940.

Additional crystallographic data and figures, DFT-calculated vibrational frequencies and structural parameters of the $[MF_3(XeF_2)_3]^+$ cations and their comparison with experimental values, a table of observed Raman band positions and their relative intensities, and ATR-IR spectra (PDF)

Accession Codes

Deposition Numbers 2517118−2517120 contain the supplementary crystallographic data for this paper. These data can be obtained free of charge via the joint Cambridge Crystallographic Data Centre (CCDC) and Fachinformationszentrum Karlsruhe Access Structures service.

■ AUTHOR INFORMATION

Corresponding Author

Matic Lozinšek − *Extreme Conditions Chemistry Laboratory (ECCL K2), Jožef Stefan Institute, 1000 Ljubljana, Slovenia; Jožef Stefan International Postgraduate School, 1000 Ljubljana, Slovenia;* orcid.org/0000-0002-1864-4248; Email: matic.lozinsek@ijs.si

Authors

Klemen Motaln − *Extreme Conditions Chemistry Laboratory (ECCL K2), Jožef Stefan Institute, 1000 Ljubljana, Slovenia; Jožef Stefan International Postgraduate School, 1000 Ljubljana, Slovenia;* orcid.org/0000-0003-0051-8611

Miha Virant − *Extreme Conditions Chemistry Laboratory (ECCL K2), Jožef Stefan Institute, 1000 Ljubljana, Slovenia;* orcid.org/0000-0002-5919-3631

Complete contact information is available at: https://pubs.acs.org/10.1021/acs.inorgchem.5c05940

Notes

The authors declare no competing financial interest.

■ ACKNOWLEDGMENTS

The authors gratefully acknowledge financial support from the European Research Council (ERC) under the European Union's Horizon 2020 Research and Innovation Programme (Starting Grant 950625), the Slovenian Research and Innovation Agency (ARIS) (Grant N1-0189), and the Jožef Stefan Institute Director's Fund.

■ DEDICATION

In memory of Professor Dr. Boris Frlec (1936−2026).

■ REFERENCES

(1) Tramšek, M.; Žemva, B. Synthesis, Properties and Chemistry of Xenon(II) Fluoride. *Acta Chim. Slov.* **2006**, *53*, 105−116.

(2) Bartlett, N.; Sladky, F. O. The Relative Fluoride Ion Donor Abilities of XeF_2, XeF_4, and XeF_6 and a Chemical Purification of XeF_4. *J. Am. Chem. Soc.* **1968**, *90* (19), 5316−5317.

(3) Uran, E.; Lozinšek, M. Hydrogen-Bonded Salt Cocrystals of Xenon Difluoride and Protonated Perfluoroamides. *CrystEngComm* **2025**, *27* (48), 7776−7784.
(4) Žemva, B. Binary Fluorides of Noble-Gases and Their Compounds. *Croat. Chem. Acta* **1988**, *61* (1), 163−187.
(5) Žemva, B.; Jesih, A.; Templeton, D. H.; Zalkin, A.; Cheetham, A. K.; Bartlett, N. Phases in the System XeF_2/XeF_5AsF_6 and Structural and Vibrational Evidence for the Following Ionization Pathway: $XeF_2 \rightarrow XeF^+ + F^-$. *J. Am. Chem. Soc.* **1987**, *109* (24), 7420−7427.
(6) Mrzljak, T.; Goreshnik, E.; Tavčar, G.; Tramšek, M. Coordination Chemistry of Copper and Nickel with Xenon Difluoride and the Hexafluororuthenate(V) Anion: Synthesis and Structural Studies. *Eur. J. Inorg. Chem.* **2025**, *28* (24), No. e202500275.
(7) Gerken, M.; Hazendonk, P.; Iuga, A.; Nieboer, J.; Tramšek, M.; Goreshnik, E.; Žemva, B.; Zheng, S.; Autschbach, J. Solid-State NMR Spectroscopic Study of Coordination Compounds of XeF_2 with Metal Cations and the Crystal Structure of $[Ba(XeF_2)_5][AsF_6]_2$. *Inorg. Chem.* **2007**, *46* (15), 6069−6077.
(8) Lutar, K.; Leban, I.; Ogrin, T.; Žemva, B. $XeF_2{\cdot}CrF_4$ and $(XeF_5^+CrF_5^-)_4{\cdot}XeF_4$: Syntheses, Crystal Structures and Some Properties. *Eur. J. Solid State Inorg. Chem.* **1992**, *29*, 713−727.
(9) Motaln, K.; Gurung, K.; Brázda, P.; Kokalj, A.; Radan, K.; Dragomir, M.; Žemva, B.; Palatinus, L.; Lozinšek, M. Reactive Noble-Gas Compounds Explored by 3D Electron Diffraction: XeF_2-MnF_4 Adducts and a Facile Sample Handling Procedure. *ACS Cent. Sci.* **2024**, *10* (9), 1733−1741.
(10) Mercier, H. P. A.; Breddemann, U.; Brock, D. S.; Bortolus, M. R.; Schrobilgen, G. J. Syntheses, Structures, and Bonding of $NgF_2{\cdot}CrOF_4$, $NgF_2{\cdot}2CrOF_4$ (Ng = Kr, Xe), and $(CrOF_4)_\infty$. *Chem.−Eur. J.* **2019**, *25* (52), 12105−12119.
(11) Bortolus, M. R.; Mercier, H. P. A.; Brock, D. S.; Schrobilgen, G. J. Noble-Gas Difluoride Complexes of MOF_4 (M = Mo, W); Syntheses, Structures and Bonding of $NgF_2{\cdot}MOF_4$ and $XeF_2{\cdot}2MOF_4$ (Ng = Kr, Xe). *Chem.−Eur. J.* **2022**, *28* (15), No. e202103729.
(12) Frlec, B.; Holloway, J. H. The XeF_2-MF_5 (M = Sb, Ta, or Nb) Systems: Vibrational Spectra of Solid Xenon Difluoride Adducts. *J. Chem. Soc., Dalton Trans.* **1975**, No. 6, 535−540.
(13) Elliott, H. St. A.; Lehmann, J. F.; Mercier, H. P. A.; Jenkins, H. D. B.; Schrobilgen, G. J. X-Ray Crystal Structures of $[XeF][MF_6]$ (M = As, Sb, Bi), $[XeF][M_2F_{11}]$ (M = Sb, Bi) and Estimated Thermochemical Data and Predicted Stabilities for Noble-Gas Fluorocation Salts Using Volume-Based Thermodynamics. *Inorg. Chem.* **2010**, *49* (18), 8504−8523.
(14) Gillespie, R. J.; Martin, D.; Schrobilgen, G. J. A Raman Spectroscopic Study of Noble-Gas Fluoride Adduct Formation with Bismuth Pentafluoride. *J. Chem. Soc., Dalton Trans.* **1980**, No. 10, 1898−1903.
(15) Fir, B. A.; Gerken, M.; Pointner, B. E.; Mercier, H. P. A.; Dixon, D. A.; Schrobilgen, G. J. An X-Ray Crystallographic Study of $[Xe_2F_3][SbF_6]$ and Dimorphism in $[Xe_2F_3][AsF_6]$; and a Density Functional Theory Study of the $Xe_2F_3^+$ Cation. *J. Fluorine Chem.* **2000**, *105* (1), 159−167.
(16) Radan, K.; Goreshnik, E.; Žemva, B. Xenon(II) Polyfluoridotitanates(IV): Synthesis and Structural Characterization of $[Xe_2F_3]^+$ and $[XeF]^+$ Salts. *Angew. Chem. Int. Ed.* **2014**, *53* (50), 13715−13719.
(17) Motaln, K.; Gurung, K.; Dragomir, M.; Kurzydłowski, D.; Palatinus, L.; Lozinšek, M. Crystal Structures of $XeF_2{\cdot}2PtF_4$ and $XeF_2{\cdot}2PdF_4$ Determined by 3D Electron Diffraction and Structural Models of $XePtF_6$. *Inorg. Chem.* **2025**, *64* (29), 14968−14976.
(18) De Backere, J. R.; Mercier, H. P. A.; Schrobilgen, G. J. A Structurally Diverse Series of Eight-Coordinate Hg^{2+} Complexes of KrF_2 Derived from $Hg(PnF_6)_2$ (Pn = As, Sb) and $FHg(AsF_6)$. *Inorg. Chem.* **2025**, *64* (29), 15234−15247.
(19) Bartlett, N. Xenon Hexafluoroplatinate(V) $Xe^+[PtF_6]^-$. *Proc. Chem. Soc.* **1962**, 218.
(20) Graham, L.; Graudejus, O.; Jha, N. K.; Bartlett, N. Concerning the Nature of $XePtF_6$. *Coord. Chem. Rev.* **2000**, *197* (1), 321−334.
(21) Bartlett, N.; Žemva, B.; Graham, L. Redox Reactions in the XeF_2/Platinum Fluoride and XeF_2/Palladium Fluoride Systems and the Conversion of XeF_2 to XeF_4 and Xe. *J. Fluorine Chem.* **1976**, *7* (1), 301−320.
(22) Lutar, K.; Borrmann, H.; Žemva, B. $XeF_2{\cdot}2CrF_4$ and $XeF_5^+CrF_5^-$: Syntheses, Crystal Structures, and Some Properties. *Inorg. Chem.* **1998**, *37* (12), 3002−3006.
(23) Alvarez, S. A Cartography of the van Der Waals Territories. *Dalton Trans.* **2013**, *42* (24), 8617−8636.
(24) Vogt, J.; Alvarez, S. Van Der Waals Radii of Noble Gases. *Inorg. Chem.* **2014**, *53* (17), 9260−9266.
(25) Neese, F. The ORCA Program System. *Wiley Interdiscip. Rev.: Comput. Mol. Sci.* **2012**, *2* (1), 73−78.
(26) Arunan, E.; Metrangolo, P.; Resnati, G.; Scheiner, S. IUPAC Recommendations: (Un)Equivocal Understanding of Hydrogen and Halogen Bonds and Their (Un)Equivocal Naming! *Cryst. Growth Des.* **2024**, *24* (20), 8153−8158.
(27) Bader, R. F. W. *Atoms in Molecules: A Quantum Theory*; Oxford University Press: Oxford, 1990.
(28) Gillespie, R. J.; Landa, B. Raman Spectra of Some Xenon(II) Compounds. *Inorg. Chem.* **1973**, *12* (6), 1383−1389.
(29) Milićev, S.; Lutar, K.; Žemva, B.; Ogrin, T. Vibrational Spectra of Solid CrF_4 and of Three New Fluorochromate(IV) Complexes with Xe Fluorides, $XeF_2{\cdot}CrF_4$, $(XeF_5^+CrF_5^-)_4{\cdot}XeF_4$ and $XeF_5^+CrF_5^-$. *J. Mol. Struct.* **1994**, *323*, 1−6.
(30) Peters, D.; Miethchen, R. Symptoms and Treatment of Hydrogen Fluoride Injuries. *J. Fluorine Chem.* **1996**, *79* (2), 161−165.
(31) Segal, E. B. First Aid for a Unique Acid, HF: A Sequel. *Chem. Health Saf.* **2000**, *7* (1), 18−23.
(32) Möbs, M.; Kraus, F. Tips and Procedures for Safe Handling of Anhydrous Hydrogen Fluoride and Pure Elemental Fluorine in Chemical University Laboratories. *ACS Chem. Health Saf.* **2025**, *32* (55), 662−672.
(33) Šmalc, A.; Lutar, K. Xenon Difluoride (Modification). In *Inorganic Syntheses*; Grimes, R. N., Ed.; John Wiley & Sons, 1992; Vol. *29*, pp 1−4.
(34) Mazej, Z.; Žemva, B. Synthesis of Arsenic Pentafluoride by Static Fluorination of As_2O_3 in a Closed System. *J. Fluorine Chem.* **2005**, *126* (9), 1432−1434.
(35) Lucier, G. M.; Elder, S. H.; Chacon, L.; Bartlett, N. The Room Temperature Oxidation of Gold, Ruthenium, Osmium, Iridium, Platinum, or Palladium with Fluorine in Anhydrous Hydrogen Fluoride. *Eur. J. Solid State Inorg. Chem.* **1996**, *33*, 809−820.
(36) Drews, T.; Rusch, D.; Seidel, S.; Willemsen, S.; Seppelt, K. Systematic Reactions of $[Pt(PF_3)_4]$. *Chem.−Eur. J.* **2008**, *14* (14), 4280−4286.
(37) Casteel, W. J.; Lohmann, D. H.; Bartlett, N. Room Temperature Preparations of Second and Third Transition Series Tetrafluorides and a Possible Novel Structure Type for OsF_4 and RhF_4. *J. Fluorine Chem.* **2001**, *112* (2), 165−171.
(38) Mazej, Z. Photochemical Syntheses of Fluorides in Liquid Anhydrous Hydrogen Fluoride. In *Modern Synthesis Processes and Reactivity of Fluorinated Compounds*; Groult, H.; Leroux, F. R.; Tressaud, A., Eds.; Elsevier, 2017; pp 587−607.
(39) Rigaku, OD *CrysAlisPro*; Rigaku Corporation: Wrocław, Poland, 2025.
(40) Palatinus, L.; Chapuis, G. *SUPERFLIP* − a Computer Program for the Solution of Crystal Structures by Charge Flipping in Arbitrary Dimensions. *J. Appl. Crystallogr.* **2007**, *40* (4), 786−790.
(41) Sheldrick, G. M. *SHELXT* − Integrated Space-Group and Crystal-Structure Determination. *Acta Crystallogr. A* **2015**, *71* (1), 3−8.
(42) Sheldrick, G. M. Crystal Structure Refinement with *SHELXL*. *Acta Crystallogr. C* **2015**, *71* (1), 3−8.
(43) Dolomanov, O. V.; Bourhis, L. J.; Gildea, R. J.; Howard, J. a. K.; Puschmann, H. *OLEX2*: A Complete Structure Solution, Refinement and Analysis Program. *J. Appl. Crystallogr.* **2009**, *42* (2), 339−341.
(44) Spek, A. L. Single-Crystal Structure Validation with the Program *PLATON*. *J. Appl. Crystallogr.* **2003**, *36* (1), 7−13.

https://doi.org/10.1021/acs.inorgchem.5c05940
Inorg. Chem. 2026, 65, 5668−5677

(45) Putz, H.; Brandenburg, K. *Diamond – Crystal and Molecular Structure Visualization*, 2025.
(46) Neese, F. Software Update: The ORCA Program System—Version 5.0. *Wiley Interdiscip. Rev.: Comput. Mol. Sci.* **2022**, *12* (5), No. e1606.
(47) Neese, F. Software Update: The ORCA Program System—Version 6.0. *Wiley Interdiscip. Rev.: Comput. Mol. Sci.* **2025**, *15* (2), No. e70019.
(48) Adamo, C.; Barone, V. Toward Reliable Density Functional Methods without Adjustable Parameters: The PBE0 Model. *J. Chem. Phys.* **1999**, *110* (13), 6158–6170.
(49) Grimme, S.; Antony, J.; Ehrlich, S.; Krieg, H. A Consistent and Accurate Ab Initio Parametrization of Density Functional Dispersion Correction (DFT-D) for the 94 Elements H-Pu. *J. Chem. Phys.* **2010**, *132* (15), 154104.
(50) Grimme, S.; Ehrlich, S.; Goerigk, L. Effect of the Damping Function in Dispersion Corrected Density Functional Theory. *J. Comput. Chem.* **2011**, *32* (7), 1456–1465.
(51) Kendall, R. A.; Dunning, T. H., Jr.; Harrison, R. J. Electron Affinities of the First-row Atoms Revisited. Systematic Basis Sets and Wave Functions. *J. Chem. Phys.* **1992**, *96* (9), 6796–6806.
(52) Peterson, K. A.; Figgen, D.; Dolg, M.; Stoll, H. Energy-Consistent Relativistic Pseudopotentials and Correlation Consistent Basis Sets for the 4*d* Elements Y–Pd. *J. Chem. Phys.* **2007**, *126* (12), 124101.
(53) Figgen, D.; Peterson, K. A.; Dolg, M.; Stoll, H. Energy-Consistent Pseudopotentials and Correlation Consistent Basis Sets for the 5*d* Elements Hf–Pt. *J. Chem. Phys.* **2009**, *130* (16), 164108.
(54) Peterson, K. A.; Figgen, D.; Goll, E.; Stoll, H.; Dolg, M. Systematically Convergent Basis Sets with Relativistic Pseudopotentials. II. Small-Core Pseudopotentials and Correlation Consistent Basis Sets for the Post-*d* Group 16–18 Elements. *J. Chem. Phys.* **2003**, *119* (21), 11113–11123.
(55) Bykov, D.; Petrenko, T.; Izsák, R.; Kossmann, S.; Becker, U.; Valeev, E.; Neese, F. Efficient Implementation of the Analytic Second Derivatives of Hartree–Fock and Hybrid DFT Energies: A Detailed Analysis of Different Approximations. *Mol. Phys.* **2015**, *113* (13–14), 1961–1977.
(56) Zhurko, G. A. *Chemcraft - Graphical Program for Visualization of Quantum Chemistry Computations*, 2005. https://chemcraftprog.com/.
(57) Lu, T.; Chen, F. Multiwfn: A Multifunctional Wavefunction Analyzer. *J. Comput. Chem.* **2012**, *33* (5), 580–592.
(58) Lu, T. A Comprehensive Electron Wavefunction Analysis Toolbox for Chemists, Multiwfn. *J. Chem. Phys.* **2024**, *161* (8), No. 082503.
(59) Mayer, I. Charge, Bond Order and Valence in the AB Initio SCF Theory. *Chem. Phys. Lett.* **1983**, *97* (3), 270–274.
(60) Mayer, I. Improved Definition of Bond Orders for Correlated Wave Functions. *Chem. Phys. Lett.* **2012**, *544*, 83–86.
(61) Lu, T.; Chen, F. Quantitative Analysis of Molecular Surface Based on Improved Marching Tetrahedra Algorithm. *J. Mol. Graphics Modell.* **2012**, *38*, 314–323.
(62) Zhang, J.; Lu, T. Efficient Evaluation of Electrostatic Potential with Computerized Optimized Code. *Phys. Chem. Chem. Phys.* **2021**, *23* (36), 20323–20328.
(63) Dennington, R.; Keith, T. A.; Millam, J. M. *GaussView, Version 6.1.1*, 2016.

https://doi.org/10.1021/acs.inorgchem.5c05940
Inorg. Chem. 2026, 65, 5668–5677

4.4 Structural Investigations of the XeF_2–PtF_5 System: Crystal Structures of $[Xe_2F_3][PtF_6] \cdot XeF_2$, $[Xe_2F_3][PtF_6]$, and $[XeF][PtF_6]$

K. Motaln and M. Lozinšek

Published in: *Acta Chimica Slovenica*, 2026, 73, 1, 62–69.

DOI: 10.17344/acsi.2026.9768

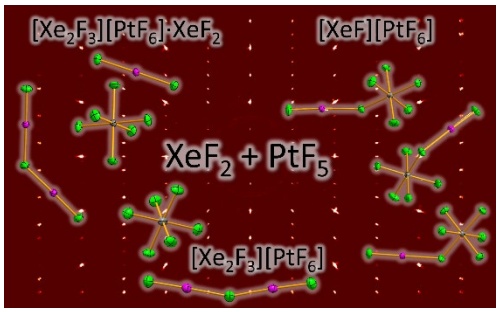


Figure 4.4: Graphical abstract of the publication "Structural investigations of the XeF_2–PtF_5 system: crystal structures of $[Xe_2F_3][PtF_6] \cdot XeF_2$, $[Xe_2F_3][PtF_6]$, and $[XeF][PtF_6]$" [200].

As outlined in Section 1.4, the XeF_2–PtF_5 system is of particular historical interest because it is directly connected to the chemistry associated with the discovery of the first noble-gas compound, $XePtF_6$. Early investigations of the reaction between Xe and PtF_6 established the presence of products containing quinquivalent platinum [98]. In particular, the powder pattern of the material described as $Xe(PtF_6)_2$ was later matched to $[XeF][PtF_6]$, and heating this material above 60 °C produced a more friable solid that was subsequently identified as $[XeF][Pt_2F_{11}]$ [99]. These assignments were based on a study which probed the interaction of XeF_2 with strongly Lewis acidic pentafluorides, namely AsF_5, RuF_5, OsF_5, IrF_5, and PtF_5, in BrF_5 solvent. The results showed that such reactions generally yield compounds in three stoichiometries: 2:1, 1:1, and 1:2. On the basis of vibrational spectroscopy, these phases were formulated as the ionic $[Xe_2F_3][AF_6]$, or as tight ion-pair species $[XeF][AF_6]$ and $[XeF][A_2F_{11}]$, while PXRD indicated that the compounds formed with noble-metal pentafluorides constitute an isomorphous series [99]. However, for many of these phases, including the entire XeF_2–PtF_5 system, complete structural information remained unavailable.

In this work, we aimed to reinvestigate the XeF_2–PtF_5 system by pursuing reactions in anhydrous HF and at elevated temperatures, reporting the first crystal structures for members of this family. Four phases were structurally characterized in detail: two polymorphs of the new compound $[Xe_2F_3][PtF_6] \cdot XeF_2$, together with $[Xe_2F_3][PtF_6]$ and $[XeF][PtF_6](mP108)$. The two $[Xe_2F_3][PtF_6] \cdot XeF_2$ polymorphs, $mC120$ and $oP120$, were both shown to contain well-separated $[Xe_2F_3]^+$ and $[PtF_6]^-$ ions with co-crystallized XeF_2, while differing in their crystal packing. The $[Xe_2F_3][PtF_6]$ salt was found to be isostructural with the Ru and Ir analogues [201], thereby confirming the expected structural relationship across the platinum-group series. Likewise, $[XeF][PtF_6]$ ($mP108$) was found to be isostructural with $[XeF][IrF_6]$ [202], whereas another detected polymorph, $[XeF][PtF_6](mP36)$, which is isostructural with $[XeF][RuF_6]$ [203], did not yield crystals of sufficient quality for complete SCXRD characterization. The structure of $[XeF][PtF_6](mP108)$ contains three crystallographically independent ion pairs in the asymmetric unit. The XeF_2 fragments coordinated to the Pt^V centers display pronounced asymmetry in their Xe—F bond lengths, consistent with substantial ionization along the $XeF_2 \rightarrow XeF^+ + F^-$ pathway [84].

Low-temperature Raman spectra of the four phases supported the crystallographic assignments and in the case of $[Xe_2F_3][PtF_6]$ and $[XeF][PtF_6](mP108)$ agreed well with previous reports [79]. Unfortunately, all attempts to isolate crystalline $[XeF][Pt_2F_{11}]$ were unsuccessful, and under the explored conditions only $[XeF][PtF_6]$ together with residual PtF_5 were obtained. Overall, the results of this work establish the historically important yet structurally underexplored XeF_2–PtF_5 system as one of the best structurally characterized XeF_2–AF_5 families.

K. Motaln, the author of this dissertation, synthesized all of the XeF_2–PtF_5 compounds, determined their crystal structures from SCXRD data, collected their low-temperature Raman spectra, prepared the initial draft of the manuscript, and contributed to the review, editing, and revision of the final manuscript.

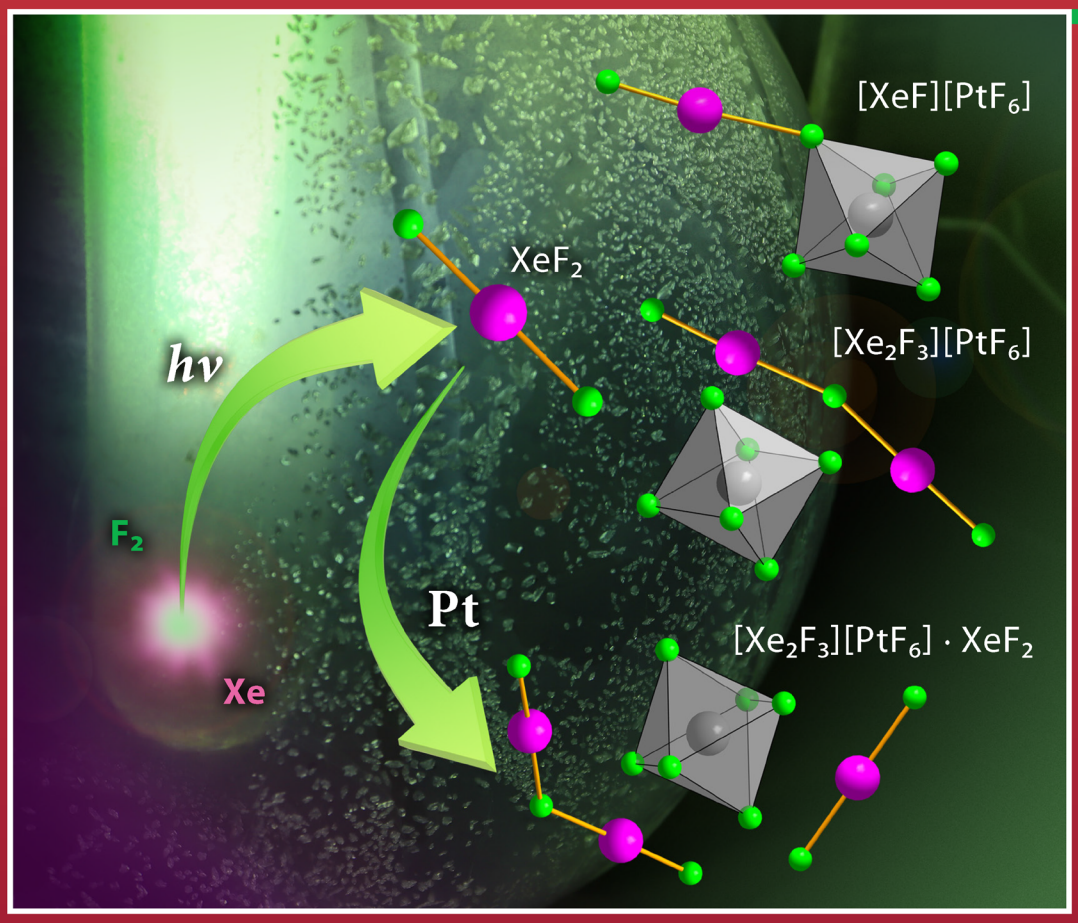
ISSN 1580-3155 Pages 1–288 ■ Year 2026, Vol. 73, No. 1

Slovensko kemijsko društvo
Slovenian Chemical Society

Acta Chimica Slovenica

1

73/2026



http://acta.chem-soc.si

62 **DOI:** 10.17344/acsi.2026.9768 *Acta Chim. Slov.* **2026,** *73,* 62–69

creative commons

Scientific paper

Structural investigations of the XeF_2–PtF_5 system: crystal structures of $[Xe_2F_3][PtF_6]\cdot XeF_2$, $[Xe_2F_3][PtF_6]$, and $[XeF][PtF_6]$

Klemen Motaln[1,2] and Matic Lozinšek*[,1,2]

[1] *Extreme Conditions Chemistry Laboratory (ECCL K2), Jožef Stefan Institute, Jamova cesta 39, 1000 Ljubljana, Slovenia*

[2] *Jožef Stefan International Postgraduate School, Jamova cesta 39, 1000 Ljubljana, Slovenia*

* *Corresponding author: E-mail: matic.lozinsek@ijs.si*

Received: 02-06-2026

Dedicated to the memory of Prof. Dr. Boris Žemva (1940–2023), whose passion for noble-gas chemistry was infectious and inspired our work in this fascinating field.

Abstract

The XeF_2–PtF_5 system was reinvestigated by exploring reactions in either anhydrous HF or at elevated temperatures. This approach enabled the structural characterization of four members of the system, namely $[Xe_2F_3][PtF_6]\cdot XeF_2$(*mC*120), $[Xe_2F_3][PtF_6]\cdot XeF_2$(*oP*120), $[Xe_2F_3][PtF_6]$, and $[XeF][PtF_6]$(*mP*108), by means of single-crystal X-ray diffraction and low-temperature Raman spectroscopy.

Keywords Noble-gas compounds; xenon(II); platinum(V); fluorides; single-crystal X-ray diffraction

1. Introduction

Owing to its commercial availability and relative ease of handling, XeF_2 remains the most extensively studied and widely used noble-gas compound.[1] It is a moderately strong fluoride-ion donor, and studies of its reactions with Lewis-acidic pentafluorides AF_5 (e.g., A = As, Sb, Bi, V, Nb, Ta, Ru, Os, Rh, Ir, Pt, Au) have shown that such systems predominantly yield phases with three stoichiometries, namely 2:1, 1:1, and 1:2.[2–8] Structural investigations have established that the 2:1 phases are ionic, comprising discrete V-shaped $[Xe_2F_3]^+$ cations and octahedral $[AF_6]^-$ anions, and are formulated as $[Xe_2F_3][AF_6]$.[2,9] The 1:1 and 1:2 stoichiometry phases have molecular structures comprising tight ion pairs formulated as $[XeF][AF_6]$ and $[XeF][A_2F_{11}]$, respectively, in which the coordinated XeF_2 units exhibit substantial ionization.[10–12] Investigations of the reactions between XeF_2 and platinum-group metal pentafluorides, namely RuF_5, RhF_5, OsF_5, IrF_5, and PtF_5, in BrF_5 solvent indicated that, for each of the three stoichiometries, the corresponding compounds form isomorphous series across the platinum-group metals.[2,3] To date, however, only a limited subset of their crystal structures has been reported, including $[XeF][RuF_6]$,[13] $[XeF][IrF_6]$,[14] $[Xe_2F_3][RuF_6]$, $[Xe_2F_3][IrF_6]$, and $[Xe_2F_3][RuF_6]\cdot XeF_2$.[15] Consequently, structural investigations of these systems remain incomplete, which is particularly notable in the case of the XeF_2–PtF_5 system, given the historical relevance of these compounds.

The investigations that followed the preparation of the first noble-gas compound $XePtF_6$ ($XeF_2\cdot PtF_4$),[16] revealed that reaction of Xe with a large excess of PtF_6 yields a material with a stoichiometry close to $Xe(PtF_6)_n$ ($n \approx 2$), containing pentavalent platinum.[17] The powder X-ray diffraction (PXRD) pattern of this material was later revealed to match that of $[XeF][PtF_6]$ prepared from the reaction of XeF_2 with PtF_5 in BrF_5 solvent.[3] Moreover, it was revealed that upon warming $Xe(PtF_6)_n$ ($n \approx 2$) above 60 °C, the product became more friable and identified by diffraction pattern as $[XeF][Pt_2F_{11}]$, implying that the original $Xe(PtF_6)_n$ ($n \approx 2$) material consists of $[XeF][PtF_6]$ and amorphous PtF_5.[3,18] Subsequently, it was demonstrated that molten XeF_2 can oxidize PtF_4 to yield $[Xe_2F_3][PtF_6]$, which can in turn be decomposed by heating to 70 °C under dynamic vacuum to give $[XeF][PtF_6]$. Both compounds were characterized by vibrational spectroscopy and powder X-ray diffraction.[19]

Acta Chim. Slov. **2026,** *73,* 62–69

In the present study, the XeF_2–PtF_5 system was reinvestigated, resulting in the crystal structure determination of two polymorphs of $[Xe_2F_3][PtF_6]\cdot XeF_2$, as well as $[Xe_2F_3][PtF_6]$, and $[XeF][PtF_6]$(*mP*108). These results establish the XeF_2–PtF_5 family as one of the more comprehensively explored among XeF_2–AF_5 systems and provide detailed crystallographic data for compounds that are among the earliest reported examples of noble-gas chemistry.

2. Experimental

Caution: Handling of anhydrous HF (aHF), F_2, and strongly-oxidizing fluorides requires great care and should be conducted only in a well-ventilated fume hood by appropriately trained personnel. It is imperative that suitable personal protective equipment is worn at all times and that access to proper treatment procedures is available in case of exposure.[20–22]

2.1. General experimental procedures

A previously described fluorine-resistant vacuum line was used for work involving F_2 or aHF.[23] Solid materials were handled in a nitrogen-atmosphere glovebox (Vigor SG1200/750E), with moisture levels consistently maintained below 1 ppm. Thermal reactions were performed in PTFE-gasketed nickel reactors equipped with nickel valves. Reactions involving the use of aHF solvent were conducted in vessels constructed from fluorinated ethylene propylene copolymer (FEP) tubing, heat-flared at one end and heat-sealed at the other, and capped with brass-encased PTFE valves. Modified, h-shaped FEP reactors[24] were used for crystallization experiments involving the evaporation of aHF induced by a temperature gradient. These reactors were constructed from two FEP tubes, one straight and one bent at 90°, both connected to the valve via a brass-encased PTFE T-junction and male-to-male connectors. Prior to use, all reaction vessels were passivated overnight with 300–600 Torr of F_2.

2.2. Reagents

F_2 (Solvay Fluor, 98–99%) and Pt powder (Thermo Scientific, 99.98%) were used as supplied. Commercial HF (Linde, 99.995%) was condensed into a FEP vessel loaded with K_2NiF_6 (Advance Research Chemicals, 99.9%) and stirred overnight to eliminate residual traces of moisture. XeF_2 was synthesized via a gas-phase photochemical reaction between UV-photolyzed F_2 and Xe, as previously described.[25]

PtF_5 was synthesized by static fluorination of Pt powder enclosed in a nickel pressure vessel, as outlined previously.[26] Approximately 4 bar of F_2 was introduced into a reactor containing Pt powder at ambient temperature, corresponding to an F_2:Pt molar ratio of 3.5–2.8:1, and the mixture was then maintained at 350 °C for 8 hours. The reactor was subsequently recharged with F_2 and heated again to the same temperature. This procedure also generated some volatile PtF_6, which was readily removed under dynamic vacuum, leaving the non-volatile, deep-red PtF_5 adhering to the reactor walls. $RbPtF_6$ was prepared by UV irradiation of a mixture of Pt and RbF in aHF solvent in the presence of a slight excess of F_2, following the procedure previously employed for the synthesis of $CsPtF_6$.[27]

2.3. Synthesis and crystallization

2.3.1. $[Xe_2F_3][PtF_6]\cdot XeF_2$(*mC*120)

In a typical experiment, $nXeF_2\cdot PtF_4$ ($1 < n < 1.6$) (178 mg), obtained by the interaction of XeF_2 with Pt powder in aHF,[28,29] was loaded into a nickel reactor together with XeF_2 (188 mg, 1.11 mmol). The reactor was then placed in an oven at 130 °C for 22 hours. The reactor was then removed from the oven and allowed to cool to room temperature. Inspection of the reactor contents revealed the formation of a bright-yellow powder together with larger yellow crystals suitable for single-crystal X-ray diffraction (SCXRD) analysis.

2.3.2. $[Xe_2F_3][PtF_6]\cdot XeF_2$(*oP*120)

XeF_2 (80 mg, 0.473 mmol) was added to an h-shaped FEP reaction vessel containing $RbPtF_6$, which had been synthesized photochemically from Pt (30 mg, 0.154 mmol), RbF (16 mg, 0.153 mmol), and an excess of F_2. aHF solvent (1.4 mL) was then added, forming a bright orange-yellow solution with an insoluble yellow precipitate remaining at the bottom of the main arm. The clear yellow supernatant was decanted into the side arm of the reactor, which was subsequently placed in a thermostated cooling bath, with the main arm submerged in chilled EtOH. The temperature gradient between the two arms was increased from 4 to 16 °C over two days, facilitating the crystal growth. SCXRD analysis of the yellow crystals from the side arm identified them as $[Xe_2F_3][PtF_6]\cdot XeF_2$(*oP*120) and $RbPtF_6$. The Raman spectrum of the yellow precipitate from the main arm showed only bands attributable to $RbPtF_6$.

2.3.3. $[Xe_2F_3][PtF_6]$

A nickel reaction vessel containing $[Xe_2F_3][PtF_6]\cdot XeF_2$(*mC*120), prepared as described above, was connected to the vacuum line via a U-shaped FEP trap immersed in liquid nitrogen and pumped under dynamic vacuum for a period of 9 hours, until the accumulation of XeF_2 in the trap ceased. The resulting yellow powder was transferred to an FEP reactor and dissolved in aHF. The solution was then gradually cooled to −60 °C in an EtOH bath, during which the precipitation of small yellow crystals was observed. The solvent was removed under dynamic vacuum at −50 °C.

2.3.4. $[XeF][PtF_6]$(*mP*108)

PtF_5 (21 mg, 0.072 mmol) and XeF_2 (6 mg, 0.035 mmol) were weighed into the main arm of an h-shaped FEP reactor, and aHF (1 mL) was condensed onto the solids. The mixture was stirred overnight, resulting in the formation of a yellow solution above a smaller amount of yellow powder precipitate. The solution was decanted into the side arm, and crystal growth was induced by solvent evaporation in a cooling bath thermostat. As soon as the temperature gradient between the two arms exceeded 7 °C, long needle-shaped crystals (> 2 cm in length) of $[XeF][PtF_6]$(*mP*108) precipitated from the solution (Figure 1).

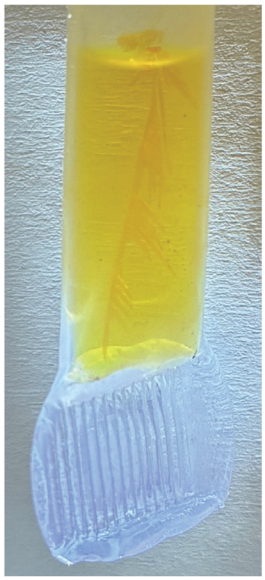


Figure 1. Needle-shaped crystals of $[XeF][PtF_6]$(*mP*108) growing from an aHF solution contained in an FEP tube (6 mm internal diameter; 8 mm outer diameter).

2.3.5. $[XeF][PtF_6]$(*mP*36)

XeF_2 (6 mg, 0.035 mmol) and PtF_5 (24 mg, 0.083 mmol) were loaded into a 6 mm i.d. FEP reactor under N_2 atmosphere. The lower portion of the FEP tube containing the reactants was heat-sealed, and the resulting FEP ampoule was placed in a larger FEP vessel, containing dry N_2 atmosphere. The vessel with the ampoule was then placed in an oven preheated to 70 °C and held at this temperature for 2 hours, after which the oven was gradually cooled by 2 °C/h, until it reached 40 °C. Analysis of the ampoule contents revealed only poorly crystalline $[XeF][PtF_6]$(*mP*36) and its Raman spectrum showed signals belonging to the starting PtF_5 and $[XeF][PtF_6]$.

2.4. Single-crystal X-ray diffraction

Crystalline samples were placed on a watch glass and covered with inert perfluorodecalin oil (ABCR, AB102850, 98%, *cis* and *trans*) inside an inert-atmosphere glovebox. Suitable crystals were selected under a polarized-light stereomicroscope outside the glovebox and mounted on the tip of a MiTeGen dual-thickness polymer loop using Baysilone paste (Bayer-Silicone, mittelviskos). The pin assembly was then grasped with cryo-pin tongs cooled to −196 °C and rapidly transferred to the goniometer head of the diffractometer, where the crystal was protected by a cold nitrogen stream (100 K) during the measurement.

Single-crystal X-ray diffraction data was collected at low temperature (100 K) on a Rigaku OD XtaLAB Synergy-S diffractometer equipped with a Dectris EIGER2 R CdTe 1M hybrid pixel array detector and an Oxford Cryosystems 800 Series Cryostream, using microfocused Ag *K*α radiation (λ = 0.56087 Å). *CrysAlisPro* software was employed for data processing, utilizing empirical and numerical absorption corrections.[30] All crystal structures were solved using *SUPERFLIP*[31] and refined with *SHELXL*[32] within *Olex2* software.[33] Figures were prepared using the *DIAMOND* software.[34]

2.5. Raman spectroscopy

Low-temperature Raman spectra were measured on a Bruker Senterra II confocal Raman microscope using a 785 nm laser. Spectra were measured in the 50–1410 cm^{-1} range with a spectral resolution of 1.5 cm^{-1} using a 15 × 1000 µm aperture. Measurements were performed at 100 K using a Linkam LTS420 low-temperature stage. Background subtraction was applied using three iterations of concave rubber-band correction with 64 baseline points, as implemented in the Bruker *OPUS 8.7* software suite. Prior to analysis, samples were loaded inside an inert-atmosphere glovebox into rigorously dried and F_2-passivated 500 µm quartz capillaries, which were then flame-sealed prior to measurement.

3. Results and discussion

3.1. Syntheses

Reaction of $nXeF_2 \cdot PtF_4$ ($1 < n < 1.6$) with an excess of XeF_2 at temperatures above the melting point of XeF_2 predictably resulted in oxidation of Pt^{IV} to Pt^{V},[19] and characterization of the resulting yellow solid identified it as a previously unobserved phase, $[Xe_2F_3][PtF_6] \cdot XeF_2$(*mC*120) (eq 1).

$$nXeF_2 \cdot PtF_4 + (3.5 - n)XeF_2 \xrightarrow{130\ ^\circ C} [Xe_2F_3][PtF_6] \cdot XeF_2(mC120) + 0.5Xe \quad (1)$$

As previously reported, $[Xe_2F_3][PtF_6]$ was the sole isolated product obtained following oxidation of PtF_4 with excess XeF_2 and subsequent removal of "unreacted" XeF_2 under vacuum.[19] This observation suggested that $[Xe_2F_3][PtF_6] \cdot XeF_2$ undergoes loss of XeF_2 upon prolonged exposure to dynamic vacuum at room temperature. This hy-

Acta Chim. Slov. **2026,** *73,* 62–69

pothesis was confirmed, as $[Xe_2F_3][PtF_6]$ readily formed when $[Xe_2F_3][PtF_6]\cdot XeF_2$ was subjected to dynamic vacuum for several hours (eq 2). The resulting poorly crystalline material could subsequently be recrystallized from aHF to afford yellow crystals suitable for structural characterization.

$$[Xe_2F_3][PtF_6]\cdot XeF_2 \xrightarrow{\text{dyn. vac.}} [Xe_2F_3][PtF_6] + XeF_2 \qquad (2)$$

A second polymorph of $[Xe_2F_3][PtF_6]\cdot XeF_2$ was obtained from reactions in aHF solution employing an approximately threefold excess of XeF_2 relative to $RbPtF_6$. Its formation could be rationalized by partial displacement of the alkali metal as RbF, which is released into solution (eq 3).

$$3XeF_2 + RbPtF_6 \longrightarrow [Xe_2F_3][PtF_6]\cdot XeF_2(oP120) + RbF \qquad (3)$$

All attempts to synthesize $[XeF][Pt_2F_{11}]$ in this work were unsuccessful. Crystallization from aHF solution at ambient temperature employing the targeted stoichiometry yielded only $[XeF][PtF_6](mP108)$ as large single crystals, accompanied by unreacted PtF_5. Likewise, heating a 1:2 mixture of XeF_2 and PtF_5 in a heat-sealed FEP ampoule at 70 °C produced the *mP*36 polymorph of $[XeF][PtF_6]$. Interestingly, the structure of $[XeF][PtF_6](mP108)$ was found to be related to that of $[XeF][IrF_6]$, which was likewise isolated from aHF solution,[14] whereas $[XeF][PtF_6]$ (*mP*36) appears to be structurally related to $[XeF][RuF_6]$, obtained by thermal reaction of XeF_2 with RuF_5.[13] These parallels suggest that polymorph selectivity in such systems is influenced by the employed synthetic approach.

Additionally, the synthesis of $[XeF][Pt_2F_{11}]$ was also attempted from aHF solutions containing XeF_2 and PtF_5 in an approximate 1:2.5 molar ratio, either by slow removal of the solvent at temperatures between −45 °C and −55 °C, or by gradual cooling of the solution to −60 °C. Furthermore, an attempt was made to react $[XeF][PtF_6]$ with a slight excess of PtF_5 at 65 °C, thus emulating the previously reported synthesis of $[XeF][Pt_2F_{11}]$ from $Xe(PtF_6)_2$.[18] None of these experiments yielded crystals of the targeted $[XeF][Pt_2F_{11}]$ compound, and no Raman bands unambiguously attributable to this phase were detected. Instead, only the presence of $[XeF][PtF_6]$ and unreacted PtF_5 were confirmed.

3.2. Single-crystal X-ray diffraction

The members of the XeF_2–PtF_5 system obtained in this work were structurally characterized by low-temperature (100 K) single-crystal X-ray diffraction. A summary of the crystallographic data is provided in Table 1, and selected bond distances and angles are listed in Table 2. Complete crystallographic parameters are compiled in the Supporting information (Tables S1–S6).

3.2.1. Crystal structures of $[Xe_2F_3][PtF_6]\cdot XeF_2$(*mC*120) and $[Xe_2F_3][PtF_6]\cdot XeF_2$(*oP*120)

$[Xe_2F_3][PtF_6]\cdot XeF_2$ crystallizes in two polymorphs, namely in the monoclinic space group *C*2/*c* with Pearson symbol *mC*120 and in the orthorhombic space group *Pbca* with Pearson symbol *oP*120. Both structures feature eight formula units per unit cell ($Z = 8$) and one formula unit in the asymmetric unit ($Z' = 1$) and comprise well-separated $[Xe_2F_3]^+$ and $[PtF_6]^-$ ions together with cocrystallized XeF_2 molecules (Figures 2, 3). The two polymorphs differ, however, in their crystal packing (Figures S1, S2). Despite the established parallels between the XeF_2–PtF_5 and XeF_2–RuF_5 systems and the known isostructural relationship between [XeF]

Table 1. Summary of crystal data and refinement results.

Compound	**$[Xe_2F_3][PtF_6]\cdot XeF_2$(*mC*120)**	**$[Xe_2F_3][PtF_6]\cdot XeF_2$(*oP*120)**	**$[Xe_2F_3][PtF_6]$**	**$[XeF][PtF_6]$(*mP*108)**
T (K)	100	100	100	100
Crystal system, space group	Monoclinic, *C*2/*c*	Orthorhombic, *Pbca*	Monoclinic, *Ia*	Monoclinic, $P2_1/n$
a (Å)	15.82016(16)	8.99866(8)	10.8860(2)	7.91407(6)
b (Å)	9.44604(9)	13.29342(14)	8.09069(16)	10.79245(8)
c (Å)	15.56492(16)	18.61809(18)	9.82822(19)	21.17145(16)
β (°)	109.7185(12)	90	92.1157(16)	91.6071(7)
V (Å^3)	2189.60(4)	2227.15(4)	865.03(3)	1807.59(2)
Z	8	8	4	12
M_w (g mol^{-1})	797.99	797.99	628.69	459.39
D_{calcd} (g cm^{-3})	4.841	4.760	4.827	5.064
μ (mm^{-1})	11.85	11.65	12.93	15.60
R_1	0.027	0.020	0.036	0.023
wR_2	0.070	0.039	0.094	0.052
S	1.044	1.043	1.076	1.026
$\Delta\rho_{min}$, $\Delta\rho_{max}$ (e Å^{-3})	−4.08, 2.46	−1.05, 1.53	−1.36, 2.35	−2.91, 2.28

Table 2. Selected bond distances (Å) and angles (°).

	$[Xe_2F_3][PtF_6]\cdot XeF_2$(*mC*120)	$[Xe_2F_3][PtF_6]\cdot XeF_2$(*oP*120)	$[Xe_2F_3][PtF_6]$	$[XeF][PtF_6]$(*mP*108)
Xe–F [a]	1.9779(12), 1.9993(12)	1.9855(12), 1.9900(13)		
Xe–F_t [b]	1.9118(12), 1.9133(12)	1.9187(13), 1.9232(12)	1.914(9), 1.917(9)	
Xe–F_b(Xe)	2.1690(12), 2.1825(12)	2.1612(12), 2.1757(12)	2.143(9), 2.143(9)	
Xe–F_t [c]				1.8934(16)–1.9023(15)
Xe–F_b(Pt)				2.2255(14)–2.2741(14)
Pt–F_t	1.8771(13)–1.8909(13)	1.8744(12)–1.8871(12)	1.877(7)–1.894(9)	1.8637(14)–1.8809(13)
Pt–F_b				1.9552(14)–1.9590(14)
F–Xe–F [a]	178.48(6)	179.23(6)		
F–Xe–F [b]	178.75(5), 179.28(5)	177.05(6), 178.16(5)	176.6(4), 178.7(4)	
F–Xe–F [c]				175.97(7)–179.26(7)
Xe–F_b–Xe	136.77(6)	134.03(6)	158.2(4)	
Pt–F–Xe				117.33(6)–138.42(8)
cis-F–Pt–F	89.11(7)–90.86(7)	89.65(6)–90.79(6)	88.6(4)–91.4(4)	87.87(7)–91.96(7)
trans-F–Pt–F	179.89(8)–179.97(7)	179.41(6)–179.63(6)	179.0(5)–179.1(4)	177.72(8)–179.74(9)

[a] cocrystallized XeF_2 molecule; [b] $[Xe_2F_3]^+$ cation; [c] XeF_2 molecule bound to Pt^V center; F_t: terminal, F_b: bridging.

$[RuF_6]$ and $[XeF][PtF_6]$,[3,13,18] neither of the two polymorphic forms of $[Xe_2F_3][PtF_6]\cdot XeF_2$ is isostructural with the previously structurally characterized $[Xe_2F_3][RuF_6]\cdot XeF_2$.[15]

The V-shaped $[Xe_2F_3]^+$ cations display among the least obtuse Xe–F–Xe angles reported for this motif to date (136.77(6)° in *mC*120; 134.03(6)° in *oP*120) (Table 2),[9,15,35,36] and are markedly more closed than the corresponding angle in $[Xe_2F_3][RuF_6]\cdot XeF_2$ (154.3(4)°).[15] In neither polymorph is the cation perfectly symmetric, as the two longer Xe–F_b distances are unequal (2.1690(12), 2.1825(12) Å in *mC*120; 2.1612(12), 2.1757(12) Å in *oP*120), whereas the shorter Xe–F_t bonds do not differ significantly (1.9118(12), 1.9133(12) Å in *mC*120; 1.9187(13), 1.9232(12) Å in *oP*120). The F–Xe–F angles within the $[Xe_2F_3]^+$ cations deviate only slightly from linearity (178.75(5), 179.28(5)° in *mC*120; 177.05(6), 178.16(5)° in *oP*120).

In both structures, the fluorine coordination environment around the Pt^V centers deviates only marginally from ideal octahedral (O_h) symmetry. The Pt–F bond lengths span comparable ranges in the two polymorphs (1.8771(13)–1.8909(13) Å in *mC*120; 1.8744(12)–1.8871(12) Å in *oP*120), and the *cis*- and *trans*-F–Pt–F angles remain close to those expected for an octahedral environment (89.11(7)–90.86(7) and 179.89(8)–179.97(7) in *mC*120; 89.65(6)–90.79(6)° and 179.41(6)–179.63(6)° in *oP*120). The observed Pt–F distances are in good agreement with those reported for previously characterized salts containing discrete $[PtF_6]^-$ anions.[27,37,38]

The cocrystallized XeF_2 molecules adopt a geometry close to the ideal linear, centrosymmetric $D_{\infty h}$ arrangement observed in the crystal structure of XeF_2. The observed Xe–F bond distances (1.9779(12), 1.9994(12) Å in *mC*120; 1.9855(12), 1.9900(13) Å in *oP*120) are in good agreement with the Xe–F bond distance reported for XeF_2 (1.999(4) Å),[12] and the F–Xe–F angles remain nearly linear (178.48(6)° in *mC*120; 179.23(6)° in *oP*120).

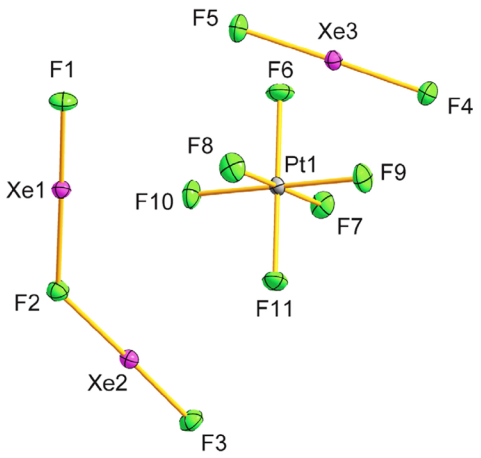


Figure 2. Asymmetric unit of $[Xe_2F_3][PtF_6]\cdot XeF_2$(*mC*120), showing atom labeling. Ellipsoids are drawn at the 50% probability level.

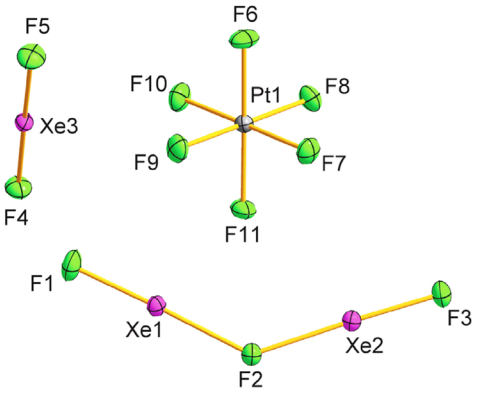


Figure 3. Asymmetric unit of $[Xe_2F_3][PtF_6]\cdot XeF_2$(*oP*120), showing atom labeling. Ellipsoids are drawn at the 50% probability level.

Acta Chim. Slov. **2026,** *73,* 62–69

3.2.2 Crystal structure of $[Xe_2F_3][PtF_6]$

$[Xe_2F_3][PtF_6]$ crystallizes in the monoclinic space group *Ia* (Z = 4, Z' = 1) and comprises discrete $[Xe_2F_3]^+$ and $[PtF_6]^-$ ions (Figure 4). The compound is isostructural with the previously structurally characterized $[Xe_2F_3][RuF_6]$ and $[Xe_2F_3][IrF_6]$; however, an *Ia* setting was chosen for $[Xe_2F_3][PtF_6]$ instead of *Cc*, which was used for the Ru and Ir analogues.[15] This choice affords a monoclinic angle β (92.116(2)°), which is substantially closer to 90°,[39] than the values reported for $[Xe_2F_3][RuF_6]$ (136.825(6)°) and $[Xe_2F_3][IrF_6]$ (136.954(7)°).[15]

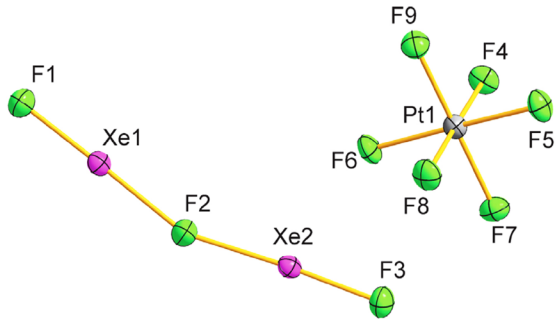


Figure 4. Asymmetric unit of $[Xe_2F_3][PtF_6]$, showing atom labeling. Ellipsoids are drawn at the 50% probability level.

The Xe–F–Xe angle (158.2(4)°) in the $[Xe_2F_3]^+$ cation is markedly more open than in the $[Xe_2F_3][PtF_6]\cdot XeF_2$ structures, albeit slightly less so than in the related $[Xe_2F_3][RuF_6]$ (161.5(5)°) and $[Xe_2F_3][IrF_6]$ (161.3(8)°). Within experimental uncertainty, the two Xe–F_b distances are equivalent (2.143(9), 2.143(9) Å), as are the two Xe–F_t bonds (1.914(9), 1.917(9) Å). The $[PtF_6]^-$ anion exhibits only minor deviations from octahedral geometry, as reflected in *cis*- and *trans*-F–Pt–F angles (88.6(4)–91.4(4)° and 179.0(5)–179.1(4)°, respectively). The Pt–F bond lengths (1.877(7)–1.894(9) Å) fall in the same range as those observed in the $[Xe_2F_3][PtF_6]\cdot XeF_2$ structures.

3.2.3. Crystal structure of $[XeF][PtF_6]$(*mP*108)

$[XeF][PtF_6]$(*mP*108) crystallizes in the monoclinic space group $P2_1/n$ and contains three crystallographically independent $[XeF][PtF_6]$ tight ion pairs in the asymmetric unit (Z' = 3) (Figure 5). Its unit-cell parameters closely resemble those reported for $[XeF][IrF_6]$, although the structure of the Ir analogue was reported in the $P2_1/c$ space group.[14]

The XeF_2 units bound to the Pt^V center retain a nearly linear F–Xe–F geometry (175.97(7)–179.26(7)°) but exhibit a pronounced asymmetry in their Xe–F bond lengths, characterized by elongation of the bridging Xe–F_b bonds (2.2255(14)–2.2741(14) Å) accompanied by contraction of the terminal Xe–F_t bonds (1.8934(16)–1.9023(15) Å), indicative of ionization of XeF_2 along the $XeF_2 \rightarrow XeF^+ + F^-$ pathway.[40] The Xe–F_b bond lengths closely match those

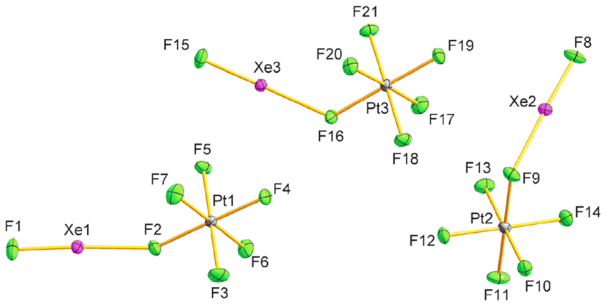


Figure 5. Asymmetric unit of $[XeF][PtF_6]$, featuring the three symmetry-inequivalent units and showing atom labeling. Ellipsoids are drawn at the 50% probability level.

reported for $[XeF][IrF_6]$ (2.220(4)–2.272(4) Å), whereas the corresponding Xe–F_t bonds in the Ir analogue are appreciably shorter (1.854(5)–1.867(5) Å).[14] The Pt–F–Xe angles within the three crystallographically independent moieties vary substantially (117.33(6), 124.20(7), and 138.42(8)°), closely matching those reported for $[XeF][IrF_6]$ (119.3–141.9°). The smallest value represents the least obtuse A–F–Xe angle observed in a $[XeF][AF_6]$ structure to date.[12–14]

The Pt–F_b bond lengths (1.9552(14)–1.9590(14) Å) are notably elongated relative to Pt–F_t bonds (1.8637(14)–1.8809(13) Å), the latter being comparable to those observed for discrete $[PtF_6]^-$ anions characterized in this work. Nevertheless, the coordination environment of Pt^V remains close to octahedral, as reflected by *cis*- and *trans*-F–Pt–F angles (87.87(7)–91.96(7)° and 177.72(8)–179.74(9)°, respectively).

3.2.4. Crystal structure of $[XeF][PtF_6]$(*mP*36)

Crystals of $[XeF][PtF_6]$(*mP*36) were of poor quality and yielded only low-resolution diffraction data, precluding a detailed structural analysis. Consequently, only the unit-cell parameters could be determined (a = 7.0440(4), b = 10.8225(5), c = 7.9242(4), β = 91.212(5), V = 603.96(5), Z' = 1, space group $P2_1/n$). These closely resemble both the parameters derived from PXRD data[18] and those reported for $[XeF][RuF_6]$ (with the a and c axes interchanged),[13] corroborating earlier observations based on PXRD patterns that the two compounds are isostructural.[18]

3.3. Raman spectroscopy

Low-temperature (100 K) Raman spectra of the two polymorphs of $[Xe_2F_3][PtF_6]\cdot XeF_2$, $[Xe_2F_3][PtF_6]$, and $[XeF][PtF_6]$(*mP*108) are shown in Figure 6, with peak positions and relative intensities tabulated in the Supporting Information (Table S7).

The Raman spectra of both $[Xe_2F_3][PtF_6]\cdot XeF_2$ polymorphs exhibit their most intense features in the region attributable to the symmetric and asymmetric Xe–F_t stretching modes of the $[Xe_2F_3]^+$ cation (580–598 cm^{-1}).[9]

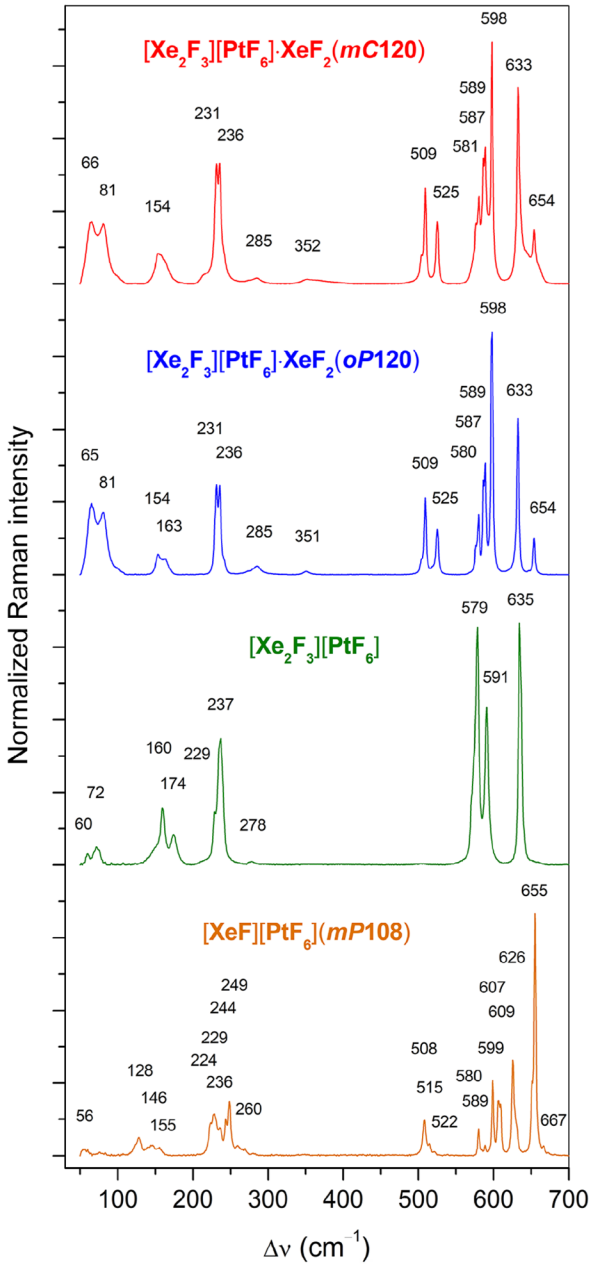


Figure 6. Low-temperature (100 K) Raman spectra of $[Xe_2F_3][PtF_6]\cdot XeF_2$(*mC*120), $[Xe_2F_3][PtF_6]\cdot XeF_2$(*oP*120), $[Xe_2F_3][PtF_6]$, and $[XeF][PtF_6]$(*mP*108).

Bands associated with the $[PtF_6]^-$ anion, corresponding to the ν_1 (633, 654 cm^{-1}) and ν_5 (231, 236 cm^{-1}) modes, are likewise readily identified.[19,27] The presence of cocrystallized XeF_2 is reflected by two medium-intensity bands (509, 525 cm^{-1}). Corresponding bands were also reported in the ambient-temperature spectra of the Ru (506, 515 cm^{-1}) and Ir (506, 516 cm^{-1}) analogues.[15] Overall, the spectra of the *mC*120 and *oP*120 polymorphs are nearly identical.

The low-temperature Raman spectra of $[Xe_2F_3][PtF_6]$ and $[XeF][PtF_6]$(*mP*108) recorded in this work are also consistent, in terms of the positions of their strongest bands, with previously reported ambient-temperature spectra of these compounds.[3,19]

4. Conclusions

Reexploration of the XeF_2–PtF_5 system has resulted in the synthesis of the novel compound $[Xe_2F_3][PtF_6]\cdot XeF_2$, along with $[Xe_2F_3][PtF_6]$ and $[XeF][PtF_6]$, all of which were characterized by SCXRD and Raman spectroscopy. Both $[Xe_2F_3][PtF_6]\cdot XeF_2$ and $[XeF][PtF_6]$ were found to occur in two polymorphs, with polymorph selectivity apparently depending on the synthetic approach employed. In the low-temperature Raman spectra of the $[Xe_2F_3][PtF_6]\cdot XeF_2$ phases, main bands attributable to the constituent moieties could be readily assigned, whereas the spectra of $[Xe_2F_3][PtF_6]$ and $[XeF][PtF_6]$(*mP*108) are consistent with literature data. Collectively, these results provide the first crystallographically characterized representatives of the XeF_2–PtF_5 family and expand the set of structurally elucidated phases formed by interaction of XeF_2 with strongly Lewis-acidic pentafluorides.

Supplementary material

Additional crystallographic data, figures, and a table listing the observed Raman band positions with their relative intensities are provided in the Supporting Information. Supplementary crystallographic data (CIF files) may be obtained free of charge from FIZ Karlsruhe via www.ccdc.cam.ac.uk/structures by quoting the depository numbers CSD 2529289 ($[Xe_2F_3][PtF_6]\cdot XeF_2$(*mC*120)), 2529288 ($[Xe_2F_3][PtF_6]\cdot XeF_2$(*oP*120)), 2529287 ($[Xe_2F_3][PtF_6]$), and 2529290 ($[XeF][PtF_6]$(*mP*108)). Full experimental data for this article, including SCXRD datasets and Raman spectra, is available from the Zenodo open repository at https://doi.org/10.5281/zenodo.18428037.

Acknowledgements

The authors gratefully acknowledge the financial support from the Slovenian Research and Innovation Agency (ARIS) (N1-0189, N1-0225), the European Research Council (ERC) under the European Union's Horizon 2020 Research and Innovation Programme (Starting Grant No. 950625), and the Jožef Stefan Institute Director's Fund.

5. References

1. M. Tramšek, B. Žemva, *Acta Chim. Slov.* **2006**, *53*, 105–116.
2. F. O. Sladky, P. A. Bulliner, N. Bartlett, B. G. DeBoer, A. Zalkin, *Chem. Commun. (London)* **1968**, 1048–1049. **DOI:**10.1039/c19680001048

3. F. O. Sladky, P. A. Bulliner, N. Bartlett, *J. Chem. Soc. A* **1969**, 2179–2188. **DOI:**10.1039/J19690002179
4. B. Žemva, J. Slivnik, *J. Inorg. Nucl. Chem.* **1971**, *33(11)*, 3952–3953. **DOI:**10.1016/0022-1902(71)80304-4
5. R. J. Gillespie, B. Landa, *Inorg. Chem.* **1973**, *12(6)*, 1383–1389. **DOI:**10.1021/ic50124a034
6. B. Frlec, J. H. Holloway, *J. Chem. Soc., Dalton Trans.* **1975**, 535–540. **DOI:**10.1039/DT9750000535
7. J. H. Holloway, G. J. Schrobilgen, *J. Chem. Soc., Chem. Commun.* **1975**, 623–624. **DOI:**10.1039/C39750000623
8. B. Žemva, *Croat. Chem. Acta* **1988**, *61(1)*, 163–187.
9. B. A. Fir, M. Gerken, B. E. Pointner, H. P. A. Mercier, D. A. Dixon, G. J. Schrobilgen, *J. Fluorine Chem.* **2000**, *105(1)*, 159–167. **DOI:**10.1016/S0022-1139(00)00306-7
10. J. Burgess, C. J. W. Fraser, V. M. McRae, R. D. Peacock, D. R. Russell, *J. Inorg. Nucl. Chem.* **1976**, *28*, 183–188. **DOI:**10.1016/0022-1902(76)80624-0
11. A. Zalkin, D. L. Ward, R. N. Biagioni, D. H. Templeton, N. Bartlett, *Inorg. Chem.* **1978**, *17(5)*, 1318–1322. **DOI:**10.1021/ic50183a044
12. H. St. A. Elliott, J. F. Lehmann, H. P. A. Mercier, H. D. B. Jenkins, G. J. Schrobilgen, *Inorg. Chem.* **2010**, *49(18)*, 8504–8523. **DOI:**10.1021/ic101152x
13. N. Bartlett, M. Gennis, D. D. Gibler, B. K. Morrell, A. Zalkin, *Inorg. Chem.* **1973**, *12(8)*, 1717–1721. **DOI:**10.1021/ic50126a002
14. F. Tamadon, S. Seidel, K. Seppelt, *Acta Chim. Slov.* **2013**, *60(3)*, 491–494.
15. M. Tramšek, E. Goreshnik, G. Tavčar, *Acta Chim. Slov.* **2016**, *63(2)*, 369–375. **DOI:**10.17344/acsi.2016.2373
16. N. Bartlett, *Proc. Chem. Soc.* **1962**, 218. **DOI:**10.1039/ps9620000197
17. N. Bartlett, N. K. Jha, in: H. H. Hyman (Ed.): Noble-gas compounds, The University of Chicago Press, Chicago, **1963**, pp. 23–30.
18. L. Graham, O. Graudejus, N. K. Jha, N. Bartlett, *Coord. Chem. Rev.* **2000**, *197(1)*, 321–334. **DOI:**10.1016/S0010-8545(99)00190-3
19. N. Bartlett, B. Žemva, L. Graham, *J. Fluorine Chem.* **1976**, *7(1–3)*, 301–320. **DOI:**10.1016/S0022-1139(00)84003-8
20. D. Peters, R. Miethchen, *J. Fluorine Chem.* **1996**, *79(2)*, 161–165. **DOI:**10.1016/S0022-1139(96)03484-7
21. E. B. Segal, *Chem. Health Saf.* **2000**, *7(1)*, 18–23. **DOI:**10.1016/S1074-9098(99)00077-5
22. M. Möbs, F. Kraus, *ACS Chem. Health Saf.* **2025,** *32(5),* 662–672. **DOI:**10.1021/acs.chas.5c00117
23. K. Motaln, K. Gurung, P. Brázda, A. Kokalj, K. Radan, M. Dragomir, B. Žemva, L. Palatinus, M. Lozinšek, *ACS Cent. Sci.* **2024**, *10(9)*, 1733–1741. **DOI:**10.1021/acscentsci.4c00815
24. M. Lozinšek, E. Goreshnik, B. Žemva, *Z. Anorg. Allg. Chem.* **2012**, *638(12–13)*, 2123–2128. **DOI:**10.1002/zaac.201200176
25. A. Šmalc, K. Lutar, in: R. N. Grimes (Ed.): Inorganic Syntheses, John Wiley & Sons, **1992**, *29,* pp. 1–4. **DOI:**10.1002/9780470132609.ch1
26. W. E. Falconer, G. R. Jones, W. A. Sunder, M. J. Vasile, A. A. Muenter, T. R. Dyke, W. Klemperer, *J. Fluorine Chem.* **1974**, *4(2)*, 213–234. **DOI:**10.1016/S0022-1139(00)82515-4
27. Z. Mazej, E. Goreshnik, K. O. Christe, *J. Fluorine Chem.* **2023**, *268*, 110128. **DOI:**10.1016/j.jfluchem.2023.110128
28. T. Drews, D. Rusch, S. Seidel, S. Willemsen, K. Seppelt, *Chem. Eur. J.* **2008**, *14(14)*, 4280–4286. **DOI:**10.1002/chem.200701786
29. K. Motaln, K. Gurung, M. Dragomir, D. Kurzydłowski, L. Palatinus, M. Lozinšek, *Inorg. Chem.* **2025**, *64(29)*, 14968–14976. **DOI:**10.1021/acs.inorgchem.5c01740
30. Rigaku OD, CrysAlisPro, Rigaku Corporation, Wrocław, Poland, **2025.**
31. L. Palatinus, G. Chapuis, *J. Appl. Crystallogr.* **2007**, *40(4)*, 786–790. **DOI:**10.1107/S0021889807029238
32. G. M. Sheldrick, *Acta Crystallogr. C* **2015**, *71(1)*, 3–8. **DOI:**10.1107/S2053229614024218
33. O. V. Dolomanov, L. J. Bourhis, R. J. Gildea, J. A. K. Howard, H. Puschmann, *J. Appl. Crystallogr.* **2009**, *42(2)*, 339–341. **DOI:**10.1107/S0021889808042726
34. H. Putz, K. Brandenburg, Diamond – Crystal and Molecular Structure Visualization, Crystal Impact, Bonn, Germany, **2025.**
35. K. Radan, E. Goreshnik, B. Žemva, *Angew. Chem Int. Ed.* **2014**, *53(50)*, 13715–13719. **DOI:**10.1002/anie.201406404
36. K. Motaln, M. Virant, M. Lozinšek, *Inorg. Chem.* **2026**, *65 (10)* 5668–5677. **DOI:**10.1021/acs.inorgchem.5c05940
37. O. Graudejus, B. G. Müller, *Z. Anorg. Allg. Chem.* **1996**, *622(6)*, 1076–1082. **DOI:**10.1002/zaac.19966220623
38. O. Graudejus, A. P. Wilkinson, L. C. Chacón, N. Bartlett, *Inorg. Chem.* **2000**, *39(13)*, 2794–2800. **DOI:**10.1021/ic000041w
39. A. D. Mighell, *Acta Crystallogr. B* **2003**, *59(2)*, 300–302. **DOI:**10.1107/S0108768103002829
40. B. Žemva, A. Jesih, D. H. Templeton, A. Zalkin, A. K. Cheetham, N. Bartlett, *J. Am. Chem. Soc.* **1987**, *109(24)*, 7420–7427. **DOI:**10.1021/ja00258a028

Povzetek

Sistem XeF_2–PtF_5 je bil ponovno raziskan s preučevanjem reakcij, ki so potekale v brezvodnem HF ali pri povišanih temperaturah. Ta pristop je omogočil strukturno karakterizacijo štirih predstavnikov sistema, in sicer $[Xe_2F_3][PtF_6]\cdot XeF_2$(*mC*120), $[Xe_2F_3][PtF_6]\cdot XeF_2$(*oP*120), $[Xe_2F_3][PtF_6]$ in $[XeF][PtF_6]$(*mP*108), z uporabo rentgenske difrakcije na monokristalu in nizkotemperaturne ramanske spektroskopije.

Except when otherwise noted, articles in this journal are published under the terms and conditions of the Creative Commons Attribution 4.0 International License

4.5 Revisiting the Coordination of XeF_2 to Alkali Metal Cations: Synthesis and Structural Characterization of $[Li(XeF_2)_3PtF_6]$, $[Na(XeF_2)PtF_6]$, and $[K(XeF_2)_2PtF_6]$

4.5.1 Background

Due to its commercial availability and relative ease of handling, compared to its higher-valent binary fluorides relatives XeF_4 and XeF_6, XeF_2 remains one of the best studied and widely used noble-gas compounds [70]. In the context of inorganic chemistry, a particularly well explored facet of its behavior is its ability to act as a ligand to metal centers. The first compound demonstrating coordination of XeF_2 to a metal center, $[Ag(XeF_2)_2AsF_6]$, was obtained upon the oxidation of Xe gas by a solution of $AgFAsF_6$ in aHF [204]. In the three decades that followed, numerous XeF_2 coordination complexes have been prepared involving mono- [205], di- [206], [207], [208], and trivalent metal centers [209], [210], [211], and the coordination chemistry of noble-gas fluorides has been further extended to include XeF_4 and KrF_2 [212], [213]. Although a relatively large number of structures involving coordination of XeF_2 to divalent metal centers have been reported (31 entries in the ICSD) [214], [215], only five examples featuring monovalent cations have been crystallographically characterized to date. This is in no small part due to the oxidizing power of XeF_2 in aHF solution [76], which leaves only a limited subset of oxidation-resistant monovalent metal fluorides as viable candidates for ligation by XeF_2. In this view, alkali metal cations offer a suitable choice for preparation of novel coordination compounds. At present, XeF_2 is known to ligate both Li^+ and Na^+, and the species $[Li(XeF_2)_3AsF_6]$, $[Li_2(XeF_2)(V_2O_2F_8)]$, and $[Na_2(XeF_2)(V_2O_2F_8)]$ have been structurally characterized [92], [216], [217]. These studies have also shown that the anion plays an important role in stabilizing XeF_2 coordination complexes. Investigations of $LiMF_6$–XeF_2 systems (M = P, As, V, Ru, Ir, Sb, Nb, Ta) showed that XeF_2–alkali metal complexes were obtained only for M = P, As, Ru, and Ir, all of which decomposed slowly at ambient temperature, and no coordination compounds with heavier alkali metals were isolated [216]. By contrast, reactions of XeF_2 with fluoridooxidovanadates(V) afforded Li^+ and Na^+ complexes $[Li_2(XeF_2)(V_2O_2F_8)]$ and $[Na_2(XeF_2)(V_2O_2F_8)]$, which do not lose XeF_2 at ambient temperature [92], [217].

In the present work, the role of XeF_2 as a ligand for alkali-metal cations was reexamined by investigating its reactions in aHF with alkali metal hexafluoridoplatinates(V). This approach afforded $[Li(XeF_2)_3PtF_6]$, $[Na(XeF_2)PtF_6]$, and $[K(XeF_2)_2PtF_6]$, which were structurally characterized by low-temperature SCXRD and low-temperature Raman spectroscopy. Notably, $[K(XeF_2)_2PtF_6]$ constitutes the first crystallographically characterized example of XeF_2 coordinated to a K^+ cation, thereby extending the scope of alkali metals known to be ligated by XeF_2 and underscoring the influence of the anion choice in enabling XeF_2 coordination to new Lewis-acidic centers. In addition, the structures of the parent alkali metal hexafluoridoplatinates(V) $LiPtF_6$, $NaPtF_6$, $KPtF_6$, and $RbPtF_6$, were determined from single-crystal data for the first time.

4.5.2 Results and discussion

4.5.2.1 Syntheses

In the first step of the preparation of the titular compounds, alkali metal hexafluoridoplatinates(V) were synthesized by direct oxidation of Pt powder with photodissociated F_2, generated by UV irradiation of the reaction mixture using an LED

light source (see Section 3.2.4), in the presence of the corresponding alkali fluoride in aHF solvent (Eq 4.1).

$$\mathrm{AF} + \mathrm{Pt} + \tfrac{5}{2}\mathrm{F_2} \xrightarrow{\text{UV, aHF}} \mathrm{APtF_6} \qquad \mathrm{A = Li, Na, K, Rb} \tag{4.1}$$

During the syntheses, it was observed that the formed $LiPtF_6$ and $NaPtF_6$ fully dissolved in aHF, affording bright orange-yellow solutions, whereas $KPtF_6$ and $RbPtF_6$ did not dissolve completely, leaving a small amount of yellow precipitate beneath an orange-yellow supernatant. After solvent removal, the $APtF_6$ salts were isolated as yellow crystalline solids. In order to achieve ligation of the alkali metal cations by XeF_2, approximately 3–4-fold molar excess of XeF_2 was introduced into the reactors containing these salts, and the mixtures were dissolved in aHF at room temperature (Eq. 4.2).

$$\mathrm{APtF_6} + n\mathrm{XeF_2} \xrightarrow{\text{aHF}} [\mathrm{A(XeF_2)}_n\mathrm{PtF_6}] \qquad \mathrm{A = Li, Na, K} \tag{4.2}$$

Upon dissolution of the alkali hexafluoridoplatinates(V) in aHF with excess XeF_2, the solutions retained the same coloration as before the addition of XeF_2, and in the cases of $KPtF_6$ and $RbPtF_6$, a yellow precipitate persisted. After a brief period of stirring with a magnetic stirrer the clear, intensely colored solutions were decanted into the side arm of the reaction vessels, and the reactors were positioned with the main arm immersed in a cooling-bath thermostat. This established a temperature gradient between the two reactor arms, facilitating solvent evaporation and enabling slow crystal growth. Once crystals had formed and all the aHF had recondensed back into the cooled reactor arm, the products were isolated by removing the solvent under dynamic vacuum. As it was expected that all the isolated XeF_2 coordination complexes would be thermodynamically unstable at ambient temperature, solvent removal was performed while the products were cooled in an EtOH bath, kept at temperatures below −15 °C throughout the process.

Following this procedure, the coordination of XeF_2 to Li^+, Na^+, and K^+ cations was achieved, affording $[Li(XeF_2)_3PtF_6]$, $[Na(XeF_2)PtF_6]$, and $[K(XeF_2)_2PtF_6]$, whereas no evidence for the ligation of Rb^+ by XeF_2 was observed under these reaction conditions. Once isolated, the XeF_2 coordination compounds were stored in the glovebox freezer, where the temperature was maintained between −5 and −10 °C. Under these conditions, crystals of $[Li(XeF_2)_3PtF_6]$ and $[Na(XeF_2)PtF_6]$ retained XeF_2 for more than six months, whereas $[K(XeF_2)_2PtF_6]$ decomposed, yielding XeF_2 and $KPtF_6$. Raman spectra of the insoluble precipitates remaining in the main arms of the reactors containing $KPtF_6$ and $RbPtF_6$ confirmed that they consisted solely of the starting alkali hexafluoridoplatinate(V) salts.

Analysis of solids recovered in the side arms of the $LiPtF_6$–XeF_2 and $RbPtF_6$–XeF_2 reactions revealed that in addition to the aforementioned products, $[Xe_2F_3][PtF_6] \cdot XeF_2$(*oP*120) had also been isolated [200]. Its presence could be explained by the formation of an equilibrium between the $[Xe_2F_3]^+$ salt and the XeF_2 coordination compound, resulting in the release of the alkali fluoride (Eq. 4.3). Similar equilibria have been documented in the $Cu[RuF_6]_2$–XeF_2 and $Cu[SbF_6]_2$–XeF_2 systems [208], [218].

$$\mathrm{APtF_6} + \mathrm{XeF_2} \xrightarrow{\text{aHF}} a[\mathrm{A(XeF_2)}_n\mathrm{PtF_6}] + b[\mathrm{Xe_2F_3}][\mathrm{PtF_6}]\cdot\mathrm{XeF_2} + c\mathrm{AF} \qquad \mathrm{A = Li, Rb} \tag{4.3}$$

4.5.2.2 Crystal structures

Table 4.1 contains the summary of crystal data and refinement results for the alkali-metal coordination complexes of XeF_2, with the bond distances and angles summarized in Table 4.2. Crystallographic data for the structures of $APtF_6$ (A = Li, Na, K, Rb) are summarized in Table 4.3 and selected bond lengths and angles are given in Table 4.4. Complete tables of crystallographic data, fractional atomic coordinates, and equivalent isotropic displacement parameters are provided in the Appendix (Appendix Table B.1–Appendix Table B.6). In the course of data reduction, it was found that crystals of $[Na(XeF_2)PtF_6]$ were twinned, which was treated by integrating both domains and generating the corresponding .hkl4 and .hkl5 files in *CrysAlisPro* [178]. During refinement, the ratio between the twin domains converged to 0.8983(6):0.1017(6). The crystal structure of $[Li(XeF_2)_3PtF_6]$ was modeled as a two-component inversion twin, with refined twin fractions of 0.976(3) and 0.024(3).

Table 4.1: Summary of crystal data and refinement results for the structures of $[Li(XeF_2)_3PtF_6]$, $[Na(XeF_2)PtF_6]$, and $[K(XeF_2)_2PtF_6]$, collected at a temperature of 100 K.

	$[Li(XeF_2)_3PtF_6]$	$[Na(XeF_2)PtF_6]$	$[K(XeF_2)_2PtF_6]$
Space group	$P2_1$	$P2_1/c$	$I4/mcm$
a (Å)	6.80526(6)	7.1459(3)	8.73777(9)
b (Å)	26.79621(19)	10.0427(4)	8.73777(9)
c (Å)	6.81133(6)	10.2322(4)	13.3131(2)
α (°)	90	90	90
β (°)	92.6673(8)	95.852(4)	90
γ (°)	90	90	90
V (Å^3)	1240.736(17)	730.47(5)	1016.44(3)
Z	4	4	4
F_w (g mol^{-1})	823.93	501.38	686.79
ρ_{calc} (g cm^{-3})	4.411	4.559	4.488
μ (mm^{-1})	10.363	12.918	11.227
R_1[a]	0.0284	0.0358	0.0174
wR_2[b]	0.0706	0.1042	0.0495
$\Delta\rho_{max}$, $\Delta\rho_{min}$ (e Å^{-3})	3.445, −3.231	3.440, −3.226	1.525, −1.576

[a] $R_1 = \Sigma||F_o|-|F_c||/\Sigma|F_o|$; [b] $wR_2 = [\Sigma(w(F_o^2-F_c^2)^2)/\Sigma(w(F_o^2)^2)]^{1/2}$.

Table 4.2: Selected bond lengths (Å) and angles (°) in the crystal structures of $[Li(XeF_2)_3PtF_6]$, $[Na(XeF_2)PtF_6]$, and $[K(XeF_2)_2PtF_6]$.

	$[Li(XeF_2)_3PtF_6]$	$[Na(XeF_2)PtF_6]$	$[K(XeF_2)_2PtF_6]$
Xe–F$_t$	1.967(4)		
Xe–F(A)	1.994(2)–2.020(3)	1.977(2), 1.997(2)	1.9829(10)
Pt–F$_t$	1.868(4)–1.889(4)	1.868(2)	1.8766(18)
Pt–F(A)	1.909(3)	1.880(2)–1.897(2)	1.8787(9)
A–F(Xe)	1.943(9)–2.032(8)	2.250(3), 2.254(3)	2.6121(10)
A–F(Pt)	1.927(8)	2.292(3)–2.910(3)	2.7542(9)
F–Xe–F	177.68(10)–179.87(13)	179.03(12)	180.0
***cis* F–Pt–F**	88.37(17)–90.78(16)	87.57(12)–92.21(12)	90.0
***trans* F–Pt–F**	178.78(15)–179.8(2)	178.98(12)–179.65(11)	180.0

4.5.2.2.1 Crystal structure of $[Li(XeF_2)_3PtF_6]$

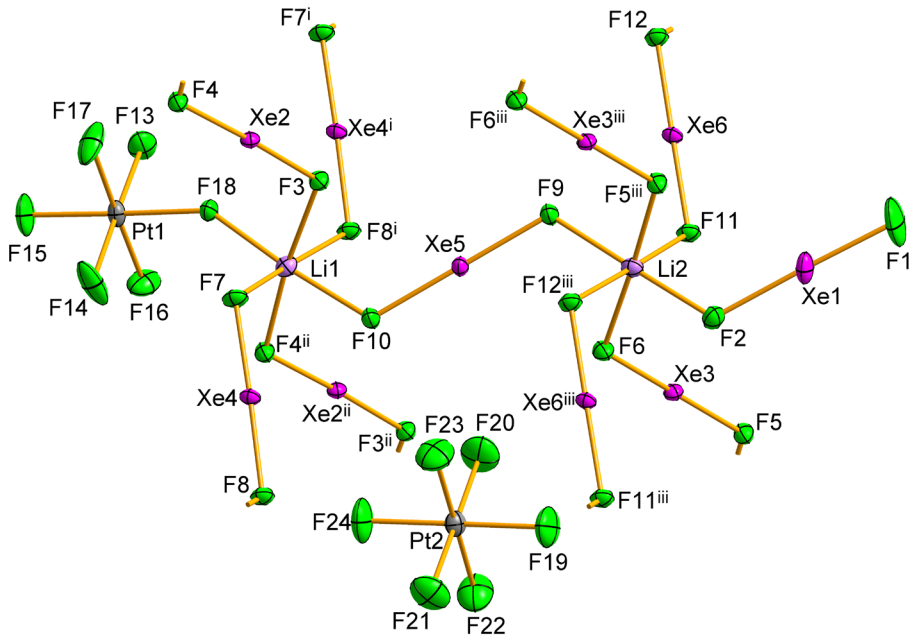


Figure 4.5: Sections of the crystal structure of $[Li(XeF_2)_3PtF_6]$ displaying the coordination surrounding the symmetry inequivalent Li^+ sites. Ellipsoids are set at 50% probability level. Symmetry codes used for generation of equivalent atoms: (i) x, y, $z + 1$; (ii) $x + 1$, y, z; (iii) $-x + 1$, $y - 1/2$, $-z + 1$.

The crystal structure of $[Li(XeF_2)_3][PtF_6]$ shares the monoclinic space group $P2_1$ with the previously characterized $[Li(XeF_2)_3][AsF_6]$, and their unit cells are appear closely related. The a and c lattice parameters are comparable across both phases, whereas the b parameter in $[Li(XeF_2)_3][PtF_6]$ is approximately twice that of $[Li(XeF_2)_3][AsF_6]$. The larger unit cell arises from the presence of two symmetry inequivalent Li^+ sites, while only one is present in the structure of $[Li(XeF_2)_3][PtF_6]$. Both Li^+ centers are approximately octahedrally

coordinated by fluorine ligands, with *cis*-F–Li–F angles of 84.6(3)–98.1(4)° and *trans*-F–Li–F angles of 172.0(5)–179.1(5)° (Figure 4.5). One Li^+ site is homoleptically coordinated by XeF_2 ligands, representing the first such instance for a monovalent metal center, whereas at the second site one fluoride ligand is provided by the coordinated $[PtF_6]^-$ anion. The latter arrangement mirrors that in $[Li(XeF_2)_3][AsF_6]$, where the sole crystallographically independent Li^+ cation is coordinated by five XeF_2 molecules and one $[AsF_6]^-$ anion. The Li–F(Xe) distances span 1.943(9)–2.032(8) Å, while the single Li–F(Pt) contact is shorter at 1.927(8) Å. The Li^+ centers are linked by bridging XeF_2 molecules to generate a double-layer structure, with layers parallel to the *ac* crystallographic plane. Within each layer, pairs of Li^+ sites stack along *b*, and further propagation in this direction is interrupted by a terminal XeF_2 unit at one end and a terminal $[PtF_6]^-$ ligand at the other (Appendix Figure B.1). The six crystallographically independent XeF_2 ligands observed in the structure are close to the ideal linear shape of free XeF_2, with F–Xe–F angles of 177.68(10)–179.87(13)°. The geometry of the sole terminally bound XeF_2 ligand is notably distorted, exhibiting a shortened Xe–F_t bond of 1.967(4) Å and an elongated Xe–F(Li) bond measuring 2.020(3) Å. In contrast, in all bridging XeF_2 units the Xe–F(Li) distances lie within 3σ of the Xe–F bond length in free XeF_2 [1.999(4) Å]. Charge balance in the structure is provided by two symmetry-inequivalent $[PtF_6]^-$ anions, one of which ligates the Li^+ cation, whereas the other is well separated and resides in structure voids (Appendix Figure B.1). Both anions display near-ideal octahedral geometry, with *cis*-F–Pt–F angles of 88.37(17)–90.78(16)° and *trans*-F–Pt–F angles of 178.78(15)–179.8(2)°. The Pt–F_t bonds measure 1.868(4)–1.889(4) Å, whereas the Pt–F(Li) bond to the fluorine atom that also coordinates Li^+ is appreciably longer at 1.909(3) Å.

4.5.2.2.2 Crystal structure of $[Na(XeF_2)PtF_6]$

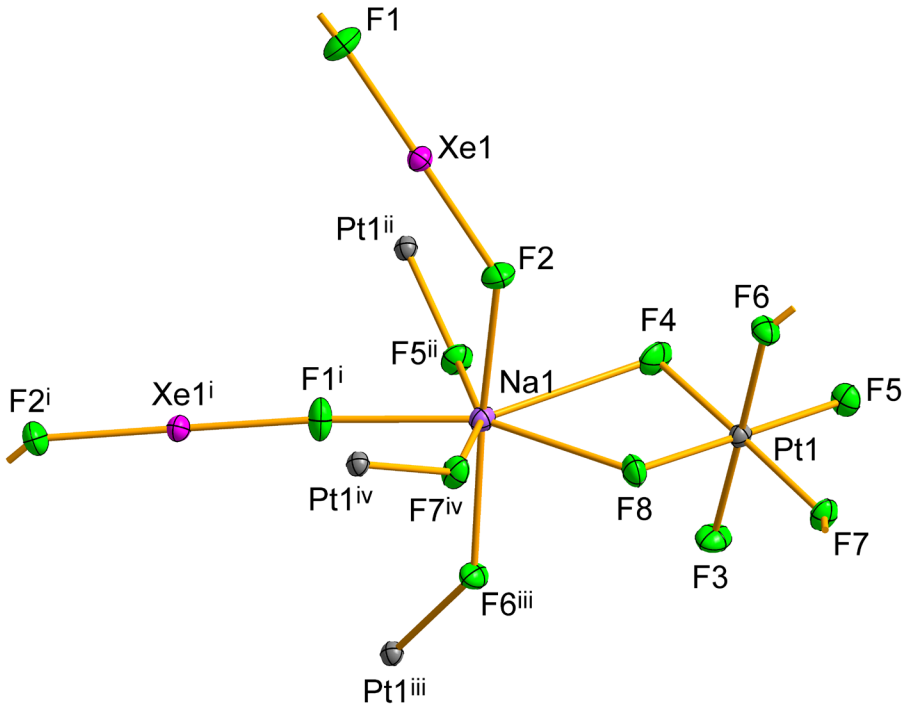


Figure 4.6: Coordination sphere of Na^+ in $[Na(XeF_2)PtF_6]$. Thermal ellipsoids are drawn at the 50% probability level. Symmetry codes used for generation of equivalent atoms: (i) x, $-y + 1/2$, $z + 1/2$; (ii) $-x + 1$, $y - 1/2$, $-z + 3/2$; (iii) x, $-y + 3/2$, $z + 1/2$; (iv) $-x$, $y - 1/2$, $-z + 3/2$.

$[Na(XeF_2)PtF_6]$ crystallizes in the monoclinic space group $P2_1/c$ with one formula unit in the asymmetric unit ($Z' = 1$) and all atoms occupying general positions. The coordination sphere surrounding the Na^+ cation consists of seven F atoms arranged in a distorted pentagonal bipyramidal geometry (Figure 4.6). Two F ligands are contributed by XeF_2 molecules, positioned *cis* with respect to one another, with one of the XeF_2 coordinating the sodium center through the apical position. In addition, the Na^+ cation is coordinated by four $[PtF_6]^-$ anions, one of which binds in a bidentate fashion. The Na–F(Xe) distances are 2.250(3) Å and 2.254(3) Å, whereas four Na–F(Pt) bonds span 2.292(3)–2.365(3) Å, and a longer Na–F(Pt) bond measuring 2.910(3) Å is formed with the bidentate $[PtF_6]^-$ ligand. Both XeF_2 molecules bridge two adjacent Na^+ cations, linking the alkali metal centers through a zigzag chain motif that propagates along the *c* axis. Further connectivity through the $[PtF_6]^-$ anions, each of them coordinating four neighboring Na^+ centers, yields a three-dimensional network structure (Appendix Figure B.2). Despite their bridging role, the Xe–F bonds within each XeF_2 ligand are unequal, measuring 1.977(2) Å and 1.997(2) Å, and the molecules remain nearly linear, with an F–Xe–F angle of 179.03(12)°. The $[PtF_6]^-$ anion adopts a slightly distorted octahedral geometry, with *cis*-F–Pt–F angles of 87.57(12)–92.21(12)° and *trans*-F–Pt–F angles of 178.98(12)–179.65(11)°. The Pt–F_t bond to the sole terminal fluoride is notably shorter at 1.868(2) Å, whereas the bridging Pt–F(Na) bonds range between 1.880(2) Å and 1.897(2) Å.

4.5.2.2.3 Crystal structure of $[K(XeF_2)_2PtF_6]$

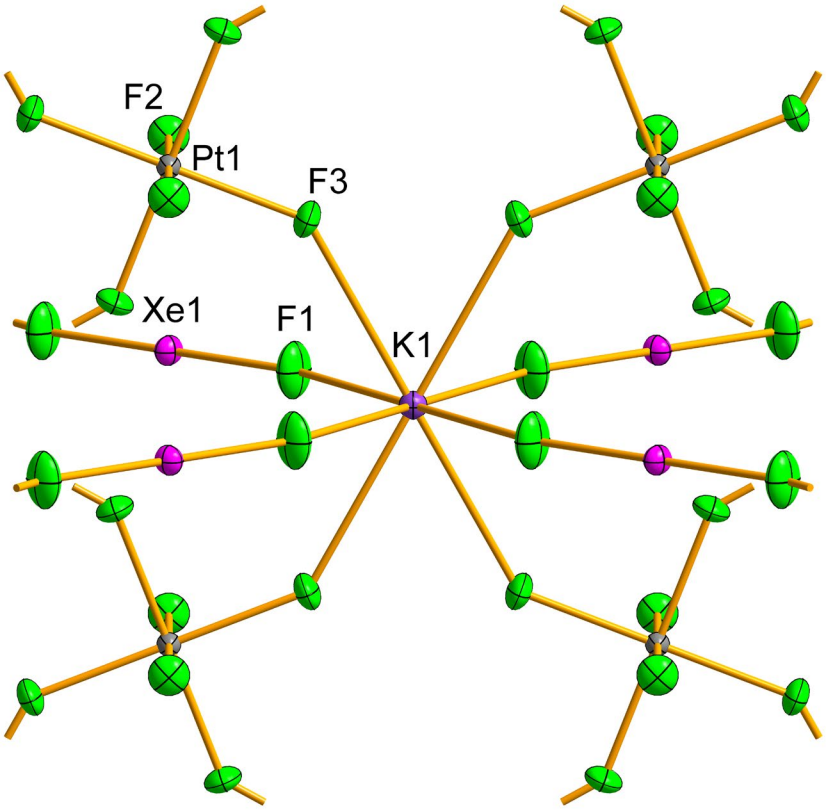


Figure 4.7: Section of the crystal structure of $[K(XeF_2)_2PtF_6]$ displaying the coordination environment of K^+. Thermal ellipsoids are drawn at the 50% probability level.

$[K(XeF_2)_2PtF_6]$ crystallizes in a tetragonal unit cell with unit cell parameters $a = 8.73777(9)$ Å and $c = 13.3131(2)$ Å and $I4/mcm$ symmetry. Its unit cell parameters closely resemble

those of the previously characterized, isostructural pair $[Ag(XeF_2)_2AsF_6]$ [a = 8.4558(12) Å and c = 12.8645(19) Å] and $[Ag(XeF_2)_2PF_6]$ [a = 8.467(3) Å and c = 12.745(3) Å] [204], [205], albeit with a larger unit cell volume required to accommodate the bulkier $[PtF_6]^-$ anions. In spite of these similarities, the structures do not share the same space group. The structures of the Ag^+ analogues were solved in the noncentrosymmetric space group $I\bar{4}c2$, whereas the intensity distribution statistics for $[K(XeF_2)_2PtF_6]$ strongly support a centrosymmetric space group, and the structure refinement in the $I4/mcm$ symmetry yields lower R_1 and wR_2 values than a model in the related $I\bar{4}c2$ symmetry. Nevertheless, the structures of $[K(XeF_2)_2PtF_6]$ remains very similar to those of the Ag^+ compounds. Layers of K and Pt atoms arranged in a NaCl-type pattern extend parallel to the ab crystallographic plane, while bridging XeF_2 ligands connect adjacent layers along c to generate a three-dimensional network (Appendix Figure B.3). K^+ cation is coordinated by eight F ligands, four of them donated by XeF_2 molecules and four by $[PtF_6]^-$ anions, forming a coordination environment in the shape of a slightly distorted cube (Figure 4.7). The K–F(Xe) bonds measure 2.6121(10) Å and are shorter than the K–F(Pt) bonds, which measure 2.7542(9) Å. The bridging XeF_2 molecules which link pairs of two K^+ centers retain ideal linear $D_{\infty h}$ symmetry, with the Xe–F distances at 1.9829(10) Å only slightly shortened than in solid XeF_2. Similarly, the octahedral $[PtF_6]^-$ anion exhibits ideal F–Pt–F right angles, with the four axial Pt–F(K) bonds measuring 1.8787(9) Å and the apical Pt–F_t bonds of 1.8766(18) Å.

4.5.2.2.4 Crystal structures of $APtF_6$-type compounds (A = Li, Na, K, Rb)

Previous structural studies of $APtF_6$ salts (A = Li, K, Rb) relied on PXRD, reporting only rhombohedral lattice parameters for $KPtF_6$ and $RbPtF_6$ [98], [219], whereas a more detailed characterization of $LiPtF_6$ at 299 K was achieved using synchrotron-based PXRD [220]. Single-crystal structure determinations of the $APtF_6$ compounds examined herein provide more detailed and accurate structural models and reveal that these compounds crystallize in two distinct structure types: the lighter congeners Li and Na adopt the $LiSbF_6$-type structure [221], whereas the heavier K and Rb crystallize in the $KAsF_6$-type structure [222], [223], [224]. The latter two compounds are also isostructural with $CsPtF_6$, whose structure was previously solved from single-crystal data [163]. All four phases crystallize in the space group $R\bar{3}$ with $Z = 3$ (Table 4.3).

Table 4.3: Crystal data and refinement results for the structures of $LiPtF_6$, $NaPtF_6$, $KPtF_6$, and $RbPtF_6$ collected at a temperature of 100 K.

	$LiPtF_6$	**$NaPtF_6$**	**$KPtF_6$**	**$RbPtF_6$**
Space group	$R\bar{3}$	$R\bar{3}$	$R\bar{3}$	$R\bar{3}$
a **(Å)**	4.97492(11)	5.16973(7)	7.41013(13)	7.55677(11)
b **(Å)**	4.97492(11)	5.16973(7)	7.41013(13)	7.55677(11)
c **(Å)**	13.5916(3)	14.7717(2)	7.28292(15)	7.54000(12)
α (°)	90	90	90	90
β (°)	90	90	90	90
γ (°)	120	120	120	120
V **(Å^3)**	291.321(15)	341.898(10)	346.329(14)	372.884(13)
Z	3	3	3	3
F_w **(g mol^{-1})**	316.03	332.08	348.19	394.56
ρ_{calc} **(g cm^{-3})**	5.404	4.839	5.008	5.271
μ (mm^{-1})	19.636	16.782	16.977	20.585
R_1[a]	0.0192	0.0178	0.0183	0.0181
wR_2[b]	0.0462	0.0413	0.0427	0.0436
$\Delta\rho_{max}$, $\Delta\rho_{min}$ **(e Å^{-3})**	2.805, −3.112	3.295, −2.219	2.138, −3.421	2.573, −2.411

[a] $R_1 = \Sigma||F_o|-|F_c||/\Sigma|F_o|$; [b] $wR_2 = [\Sigma(w(F_o^2-F_c^2)^2)/\Sigma(w(F_o^2)^2)]^{1/2}$.

Table 4.4: Selected bond lengths (Å) and angles (°) in the crystal structures of $LiPtF_6$, $NaPtF_6$, $KPtF_6$, and $RbPtF_6$.

	$LiPtF_6$	**$NaPtF_6$**
Pt–F	6 × 1.8841(15)	6 × 1.8841(12)
A–F	6 × 2.0179(15)	6 × 2.2900(13)
cis **F–Pt–F**	6 × 89.78(7), 6 × 90.22(7)	6 × 89.52(6), 6 × 90.48(6)
trans **F–Pt–F**	3 × 180.0	3 × 180.0
	$KPtF_6$	$RbPtF_6$
Pt–F	6 × 1.8855(13)	6 × 1.8843(11)
A–F	6 × 2.8369(14), 6 × 2.9367(15)	6 × 2.9291(12), 6 × 3.0601(13)
cis **F–Pt–F**	6 × 88.07(7), 6 × 91.93(7)	6 × 88.61(6), 6 × 91.39(6)
trans **F–Pt–F**	3 × 180.0	3 × 180.0

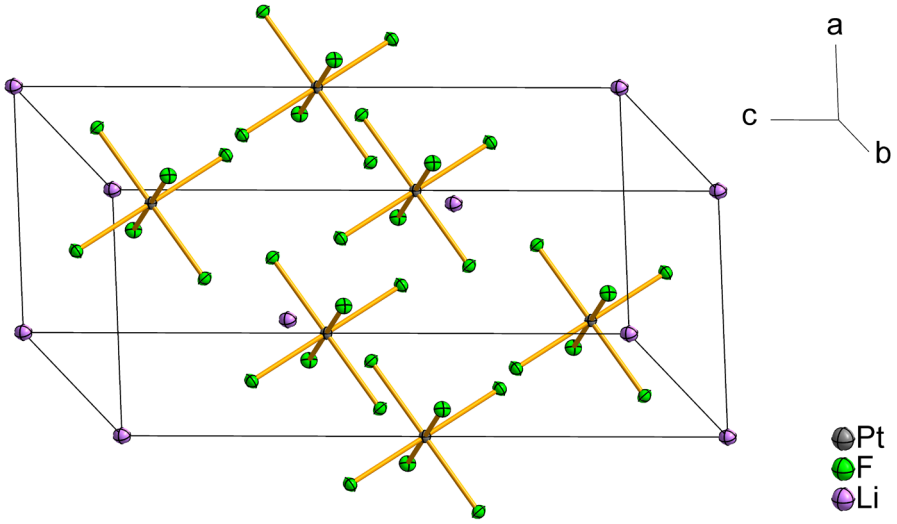


Figure 4.8: Section of the crystal structure of $LiPtF_6$. Li–F bonds have been omitted for clarity. Displacement ellipsoids are shown at the 50% probability level.

In the isotypic $LiPtF_6$ and $NaPtF_6$ structures (Figure 4.8), the alkali metal cations are coordinated by six fluorine atoms, forming a slightly distorted octahedral coordination. The Li–F distances are 2.0179(15) Å, notably shorter than the Na–F distances of 2.2900(13) Å. Each of the fluorine ligands is contributed by a different $[PtF_6]^-$ anion, resulting in the formation of a three-dimensional network, in which the Li^+/Na^+ cations and Pt adopt a NaCl-like face-centered cubic arrangement (Appendix Figure B.4). Pt–F bond lengths in both compounds are indistinguishable within standard uncertainties, measuring 1.8841(15) Å in $LiPtF_6$ and 1.8841(12) Å in $NaPtF_6$. The former corresponds well with the value previously obtained from synchrotron PXRD, where the Pt–F bond length in $LiPtF_6$ was reported to measure 1.887(6) Å at a temperature of 299 K [220]. The $[PtF_6]^-$ anions in both compounds deviate slightly from ideal octahedral geometry, as evidenced by small departures of the *cis*-F–Pt–F angles from 90° (Table 4.4).

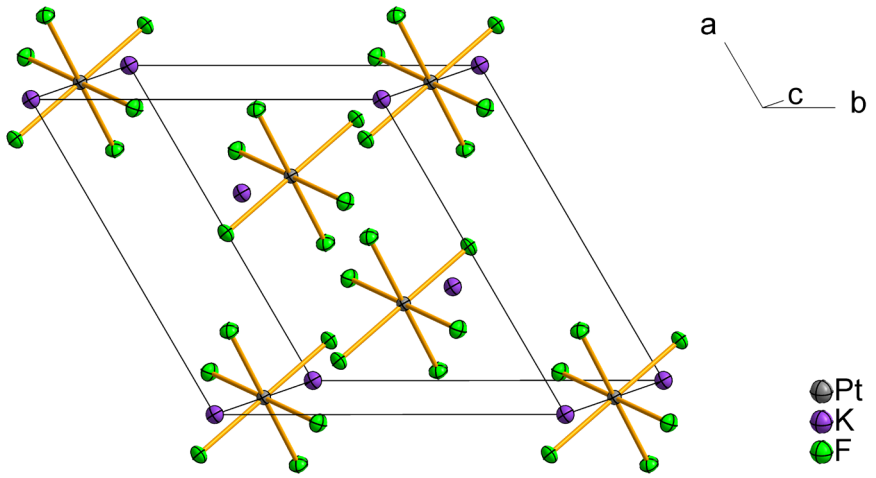


Figure 4.9: Section of the crystal structure of $KPtF_6$. K–F bonds have been omitted for clarity. Displacement ellipsoids are shown at the 50% probability level.

In the $KAsF_6$-type structures (Figure 4.9), the coordination sphere of K^+ and Rb^+ cations consist of 12 fluorine atoms, forming a slightly distorted cuboctahedron arrangement. The A–F interatomic distances are significantly longer than in the lighter analogues, measuring 2.8369(14)–2.9368(15) Å for $KPtF_6$ and 2.9291(12)–3.0601(13) Å for $RbPtF_6$. The twelve fluorine ligands derive from eight distinct $[PtF_6]^-$ anions, two interacting with the cation in a tridentate manner and six bind monodentately, arranged so that the Pt centers and alkali cations form a CsCl-like body-centered cubic lattice (Appendix Figure B.5). Pt–F bonds remain within 3σ of those observed in $LiPtF_6$ and $NaPtF_6$, measuring 1.8855(13) Å in $KPtF_6$, and 1.8843(11) Å in $RbPtF_6$. The *cis*-F–Pt–F angles show larger deviations from 90° than in the lighter relatives, spanning 88.07(7)–91.93(7)° in $KPtF_6$ and 88.61(6)–91.39(6) $RbPtF_6$, while the *trans*-F–Pt–F angles remain perfectly linear.

4.5.2.3 Raman spectroscopy

In the coordination chemistry of XeF_2, Raman spectroscopy provides a rapid and straightforward method for establishing the presence of XeF_2 bound to metal centers. Relative to the Raman spectrum of free XeF_2, whose intense symmetric Xe–F stretch is observed at 497 cm^{-1} [225], bands attributable to coordinated XeF_2 are typically blue-shifted to frequencies above 500 cm^{-1}. Their exact positions depend on the Lewis acidity of the metal cation and on whether XeF_2 acts as a terminal or bridging ligand. For weakly Lewis-acidic monovalent centers, the Raman bands associated with Xe–F stretching modes are generally observed in the 500–540 cm^{-1} range [204], [205], [216], whereas coordination to more strongly Lewis-acidic species, such as Mg^{2+} or Cu^{2+}, can shift these bands to beyond 575 cm^{-1} [226], [227]. The Raman spectrum of $[Li(XeF_2)_3][PtF_6]$ exhibits a very strong, slightly broadened band at 519 cm^{-1} (Figure 4.10), which is comparable to the Raman spectra of other $[Li(XeF_2)_n][MF_6]$ compounds [216]. By contrast, in the Raman spectrum of the $[Na(XeF_2)PtF_6]$, which features only bridging XeF_2 ligands, the intensity of the bands associated with Xe–F stretch are markedly weaker and present as four bands between 509 and 548 cm^{-1}. For $[K(XeF_2)_2PtF_6]$, the Xe–F stretch again appears as a strong band centered at 523 cm^{-1} with a shoulder at 527 cm^{-1}. Both of these frequencies are appreciably higher than observed in the Raman spectra of the related $[Ag(XeF_2)_2AsF_6]$ and $[Ag(XeF_2)_2PF_6]$, which show a doublet in the 500–510 cm^{-1} region [204], [205]. Additional characteristic features in the Raman spectra of $[A(XeF_2)_nPtF_6]$ compounds arise from octahedral modes ν_1, ν_2, and ν_5 of the $[PtF_6]^-$ anion. Owing to lowered symmetry and distinct coordination environments of the fluoride ligands, these modes are split and occur in the regions 630–660 cm^{-1} (ν_1), 570–590 cm^{-1} (ν_2), and 220–250 cm^{-1} (ν_5).

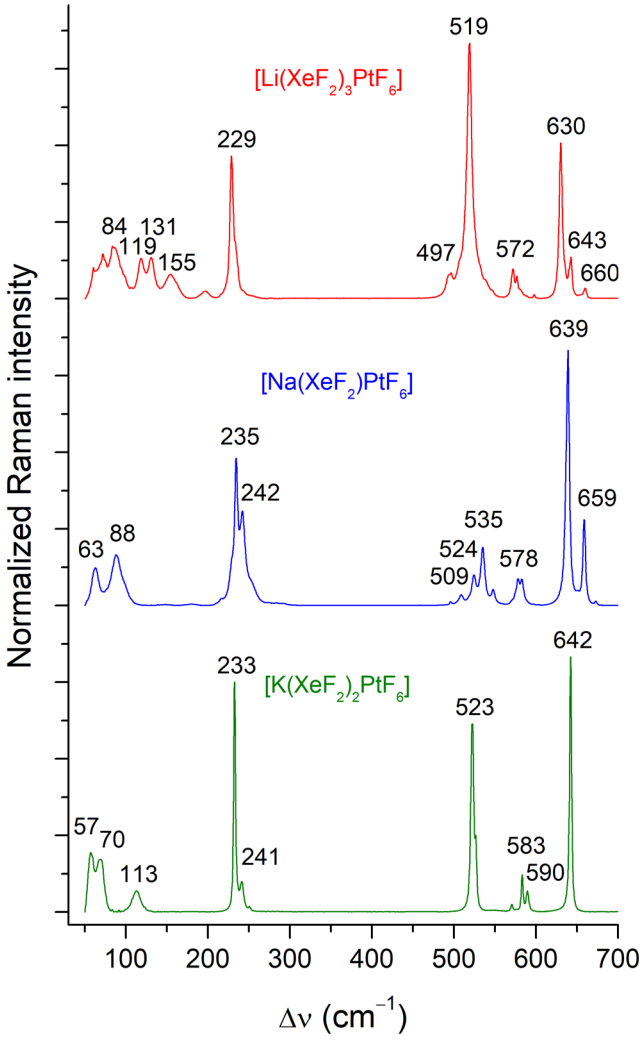


Figure 4.10: Low-temperature (100 K) Raman spectra of $[Li(XeF_2)_3PtF_6]$, $[Na(XeF_2)PtF_6]$, and $[K(XeF_2)_2PtF_6]$.

Raman spectra for $APtF_6$ (A = Li, Na, K, Rb) compounds, which have not been previously reported, are presented in Figure 4.11. The spectra clearly exhibit the three Raman-active modes of the octahedral $[PtF_6]^-$ anion, ν_1, ν_2, and ν_5, with the latter split for A = Li, K, and Rb, reflecting slight departures from ideal octahedral symmetry. The position of the ν_1 band decreases systematically with increasing alkali-metal atomic number, shifting from 652 cm^{-1} for Li^+ to 639 cm^{-1} for Rb^+. This trend extends to the previously characterized $CsPtF_6$, where ν_1 is observed at 636 cm^{-1} [163], and a similar behavior is observed for the alkali metal hexafluoridomolybdates(V) [228].

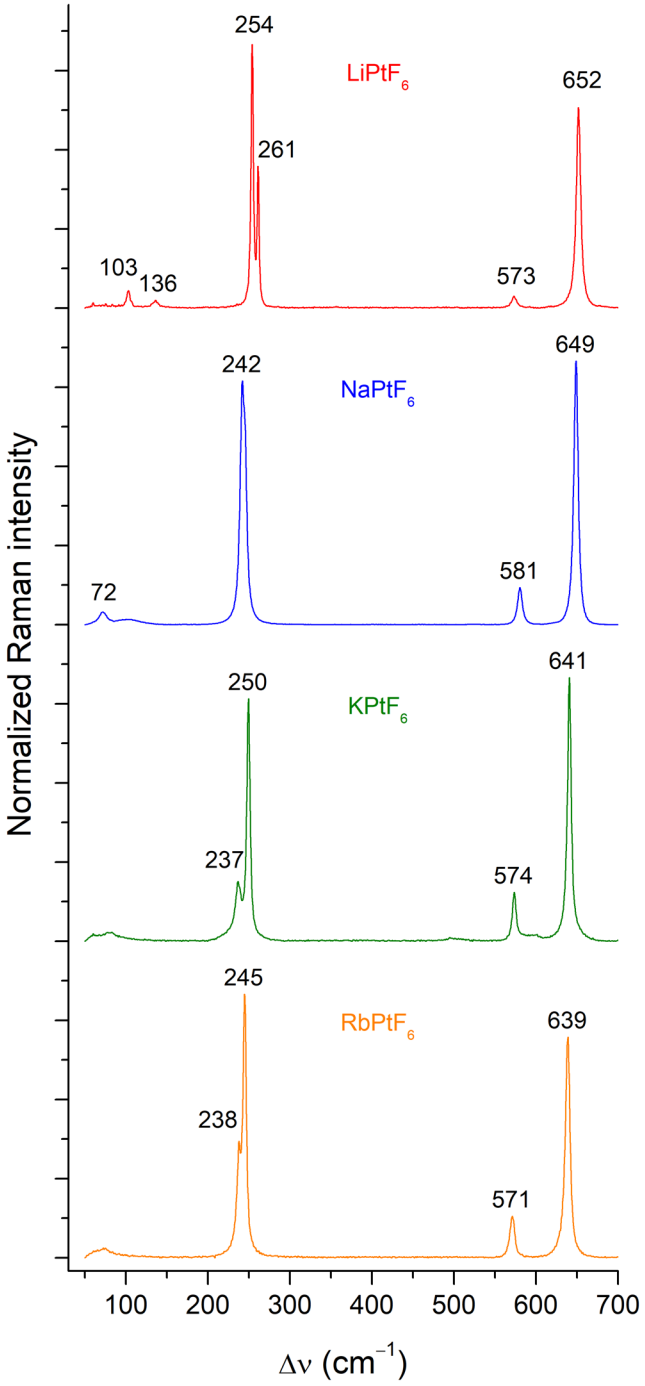


Figure 4.11: Ambient temperature Raman spectra of $LiPtF_6$, $NaPtF_6$, $KPtF_6$ and $RbPtF_6$.

4.5.3 Summary

In the present work, we reexamined the ability of XeF_2 to act as a ligand to alkali metal centers by reacting it with $APtF_6$ salts (A = Li, Na, K, Rb) in aHF solvent. Slow crystallization by solvent evaporation at ambient temperatures from the resulting orange-yellow solutions afforded single crystals for A = Li, Na, or K, and SCXRD analyses established the products as $[Li(XeF_2)_3PtF_6]$, $[Na(XeF_2)PtF_6]$, and $[K(XeF_2)_2PtF_6]$, respectively. These outcomes contrast with earlier attempts to synthesize XeF_2

coordination compounds from related AMF_6 salts (A = Li, Na, K, Rb, Cs; M = P, As, Ru, Ir), in which only Li^+ complexes were unambiguously identified and single crystals of $[Li(XeF_2)_3][AsF_6]$ could be obtained only by removing the solvent at −50 °C. The present results further highlight the decisive influence of anion selection on the stability of the compounds and on the range of alkali-metal cations that can be ligated by XeF_2. This series of compounds notably advances the coordination chemistry of XeF_2 by delivering the first example of XeF_2 bound to K^+ and the first monovalent metal center homoleptically coordinated by XeF_2 ligands, as observed in $[Li(XeF_2)_3PtF_6]$. Moreover, we determined the single-crystal structures of the parent $APtF_6$ salts (A = Li, Na, K, Rb), which had remained poorly characterized despite being reported more than 60 years ago. Their Raman spectra, presented here for the first time, should also aid the identification of these compounds in future studies.

4.5.4 Experimental

4.5.4.1 Synthesis and crystal growth of $[Li(XeF_2)_3PtF_6]$

230 mg (1.359 mmol) of XeF_2 were added to the main arm of a reactor, which also contained $LiPtF_6$, synthesized from 10 mg (0.386 mmol) of LiF and 75 mg (0.384 mmol) of Pt. 1.2 mL of aHF was added to the reactor, forming a orange-yellow solution with no visible precipitate. The solution was decanted into the side arm of the reactor, which was then placed in a cooling bath thermostat containing EtOH. In the course of the next 4 days, the temperature difference between the two arms was gradually increased from 8 to 43 °C, resulting in formation of yellow crystals. The product was isolated by removing the volatiles from the reactor while keeping the contents of the side arm cooled in an EtOH bath, maintained at temperatures below −25 °C.

4.5.4.2 Synthesis and crystal growth of $[Na(XeF_2)PtF_6]$

XeF_2 (125 mg, 0.738 mmol) was added to the main arm of a reactor that also contained $NaPtF_6$, prepared from NaF (9 mg, 0.214 mmol) and Pt (41 mg, 0.210 mmol). aHF (1.2 mL) was introduced, affording a bright orange-yellow solution with no visible precipitate. After 30 min of stirring, the solution was decanted into the side arm, and the reactor was placed in a cooling-bath thermostat. Over the next four days, the temperature differential between the two arms was gradually increased from 4 to 48 °C, after which a yellow-orange solid containing crystals of the title compounds remained in the side arm. The product was isolated by removing the volatiles from the reactor at temperatures below −25 °C.

4.5.4.3 Synthesis and crystal growth of $[K(XeF_2)_2PtF_6]$

To the main arm of a reactor, which also contained $KPtF_6$, synthesized from 9 mg (0.155 mmol) of KF and 30 mg (0.154 mmol) of Pt, 84 mg (0.496 mmol) of XeF_2 were added. 1 mL of aHF was condensed to the reactor, forming a vibrant orange-yellow solution with small amount of insoluble yellow precipitate. To attempt to dissolve the precipitate, the reaction mixture was stirred overnight, however, by the following morning approximately the same amount of yellow solid persisted, having consolidated into a single chunk. Stirring was then halted, and the clear supernatant was decanted into the side arm of the reactor, which was placed in a cooling-bath thermostat. When the temperature gradient between the two arms exceeded 18 °C, large cubic yellow crystals began to form. The product was isolated by removing the volatiles while maintaining the side arm at temperatures below −15 °C.

4.5.4.4 Attempted synthesis of $[Rb(XeF_2)_zPtF_6]$

80 mg (0.473 mmol) of XeF_2 were added to the reactor arm, which contained $RbPtF_6$, synthesized from 16 mg (0.153 mmol) of RbF and 30 mg (0.154 mmol) of Pt. 1.4 mL of aHF solvent was added to the reactor, forming a bright orange-yellow solution with insoluble yellow precipitate remaining at the bottom of the reactor, which persisted even after 24 hours of stirring. The clear yellow supernatant was decanted into the side arm of the reactor, which was then placed in on a cooling bath thermostat. As the temperature difference between the two arms was increased above 7 °C the formation of small yellow crystals was observed. The crystals were isolated by removing the volatiles from the reactor while keeping the contents of the side arm cooled at temperatures below −20 °C. SCXRD showed that the isolated crystals comprise a mixture of $RbPtF_6$ and $[Xe_2F_3][PtF_6] \cdot XeF_2$ [200].

4.6 Structural Investigations of the XeF_2–PtF_4 System Under Extreme Conditions

4.6.1 Background

The dogmatic assumption that noble gases cannot form true chemical compounds was decisively overturned by Neil Bartlett's famous experiment in which he reacted xenon with platinum hexafluoride to produce an orange–yellow solid. Its stoichiometry was established as $XePtF_6$, and the compound was tentatively formulated as $Xe^+PtF_6^-$ [29]. Notwithstanding the indisputable historical significance of this species, its chemical nature and structure remain enigmatic. In the final report on the Xe and PtF_6 interaction, Bartlett proposed that the initial product of the reaction likely contains platinum in the tetravalent state and can be formulated as a 1:1 adduct between XeF_2 and PtF_4 – $XeF_2 \cdot PtF_4$ [100]. This adduct, in turn, reacts with excess PtF_6 to yield platinum(V) compounds. Whereas the diffraction pattern of $[XeF][PtF_6]$ has been observed in various preparations of "$XePtF_6$", $XeF_2 \cdot PtF_4$ was always found to be amorphous, effectively precluding any detailed structural investigations [100], [197]. It has been postulated that the structure of this compound may contain motifs analogous to those observed in other XeF_2–MF_4 compounds and consist of $[PtF_6]$ octahedra connected into poly- or oligomeric species, with each $[PtF_6]$ unit featuring one coordinated XeF_2 molecule. A recent computational evaluation of the likely models for the structure of $XeF_2 \cdot PtF_4$ revealed that *cis*-bridging among the neighboring $[PtF_6]$ octahedra is preferred, thereby highlighting the polymeric *cis*-chain and tetrameric ring structures derived from the structures of $3XeF_2 \cdot 2MnF_4$ and $XeF_2 \cdot MnF_4$ [191], respectively, as likely candidates for the structure of $XeF_2 \cdot PtF_4$ [197].

In the present study, the behavior of $XeF_2 \cdot PtF_4$ under high-pressure and high-temperature conditions afforded by the use of laser-heated diamond anvil cells (LH-DAC) was investigated. High-pressure and high-temperature investigations on noble-gas fluorides have been limited in scope due to the inherent challenges associated with loading these highly moisture-sensitive and reactive compounds within the DAC and have thus far been focused solely on XeF_2, a commercially accessible compound [229], [230], [231], [232]. Laser heating of $XeF_2 \cdot PtF_4$ pressurized to 14.5 GPa resulted in its recrystallization and the compound was crystallographically characterized for the first time. Its structure was revealed to contain polymeric chains, a structural motif that is in close agreement with a previously proposed structural model, derived from the *cis*-chains observed in the structure of $3XeF_2 \cdot 2MnF_4$ [191], [197]. Additional experimental runs were conducted in which $XeF_2 \cdot PtF_4$ was laser-heated at lower pressures, ranging from 4.0 to 8.6 GPa, revealing additional crystalline phases with XeF_2:PtF_4 stoichiometries below 1:1. These phases include three polymorphs of $XeF_2 \cdot 2PtF_4$, two of which were previously unobserved, and a novel compound, $[PtF_2(XeF_2)_4][Pt_4F_{18}]$, hitherto unobserved under ambient conditions.

4.6.2 Results and discussion

The results reported herein stem from three independent experimental runs: two conducted in SSDAC80-type cells and one in a Merrill–Bassett type DAC. A table summarizing the results of all experimental runs is presented in the Appendix (Appendix Table B.7).

Recrystallization of $XeF_2 \cdot PtF_4$, loaded into a SSDAC80 cell closed at a pressure of 15.3 GPa, was accomplished by laser heating the amorphous powdered sample from both sides using a 1064 nm laser operated at a power of approximately 2.4 W. SCXRD data were collected with synchrotron radiation and processed using *DAFi* [190], revealing that the majority of observed reflections stemmed from different crystalline domains of $XeF_2 \cdot PtF_4$,

with a small number of reflections indexable to PtF_4 also found. Consistent with these observations, Raman spectra acquired across the sample chamber produced a map that identified a region whose spectrum could be tentatively assigned to $XeF_2 \cdot PtF_4$, and showed that following the laser heating the pressure in the cell decreased to 14.5 GPa. In addition to the starting amorphous $XeF_2 \cdot PtF_4$, Raman spectroscopy also identified regions assignable to $XeF_2 \cdot 2PtF_4$ by comparison with its ambient pressure spectrum [79], [197], as well as an additional unknown, amorphous phase, characterized by a broad band, centered at 144 cm^{-1} (Figure 4.12).

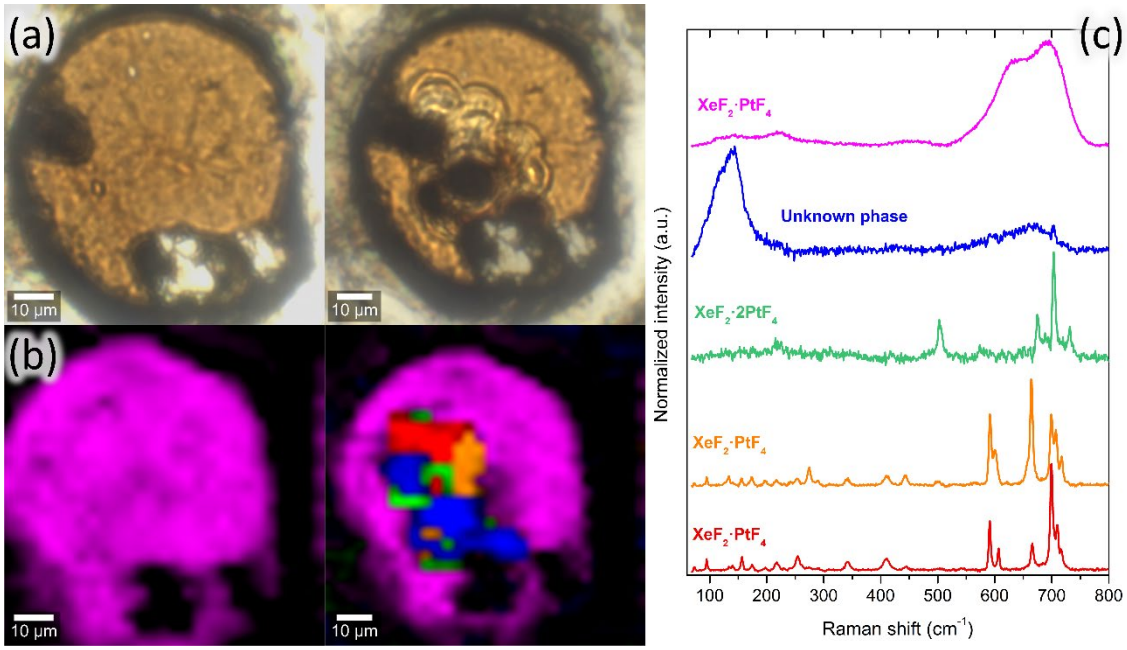


Figure 4.12: Raman analysis of the DAC loaded with $XeF_2 \cdot PtF_4$ following laser heating at 14.5 GPa. (a) View of the sample chamber prior to (left) and after (right) laser heating, (b) Raman map prior to (left) and after (right) laser heating, and (c) Raman spectra of the phases observed in the sample chamber.

Subsequently, the pressure in the cell was lowered to 10 GPa, and the sample was subjected to a second round of laser heating, which led to a further pressure decrease to 8.0 GPa. SCXRD data were collected at multiple positions across the sample chamber, again revealing only crystalline domains with unit-cell parameters matching $XeF_2 \cdot PtF_4$ and PtF_4. From these reflections, the crystal structure of $XeF_2 \cdot PtF_4$ could be solved, although the resulting model exhibited significantly poorer agreement factors and larger standard uncertainties than the structure determined at higher pressure (Appendix Table B.8).

In contrast, Raman mapping of the cell contents showed that the annular region surrounding the newly heated spot contained $XeF_2 \cdot 2PtF_4$, whereas the material at the center of the spot gave a spectrum similar to that of the starting amorphous $XeF_2 \cdot PtF_4$, but with additional broad features and a shoulder centered at 550 cm^{-1} (Figure 4.13). The latter is consistent with weakly bound XeF_2 in the structure and was assigned to $nXeF_2 \cdot PtF_4$ [197]. Raman signatures attributable to $XeF_2 \cdot PtF_4$ persisted at 8.0 GPa, although several bands became less well defined than in spectra collected at higher pressure.

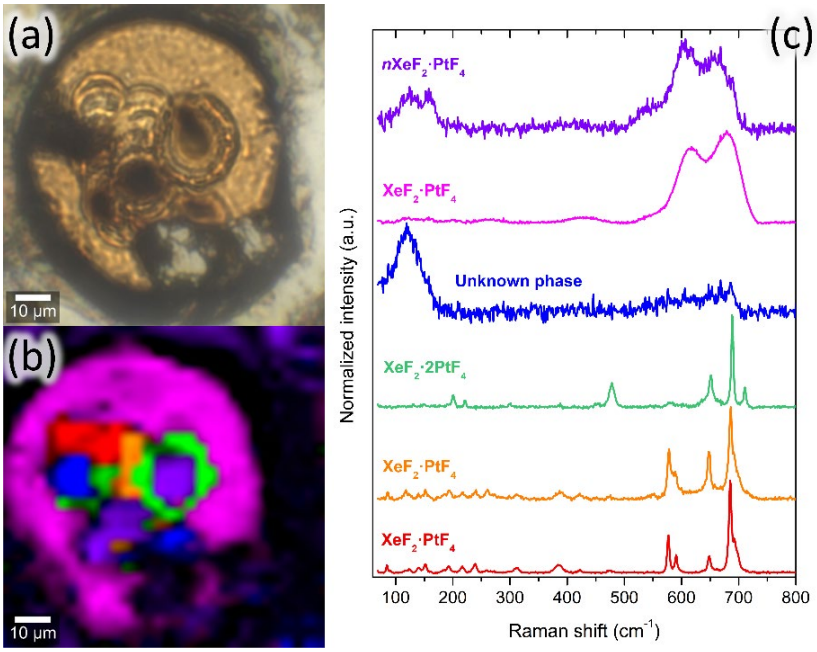


Figure 4.13: Raman analysis of the DAC loaded with $XeF_2 \cdot PtF_4$ following laser heating at 8.0 GPa. (a) View of the sample chamber, (b) Raman map, and (c) Raman spectra of the phases observed in the sample chamber.

Attempts to recover recrystallized $XeF_2 \cdot PtF_4$ by decompression to ambient pressure were unsuccessful: once the pressure dropped below 2 GPa, the material reverted to an amorphous state, as confirmed by Raman spectra showing pronounced peak broadening and convergence towards those recorded prior to laser heating (Figure 4.14).

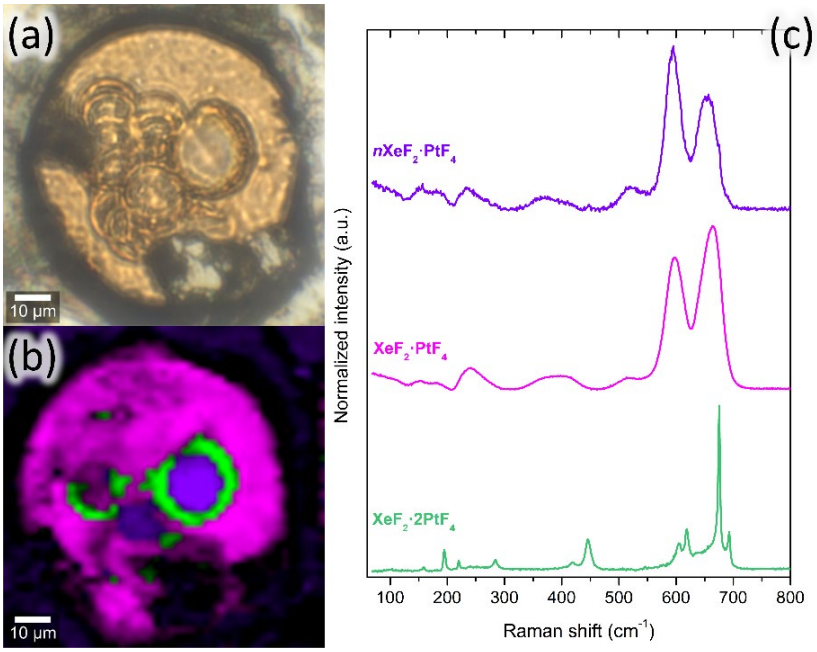


Figure 4.14: Raman analysis of the DAC loaded with $XeF_2 \cdot PtF_4$ following decompression to 2 GPa. (a) View of the sample chamber, (b) Raman map, and (c) Raman spectra of the phases observed in the sample chamber.

Further attempts to recrystallize $XeF_2 \cdot PtF_4$ at lower pressures yielded similar outcomes, with phase separation into XeF_2-rich and PtF_4-rich regions again observed. Raman mapping of compressed $XeF_2 \cdot PtF_4$ after double-sided laser heating to 2824/2740 K (temperatures at the two sides of the DAC, measured by pyrometry) at 4.0 GPa in a SSDAC80 cell, and to 3142/3141 K at 4.7 GPa in a Merrill-Bassett DAC, showed that the center of the heated spot contained $n XeF_2 \cdot PtF_4$ together with XeF_2, whereas the surrounding annular region comprised of $XeF_2 \cdot 2PtF_4$ (Figure 4.15, Figure 4.16). The presence of $XeF_2 \cdot 2PtF_4$ was corroborated by SCXRD measurements, which further revealed that at these pressures two polymorphs can be obtained: a monoclinic phase ($mP52$) corresponding to the ambient-pressure structure [197] and a new triclinic modification, ($aP26$)-I.

The Merrill-Bassett DAC containing $XeF_2 \cdot PtF_4$ was further compressed to about 9 GPa, and laser heated to 2793/3173 K, upon which the pressure in the cell decreased to 8.6 GPa. As before, $n XeF_2 \cdot PtF_4$ was detected at the center of the heated spot, whereas the surrounding region exhibited a complex Raman spectrum indicative of a phase mixture (Figure 4.16). Analysis of the diffraction data collected from this region revealed that this mixture contained crystallites of $XeF_2 \cdot PtF_4$, $[PtF_2(XeF_2)_4][Pt_4F_{18}]$, two polymorphic forms of $XeF_2 \cdot 2PtF_4$ [($mP52$) and ($aP26$)-II], and PtF_4.

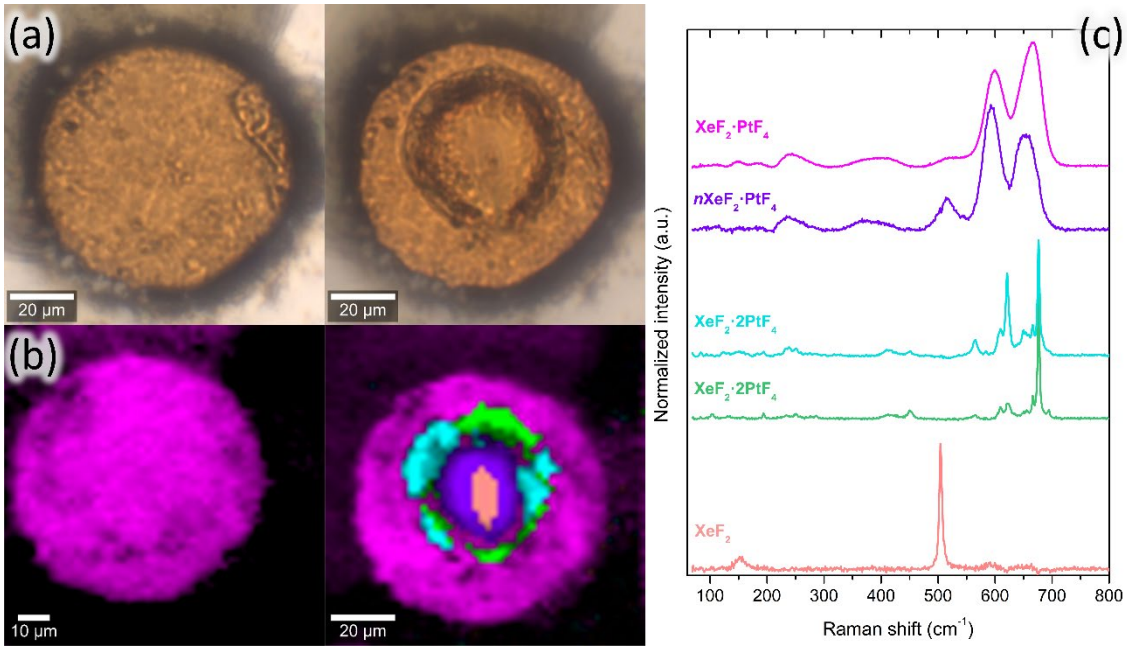


Figure 4.15 Raman analysis of the SSDAC80 cell loaded with $XeF_2 \cdot PtF_4$ following laser heating at 4.0 GPa. (a) View of the sample chamber prior to (left) and after (right) laser heating, (b) Raman map prior to (left) and after (right) laser heating, and (c) Raman spectra of the phases observed in the sample chamber.

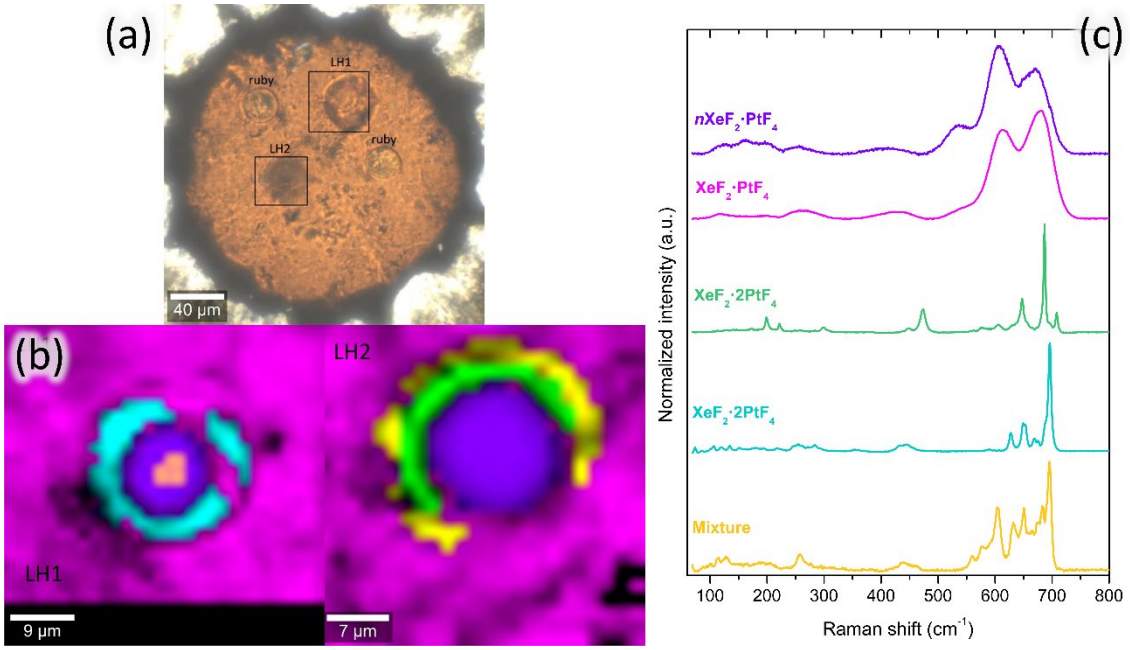


Figure 4.16 Raman analysis of the Merrill-Bassett cell loaded with $XeF_2 \cdot PtF_4$ following laser heating at 8.6 GPa. (a) View of the sample chamber after laser heating, (b) Raman map of the spot laser heated at 4.7 GPa (left) and at 8.6 GPa (right), and (c) Raman spectra of the phases observed in the sample chamber.

The results demonstrate that, to reliably recrystallize $XeF_2{\cdot}PtF_4$, the pressure in the cell must likely exceed 10 GPa. Below this threshold, $XeF_2 \cdot PtF_4$ decomposition and phase separation is favored, yielding amorphous XeF_2-rich regions (XeF_2, $n XeF_2{\cdot}PtF_4$) and crystalline PtF_4-rich phases (PtF_4, $XeF_2{\cdot}2PtF_4$, $[PtF_2(XeF_2)_4][Pt_4F_{18}]$). Although unit cell parameters consistent with ambient-pressure structure of PtF_4 [233] were frequently identified among the crystalline domains, attempts to solve its structure from high-pressure diffraction data produced only models with very high agreement factors ($R_1 > 15\%$) and are therefore not discussed in detail.

4.6.2.1 Crystal structure of $XeF_2 \cdot PtF_4$

The structure of $XeF_2 \cdot PtF_4$ was solved in the noncentrosymmetric monoclinic space group $P2_1$, with two formula units ($Z = 2$) per unit cell, and all atoms occupying general positions (Appendix Table B.9). The bond distances and angles discussed in this section originate from the structure determined at 14.5 GPa, which exhibits the best agreement parameters and more precise bond distances and angles than structures elucidated at lower pressures (Appendix Table B.8). The crystal structure comprises polymeric zigzag chains of *cis*-F-bridged $[PtF_6]$ units, each bearing a coordinated XeF_2 molecule, which alternate above and below the chain (Figure 4.17). The possibility that the structure of $XeF_2 \cdot PtF_4$ is polymeric has been noted previously, based in part on the observation of its low solubility in aHF [100].

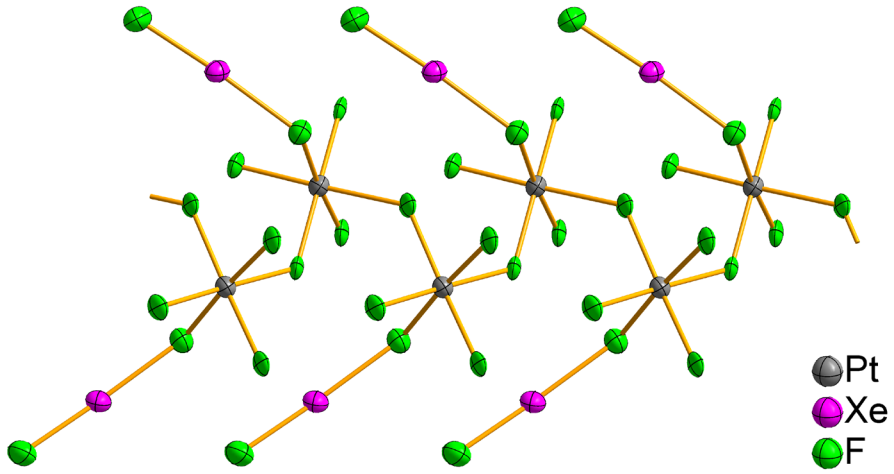


Figure 4.17: Section of the crystal structure of $XeF_2 \cdot PtF_4$ displaying the *cis*-bridged $^1_\infty[PtF_3F_{2/2}(XeF_2)]$ chains propagating along the *b* crystallographic axis. Thermal ellipsoids are set at the 50% probability level.

The chains run in parallel to the *b* crystallographic axis and can be described by the crystal coordination formula $^1_\infty[PtF_3F_{2/2}(XeF_2)]$. This structural motif closely resembles the likewise *cis*-bridged $^1_\infty[MnF_3F_{2/2}(XeF_2)]$ chains observed in the crystal structure of $3XeF_2 \cdot 2MnF_4$, which had previously been proposed as a model for the structure of $XeF_2 \cdot PtF_4$ [197] (Figure 4.18). The coordination environment around the Pt^{IV} center can be described as distorted octahedral, with the *cis*-F–Pt–F angles measuring between 81.2(9)° and 98.2(8)° (Table 4.5).

Table 4.5: Selected bond lengths (Å) and angles (°) in the crystal structures of $XeF_2 \cdot PtF_4$ and $[PtF_2(XeF_2)_4][Pt_4F_{18}]$ determined at 14.5 GPa and 8 GPa, respectively.

	$\mathbf{XeF_2 \cdot PtF_4}$	$\mathbf{[PtF_2(XeF_2)_4][Pt_4F_{18}]}$
Xe–F_t	1.95(3)	1.86(4), 1.87(3)
Xe–F_b	2.13(3)	2.26(2), 2.29(3)
Pt–F_b(Xe)	1.96(4)	1.962(13), 1.962(13)
Pt–F_b(Pt)	1.942(17), 2.01(3)	1.96(3)–2.05(4)
Pt–F_t	1.84(4)–1.88(2)	1.82(3)–1.89(3)
Pt–F–Pt	129.3(13)	122.1(10)–127.6(12)
F–Xe–F	174(2)	174.9(12), 177.0(18)
***cis* F–Pt–F**	81.2(9)°–98.2(8)°	86.4(11)–94.2(2)
***trans* F–Pt–F**	176.0(11)–177.5(15)	174.4(17)–180.0

The Pt–F_b linkages connecting the adjacent $[PtF_6]$ units measure 1.942(17) Å and 2.01(3) Å, whereas the terminal Pt–F_t bonds range between 1.84(4) Å and 1.88(2) Å, with another longer Pt–F_b(Xe) bond involving the XeF_2 ligand [1.96(4) Å]. All of these distances fall within three times the estimated standard deviation ("3σ rule") of those found for the

ambient-pressure structure of $XeF_2 \cdot 2PtF_4$ determined by 3D ED, where Pt–F_t = 1.863(7)–1.905(11) Å, Pt–F_b = 1.957(7)–2.032(7) Å, and Pt–F_b(Xe) = 1.932(8) Å [197]. The XeF_2 ligand coordinated to the Pt center exhibits an F–Xe–F angle of 174(2)°, with Xe–F_t and Xe–F_b bond lengths of 1.95(3) Å and 2.13(3) Å, respectively, and thus slightly deviates from the ideal $D_{\infty h}$ symmetry of free XeF_2 [Xe–F bond length of 1.999(4) Å] [39]. The observed distances suggest an intermediate degree of XeF_2 ionization, although the relatively large standard uncertainties associated with these bond lengths preclude a more precise assignment along the XeF_2 ionization pathway. In the ambient-pressure structures of the related $3XeF_2 \cdot 2MnF_4$, $XeF_2 \cdot MnF_4$, and $XeF_2 \cdot CrF_4$ compounds [108], [191], Xe–F_t bonds range from 1.906(3) Å to 1.93(2) Å and Xe–F_b bond span from 2.13(2) Å to 2.180(3) Å. By contrast, in $XeF_2 \cdot 2MF_4$ (M = Mn, Pd, Pt) compounds the bound XeF_2 molecule is substantially more ionized, with Xe–F_t bonds shorter than 1.9 Å and Xe–F_b bonds longer than 2.25 Å are observed [191], [197].

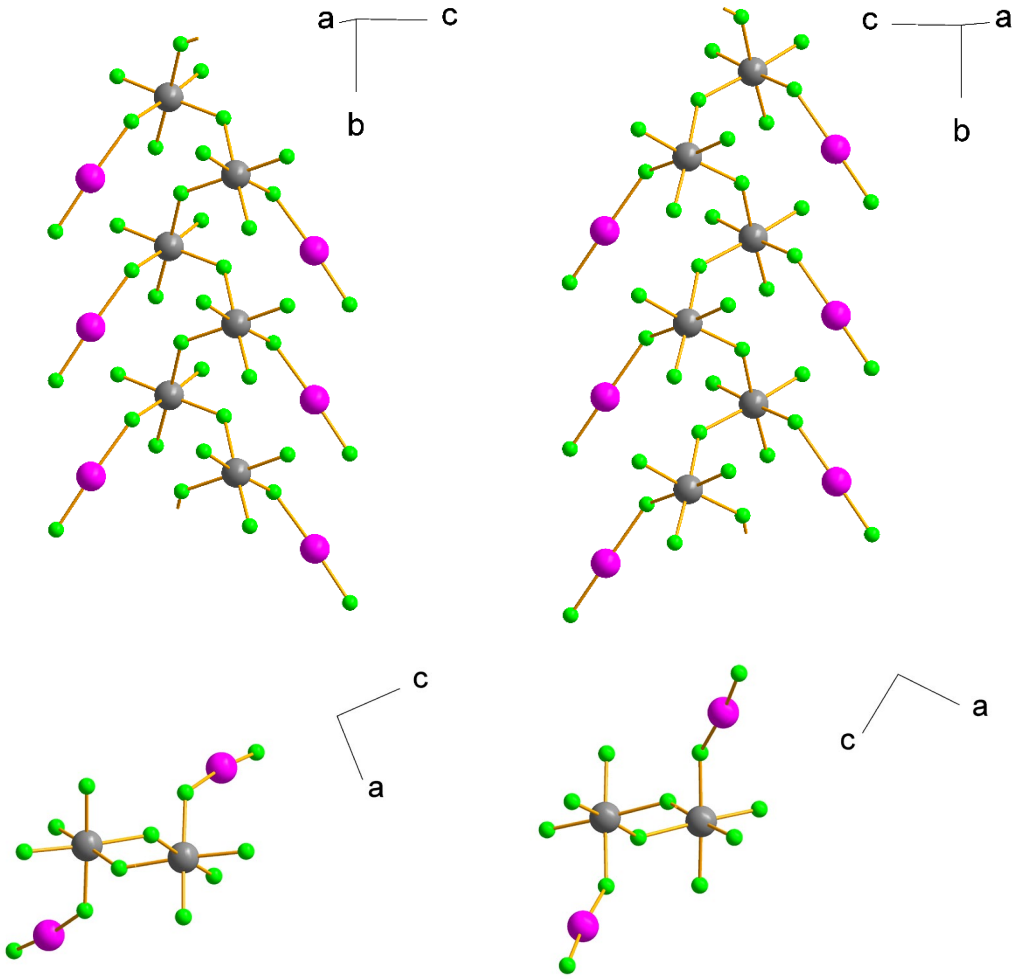


Figure 4.18: Comparison of the *cis*-bridged chains in the high-pressure structure of $XeF_2 \cdot PtF_4$ (left) and the previously proposed structural model for $XeF_2 \cdot PtF_4$, derived from $3XeF_2 \cdot 2MnF_4$ (right) [197] , viewed perpendicular to (top) and along the direction of the *b* crystallographic axis (bottom).

As a consequence of compression, the second coordination sphere of Xe exhibits several short, nonbonded Xe$\cdot\cdot\cdot$F contacts at distances markedly shorter than those typically observed for related compounds at ambient conditions. In total, eleven Xe$\cdot\cdot\cdot$F interactions lie below the sum of the van der Waals radii for Xe and F (3.74 Å) [234], [235],

measuring between 2.60(4) Å and 3.23(2) Å (Appendix Table B.10). For comparison, the ambient-pressure structure of $XeF_2 \cdot 2PtF_4$ displays nine such contacts, ranging from 3.019(10) Å to 3.637(9) Å [197].

4.6.2.2 Crystal structure of $[PtF_2(XeF_2)_4][Pt_4F_{18}]$

In contrast to $XeF_2 \cdot PtF_4$ and $XeF_2 \cdot 2PtF_4$, which are phases that had previously been prepared and, in the case of $XeF_2 \cdot 2PtF_4$, even structurally characterized [197], the existence of $[PtF_2(XeF_2)_4][Pt_4F_{18}]$ had not been observed in the earlier investigations of the XeF_2–PtF_4 system at ambient pressure. $[PtF_2(XeF_2)_4][Pt_4F_{18}]$ exhibits a XeF_2:PtF_4 stoichiometric ratio of 4:5, suggesting that it arises as a product of the heating-induced decomposition of $XeF_2 \cdot PtF_4$, forming as one of the phases within the XeF_2-depleated region. The crystal structure of this salt was determined at a pressure of 8.6 GPa, and it crystallizes in the triclinic $P\bar{1}$ space group (Appendix Table B.11). Its structure consists of well-separated double chain-like $[Pt_4F_{18}]^{2-}$ anions and mononuclear $[PtF_2(XeF_2)_4]^{2+}$ cations (Figure 4.19).

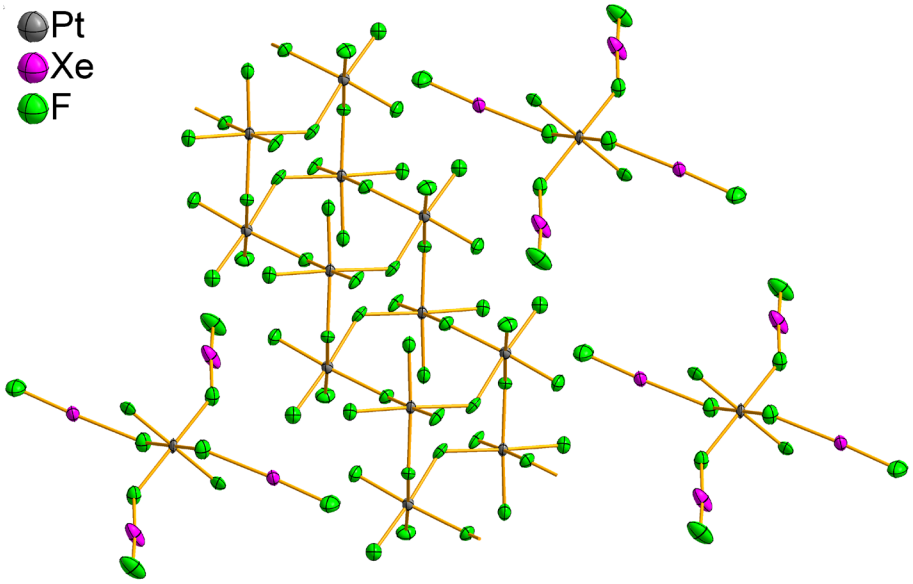


Figure 4.19: Crystal structure of $[PtF_2(XeF_2)_4][Pt_4F_{18}]$ displaying the corrugated ladder-like $[Pt_4F_{18}]^{2-}$anion and the mononuclear *trans*-$[PtF_2(XeF_2)_4]^{2+}$ cations. All atoms were refined anisotropically and are drawn as ellipsoids set at the 50% probability level.

The polymeric anion is constructed from $[PtF_6]$ octahedra linked to neighboring units via three adjacent fluoride vertices, with the remaining three terminal F ligands arranged in a *fac* configuration. This connectivity generates a corrugated ladder motif, analogous to that observed in the crystal structures of $XeF_2 \cdot 2MF_4$-type compounds (M = Mn, Pd, Pt). The fluorine coordination around the Pt centers can be described as distorted octahedral, with *cis*-F–Pt–F angles of 86.4(11)–94.2(2)°. The bridging Pt–F_b bonds measure 1.96(3)–2.05(4) Å, whereas terminal Pt–F_t bonds span 1.82(3)–1.99(4) Å (Table 4.5).

Within the voids formed between adjacent fluoridoplatinate(IV) double chain anions, the charge-balancing $[PtF_2(XeF_2)_4]^{2+}$ cations are accommodated, with the central Pt atom lying on an inversion center (Appendix Table B.12). These mononuclear cations arise from octahedrally coordinated Pt^{IV} centers bearing four XeF_2 ligands arranged in the equatorial positions and two terminal F ligands located at apical positions (Figure 4.20). Related adduct cations, formed by coordination of XeF_2 to a mononuclear fluoridometal(IV) center,

have only recently been structurally characterized as *fac*-$[MF_3(XeF_2)_3]^+$ and isolated as $[Xe_2F_3][MF_3(XeF_2)_3][AsF_6]_2$ salts (M = Pd, Pt) [199]. Together with the $[PtF_2(XeF_2)_4]^{2+}$ cation reported here, these species constitute the only known members of a new family of cationic XeF_2 coordination complexes in which the metal center is ligated by both XeF_2 and fluoride ligands. The Pt–F_t bond lengths involving the terminal F ligands measure 1.88(4) Å and the Pt–F_b(Xe) bonds measure 1.96(3) Å and 1.962(13) Å. Interestingly, the bound XeF_2 molecules exhibit a pronouncedly distorted geometry, consistent with sizeable ionization along the $XeF_2 \rightarrow [XeF]^+ + F^-$ pathway [84]. The Xe–F_b bonds are elongated to 2.26(2) Å and 2.29(3) Å, with the contracted Xe–F_t bonds measuring 1.86(4) Å and 1.87(3) Å.

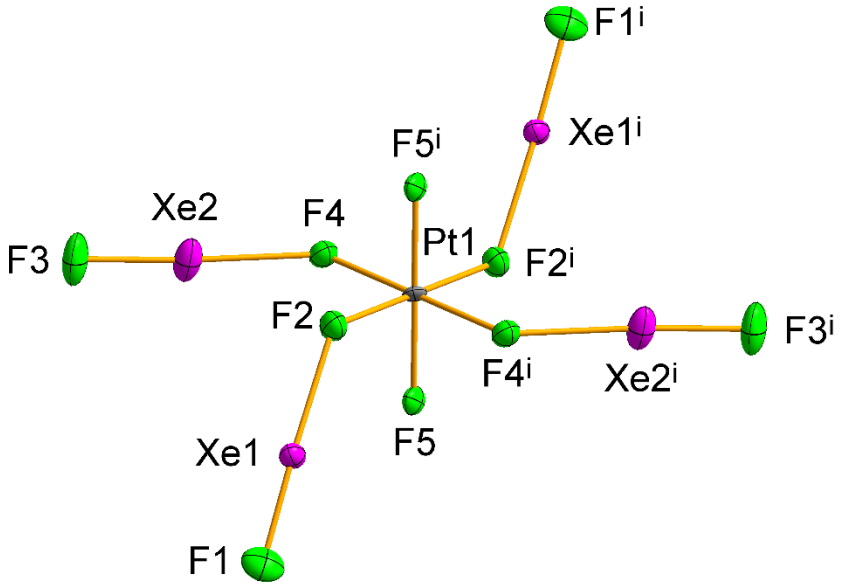


Figure 4.20: The adduct cation $[PtF_2(XeF_2)_4]^{2+}$. Thermal ellipsoids are set at the 50% probability level. Symmetry code used for generation of equivalent atoms: (i) $-x+1$, $-y+2$, $-z+1$.

Analogous to the observations in $XeF_2 \cdot PtF_4$, the second coordination sphere of the Xe atoms features several Xe · · · F contacts, shorter than those typically observed in related XeF_2-derived structures at ambient pressure. For the Xe1 atom, these contacts span 2.70(4)–3.61(4) Å, whereas for Xe2 they range from 2.701(15) to 3.611(18) Å (Appendix Table B.13).

4.6.2.3 High-pressure polymorphism of $XeF_2 \cdot 2PtF_4$

Following laser heating of pressurized $XeF_2 \cdot PtF_4$ samples, formation of $XeF_2 \cdot 2PtF_4$ was observed in all experiments. At 14.5 GPa, only minor amounts of this phase were produced, detectable solely by Raman spectroscopy, with no corresponding unit cells identified in the single-crystal data. At lower pressures, however, most of the crystalline domains could be assigned to various polymorphs of $XeF_2 \cdot 2PtF_4$, and its formation at the periphery of the laser-heated spots was clearly evident in the Raman maps. The monoclinic polymorph, $XeF_2 \cdot 2PtF_4$(*mP*52), matching the ambient pressure structure elucidated by 3D ED, was identified at 4.0, 4.7, and 8.6 GPa. Increasing pressure leads to a substantial reduction in the unit cell volume, which contracts from 799.5(9) $Å^3$ at ambient pressure to 656.43(10) $Å^3$ at 8 GPa (Appendix Table B.14, Appendix Table B.15). Comparison of the bond

distances in the high-pressure structures with those of the ambient-pressure phase shows that most bond lengths lie within 3σ of the ambient-pressure values, and no clear systematic trends can therefore be discerned (Appendix Table B.16). By contrast, examination of the Pt–F–Pt and F–Xe–F angles reveals that these become more acute with increasing pressure, enabling a more compact packing of the chains within the contracted unit cell.

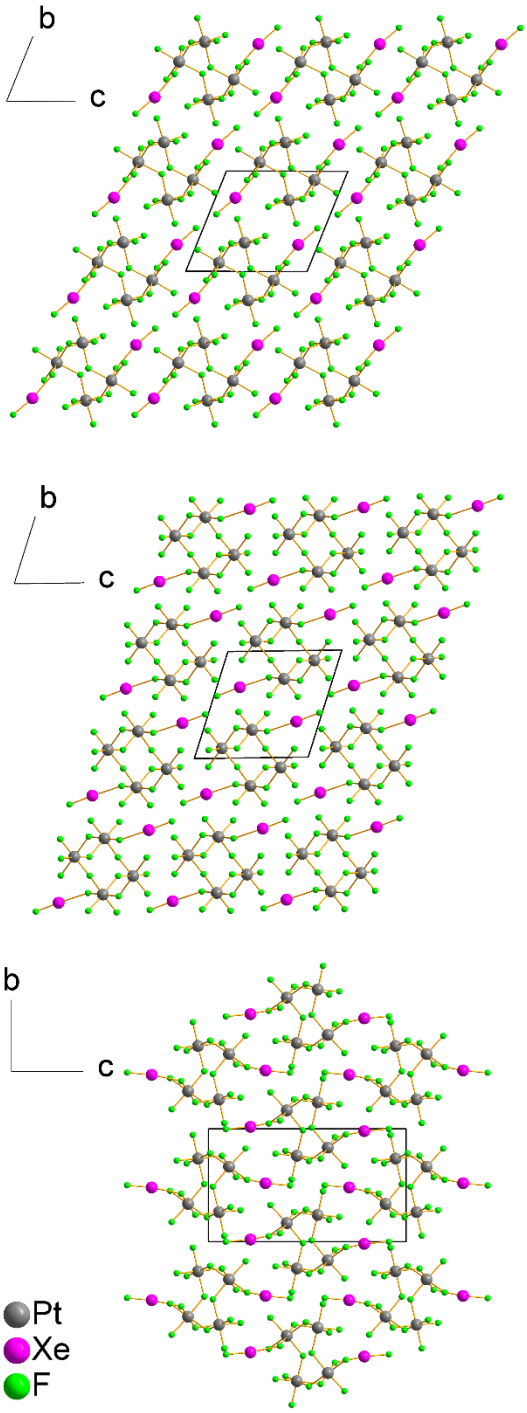


Figure 4.21: Comparison of crystal packing in $XeF_2 \cdot 2PtF_4$($aP26$)-I (top), $XeF_2 \cdot 2PtF_4$($aP26$)-II (middle), and $XeF_2 \cdot 2PtF_4$($mP52$) (bottom).

Additionally, SCXRD analysis revealed the existence of two triclinic polymorphs of $XeF_2 \cdot 2PtF_4$ present at 4.0 and 8.6 GPa. The former, labelled $XeF_2 \cdot 2PtF_4(aP26)$-I, crystallizes in the $P\bar{1}$ space group with lattice parameters of a = 5.3010(11) Å, b = 8.3438(9) Å, c = 9.4937(18) Å, α = 65.851(14)°, β = 74.318(17)°, γ = 77.911(13)°, and V = 366.56(12) Å^3 (Appendix Table B.17). The modification observed at higher pressure, $XeF_2 \cdot 2PtF_4(aP26)$-II, also possesses $P\bar{1}$ space group symmetry with unit cell parameters a = 4.7094(9) Å, b = 8.5969(15) Å, c = 8.7976(18) Å, α = 70.081(17)°, β = 77.060(17)°, γ = 79.315(16)°, V = 324.05(12) Å^3, and all atoms located on general positions (Appendix Table B.18). Both polymorphs share the corrugated, ladder-like double-chain motif of the monoclinic modification, with the chains, as in the monoclinic structure, propagating along the a-crystallographic axis (Figure 4.21).

As in the high-pressure structures of $XeF_2 \cdot 2PtF_4(mP52)$, the relatively large standard uncertainties associated with bond lengths and angles preclude identification of any clear pressure dependence, with even the Pt–F–Pt angles spanning a similar range of values (Appendix Table B.19). Despite these similarities, and the fact that both phases crystallize in closely related unit cells, the $^1_\infty[\langle PtF_2F_{3/1+1}(XeF_2)\rangle\langle PtF_3F_{3/1+1}\rangle]$ chains present in the two structures exhibit substantial differences in their conformations (Figure 4.22).

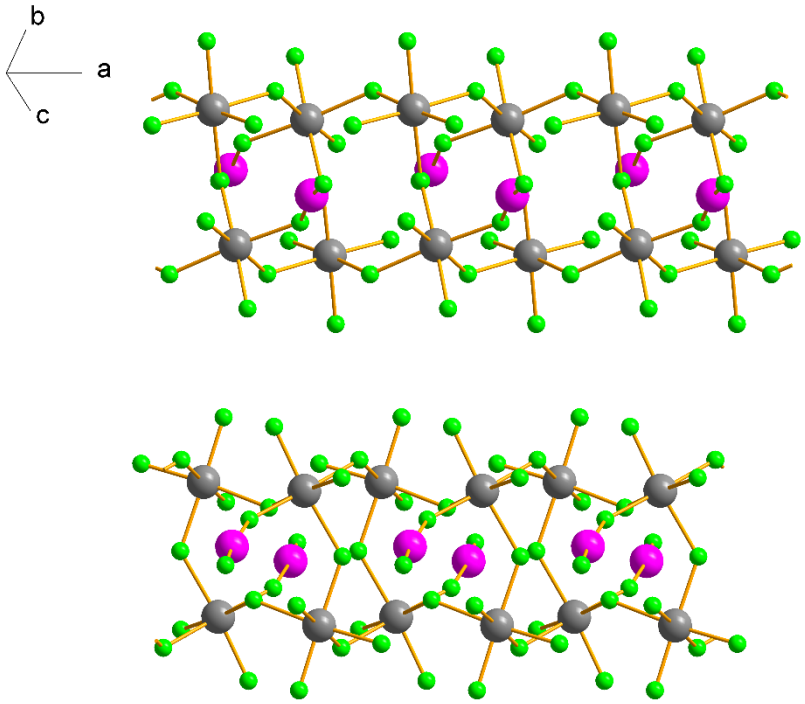


Figure 4.22: View of the double chains in $XeF_2 \cdot 2PtF_4(aP26)$-I (top) and $XeF_2 \cdot 2PtF_4(aP26)$-II (bottom) along [−111] direction, highlighting the differences in chain architecture.

4.6.3 Summary

The work presented in this chapter focused on investigating the behavior of the first noble-gas compound, $XeF_2 \cdot PtF_4$, which has thus far eluded complete structural characterization, under high-pressure and high-temperature conditions by the use of LH-DACs. Laser heating of a $XeF_2 \cdot PtF_4$ sample compressed to the highest pressure examined in this work

(14.5 GPa) led predominantly to its recrystallization, and its crystal structure was subsequently elucidated by synchrotron-based SCXRD. Determination of the high-pressure structure of $XeF_2 \cdot PtF_4$ finally provides direct structural insight into one of the most important chemical species discovered over the past century. At 8.6 GPa, a previously unobserved compound, $[PtF_2(XeF_2)_4][Pt_4F_{18}]$, was also identified, representing a rare example of a salt containing a mononuclear XeF_2 adduct cation. Collectively, these findings underscore the considerable potential of the largely unexplored noble-gas chemistry under extreme conditions to access new compounds that are not attainable at ambient pressure, as well as to facilitate recrystallization of otherwise amorphous phases. Of particular interest is also the unidentified phase detected at 14.5 GPa in the laser-heated DAC, characterized by a broad Raman band centered at 144 cm^{-1}. Notably, at ambient conditions, vibrational features in a similar Raman-shift range are associated with fascinating species containing xenon–xenon (Xe–Xe stretch of the Xe_2^+ cation at 123 cm^{-1}) [236] or xenon–metal bonds (Au–Xe stretches between 121 and 153 cm^{-1}) [237], [238]. Further exploration of $XeF_2 \cdot PtF_4$ at even higher pressures, as well as systematic studies of related XeF_2 complexes, therefore holds substantial promise for uncovering additional unprecedented species and deepening our understanding of noble-gas chemistry in general.

Chapter 5

Conclusions

The results presented in this thesis significantly advance our understanding of the chemistry of XeF_2–MF_4 systems. By reinvestigating the XeF_2–MnF_4 system, three compounds, namely $3XeF_2 \cdot 2MnF_4$, $XeF_2 \cdot MnF_4$, and $XeF_2 \cdot 2MnF_4$, were comprehensively characterized by means of SCXRD, 3D ED, vibrational spectroscopy and periodic DFT calculations. To enable the study of these highly air-sensitive compounds by 3D ED, a novel sample-transfer method was developed, ensuring that the samples could be introduced into the TEM without loss of crystallinity. There, the compounds proved sufficiently beam-stable for crystal structure determination by 3D ED, and the resulting structures showed good agreement with results derived from SCXRD. The structures of $3XeF_2 \cdot 2MnF_4$ and $XeF_2 \cdot 2MnF_4$ were shown to contain polymeric chains or double-chains composed of $[MnF_6]$ octahedra, with the former also containing cocrystallized XeF_2 molecules. In contrast, the structure of $XeF_2 \cdot MnF_4$ comprises discrete tetrameric rings, closely related to ring motifs encountered in the crystal structures of certain transition-metal pentafluorides. Across this series, a progressive increase in Lewis acidity of the fluoridomanganate(IV) backbone with the increase of the XeF_2:MnF_4 ratio is observed, culminating in $XeF_2 \cdot 2MnF_4$ where ionization of XeF_2 is sufficient to justify a tight-ion pair salt formulation, $[XeF][Mn_2F_9]$. The degree of XeF_2 ionization is supported by diffraction-derived bond lengths, the progressive blue shift of Xe–F_t stretching modes in Raman spectra, and periodic DFT results showing increasingly positive Bader charges on Xe and on the coordinated XeF_2 units.

The XeF_2–PtF_4 and XeF_2–PdF_4 systems were also re-examined. 3D ED enabled crystallographic characterization of the previously known phases $XeF_2 \cdot 2PtF_4$ and $XeF_2 \cdot 2PdF_4$, which were found to be isostructural with $XeF_2 \cdot 2MnF_4$. Their structures likewise comprise corrugated ladder-like double chains and exhibit pronounced polarization of the coordinated XeF_2 moieties. By probing the interaction of XeF_2 with Pt in aHF, orange-colored solid $n XeF_2 \cdot PtF_4$ ($1 < n < 1.6$) was isolated, which yields $XeF_2 \cdot PtF_4$ upon pyrolysis at 100 °C. Owing to the amorphous nature of these materials, their characterization relied solely on vibrational spectroscopy, which produced only broad spectral features and suggested the presence of weakly bound XeF_2 in the structure of $n XeF_2 \cdot PtF_4$. To obtain further insight into plausible structural motifs for $XeF_2 \cdot PtF_4$, periodic DFT calculations were used to evaluate the relative stabilities of candidate structure types derived from experimentally established analogues. These calculations indicated a clear preference for *cis*-bridging between adjacent $[PtF_6]$ units, reinforcing the close structural parallels between the XeF_2–PtF_4 and XeF_2–MnF_4 systems.

Reacting XeF_2 with MF_4 and AsF_5 in aHF solutions afforded the double salts $[Xe_2F_3][MF_3(XeF_2)_3][AsF_6]_2$ (M = Pd, Pt), which contain discrete $[MF_3(XeF_2)_3]^+$ cations and were characterized by low-temperature SCXRD and vibrational spectroscopy. Gas-phase quantum-chemical calculations of the adduct cations reproduce the experimentally

observed bond lengths and vibrational frequencies well, and indicate that their bonding can be rationalized in terms of a regium-bonding interaction between the $[MF_3]^+$ fragment and XeF_2. These adduct cations constitute the first examples of a new family of XeF_2 coordination compounds in which XeF_2 ligates a fluoridometal cation rather than a naked metal center, thereby motivating further exploration of the coordination chemistry of noble-gas fluorides.

Reinvestigation of the XeF_2–PtF_5 system led to the isolation of a new compound, $[Xe_2F_3][PtF_6] \cdot XeF_2$, which was found to occur in two polymorphic forms, orthorhombic and monoclinic, as well as $[Xe_2F_3][PtF_6]$ and two monoclinic modifications of $[XeF][PtF_6]$. In both $[Xe_2F_3][PtF_6] \cdot XeF_2$ and $[XeF][PtF_6]$, polymorph selectivity appears to depend on the synthetic conditions employed. The compounds $[Xe_2F_3][PtF_6] \cdot XeF_2(mC120)$, $[Xe_2F_3][PtF_6] \cdot XeF_2(oP120)$, $[Xe_2F_3][PtF_6]$, and $[XeF][PtF_6](mP108)$ were structurally characterized by SCXRD and LT-Raman spectroscopy, providing the first crystal structures from the XeF_2–PtF_5 family and thereby notably expanding the set of structurally elucidated phases in XeF_2–AF_5 systems.

The ability of XeF_2 to act as a ligand to alkali metal cations was also reexplored by reacting alkali metal hexafluoridoplatinates(V) with excess XeF_2 in aHF. This approach enabled the preparation of XeF_2 coordination complexes of Li^+, Na^+, and K^+, as the compounds $[Li(XeF_2)_3PtF_6]$, $[Na(XeF_2)PtF_6]$, and $[K(XeF_2)_2PtF_6]$ were characterized by SCXRD and Raman spectroscopy. The potassium complex provides the first example of XeF_2 coordination to K^+, whereas $[Li(XeF_2)_3PtF_6]$ represents the first instance of homoleptic coordination by XeF_2 ligands around a monovalent metal center. In addition, the crystal structures of $APtF_6$ (A = Li, Na, K, Rb) were determined from single-crystal data, and their Raman spectra were reported for the first time.

The LH-DAC technique was used to investigate the behavior of $XeF_2 \cdot PtF_4$ under high-pressure and high-temperature conditions. At 14.5 GPa, $XeF_2 \cdot PtF_4$ crystallized upon laser heating, enabling its structure to be determined by synchrotron-based SCXRD. This provided, for the first time, a crystal structure of the first noble-gas compound, revealing that under such conditions its structure consists of polymeric zigzag *cis*-bridged chains that closely resemble the motif proposed from the XeF_2-defficient structure of $3XeF_2 \cdot 2MnF_4$. Crystalline $XeF_2 \cdot PtF_4$ could also be observed at 8 GPa, however, upon further decompression to 2 GPa the material amorphized, yielding a Raman spectrum indistinguishable from that of the sample prior to laser heating. Laser-heating experiments conducted at lower pressures instead resulted in decomposition and phase separation into XeF_2-rich and PtF_4-rich regions around the heated spots. The crystalline products identified under these conditions include two previously unreported polymorphs of $XeF_2 \cdot 2PtF_4$ as well as a new compound, $[PtF_2(XeF_2)_4][Pt_4F_{18}]$, which provides a further example of XeF_2 coordination to a mononuclear fluoridoplatinum(IV) cation.

Importantly, several findings of this work extend beyond the realm of XeF_2–MF_4 chemistry. The methodology developed in order to securely transfer the moisture-sensitive noble-gas compounds into a TEM for structural characterization by 3D ED is also applicable to the handling of other reactive or unstable samples. This should facilitate the use of 3D ED for the structural study of air-sensitive compounds, including other species of fundamental interest as well as functional materials such as battery components or magnetic materials, where accurate structural models are paramount for the comprehensive understanding of their properties. The LH-DAC investigations of $XeF_2 \cdot PtF_4$ likewise underscore the considerable potential of high-pressure–high-temperature approaches, both for extracting structural information from previously poorly characterized materials and for accessing new phases with compositions not observed under ambient conditions. Further application of such methods to noble-gas chemistry appears particularly promising, as this area remains largely unexplored and therefore offers substantial potential for new findings.

Appendix A

Supporting Information to the Publications Included in this Thesis

A.1 Reactive Noble-Gas Compounds Explored by 3D Electron Diffraction: XeF_2–MnF_4 Adducts and a Facile Sample Handling Procedure

Supporting information file, consisting of detailed descriptions of experimental and computational procedures, PXRD data, additional crystallographic data and figures, IR spectra of the compounds, visualizations of the calculated vibrational modes, and the coordinates of DFT-optimized crystal structures, is accessible online:

https://pubs.acs.org/doi/suppl/10.1021/acscentsci.4c00815/suppl_file/oc4c00815_si_001.pdf

Crystallographic information files for $3XeF_2 \cdot 2MnF_4$, $XeF_2 \cdot MnF_4$, and $XeF_2 \cdot 2MnF_4$, determined by both 3D ED and SCXRD can be obtained free of charge via the joint Cambridge Crystallographic Data Centre (CCDC) and Fachinformationszentrum Karlsruhe Access Structures service (http://www.ccdc.cam.ac.uk/structures) by quoting the deposition numbers CSD 2368882–2368887.

A.2 Crystal Structures of $XeF_2 \cdot 2PtF_4$ and $XeF_2 \cdot 2PdF_4$ Determined by 3D Electron Diffraction and Structural Models of $XePtF_6$

Supporting information file containing PXRD data and Rietveld refinement results, tabulated Raman data, additional crystallographic data and figures displaying crystal packing and nonbonded Xe · · · F contacts, comparison of the experimental and DFT-calculated structural parameters, ATR-IR spectra, and the coordinates of the DFT-calculated structures is accessible online:

https://pubs.acs.org/doi/suppl/10.1021/acs.inorgchem.5c01740/suppl_file/ic5c01740_si_001.pdf

Crystallographic information files for $XeF_2 \cdot 2PtF_4$ and $XeF_2 \cdot 2PdF_4$ can be obtained via the joint Cambridge Crystallographic Data Centre (CCDC) and Fachinformationszentrum Karlsruhe Access Structures service (http://www.ccdc.cam.ac.uk/structures) by quoting the deposition numbers CSD 2438371 and 2438372, respectively.

The data supporting the findings of this study are available on the Zenodo open repository https://zenodo.org/ under the DOI number: 10.5281/zenodo.15594028.

A.3 Coordination of XeF_2 to Fluoridometal Cations: The Adduct Cations $[PtF_3(XeF_2)_3]^+$ and $[PdF_3(XeF_2)_3]^+$

Supporting information file containing additional crystallographic data and figures, DFT-calculated vibrational frequencies and structural parameters of the $[MF_3(XeF_2)_3]^+$ cations and their comparison with experimental values, a table of observed Raman band positions and their relative intensities, and ATR-IR spectra of the compounds is accessible online:

https://pubs.acs.org/doi/suppl/10.1021/acs.inorgchem.5c05940/suppl_file/ic5c05940_si_001.pdf

Crystallographic information files for $[Xe_2F_3][PtF_3(XeF_2)_3][AsF_6]_2$($oP256$), $[Xe_2F_3][PtF_3(XeF_2)_3][AsF_6]_2$($aP256$), and $[Xe_2F_3][PdF_3(XeF_2)_3][AsF_6]_2$ can be obtained via the joint Cambridge Crystallographic Data Centre (CCDC) and Fachinformationszentrum Karlsruhe Access Structures service (http://www.ccdc.cam.ac.uk/structures) by quoting the deposition numbers CSD 2517119, 2517120 and 2517118, respectively.

The data supporting the findings of this study are available on the Zenodo open repository https://zenodo.org/ under the DOI number: 10.5281/zenodo.17787891.

A.4 Structural Investigations of the XeF_2–PtF_5 System: Crystal Structures of $[Xe_2F_3][PtF_6] \cdot XeF_2$, $[Xe_2F_3][PtF_6]$, and $[XeF][PtF_6]$

Supporting information file containing additional crystallographic data, figures, and a table listing the observed Raman band positions with their relative intensities is accessible online:

https://acsi-journal.eu/index.php/ACSi/article/view/9768/10392

Crystallographic information files for $[Xe_2F_3][PtF_6] \cdot XeF_2$($mC120$), $[Xe_2F_3][PtF_6] \cdot XeF_2$($oP120$), $[Xe_2F_3][PtF_6]$, and $[XeF][PtF_6]$($mP108$) can be obtained via the joint Cambridge Crystallographic Data Centre (CCDC) and Fachinformationszentrum Karlsruhe Access Structures service (http://www.ccdc.cam.ac.uk/structures) by quoting the deposition numbers CSD 2529289, 2529288, 2529287, and 2529290, respectively.

Full experimental data for this article, including SCXRD datasets and Raman spectra, is available from the Zenodo open repository https://zenodo.org/ under the DOI number: 10.5281/zenodo.18428037.

Appendix B

Additional Crystallographic Data and Figures

B.1 Revisiting the Coordination of XeF_2 to Alkali Metal Cations: Synthesis and Structural Characterization of $[Li(XeF_2)_3PtF_6]$, $[Na(XeF_2)PtF_6]$, and $[K(XeF_2)_2PtF_6]$

Table B.1: Crystallographic data and refinement results for $[Li(XeF_2)_3PtF_6]$, $[Na(XeF_2)PtF_6]$, and $[K(XeF_2)_2PtF_6]$.

Compound	$[Li(XeF_2)_3PtF_6]$	$[Na(XeF_2)PtF_6]$	$[K(XeF_2)_2PtF_6]$
Formula	Xe_3PtLiF_{12}	$XePtNaF_{12}$	Xe_2PtKF_{10}
F_w	823.93	501.38	686.79
T (K)	100.00(10)	100.00(10)	100.00(10)
Crystal system	Monoclinic	Monoclinic	Tetragonal
Space group	$P2_1$	$P2_1/c$	$I4/mcm$
a (Å)	6.80526(6)	7.1459(3)	8.73777(9)
b (Å)	26.79621(19)	10.0427(4)	8.73777(9)
c (Å)	6.81133(6)	10.2322(4)	13.3131(2)
α (°)	90	90	90
β (°)	92.6673(8)	95.852(4)	90
γ (°)	90	90	90
V (Å^3)	1240.736(17)	730.47(5)	1016.44(3)
Z	4	4	4
ρ_{calc} (g/cm^3)	4.411	4.559	4.488
Crystal size (mm)	0.164 × 0.159 × 0.13	0.111 × 0.086 × 0.085	0.188 × 0.128 × 0.114
Radiation type	Ag $K\alpha$	Ag $K\alpha$	Ag $K\alpha$
λ (Å)	0.56087	0.56087	0.56087
μ (mm^{-1})	10.363	12.918	11.227
$F(000)$	1404	860	1180
$2\theta_{max}$ (°)	36.3860	36.5000	36.8940
Index ranges	$-14 \leq h \leq 14$	$-15 \leq h \leq 14$	$-18 \leq h \leq 18$
	$-56 \leq k \leq 57$	$-21 \leq k \leq 21$	$-18 \leq k \leq 18$
	$-14 \leq l \leq 14$	$-21 \leq l \leq 21$	$-27 \leq l \leq 27$
Reflections collected	222318	9650	45162
Independent reflections	24060	9650	1396
Reflections with $[I > 2\sigma(I)]$	21733	8612	1023
R_{int}	0.0799	/	0.0810
R_{sigma}	0.0314	0.0236	0.0174
Data/restraints/ parameters	24060/1/309	9650/0/101	1396/0/26
S	1.034	1.051	1.101
R_1, wR_2 $[I > 2\sigma(I)]$	0.0284, 0.0686	0.0358, 0.0996	0.0174, 0.0458
R_1, wR_2 [all data]	0.0330, 0.0706	0.0413, 0.1042	0.0251, 0.0495
$\Delta\rho_{min}$, $\Delta\rho_{max}$ (e/Å^3)	−3.231, 3.445	−3.226, 3.440	−1.576, 1.525
Absolute structure	Refined as an inversion twin.	/	/

Table B.2: Fractional atomic coordinates and equivalent isotropic displacement parameters (Å^2) for the crystal structure of $[Li(XeF_2)_3PtF_6]$.

Atom	x	y	z	U_{eq}
Pt1	0.6738(2)	0.40505(2)	0.77777(2)	0.01752(3)
Pt2	0.72631(3)	0.64763(2)	0.81021(3)	0.01985(3)
Xe1	0.17581(5)	0.38796(2)	0.25606(5)	0.02501(5)
Xe2	0.25612(3)	0.26853(2)	0.66928(3)	0.01286(3)
Xe3	0.69572(3)	0.51852(2)	0.27846(3)	0.01340(3)
Xe4	0.75003(3)	0.26794(2)	0.16575(3)	0.01317(3)
Xe5	0.22020(4)	0.64456(2)	0.30664(4)	0.01382(3)
Xe6	0.19209(3)	0.51929(2)	0.77951(3)	0.01305(3)
F1	0.2313(9)	0.32361(14)	0.1313(8)	0.0574(14)
F2	0.1122(4)	0.45326(11)	0.3869(4)	0.0221(5)
F3	0.5135(3)	0.23895(10)	0.7600(4)	0.0169(4)
F4	0.0030(3)	0.30033(10)	0.5717(4)	0.0172(4)
F5	0.4391(3)	0.48759(10)	0.1910(4)	0.0181(4)
F6	0.9526(3)	0.54925(10)	0.3664(4)	0.0187(4)
F7	0.6174(4)	0.28670(11)	0.4109(3)	0.0185(4)
F8	0.8826(4)	0.25095(10)	−0.0821(3)	0.0174(4)
F9	0.2858(4)	0.58116(10)	0.1696(4)	0.0184(4)
F10	0.1540(4)	0.70807(9)	0.4435(4)	0.0183(4)
F11	0.0652(4)	0.49914(10)	1.0264(3)	0.0176(4)
F12	0.3216(4)	0.53894(10)	0.5329(3)	0.0177(4)
F13	0.6923(5)	0.40487(16)	1.0528(4)	0.0325(6)
F14	0.6586(7)	0.40427(18)	0.5020(5)	0.0476(11)
F15	0.6817(6)	0.47510(14)	0.7764(6)	0.0387(10)
F16	0.9497(5)	0.40262(17)	0.7775(6)	0.0347(7)
F17	0.3972(5)	0.40645(18)	0.7808(7)	0.0446(9)
F18	0.6605(4)	0.33389(11)	0.7814(4)	0.0182(4)
F19	0.7169(8)	0.57797(16)	0.8102(8)	0.0493(11)
F20	0.7129(8)	0.6478(2)	0.5353(5)	0.0510(12)
F21	0.7418(7)	0.6477(2)	1.0854(5)	0.0481(11)
F22	0.4513(6)	0.6506(2)	0.8113(8)	0.0503(11)
F23	1.0018(6)	0.6450(2)	0.8106(7)	0.0465(10)
F24	0.7355(8)	0.71810(15)	0.8108(8)	0.0485(11)
Li1	0.7568(10)	0.2737(3)	0.6644(11)	0.0168(12)
Li2	0.1961(11)	0.5166(3)	0.2805(10)	0.0164(12)

Table B.3: Fractional atomic coordinates and equivalent isotropic displacement parameters (Å^2) for the crystal structure of [Na(XeF_2)PtF_6].

Atom	*x*	*y*	*z*	U_{eq}
Pt1	0.28724(2)	0.89385(2)	0.70106(2)	0.01134(3)
Xe1	0.19890(3)	0.31100(2)	0.51528(2)	0.01358(4)
Na1	0.2206(2)	0.55900(15)	0.82015(15)	0.0139(2)
F1	0.2107(4)	0.1413(3)	0.4186(3)	0.0240(5)
F2	0.1823(4)	0.4823(3)	0.6125(3)	0.0234(4)
F3	0.3680(4)	0.9342(3)	0.8756(2)	0.0229(4)
F4	0.4612(4)	0.7530(3)	0.7080(3)	0.0241(5)
F5	0.4627(3)	1.0149(2)	0.6432(3)	0.0185(4)
F6	0.2069(3)	0.8501(2)	0.5245(2)	0.0178(3)
F7	0.1101(3)	1.0341(2)	0.6965(3)	0.0174(3)
F8	0.1109(4)	0.7713(2)	0.7584(3)	0.0190(4)

Table B.4: Fractional atomic coordinates and equivalent isotropic displacement parameters (Å^2) for the crystal structure of [K(XeF_2)$_2$$PtF_6$].

Atom	*x*	*y*	*z*	U_{eq}
Pt1	0.500000	0.500000	0.500000	0.01043(3)
Xe1	0.750000	0.750000	0.250000	0.01376(4)
K1	0.500000	1.000000	0.500000	0.01207(10)
F2	0.500000	0.500000	0.35904(13)	0.0230(3)
F3	0.41357(13)	0.69688(10)	0.500000	0.02288(19)
F1	0.62190(8)	0.87810(8)	0.33970(8)	0.0327(3)

Table B.5: Crystallographic data and refinement results for $LiPtF_6$, $NaPtF_6$, $KPtF_6$, and $RbPtF_6$.

Compound	$LiPtF_6$	$NaPtF_6$	$KPtF_6$	$RbPtF_6$
Formula	$LiPtF_6$	$NaPtF_6$	$KPtF_6$	$RbPtF_6$
F_w	316.03	332.08	348.19	394.56
T (K)	100.00(10)	99.99(10)	100.00(10)	99.99(10)
Crystal system	Trigonal	Trigonal	Trigonal	Trigonal
Space group	$R\bar{3}$	$R\bar{3}$	$R\bar{3}$	$R\bar{3}$
a (Å)	4.97492(11)	5.16973(7)	7.41013(13)	7.55677(11)
b (Å)	4.97492(11)	5.16973(7)	7.41013(13)	7.55677(11)
c (Å)	13.5916(3)	14.7717(2)	7.28292(15)	7.54000(12)
α (°)	90	90	90	90
β (°)	90	90	90	90
γ (°)	120	120	120	120
V (Å^3)	291.321(15)	341.898(10)	346.329(14)	372.884(13)
Z	3	3	3	3
ρ_{calc} (g/cm^3)	5.404	4.839	5.008	5.271
Crystal size (mm)	0.14 × 0.12 × 0.06	0.07 × 0.07 × 0.06	0.14 × 0.132 × 0.102	0.109 × 0.086 × 0.059
Radiation type	Ag $K\alpha$	Ag $K\alpha$	Ag $K\alpha$	Ag $K\alpha$
λ (Å)	0.56087	0.56087	0.56087	0.56087
μ (mm^{-1})	19.636	16.782	16.977	20.585
$F(000)$	405	429	453	507
$2\theta_{max}$ (°)	36.450	35.3660	36.8060	36.626
Index ranges	$-10 \le h \le 10$ $-10 \le k \le 10$ $-28 \le l \le 27$	$-10 \le h \le 10$ $-10 \le k \le 10$ $-30 \le l \le 31$	$-15 \le h \le 15$ $-15 \le k \le 15$ $-15 \le l \le 15$	$-15 \le h \le 15$ $-15 \le k \le 15$ $-15 \le l \le 15$
Reflections collected	7834	17232	9548	10146
Independent reflections	635	756	760	802
Reflections with $[I > 2\sigma(I)]$	635	756	760	802
R_{int}	0.0847	0.0949	0.0879	0.0958
R_{sigma}	0.0268	0.0212	0.0262	0.0277
Data/restraints/ parameters	635/0/15	756/0/14	760/0/14	802/0/15
S	1.071	1.106	1.060	1.071
R_1, wR_2 $[I > 2\sigma(I)]$	0.0192, 0.0462	0.0178, 0.0413	0.0183, 0.0427	0.0181, 0.0436
R_1, wR_2 [all data]	0.0192, 0.0462	0.0178, 0.0413	0.0183, 0.0427	0.0181, 0.0436
$\Delta\rho_{min}$, $\Delta\rho_{max}$ (e/Å^3)	−3.112, 2.805	−2.219, 3.295	−3.421, 2.138	−2.411, 2.573

Table B.6: Fractional atomic coordinates and equivalent isotropic displacement parameters (Å^2) for the crystal structures of $LiPtF_6$, $NaPtF_6$, $KPtF_6$, and $RbPtF_6$.

$LiPtF_6$				
Atom	***x***	***y***	***z***	U_{eq}
Pt1	0.000000	0.000000	0.500000	0.00611(5)
Li1	0.666667	0.333333	0.333333	0.0117(18)
F1	0.3197(4)	0.2962(4)	0.41967(11)	0.00921(18)
$NaPtF_6$				
Atom	***x***	***y***	***z***	U_{eq}
Pt1	0.000000	0.000000	0.500000	0.01005(4)
Na1	0.666667	0.333333	0.333333	0.0141(3)
F1	0.2947(3)	0.2980(3)	0.42575(9)	0.01589(17)
$KPtF_6$				
Atom	***x***	***y***	***z***	U_{eq}
Pt1	0.666667	0.333333	0.833333	0.00813(3)
K1	0.666667	0.333333	0.333333	0.01256(12)
F1	0.6024(2)	0.4977(2)	0.6789(2)	0.01356(18)
$RbPtF_6$				
Atom	***x***	***y***	***z***	U_{eq}
Pt1	0.666667	0.333333	0.333333	0.00810(5)
Rb1	0.000000	0.000000	0.500000	0.01078(6)
F1	0.44277(19)	0.2748(2)	0.48108(17)	0.01399(17)

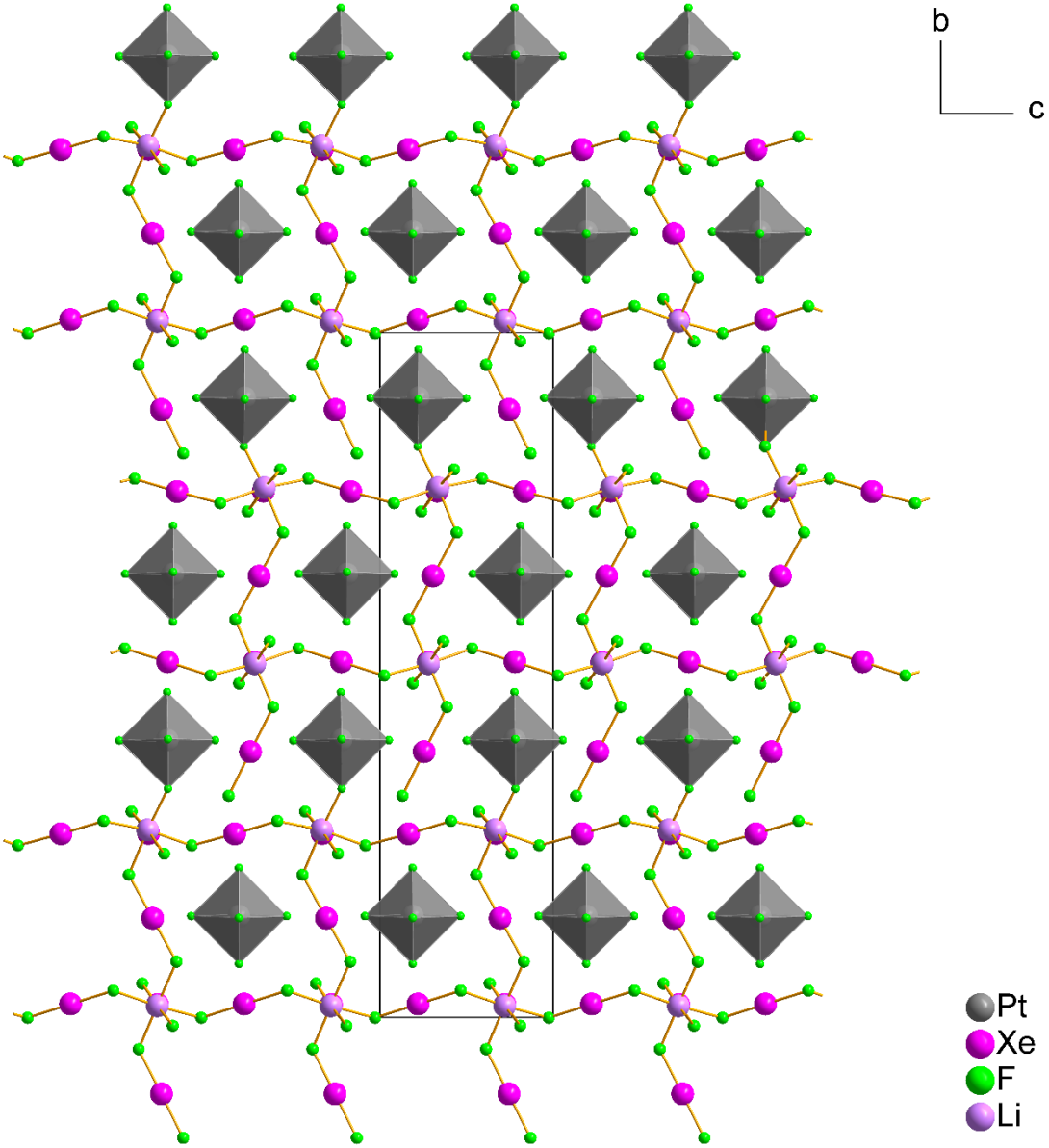


Figure B.1: Crystal packing of $[Li(XeF_2)_3PtF_6]$ viewed along the *a* axis, illustrating the double-layer structure, with the layers lying parallel to the *ac* crystallographic plane.

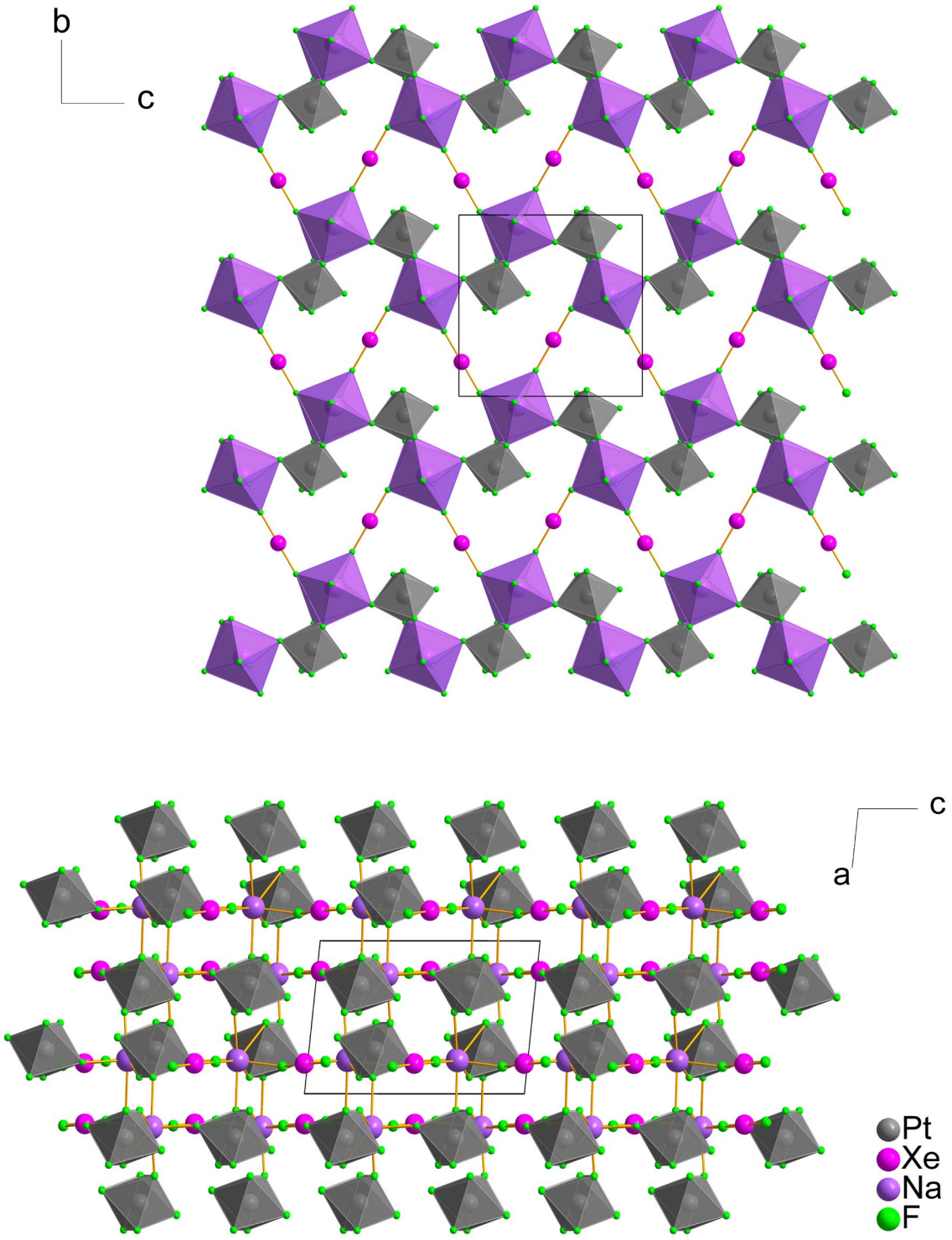


Figure B.2: Sections of the crystal structure of $[Na(XeF_2)PtF_6]$ showing a single layer parallel to the *bc* plane, highlighting the bridging role of the XeF_2 ligands (top), and the stacking of such layers along the *a* axis to generate a three-dimensional structure (bottom).

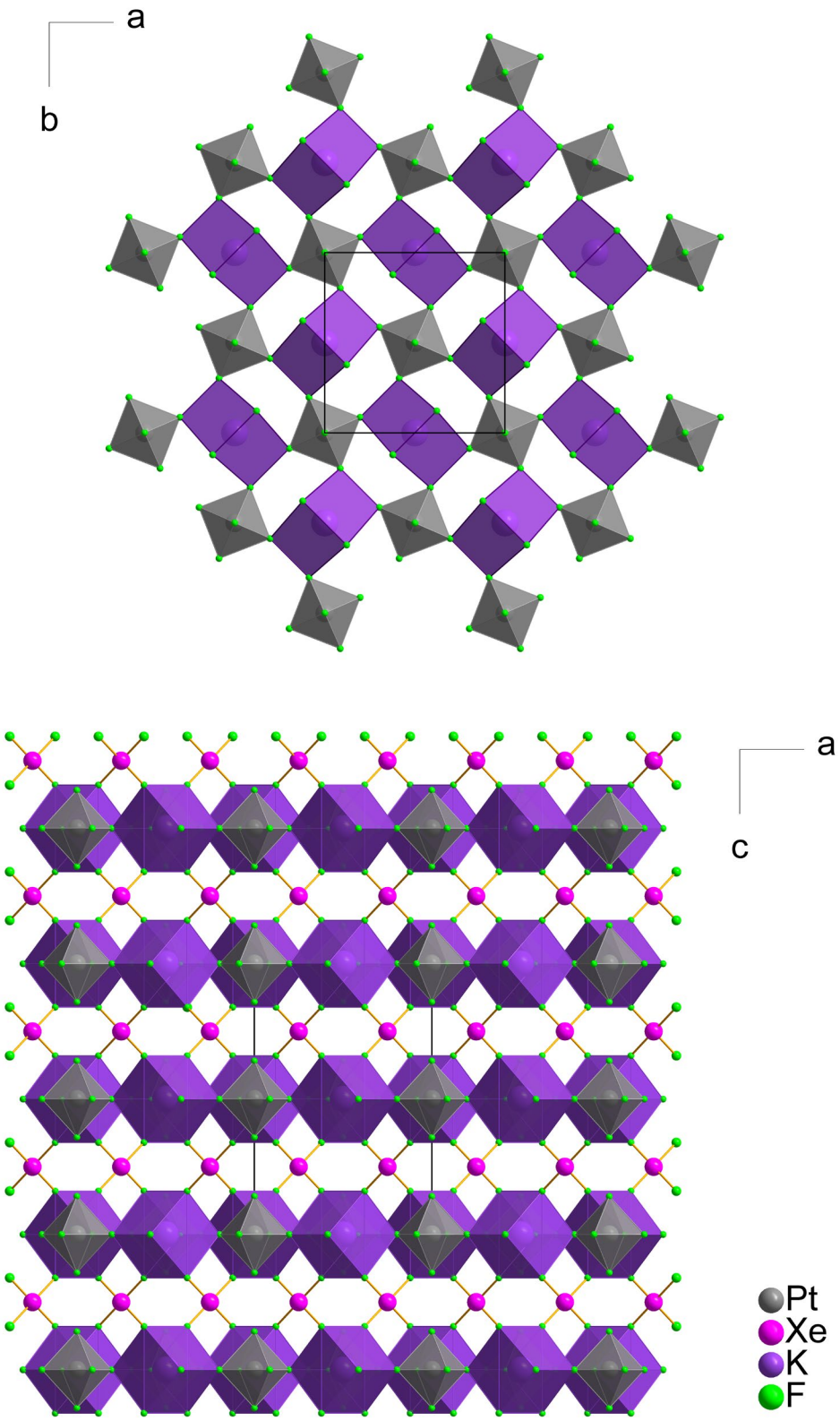


Figure B.3: Sections of the crystal structure of $[K(XeF_2)_2PtF_6]$ showing a layer composed of $[PtF_6]$ and $[KF_8]$ units (XeF_2 ligands omitted for clarity) lying parallel to the *ab* plane (top), and the interconnection of these layers into a three-dimensional structure by bridging XeF_2 ligands (bottom).

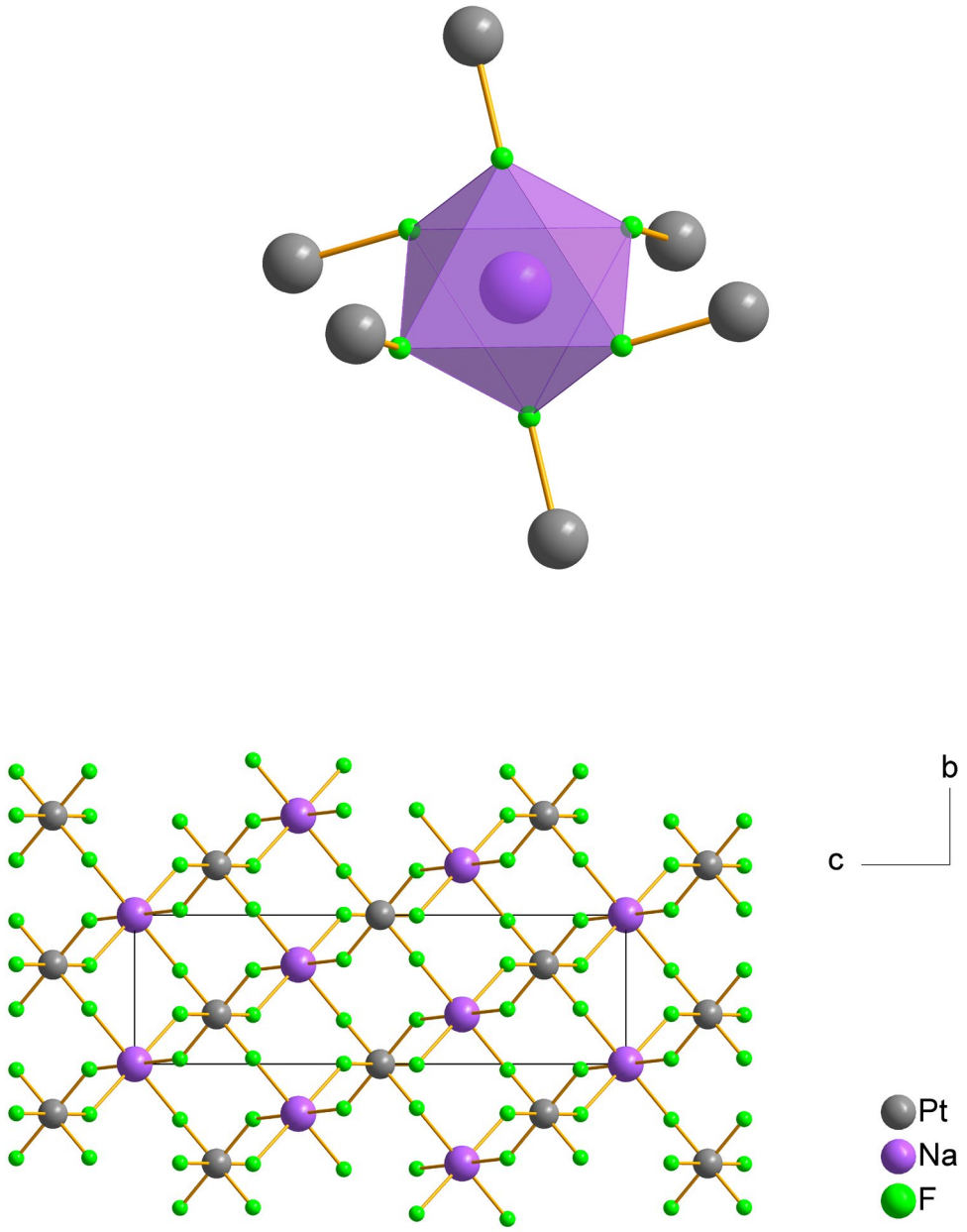


Figure B.4: Coordination environment of the Na^+ cation (top) and the crystal packing of $NaPtF_6$ viewed along the *a* crystallographic axis (bottom). An analogous arrangement is observed in the crystal structure of $LiPtF_6$.

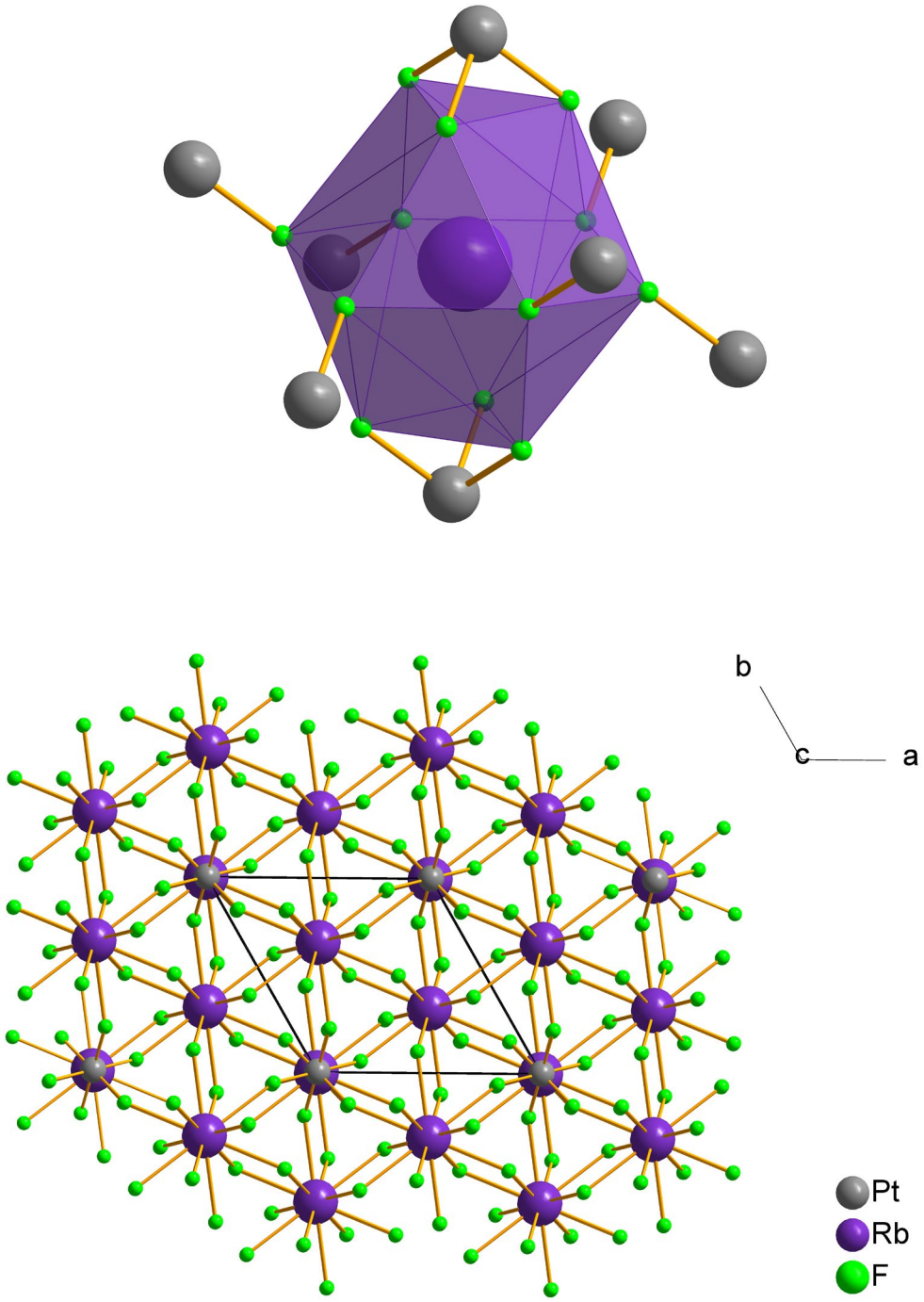


Figure B.5: Coordination environment of the Rb^+ cation (top) and the crystal packing of $RbPtF_6$ viewed along the *c* crystallographic axis (bottom). An analogous arrangement is observed in the crystal structure of $KPtF_6$.

B.2 Structural Investigations of the XeF_2–PtF_4 System Under Extreme Conditions

Table B.7: Summary of phases identified after laser heating.

Run index	Cell type	Facility	T (K)	P (GPa)	Phases identified (method)
SD1	SSDAC80	ESRF ID27	n.d. [a]	14.5	$XeF_2{\cdot}2PtF_4$ (*Raman)* $XeF_2{\cdot}PtF_4$ (*SCXRD, Raman*) PtF_4 (*SCXRD*)
		DESY P02.2	2770/3216	8.0 [b]	$XeF_2{\cdot}2PtF_4$ (*Raman*) $n XeF_2{\cdot}PtF_4$ (*Raman*)
SD2	SSDAC80	DESY P02.2	2824/2740	4.0	PtF_4 (*SCXRD*) $XeF_2{\cdot}2PtF_4$ (*SCXRD, Raman*) $n XeF_2{\cdot}PtF_4$ (*Raman*) XeF_2 (*Raman*)
MB1	Merrill-Bassett	DESY P02.2	3142/3141	4.7	$XeF_2{\cdot}2PtF_4$ (*SCXRD, Raman*) $n XeF_2{\cdot}PtF_4$ (*Raman*) XeF_2 (*Raman*)
		DESY P02.2	2793/3173	8.6 [c]	PtF_4 (*SCXRD*) $[PtF_2(XeF_2)_4][Pt_4F_{18}]$ (*SCXRD*) $XeF_2 \cdot 2PtF_4$ (*SCXRD, Raman*) $XeF_2 \cdot PtF_4$ (*SCXRD, Raman*) $n XeF_2{\cdot}PtF_4$ (*Raman*)

[a]Off-line laser heating at the ID27 beamline at ESRF facility does not enable temperature measurements.

[b]The pressure in the cell was decreased from the previous pressure point prior to laser heating and diffraction analysis.

[c]The pressure in the cell was increased from the previous pressure point prior to laser heating and diffraction analysis.

Table B.8: Crystallographic data for $XeF_2 \cdot PtF_4$ collected at different pressure points.

Compound	$XeF_2 \cdot PtF_4$		
Pressure (GPa)	8.6	8.0	14.5
Run Index	MB1	SD1	SD1
Facility	DESY P02.2	DESY P02.2	ESRF ID27
Formula		$XePtF_6$	
F_w		440.39	
Crystal system		Monoclinic	
Space group		$P2_1$[a]	
a (Å)	5.099(3)	4.966(2)	4.854(2)
b (Å)	4.6290(15)	4.5813(9)	4.5162(9)
c (Å)	8.901(8)	8.9649(10)	8.8018(10)
α (°)	90	90	90
β (°)	92.44(9)	92.42(2)	91.789(19)
γ (°)	90	90	90
V (Å^3)	209.9(2)	203.79(10)	192.85(10)
Z	2	2	2
ρ_{calc} (g/cm^3)	6.967	7.177	7.584
λ (Å)	0.2906	0.2906	0.3738
μ (mm^{-1})	7.282	7.501	8.482
$F(000)$	372	372	372
$2\theta_{max}$ (°)	35.4080	32.4220	38.5320
Index ranges	$-8 \le h \le 7$	$-7 \le h \le 3$	$-2 \le h \le 5$
	$-6 \le k \le 7$	$-6 \le k \le 8$	$-8 \le k \le 7$
	$-12 \le l \le 9$	$-16 \le l \le 16$	$-16 \le l \le 13$
Reflections collected	558	564	437
Independent reflections	476	530	409
Reflections with $[I > 2\sigma(I)]$	450	490	380
R_{int}	0.0303	0.0336	0.0086
R_{sigma}	0.0204	0.0131	0.0144
Data/restraints/parameters	476/56[b]/73	530/50[c]/73	409/50[d]/73
S	1.029	1.052	1.117
R_1, wR_2 $[I > 2\sigma(I)]$	0.0793, 0.2217	0.0745, 0.1921	0.0516, 0.1448
R_1, wR_2 [all data]	0.0817, 0.2254	0.0798, 0.2003	0.0542, 0.1468
$\Delta\rho_{min}$, $\Delta\rho_{max}$ (e/Å^3)	−5.149, 4.400	−2.830, 4.162	−1.975, 2.266

[a]Due to the small number of collected reflections Friedel pairs were merged during data processing and meaningful Flack parameters cannot be calculated.
[b]Restraints used: RIGU 0.003 0.003 and ISOR 0.005 0.1 F1
[c]Restraints used: RIGU
[d]Restraints used: RIGU 0.002 0.002

Table B.9: Fractional atomic coordinates and equivalent isotropic displacement parameters (Å^2) for the crystal structures of $XeF_2 \cdot PtF_4$.

$XeF_2 \cdot PtF_4$ (P = 8.6 GPa; MB1)				
Atom	x	y	z	U_{eq}
Pt1	0.6402(4)	0.7593(3)	0.6361(2)	0.0184(7)
Xe1	0.2544(7)	1.2480(12)	0.8590(5)	0.0235(13)
F2	0.312(11)	0.885(9)	0.725(7)	0.027(6)
F6	0.953(10)	0.606(9)	0.575(7)	0.026(6)
F1	0.224(10)	1.614(9)	0.971(8)	0.027(8)
F5	0.570(9)	0.892(7)	0.446(5)	0.021(5)
F3	0.701(12)	0.613(8)	0.809(7)	0.026(5)
F4	0.797(10)	1.091(7)	0.692(6)	0.022(5)
$XeF_2 \cdot PtF_4$ (P = 8.0 GPa; SD1)				
Atom	x	y	z	U_{eq}
Pt1	0.6417(3)	0.7400(5)	0.63611(9)	0.0151(4)
Xe1	0.2564(7)	0.2531(10)	0.85871(19)	0.0193(6)
F3	0.801(9)	0.413(6)	0.702(3)	0.017(5)
F6	0.454(9)	1.110(7)	0.564(3)	0.021(5)
F4	0.949(9)	0.887(6)	0.562(3)	0.017(4)
F5	0.738(9)	0.891(7)	0.832(2)	0.018(5)
F2	0.297(9)	0.599(7)	0.721(2)	0.019(4)
F1	0.238(11)	−0.119(7)	0.976(3)	0.029(9)
$XeF_2 \cdot PtF_4$(P = 14.5 GPa; SD1)				
Atom	x	y	z	U_{eq}
Pt1	0.6459(4)	0.73600(2)	0.63743(9)	0.0220(4)
Xe1	0.2536(10)	1.2624(7)	0.8600(2)	0.0253(8)
F1	0.252(12)	1.622(7)	0.983(2)	0.041(10)
F2	0.302(9)	0.881(6)	0.722(2)	0.031(4)
F3	0.965(9)	0.576(4)	0.566(2)	0.028(4)
F4	0.817(9)	1.083(5)	0.707(2)	0.028(4)
F5	0.760(8)	0.605(4)	0.833(2)	0.023(4)
F6	0.552(8)	0.868(5)	0.4321(19)	0.027(4)

Table B.10: Non-bonded inter- and intramolecular Xe · · · F contacts shorter than the corresponding sum of the van der Waals radii in the crystal structure of $XeF_2 \cdot PtF_4$ determined at 14.5 GPa.

Contact	**Distance (Å)**
Xe1 · · · F4^{i}	2.60(4)
Xe1 · · · F5^{ii}	2.797(18)
Xe1 · · · F1^{iii}	2.80(5)
Xe1 · · · F6^{iv}	2.81(2)
Xe1 · · · F5^{v}	2.86(3)
Xe1 · · · F5^{vi}	2.92(3)
Xe1 · · · F1^{vii}	2.92(5)
Xe1 · · · F2^{vi}	3.06(3)
Xe1 · · · F1^{viii}	3.09(3)
Xe1 · · · F4	3.19(4)
Xe1 · · · F3^{v}	3.23(2)

Symmetry codes: (i) x–1, y, z; (ii) –x+1, y+1/2, –z+2; (iii) –x+1, y–1/2, –z+2; (iv) –x+1, y+1/2, –z+1; (v) x–1, y+1, z; (vi) x, y+1, z; (vii) –x, y–1/2, –z+2; (viii) x, y–1, z.

Table B.11: Crystallographic data for $[PtF_2(XeF_2)_4][Pt_4F_{18}]$.

Compound	$[PtF_2(XeF_2)_4][Pt_4F_{18}]$
Pressure (GPa)	8.6
Run Index	MB1
Facility	DESY P02.2
Formula	$Xe_4Pt_5F_{28}$
F_w	2032.65
Crystal system	Triclinic
Space group	$P\bar{1}$
a (Å)	4.7045(9)
b (Å)	9.8913(14)
c (Å)	10.779(4)
α (°)	84.773(18)
β (°)	86.83(2)
γ (°)	76.300(14)
V (Å^3)	485.0(2)
Z	1
ρ_{calc} (g/cm^3)	6.959
λ (Å)	0.2906
μ (mm^{-1})	7.023
$F(000)$	858
$2\theta_{max}$ (°)	36.1800
Index ranges	$-7 \leq h \leq 9$
	$-19 \leq k \leq 19$
	$-7 \leq l \leq 13$
Reflections collected	1641
Independent reflections	1457
Reflections with $[I > 2\sigma(I)]$	1089
R_{int}	0.0146
R_{sigma}	0.0288
Data/restraints/parameters	1457/116[a]/169
S	1.028
R_1, wR_2 $[I > 2\sigma(I)]$	0.0520, 0.1431
R_1, wR_2 [all data]	0.0712, 0.1541
$\Delta\rho_{min}$, $\Delta\rho_{max}$ (e/Å^3)	−1.874, 1.633

[a]Restraints used: RIGU

Table B.12: Fractional atomic coordinates and equivalent isotropic displacement parameters (Å^2) for $[PtF_2(XeF_2)_4][Pt_4F_{18}]$.

Atom	x	y	z	U_{eq}
Pt2	0.3600(2)	0.31709(7)	0.86216(17)	0.0169(7)
Pt1	0.500000	1.000000	0.500000	0.0154(11)
Pt3	0.7349(2)	0.58746(7)	0.82106(17)	0.0148(7)
Xe1	0.1372(4)	0.69514(13)	0.5024(3)	0.0217(14)
Xe2	0.0938(7)	0.96340(14)	0.8143(4)	0.0371(18)
F10	0.656(4)	0.4155(13)	0.910(3)	0.021(4)
F14	1.137(4)	0.4941(12)	0.770(3)	0.018(6)
F6	0.070(5)	0.2384(14)	0.819(4)	0.027(4)
F8	0.563(5)	0.1484(12)	0.945(4)	0.027(4)
F11	0.345(5)	0.6802(14)	0.853(4)	0.025(7)
F5	0.161(5)	1.0231(15)	0.408(3)	0.023(4)
F9	0.123(4)	0.3727(14)	1.013(4)	0.023(5)
F1	−0.138(6)	0.6120(17)	0.442(5)	0.039(6)
F12	0.815(4)	0.7532(13)	0.746(3)	0.024(7)
F4	0.295(5)	1.0740(15)	0.652(4)	0.026(5)
F13	0.615(5)	0.5462(14)	0.657(4)	0.024(5)
F2	0.452(5)	0.8158(15)	0.569(4)	0.027(5)
F7	0.563(6)	0.2609(16)	0.713(4)	0.030(5)
F3	−0.066(7)	0.8778(18)	0.954(5)	0.046(11)

Table B.13: Non-bonded inter- and intramolecular Xe · · · F contacts shorter than the corresponding sum of the van der Waals radii in the crystal structure of $[PtF_2(XeF_2)_4][Pt_4F_{18}]$.

Contact	**Distance** (Å)	**Contact**	**Distance** (Å)
Xe1 · · · F7^{i}	2.70(4)	Xe2 · · · F6^{vi}	2.701(15)
Xe1 · · · F13	2.90(3)	Xe2 · · · F5^{iii}	2.72(3)
Xe1 · · · F12^{ii}	2.99(3)	Xe2 · · · F11	2.773(16)
Xe1 · · · F5^{iii}	3.026(18)	Xe2 · · · F12^{ii}	2.875(18)
Xe1 · · · F13^{i}	3.04(3)	Xe2 · · · F3^{vii}	3.05(5)
Xe1 · · · F1^{iv}	3.04(2)	Xe2 · · · F8^{viii}	3.08(3)
Xe1 · · · F4^{iii}	3.10(3)	Xe2 · · · F8^{ix}	3.11(4)
Xe1 · · · F2^{ii}	3.23(2)	Xe2 · · · F2	3.32(4)
Xe1 · · · F5	3.336(18)	Xe2 · · · F7^{viii}	3.51(2)
Xe1 · · · F14^{ii}	3.35(3)	Xe2 · · · F8^{vi}	3.60(3)
Xe1 · · · F1^{v}	3.35(3)	Xe2 · · · F12	3.611(18)
Xe1 · · · F13^{ii}	3.44(3)		
Xe1 · · · F6^{iv}	3.61(4)		

Symmetry codes: (i) $-x+1, -y+1, -z+1$; (ii) $x-1, y, z$; (iii) $-x, -y+2, -z+1$; (iv) $-x, -y+1, -z+1$; (v) $x+1, y, z$; (vi) $x, y+1, z$; (vii) $-x, -y+2, -z+2$; (viii) $x-1, y+1, z$; (ix) $-x+1, -y+1, -z+2$.

Table B.14: Crystallographic data for $XeF_2 \cdot 2PtF_4(mP52)$ collected at different pressure points.

Compound	$XeF_2 \cdot 2PtF_4(mP52)$		
Pressure (GPa)	4.0	4.7	8.6
Run Index	SD2	MB1	MB1
Facility	DESY P02.2	DESY P02.2	DESY P02.2
Formula		$XePt_2F_{10}$	
F_w		711.48	
Crystal system		Monoclinic	
Space group		$P2_1/n$	
a (Å)	5.357(9)	5.3312(2)	5.1822(3)
b (Å)	9.256(4)	9.2323(6)	8.5043(10)
c (Å)	14.68(4)	14.3574(11)	14.9219(10)
α (°)	90	90	90
β (°)	93.6(2)	95.225(5)	93.449(7)
γ (°)	90	90	90
V (Å^3)	726(2)	703.72(8)	656.43(10)
Z	4	4	4
ρ_{calc} (g/cm^3)	6.506	6.715	7.199
λ (Å)	0.2898	0.2906	0.2906
μ (mm^{-1})	6.084	6.327	6.783
$F(000)$	1200	1200	1200
$2\theta_{max}$ (°)	25.7600	35.7160	34.8100
Index ranges	$-7 \le h \le 7$	$-9 \le h \le 10$	$-9 \le h \le 10$
	$-13 \le k \le 14$	$-16 \le k \le 11$	$-13 \le k \le 9$
	$-18 \le l \le 18$	$-26 \le l \le 17$	$-27 \le l \le 21$
Reflections collected	2204	1788	1676
Independent reflections	949	1671	1571
Reflections with $[I > 2\sigma(I)]$	644	1298	1347
R_{int}	0.0443	0.0251	0.0130
R_{sigma}	0.0445	0.0244	0.0130
Data/restraints/parameters	949/95[a]/118	1671/95[a]/118	1571/95[a]/118
S	0.993	1.059	1.000
R_1, wR_2 $[I > 2\sigma(I)]$	0.0542, 0.1491	0.0910, 0.2492	0.0818, 0.2139
R_1, wR_2 [all data]	0.0784, 0.1664	0.1004, 0.2561	0.0868, 0.2228
$\Delta\rho_{min}$, $\Delta\rho_{max}$ (e/Å^3)	−1.158, 1.546	−4.664, 4.476	−4.129, 4.489

[a]Restraints used: RIGU

Table B.15: Fractional atomic coordinates and equivalent isotropic displacement parameters (Å^2) for the crystal structures of $XeF_2 \cdot 2PtF_4$($mP52$).

$XeF_2 \cdot 2PtF_4$($mP52$) (P = 4.0 GPa; SD2)				
Atom	x	y	z	U_{eq}
Pt2	0.7331(4)	0.78763(12)	0.56324(18)	0.0412(15)
Pt1	0.1915(3)	0.83246(12)	0.39877(16)	0.0361(13)
Xe1	−0.2124(6)	0.9719(2)	0.2010(3)	0.046(2)
F6	0.431(5)	0.8242(19)	0.620(3)	0.046(7)
F4	0.135(6)	0.664(2)	0.323(3)	0.054(6)
F3	0.333(6)	0.9171(18)	0.299(3)	0.046(6)
F10	0.747(5)	0.9934(17)	0.520(2)	0.045(7)
F8	1.041(5)	0.7395(16)	0.503(3)	0.042(6)
F7	0.709(6)	0.588(2)	0.591(3)	0.049(6)
F5	0.529(6)	0.7433(18)	0.450(3)	0.046(5)
F1	−0.269(7)	1.007(2)	0.081(3)	0.058(8)
F2	−0.125(6)	0.901(2)	0.355(3)	0.053(6)
F9	0.958(8)	0.819(2)	0.678(4)	0.055(6)
$XeF_2 \cdot 2PtF_4$($mP52$) (P = 4.7 GPa; MB1)				
Atom	x	y	z	U_{eq}
Pt1	0.69167(12)	0.66863(9)	0.39847(6)	0.0236(2)
Pt2	0.76798(12)	0.28601(9)	0.43634(6)	0.0244(2)
Xe1	0.2857(2)	0.52760(18)	0.20055(13)	0.0302(3)
F6	1.019(2)	0.753(2)	0.4451(12)	0.030(2)
F2	0.364(3)	0.600(2)	0.3528(14)	0.033(3)
F7	0.542(3)	0.770(2)	0.5022(13)	0.035(3)
F8	1.059(3)	0.3251(17)	0.3776(16)	0.033(3)
F9	0.788(3)	0.0890(18)	0.4074(16)	0.033(3)
F5	0.745(3)	0.4963(18)	0.4768(14)	0.031(2)
F10	0.557(3)	0.3213(18)	0.3249(14)	0.031(3)
F4	0.833(3)	0.579(2)	0.2944(14)	0.036(3)
F1	0.212(3)	0.489(2)	0.0729(14)	0.036(3)

Table B.15: Continued.

$XeF_2 \cdot 2PtF_4(mP52)$ (P = 8 GPa; MB1)				
Atom	x	y	z	U_{eq}
Pt1	0.30315(9)	0.83490(7)	0.60373(3)	0.01946(19)
Pt2	0.77746(9)	0.76275(7)	0.44698(4)	0.01991(19)
Xe1	0.69365(17)	0.98101(14)	0.78817(7)	0.0261(3)
F8	0.805(2)	0.5526(15)	0.4209(9)	0.031(2)
F7	0.4574(18)	0.7154(14)	0.5077(6)	0.0228(15)
F5	0.249(2)	1.0122(13)	0.5218(7)	0.0238(15)
F2	0.6276(17)	0.9262(15)	0.6390(7)	0.0268(19)
F3	0.359(2)	0.6743(14)	0.6873(7)	0.0268(18)
F6	−0.0286(19)	0.7377(14)	0.5675(8)	0.0250(18)
F10	1.082(2)	0.8062(18)	0.3892(8)	0.030(2)
F9	0.578(2)	0.7799(16)	0.3387(8)	0.028(2)
F4	0.157(2)	0.9511(16)	0.6951(8)	0.0272(18)
F1	0.800(2)	1.0008(17)	0.9126(8)	0.034(2)

Table B.16: Summary of selected bond distances (Å) and angles (°) for $XeF_2 \cdot 2PtF_4(mP52)$ at different pressures.

$XeF_2 \cdot 2PtF_4(mP52)$				
	1 atm, 100 K [197]	4.0 GPa	4.7 GPa	8.6 GPa
Xe–F$_t$	1.909(10)	1.80(5)	1.87(2)	1.912(12)
Xe–F$_b$	2.316(8)	2.37(4)	2.289(19)	2.280(10)
M–F$_b$(Xe)	1.932(8)	1.88(4)	1.914(15)	1.897(9)
M–F$_b$(M)	1.957(7)–2.032(7)	1.96(2)–2.09(4)	1.954(19)–2.033(17)	1.951(11)–2.018(12)
M–F$_t$	1.863(7)–1.905(11)	1.86(2)–1.93(3)	1.866(15)–1.922(16)	1.836(13)–1.897(9)
M–F–M	131.9(5)–133.0(4)	125.5(19)–130.2(10)	127.5(9)–129.6(8)	115.7(4)–128.1(6)
***cis*-F–M–F**	86.2(4)–92.2(4)	86.1(12)–95.3(14)	85.0(7)–92.9(9)	86.0(5)–94.9(5)
***trans*-F–M–F**	177.2(4)–179.5(4)	174.0(17)–179.1(15)	176.0(7)–179.1(8)	176.1(4)–179.6(6)
F–Xe–F	176.0(5)	173.9(8)	173.8(8)	169.7(5)

Table B.17: Crystallographic data for $XeF_2 \cdot 2PtF_4$(*aP*26)-I and $XeF_2 \cdot 2PtF_4$(*aP*26)-II.

Compound	$XeF_2 \cdot 2PtF_4$(*aP*26)-I	$XeF_2 \cdot 2PtF_4$(*aP*26)-II
Pressure (GPa)	4.0	8.6
Run Index	SD2	MB1
Facility	DESY P02.2	DESY P02.2
Formula	$XePt_2F_{10}$	
F_w	711.48	
Crystal system	Triclinic	
Space group	$P\bar{1}$	
a (Å)	5.3010(11)	4.7094(9)
b (Å)	8.3438(9)	8.5969(15)
c (Å)	9.4937(18)	8.7976(18)
α (°)	65.851(14)	70.081(17)
β (°)	74.318(17)	77.060(17)
γ (°)	77.911(13)	79.315(16)
V (Å^3)	366.56(12)	324.05(12)
Z	2	2
ρ_{calc} (g/cm^3)	6.446	7.292
λ (Å)	0.2898	0.2906
μ (mm^{-1})	6.028	6.870
$F(000)$	600	600
$2\theta_{max}$ (°)	35.7020	34.9660
Index ranges	$-5 \leq h \leq 7$	$-9 \leq h \leq 6$
	$-14 \leq k \leq 14$	$-17 \leq k \leq 16$
	$-13 \leq l \leq 16$	$-12 \leq l \leq 15$
Reflections collected	1911	939
Independent reflections	1330	895
Reflections with $[I > 2\sigma(I)]$	1063	826
R_{int}	0.0223	0.0131
R_{sigma}	0.0222	0.0056
Data/restraints/parameters	1330/95[a]/118	895/95[a]/118
S	1.057	1.023
R_1, wR_2 $[I > 2\sigma(I)]$	0.0587, 0.1738	0.0548, 0.1449
R_1, wR_2 [all data]	0.0680, 0.1825	0.0567, 0.1482
$\Delta\rho_{min}$, $\Delta\rho_{max}$ (e/Å^3)	−2.015, 3.307	−2.151, 2.114

[a]Restraints used: RIGU

Table B.18: Fractional atomic coordinates and equivalent isotropic displacement parameters (Å^2) for $XeF_2 \cdot 2PtF_4$(*aP*26)-I and $XeF_2 \cdot 2PtF_4$(*aP*26)-II.

$XeF_2 \cdot 2PtF_4$(*aP*26)-I (P = 4.0 GPa; SD2)				
Atom	x	y	z	U_{eq}
Pt2	0.1542(2)	0.28773(7)	0.38889(12)	0.0298(7)
Pt1	0.7911(2)	0.08832(8)	0.24507(12)	0.0293(7)
Xe1	0.6064(5)	−0.26676(15)	0.1628(2)	0.0398(14)
F5	0.531(4)	0.2811(13)	0.281(2)	0.034(4)
F9	0.108(5)	0.5237(14)	0.249(2)	0.038(5)
F7	0.779(4)	−0.0317(12)	0.478(2)	0.039(4)
F10	−0.208(5)	0.2967(16)	0.484(3)	0.040(5)
F3	1.039(5)	−0.0878(17)	0.199(3)	0.043(5)
F2	0.517(5)	−0.0340(17)	0.249(3)	0.048(4)
F6	1.077(5)	0.2245(16)	0.222(3)	0.040(4)
F1	0.676(6)	−0.4308(16)	0.060(3)	0.053(9)
F8	0.244(5)	0.3541(17)	0.536(3)	0.044(5)
F4	0.807(6)	0.2154(18)	0.025(3)	0.046(5)
$XeF_2 \cdot 2PtF_4$(*aP*26)-II (P = 8.6 GPa; MB1)				
Atom	x	y	z	U_{eq}
Pt1	0.15942(19)	0.26304(8)	0.42962(12)	0.0164(5)
Pt2	0.21289(19)	−0.09369(8)	0.78574(11)	0.0156(5)
Xe1	−0.4788(4)	0.33500(14)	0.7966(2)	0.0202(9)
F6	0.084(4)	0.0912(14)	0.347(2)	0.019(4)
F10	−0.030(4)	0.0795(17)	0.854(3)	0.021(4)
F3	0.004(4)	0.4318(17)	0.260(3)	0.023(4)
F7	0.363(4)	0.0846(17)	0.599(3)	0.020(3)
F2	−0.216(5)	0.2469(19)	0.566(3)	0.023(3)
F5	0.538(4)	0.2821(16)	0.285(3)	0.020(3)
F4	0.253(4)	0.4160(16)	0.514(2)	0.023(4)
F9	0.495(5)	−0.0781(19)	0.898(3)	0.022(5)
F8	0.083(5)	−0.262(2)	0.960(3)	0.023(4)

Table B.19: Summary of selected bond distances (Å) and angles (°) for $XeF_2 \cdot 2PtF_4$(*aP*26)-I and $XeF_2 \cdot 2PtF_4$(*aP*26)-II.

	$XeF_2 \cdot 2PtF_4$(*aP*26)-I	**$XeF_2 \cdot 2PtF_4$(*aP*26)-II**
	4.0 GPa	8.6 GPa
Xe–F_t	1.912(19)	1.871(19)
Xe–F_b	2.320(16)	2.41(2)
M–F_b(Xe)	1.93(3)	1.90(3)
M–F_b(M)	1.966(11)–2.02(3)	1.93(2)–2.010(10)
M–F_t	1.866(12)–1.91(3)	1.80(3)–1.886(11)
M–F–M	127.6(6)–132.1(6)	124.3(9)–131.2(4)
***cis*-F–M–F**	85.7(9)–94.1(11)	82.2(8)–96.8(8)
***trans*-F–M–F**	175.2(5)–177.7(12)	174.6(10)–178.5(5)
F–Xe–F	171.1(10)	173.8(8)

References

[1] H. Cavendish, "Experiments on air.," *Philos. Trans. R. Soc. London*, no. 75, pp. 372–384, 1785, doi: 10.1098/rstl.1785.0023.

[2] J. W. Strutt, "On an anomaly encountered in determinations of the density of nitrogen gas," *Proc. R. Soc. London*, vol. 55, no. 331–335, pp. 340–344, Dec. 1894, doi: 10.1098/rspl.1894.0048.

[3] Lord Rayleigh and W. Ramsay, "Argon, a New Constituent of the Atmosphere," *Philos. Trans. R. Soc., A*, vol. 186, pp. 187–241, 1895, doi: 10.1098/rsta.1895.0006.

[4] W. Ramsay, "On a gas showing the spectrum of helium, the reputed cause of D3, one of the lines in the coronal spectrum. Preliminary note," *Proc. R. Soc. London*, vol. 58, no. 347–352, pp. 65–67, Dec. 1895, doi: 10.1098/rspl.1895.0006.

[5] W. Ramsay, "Helium, a gaseous constituent of certain minerals. Part I," *Proc. R. Soc. London*, vol. 58, no. 347–352, pp. 80–89, Dec. 1895, doi: 10.1098/rspl.1895.0010.

[6] W. Ramsay and M. W. Travers, "Argon and its companions," *Proc. R. Soc. London*, vol. 67, no. 435–441, pp. 329–333, Feb. 1901, doi: 10.1098/rspl.1900.0037.

[7] H. G. J. Moseley, "The high-frequency spectra of the elements. Part II," *Philos. Mag.*, vol. 27, no. 160, pp. 703–713, Apr. 1914, doi: 10.1080/14786440408635141.

[8] A. von Antropoff, "Die Wertigkeit der Edelgase und ihre Stellung im periodischen System. II," *Angew. Chem.*, vol. 37, no. 36, pp. 695–696, 1924, doi: 10.1002/ange.19240373605.

[9] A. Von Antropoff, "Eine neue Form des periodischen Systems der Elemente," *Angew. Chem.*, vol. 39, no. 23, pp. 722–725, 1926, doi: 10.1002/ange.19260392303.

[10] M. H. Moissan, "Action du Fluor sur l'Argon," *Proc. R. Soc. London*, vol. 58, pp. 120–121, 1895, doi: 10.1098/rspl.1895.0017.

[11] G. Oddo, "Sul potere di combinarsi del cripton e dello xenon: due lettere inedite del prof. W. Ramsay",," *Gazz. Chim. Ital.*, vol. 62, pp. 380–395, 1932.

[12] G. J. Schrobilgen, "Chemistry at the Edge of the Periodic Table: The Importance of Periodic Trends on the Discovery of the Noble Gases and the Development of Noble-Gas Chemistry," in *The Periodic Table I: Historical Development and Essential Features*, D. M. P. Mingos, Ed., Cham, Switzerland: Springer International Publishing, 2019, pp. 157–196. doi: 10.1007/430_2019_49.

[13] W. L. J. Kossel, "Über Molekülbildung als Frage des Atombaus," *Ann. Phys.*, vol. 49, pp. 229–362, 1916, doi: 10.1002/andp.19163540302.

[14] G. N. Lewis, "The atom and the molecule," *J. Am. Chem. Soc.*, vol. 38, no. 4, pp. 762–785, Apr. 1916, doi: 10.1021/ja02261a002.

[15] A. von Antropoff, K. Weil, and H. Frauenhof, "Die Gewinnung von Halogenverbindungen der Edelgase," *Naturwissenschaften*, vol. 20, no. 37, pp. 688–689, Sep. 1932, doi: 10.1007/BF01494407.

[16] A. von Antropoff, H. Frauenhof, and K. H. Krüger, "Nachtrag zur vorläufigen Mitteilung über „Die Gewinnung von Halogenverbindungen der Edelgase"," *Naturwissenschaften*, vol. 21, no. 17, pp. 315–315, Apr. 1933, doi: 10.1007/BF01490925.

[17] O. Ruff and W. Menzel, "Das Verhalten von Fluor gegen Argon und Krypton unter dem Einfluß elektrischer Entladungen," *Z. Anorg. Allg. Chem.*, vol. 213, no. 1–2, pp. 206–207, 1933, doi: 10.1002/zaac.19332130121.

[18] L. Pauling, "The formulas of antimonic acid and the antimonates," *J. Am. Chem. Soc.*, vol. 55, no. 5, pp. 1895–1900, 1933, doi: 10.1021/ja01332a016.

[19] J. A. Labinger, "Why isn't noble gas chemistry 30 years older? The failed (?) 1933 experiment of Yost and Kaye," *Bull. Hist. Chem.*, vol. 40, no. 1, pp. 29–36, 2015.

[20] D. M. Yost and A. L. Kaye, "An attempt to prepare a chloride or fluoride of xenon," *J. Am. Chem. Soc.*, vol. 55, no. 9, pp. 3890–3892, 1933, doi: 10.1021/ja01336a506.

[21] J. L. Weeks, C. L. Chernick, and M. S. Matheson, "Photochemical Preparation of Xenon Difluoride," *J. Am. Chem. Soc.*, vol. 84, no. 23, pp. 4612–4613, Dec. 1962, doi: 10.1021/ja00882a063.

[22] L. Pauling, in *General chemistry: An introduction to descriptive chemistry and modern chemical theory*, San Francisco, USA: W.H. Freeman, 1947, p. 67.

[23] P. Laszlo and G. J. Schrobilgen, "One or Several Pioneers? The Discovery of Noble-Gas Compounds," *Angew. Chem. Int. Ed. Engl.*, vol. 27, no. 4, pp. 479–489, 1988, doi: 10.1002/anie.198804791.

[24] G. C. Pimentel, "The Bonding of Trihalide and Bifluoride Ions by the Molecular Orbital Method," *J. Chem. Phys.*, vol. 19, no. 4, pp. 446–448, Apr. 1951, doi: 10.1063/1.1748245.

[25] N. Bartlett, "Forty Years of Fluorine Chemistry," in *Fluorine Chemistry at the Millennium: Fascinated by Fluorine*, R. E. Banks, Ed., Amsterdam, NY, USA: Elsevier Science, 2000, pp. 29–55.

[26] N. Bartlett and D. H. Lohmann, "Two New Fluorides of Platinum," *Proc. Chem. Soc.*, pp. 14–15, 1960, doi: 10.1039/PS9600000001.

[27] N. Bartlett and D. H. Lohmann, "Dioxygenyl Hexafluoroplatinate(V) $O_2^+[PtF_6]^-$," *Proc. Chem. Soc.*, p. 118, Mar. 1962, doi: 10.1039/PS9620000097.

[28] N. Bartlett, *The oxidation of oxygen and related chemistry: selected papers of Neil Bartlett*. in World Scientific series in 20th century chemistry, no. 9. Singapore; River Edge, NJ: World Scientific, 2001.

[29] N. Bartlett, "Xenon Hexafluoroplatinate(V) $Xe^+[PtF_6]^-$," *Proc. Chem. Soc.*, p. 218, Jun. 1962, doi: 10.1039/PS9620000197.

[30] H. H. Claassen, H. Selig, and J. G. Malm, "Xenon Tetrafluoride," *J. Am. Chem. Soc.*, vol. 84, no. 18, pp. 3593–3593, Sep. 1962, doi: 10.1021/ja00877a042.

[31] F. Schreiner, G. N. McDonald, and C. L. Chernick, "Vapor pressure and melting points of xenon difluoride and xenon tetrafluoride," *J. Phys. Chem.*, vol. 72, no. 4, pp. 1162–1166, 1968, doi: 10.1021/j100850a014.

[32] D. H. Templeton, A. Zalkin, J. D. Forrester, and S. M. Williamson, "Crystal and Molecular Structure of Xenon Tetrafluoride," *J. Am. Chem. Soc.*, vol. 85, no. 2, p. 242, Jan. 1963, doi: 10.1021/ja00885a038.

[33] R. E. Rundle, "On the Problem Structure of XeF_4 and XeF_2," *J. Am. Chem. Soc.*, vol. 85, no. 1, pp. 112–113, Jan. 1963, doi: 10.1021/ja00884a026.

[34] R. J. Gillespie, "The electron-pair repulsion model for molecular geometry," *J. Chem. Educ.*, vol. 47, no. 1, p. 18, Jan. 1970, doi: 10.1021/ed047p18.

[35] C. L. Chernick *et al.*, "Fluorine Compounds of Xenon and Radon," *Science*, vol. 138, no. 3537, pp. 136–138, Oct. 1962, doi: 10.1126/science.138.3537.136.

[36] R. Hoppe, W. Dähne, H. Mattauch, and K. M. Rödder, "Fluorierung von Xenon," *Angew. Chem.*, vol. 74, no. 22, p. 903, 1962, doi: 10.1002/ange.19620742213.

[37] H. A. Levy and P. A. Agron, "The crystal and molecular structure of xenon difluoride by neutron diffraction," *J. Am. Chem. Soc.*, vol. 85, no. 2, pp. 241–242, 1963.

[38] S. Siegel and E. Gebert, "Crystallographic studies of XeF_2 and XeF_4," *J. Am. Chem. Soc.*, vol. 85, no. 2, pp. 240–240, 1963, doi: 10.1021/ja00885a035.

[39] H. St. A. Elliott, J. F. Lehmann, H. P. A. Mercier, H. D. B. Jenkins, and G. J. Schrobilgen, "X-ray Crystal Structures of $[XeF][MF_6]$ (M = As, Sb, Bi), $[XeF][M_2F_{11}]$ (M = Sb, Bi) and Estimated Thermochemical Data and Predicted Stabilities for Noble-Gas Fluorocation Salts using Volume-Based Thermodynamics," *Inorg. Chem.*, vol. 49, no. 18, pp. 8504–8523, Sep. 2010, doi: 10.1021/ic101152x.

[40] S. Hoyer, T. Emmler, and K. Seppelt, "The structure of xenon hexafluoride in the solid state," *J. Fluorine Chem.*, vol. 127, no. 10, pp. 1415–1422, Oct. 2006, doi: 10.1016/j.jfluchem.2006.04.014.

[41] D. A. Dixon, W. A. de Jong, K. A. Peterson, K. O. Christe, and G. J. Schrobilgen, "Heats of Formation of Xenon Fluorides and the Fluxionality of XeF_6 from High Level Electronic Structure Calculations," *J. Am. Chem. Soc.*, vol. 127, no. 24, pp. 8627–8634, Jun. 2005, doi: 10.1021/ja0423116.

[42] J. Slivnik *et al.*, "Uber die Synthese von XeF_6," *Croat. Chem. Acta*, vol. 34, p. 253, Dec. 1962.

[43] J. G. Malm, I. Sheft, and C. L. Chernick, "Xenon hexafluoride," *J. Am. Chem. Soc.*, vol. 85, no. 1, pp. 110–111, 1963, doi: 10.1021/ja00884a024.

[44] F. B. Dudley, G. Gard, and G. H. Cady, "Xenon hexafluoride," *Inorg. Chem.*, vol. 2, no. 1, pp. 228–229, 1963, doi: 10.1021/ic50005a064.

[45] E. E. Weaver, B. Weinstock, and C. P. Knop, "Xenon Hexafluoride," *J. Am. Chem. Soc.*, vol. 85, no. 1, pp. 111–112, 1963, doi: 10.1021/ja00884a025.

[46] R. M. Gavin and L. S. Bartell, "Molecular Structure of XeF_6. I. Analysis of Electron-Diffraction Intensities," *J. Chem. Phys.*, vol. 48, no. 6, pp. 2460–2465, Mar. 1968, doi: 10.1063/1.1669470.

[47] L. S. Bartell and R. M. Gavin, "Molecular Structure of XeF_6. II. Internal Motion and Mean Geometry Deduced by Electron Diffraction," *J. Chem. Phys.*, vol. 48, no. 6, pp. 2466–2483, Mar. 1968, doi: 10.1063/1.1669471.

[48] P. A. Agron, C. K. Johnson, and H. A. Levy, "Xenon hexafluoride: Crystallographic data and phase transitions," *Inorg. Nucl. Chem. Lett.*, vol. 1, no. 4, pp. 145–148, Dec. 1965, doi: 10.1016/S0020-1650(65)80023-X.

[49] R. D. Burbank and G. R. Jones, "Xenon Hexafluoride: Structure of a Cubic Phase at -80°C," *Science*, vol. 168, no. 3928, pp. 248–249, Apr. 1970, doi: 10.1126/science.168.3928.248.

[50] R. D. Burbank and G. R. Jones, "Xenon Hexafluoride: Structural Crystallography of Tetrameric Phases," *Science*, vol. 171, no. 3970, pp. 485–487, Feb. 1971, doi: 10.1126/science.171.3970.485.

[51] F. Schreiner, D. W. Osborne, J. G. Malm, and G. N. McDonald, "Heat Capacity and Other Thermodynamic Functions of Xenon Hexafluoride from 5 to 350°K," *J. Chem. Phys.*, vol. 51, no. 11, pp. 4838–4851, Dec. 1969, doi: 10.1063/1.1671875.

[52] B. Žemva, "Binary Fluorides of Noble-Gases and Their Compounds," *Croat. Chem. Acta*, vol. 61, no. 1, pp. 163–187, 1988.

[53] A. V. Grosse, A. D. Kirshenbaum, A. G. Streng, and L. V. Streng, "Krypton Tetrafluoride: Preparation and Some Properties," *Science*, vol. 139, no. 3559, pp. 1047–1048, Mar. 1963, doi: 10.1126/science.139.3559.1047.

[54] F. Schreiner, J. G. Malm, and J. C. Hindman, "The Preparation and Nuclear Magnetic Resonance of Krypton Difluoride," *J. Am. Chem. Soc.*, vol. 87, no. 1, pp. 25–28, 1965, doi: 10.1021/ja01079a006.

[55] J. J. Turner and G. C. Pimentel, "Krypton Fluoride: Preparation by the Matrix Isolation Technique," *Science*, vol. 140, no. 3570, pp. 974–975, May 1963, doi: 10.1126/science.140.3570.974.b.

[56] J. Slivnik, A. Šmalc, K. Lutar, B. Žemva, and B. Frlec, "A new method for the preparation of krypton difluoride," *J. Fluorine Chem.*, vol. 5, no. 3, pp. 273–274, 1975, doi: 10.1016/S0022-1139(00)82488-4.

[57] V. N. Bezmel'nitsyn, V. A. Legasov, and B. B. Chaivanov, "Synthesis of krypton difluoride using a thermally generated flow of atomic fluorine," *Dokl. Chem.*, vol. 235, pp. 365–367, 1977.

[58] S. R. Gunn, "Heat of formation of krypton difluoride," *J. Phys. Chem.*, vol. 71, no. 9, pp. 2934–2937, Aug. 1967, doi: 10.1021/j100868a025.

[59] J. F. Lehmann, H. P. A. Mercier, and G. J. Schrobilgen, "The chemistry of krypton," *Coord. Chem. Rev.*, vol. 233–234, pp. 1–39, Nov. 2002, doi: 10.1016/S0010-8545(02)00202-3.

[60] K. O. Christe and D. A. Dixon, "A quantitative scale for the oxidizing strength of oxidative fluorinators," *J. Am. Chem. Soc.*, vol. 114, no. 8, pp. 2978–2985, Apr. 1992, doi: 10.1021/ja00034a033.

[61] G. Lucier, C. Shen, W. J. Casteel, L. Chacón, and N. Barlett, "Some chemistry of high oxidation state transition metal fluorides in anhydrous HF," *J. Fluorine Chem.*, vol. 72, no. 2, pp. 157–163, Jun. 1995, doi: 10.1016/0022-1139(94)00401-Z.

[62] P. R. Fields, Lawrence. Stein, and M. H. Zirin, "Radon Fluoride," *J. Am. Chem. Soc.*, vol. 84, no. 21, pp. 4164–4165, Nov. 1962, doi: 10.1021/ja00880a048.

[63] L. Stein, "The Chemistry of Radon," *Radiochim. Acta*, vol. 32, no. 1–3, pp. 163–172, Jun. 1983, doi: 10.1524/ract.1983.32.13.163.

[64] D. Naumann and W. Tyrra, "The first compound with a stable xenon-carbon bond: ^{19}F- and ^{129}Xe-N.M.R. spectroscopic evidence for pentafluorophenylxenon(II)

fluoroborates," *J. Chem. Soc., Chem. Commun.*, no. 1, pp. 47–50, Jan. 1989, doi: 10.1039/C39890000047.

[65] H. J. Frohn and S. Jakobs, "The pentafluorophenylxenon(II) cation: $[C_6F_5Xe]^+$; the first stable system with a xenon–carbon bond," *J. Chem. Soc., Chem. Commun.*, no. 10, pp. 625–627, Jan. 1989, doi: 10.1039/C39890000625.

[66] R. D. LeBlond and D. D. DesMarteau, "Fluoro[imidobis(sulphuryl fluoride)]xenon. An example of a xenon–nitrogen bond," *J. Chem. Soc., Chem. Commun.*, no. 14, pp. 555–556, Jan. 1974, doi: 10.1039/C39740000555.

[67] M. Wechsberg, P. A. Bulliner, F. O. Sladky, R. Mews, and Neil. Bartlett, "Fluorosulfates and perchlorates of xenon(II) and the salt $[(FXeO)_2S(O)F]^+[AsF_6]^-$," *Inorg. Chem.*, vol. 11, no. 12, pp. 3063–3070, Dec. 1972, doi: 10.1021/ic50118a038.

[68] S. Seidel and K. Seppelt, "The $XeCl^+$ Ion: $[XeCl]^+[Sb_2F_{11}]^-$," *Angew. Chem. Int. Ed.*, vol. 40, no. 22, pp. 4225–4227, 2001, doi: 10.1002/1521-3773(20011119)40:22%3C4225::AID-ANIE4225%3E3.0.CO;2-3.

[69] L. Stein, J. R. Norris, A. J. Downs, and A. R. Minihan, "Formation of the dixenon cation, Xe_2^+, in fluoroantimonate(V) media by oxidation–reduction methods: spectroscopic properties of the ion," *J. Chem. Soc., Chem. Commun.*, no. 12, pp. 502–504, Jan. 1978, doi: 10.1039/C39780000502.

[70] M. Tramšek and B. Žemva, "Synthesis, Properties and Chemistry of Xenon(II) Fluoride," *Acta Chim. Slov.*, vol. 53, pp. 105–116, 2006.

[71] A. Šmalc and K. Lutar, "Xenon Difluoride (modification)," in *Inorganic Syntheses*, vol. 29, R. N. Grimes, Ed., John Wiley & Sons, 1992, pp. 1–4.

[72] C. A. Coulson, "The nature of the bonding in xenon fluorides and related molecules," *J. Chem. Soc.*, pp. 1442–1454, Jan. 1964, doi: 10.1039/JR9640001442.

[73] B. Braïda and P. C. Hiberty, "The essential role of charge-shift bonding in hypervalent prototype XeF_2," *Nat. Chem.*, vol. 5, no. 5, pp. 417–422, May 2013, doi: 10.1038/nchem.1619.

[74] N. Bartlett and F. O. Sladky, "The Chemistry of Krypton, Xenon and Radon," in *Comprehensive Inorganic Chemistry*, vol. 1, J. C. Bailar, H. J. Emeleus, R. Nyholm, and A. F. Trotman-Dickerson, Eds., Oxford and New York, pp. 213–330.

[75] B. Grüttner, M. F. A. Dove, and A. F. Clifford, *Chemistry in Anhydrous, Prototropic Inorganic Solvents, Inorganic Chemistry in Liquid Hydrogen Cyanide and Liquid Hydrogen Fluoride*, vol. 2. Oxford: Pergamon Press, 1971.

[76] R. C. Burns, I. D. MacLeod, T. A. O'Donnell, T. E. Peel, K. A. Phillips, and A. B. Waugh, "Xenon difluoride as a selective inorganic fluorinating reagent," *J. Inorg. Nucl. Chem.*, vol. 39, no. 10, pp. 1737–1739, Jan. 1977, doi: 10.1016/0022-1902(77)80193-0.

[77] T. Drews, D. Rusch, S. Seidel, S. Willemsen, and K. Seppelt, "Systematic Reactions of $[Pt(PF_3)_4]$," *Chem. Eur. J.*, vol. 14, no. 14, pp. 4280–4286, 2008, doi: 10.1002/chem.200701786.

[78] B. Žemva, J. Zupan, and J. Slivnik, "On the $XeMnF_6$ synthesis," *J. Inorg. Nucl. Chem.*, vol. 33, no. 11, pp. 3953–3955, Nov. 1971, doi: 10.1016/0022-1902(71)80305-6.

[79] N. Bartlett, B. Žemva, and L. Graham, "Redox reactions in the XeF_2/platinum fluoride and XeF_2/palladium fluoride systems and the conversion of XeF_2 to XeF_4 and Xe," *J. Fluorine Chem.*, vol. 7, no. 1, pp. 301–320, Jan. 1976, doi: 10.1016/S0022-1139(00)84003-8.

[80] R. Stine, W.-K. Lee, K. E. Jr. Whitener, J. T. Robinson, and P. E. Sheehan, "Chemical Stability of Graphene Fluoride Produced by Exposure to XeF_2," *Nano Lett.*, vol. 13, no. 9, pp. 4311–4316, Sep. 2013, doi: 10.1021/nl4021039.

[81] N. I. Denisenko *et al.*, "T_h-$C_{60}F_{24}$," *J. Am. Chem. Soc.*, vol. 126, no. 6, pp. 1618–1619, Feb. 2004, doi: 10.1021/ja039361f.

[82] H. Poleschner and K. Seppelt, "XeF_2/Fluoride Acceptors as Versatile One-Electron Oxidants," *Angew. Chem. Int. Ed.*, vol. 52, no. 49, pp. 12838–12842, 2013, doi: 10.1002/anie.201307161.

[83] J. Berkowitz, W. A. Chupka, P. M. Guyon, J. H. Holloway, and R. Spohr, "Photoionization mass spectrometric study of XeF_2, XeF_4, and XeF_6," *J. Phys. Chem.*, vol. 75, no. 10, pp. 1461–1471, 1971.

[84] B. Žemva, A. Jesih, D. H. Templeton, A. Zalkin, A. K. Cheetham, and N. Bartlett, "Phases in the system XeF_2/XeF_5AsF_6 and structural and vibrational evidence for the following ionization pathway: $XeF_2 \rightarrow XeF^+ + F^-$," *J. Am. Chem. Soc.*, vol. 109, no. 24, pp. 7420–7427, Nov. 1987, doi: 10.1021/ja00258a028.

[85] N. Bartlett, B. G. DeBoer, F. J. Hollander, F. O. Sladky, D. H. Templeton, and A. Zalkin, "Crystal structures of $[Xe_2F_3^+][AsF_6^-]$ and $[XeF_5^+][AsF_6^-]$," *Inorg. Chem.*, vol. 13, no. 4, pp. 780–785, Apr. 1974, doi: 10.1021/ic50134a004.

[86] A. Zalkin, D. L. Ward, R. N. Biagioni, D. H. Templeton, and N. Bartlett, "Crystal structure of $[XeF^+][AsF_6^-]$," *Inorg. Chem.*, vol. 17, no. 5, pp. 1318–1322, May 1978, doi: 10.1021/ic50183a044.

[87] R. J. Gillespie and B. Landa, "Raman spectra of some xenon(II) compounds1," *Inorg. Chem.*, vol. 12, no. 6, pp. 1383–1389, Jun. 1973, doi: 10.1021/ic50124a034.

[88] J. H. Holloway, G. J. Schrobilgen, and P. Taylor, "The preparation and characterisation of $XeF_2 \cdot WOF_4$ and $XeF_2 \cdot 2WOF_4$ by ^{19}F nuclear magnetic resonance and Raman spectroscopy. Examples of non-labile xenon–fluorine–metal bridges.," *J. Chem. Soc., Chem. Commun.*, no. 2, pp. 40–41, Jan. 1975, doi: 10.1039/C39750000040.

[89] J. H. Holloway and G. J. Schrobilgen, "Fluorine-19 and xenon-129 NMR studies of the $XeF_2 \cdot n WOF_4$ and $XeF_2 \cdot n MoOF_4$ (n = 1-4) adducts: examples of nonlabile xenon-fluorine-metal bridges in solution," *Inorg. Chem.*, vol. 19, no. 9, pp. 2632–2640, Sep. 1980, doi: 10.1021/ic50211a031.

[90] H. P. A. Mercier, U. Breddemann, D. S. Brock, M. R. Bortolus, and G. J. Schrobilgen, "Syntheses, Structures, and Bonding of $NgF_2 \cdot CrOF_4$, $NgF_2 \cdot 2CrOF_4$ (Ng=Kr, Xe), and $(CrOF_4)_\infty$," *Chem. Eur. J.*, vol. 25, no. 52, pp. 12105–12119, 2019, doi: 10.1002/chem.201902005.

[91] M. R. Bortolus, H. P. A. Mercier, D. S. Brock, and G. J. Schrobilgen, "Noble-Gas Difluoride Complexes of MOF_4 (M=Mo, W); Syntheses, Structures and Bonding of $NgF_2 \cdot MOF_4$ and $XeF_2 \cdot 2MOF_4$ (Ng=Kr, Xe)," *Chem. Eur. J.*, vol. 28, no. 15, p. e202103729, 2022, doi: 10.1002/chem.202103729.

[92] M. Lozinšek, "Sinteza in karakterizacija novih spojin šibko koordinirajocih fluoridoanionov," Ph. D. thesis, University of Ljubljana, Ljubljana, Slovenia, 2013.

[93] M. Tramšek and B. Žemva, "Synthesis of novel salts with HF, AsF_3 and XeF_2 as ligands to metal cations," *J. Fluorine Chem.*, vol. 127, no. 10, pp. 1275–1284, Oct. 2006, doi: 10.1016/j.jfluchem.2006.05.014.

[94] D. S. Brock, G. J. Schrobilgen, and B. Žemva, "Noble-Gas Chemistry," in *Comprehensive Inorganic Chemistry II*, vol. 1, Amsterdam, Netherlands: Elsevier, 2013, pp. 755–822. doi: 10.1016/B978-0-08-097774-4.00128-5.

[95] G. Tavčar and M. Tramšek, "XeF_2 as a ligand to a metal center, an interesting field of noble gas chemistry," *J. Fluorine Chem.*, vol. 174, pp. 14–21, Jun. 2015, doi: 10.1016/j.jfluchem.2014.08.009.

[96] D. S. Brock, J. J. Casalis de Pury, H. P. A. Mercier, G. J. Schrobilgen, and B. Silvi, "XeF_2 Coordination to a Halogen Center; Raman Spectra ($n = 1, 2$) and X-ray Crystal Structures ($n = 2$) of $[BrOF_2][AsF_6] \cdot n XeF_2$ and $[XOF_2][AsF_6]$ (X = Cl, Br)," *Inorg. Chem.*, vol. 49, no. 14, pp. 6673–6689, Jul. 2010, doi: 10.1021/ic100712y.

[97] M. R. Bortolus, G. J. LaChapelle, H. P. A. Mercier, J. Haner, and G. J. Schrobilgen, "XeF_2 Coordination Complexes of the $[BrO_2]^+$ Cation, $[O_2Br(FXeF)_n][AsF_6]$ ($n = 1$, 2) and $[O_2Br(FXeF)_2][SbF_6]$; Their Syntheses and Structural Characterizations," *Inorg. Chem.*, vol. 62, no. 23, pp. 8761–8771, Jun. 2023, doi: 10.1021/acs.inorgchem.3c01030.

[98] N. Bartlett and N. K. Jha, "The xenon-platinum hexafluoride reaction and related reactions," in *Noble-gas compounds*, H. H. Hyman, Ed., Chicago: The University of Chicago Press, 1963, pp. 23–30.

[99] F. O. Sladky, P. A. Bulliner, and N. Bartlett, "Xenon difluoride as a fluoride ion donor. Evidence for the salts $[Xe_2F_3]^+[MF_6]^-$,$[XeF]^+[MF_6]^-$ and $[XeF]^+[M_2F_{11}]^-$," *J. Chem. Soc. A*, pp. 2179–2188, 1969, doi: 10.1039/J19690002179.

[100] L. Graham, O. Graudejus, N. K. Jha, and N. Bartlett, "Concerning the nature of $XePtF_6$," *Coord. Chem. Rev.*, vol. 197, no. 1, pp. 321–334, Feb. 2000, doi: 10.1016/S0010-8545(99)00190-3.

[101] S. Rüdiger and H. Meinert, "Zur Chemie der Edelgase; Reaktionen im geschmolzenen Xenondifluorid," *Z. Chem.*, vol. 9, no. 11, pp. 434–434, 1969, doi: 10.1002/zfch.19690091119.

[102] V. A. Legasov and A. S. Marinin, "Xenon difluoride reaction with carbon, silicon, tin and titanium tetrachlorides," *Zh. Neorg. Khim.*, vol. 17, no. 9, p. 2408, 1972.

[103] B. Žemva, J. Slivnik, and M. Bohinc, "On the syntheses of xenon fluorotitanates(IV)," *J. Inorg. Nucl. Chem.*, vol. 38, no. 1, pp. 73–74, Jan. 1976, doi: 10.1016/0022-1902(76)80051-6.

[104] K. Radan, E. Goreshnik, and B. Žemva, "Xenon(II) Polyfluoridotitanates(IV): Synthesis and Structural Characterization of $[Xe_2F_3]^+$ and $[XeF]^+$ Salts," *Angew. Chem Int. Ed.*, vol. 53, no. 50, pp. 13715–13719, 2014, doi: 10.1002/anie.201406404.

[105] H. Bialowons, M. Müller, and B. G. Müller, "Titantetrafluorid – Eine überraschend einfache Kolumnarstruktur," *Z. Anorg. Allg. Chem.*, vol. 621, no. 7, pp. 1227–1231, 1995, doi: 10.1002/zaac.19956210720.

[106] K. Radan, "Interactions of xenon(II) fluoride with some metal tetrafluorides," Ph. D. thesis, Jožef Stefan International Postgraduate School, Ljubljana, Slovenia, 2017.

[107] J. Slivnik and B. Žemva, "Reaktionen von Chrom(V)—fluorid mit Xenon und Xenondifluorid," *Z. Anorg. Allg. Chem.*, vol. 385, no. 1–2, pp. 137–141, 1971, doi: 10.1002/zaac.19713850119.

[108] K. Lutar, I. Leban, T. Ogrin, and B. Žemva, "$XeF_2 \cdot CrF_4$ and $(XeF_5^+CrF_5^-)_4 \cdot XeF_4$: Syntheses, crystal structures and some properties," *Eur. J. Solid State Inorg. Chem.*, vol. 29, pp. 713–727, 1992.

[109] K. Lutar, H. Borrmann, and B. Žemva, "$XeF_2 \cdot 2CrF_4$ and $XeF_5^+CrF_5^-$: Syntheses, Crystal Structures, and Some Properties," *Inorg. Chem.*, vol. 37, no. 12, pp. 3002–3006, Jun. 1998, doi: 10.1021/ic971580c.

[110] J. Levec, J. Slivnik, and B. Žemva, "The influence of some hexafluoromanganates(IV) on the reaction between xenon and fluorine under pressure," *Vestn. Slov. Kem. Druš.*, vol. 20, pp. 13–20, 1973.

[111] M. Bohinc, J. Grannec, J. Slivnik, and B. Žemva, "On the syntheses of xenon fluoromanganates(IV)," *J. Inorg. Nucl. Chem.*, vol. 38, no. 1, pp. 75–76, Jan. 1976, doi: 10.1016/0022-1902(76)80052-8.

[112] M. Lozinšek, "Synthesis and Characterization of Xenon(II) Hexafluoromanganates(IV)," Diploma thesis, University of Ljubljana, 2008.

[113] B. K. Morrell, A. Zalkin, A. Tressaud, and N. Bartlett, "Crystal structure of rhodium pentafluoride," *Inorg. Chem.*, vol. 12, no. 11, pp. 2640–2644, Nov. 1973, doi: 10.1021/ic50129a029.

[114] B. Družina and B. Žemva, "On the synthesis of xenon(II) fluorostannates(IV)," *J. Fluorine Chem.*, vol. 34, no. 2, pp. 233–239, Dec. 1986, doi: 10.1016/S0022-1139(00)85073-3.

[115] A. Saha, S. S. Nia, and J. A. Rodríguez, "Electron Diffraction of 3D Molecular Crystals," *Chem. Rev.*, vol. 122, no. 17, pp. 13883–13914, Sep. 2022, doi: 10.1021/acs.chemrev.1c00879.

[116] C. Davisson and L. H. Germer, "Diffraction of Electrons by a Crystal of Nickel," *Phys. Rev.*, vol. 30, no. 6, pp. 705–740, Dec. 1927, doi: 10.1103/PhysRev.30.705.

[117] C. Davisson and L. H. Germer, "The Scattering of Electrons by a Single Crystal of Nickel," *Nature*, vol. 119, no. 2998, pp. 558–560, Apr. 1927, doi: 10.1038/119558a0.

[118] G. P. Thomson and A. Reid, "Diffraction of Cathode Rays by a Thin Film," *Nature*, vol. 119, no. 3007, pp. 890–890, Jun. 1927, doi: 10.1038/119890a0.

[119] W. E. Laschkarew and I. D. Usyskin, "Die Bestimmung der Lage der Wasserstoffionen im NH_4Cl-Kristallgitter durch Elektronenbeugung," *Z. Phys.*, vol. 85, no. 9, pp. 618–630, Sep. 1933, doi: 10.1007/BF01331003.

[120] A. Charlesby, G. I. Finch, and H. Wilman, "The diffraction of electrons by anthracene," *Proc. Phys. Soc.*, vol. 51, no. 3, p. 479, May 1939, doi: 10.1088/0959-5309/51/3/312.

[121] M. Gemmi and A. E. Lanza, "3D electron diffraction techniques," *Acta Crystallogr. B*, vol. 75, no. 4, Art. no. 4, Aug. 2019, doi: 10.1107/S2052520619007510.

[122] S. Nicolopoulos *et al.*, "Direct Phasing in Electron Crystallography: Ab Initio Determination of a New MCM-22 Zeolite Structure," *J. Am. Chem. Soc.*, vol. 117, no. 35, pp. 8947–8956, Sep. 1995, doi: 10.1021/ja00140a008.

[123] U. Kolb, T. Gorelik, C. Kübel, M. T. Otten, and D. Hubert, "Towards automated diffraction tomography: Part I—Data acquisition," *Ultramicroscopy*, vol. 107, no. 6, pp. 507–513, Jun. 2007, doi: 10.1016/j.ultramic.2006.10.007.

[124] U. Kolb, T. Gorelik, and M. T. Otten, "Towards automated diffraction tomography. Part II—Cell parameter determination," *Ultramicroscopy*, vol. 108, no. 8, pp. 763–772, Jul. 2008, doi: 10.1016/j.ultramic.2007.12.002.

[125] M. Gemmi *et al.*, "3D Electron Diffraction: The Nanocrystallography Revolution," *ACS Cent. Sci.*, vol. 5, no. 8, pp. 1315–1329, Aug. 2019, doi: 10.1021/acscentsci.9b00394.

[126] E. Mugnaioli, T. Gorelik, and U. Kolb, "'Ab initio' structure solution from electron diffraction data obtained by a combination of automated diffraction tomography and precession technique," *Ultramicroscopy*, vol. 109, no. 6, pp. 758–765, May 2009, doi: 10.1016/j.ultramic.2009.01.011.

[127] D. Zhang, P. Oleynikov, S. Hovmöller, and X. Zou, "Collecting 3D electron diffraction data by the rotation method," *Z. Kristallogr.*, vol. 225, no. 2–3, pp. 94–102, Mar. 2010, doi: 10.1524/zkri.2010.1202.

[128] I. Nederlof, E. van Genderen, Y.-W. Li, and J. P. Abrahams, "A Medipix quantum area detector allows rotation electron diffraction data collection from submicrometre three-dimensional protein crystals," *Acta Crystallogr. D*, vol. 69, no. 7, pp. 1223–1230, Jul. 2013, doi: 10.1107/S0907444913009700.

[129] L. Palatinus, V. Petříček, and C. A. Corrêa, "Structure refinement using precession electron diffraction tomography and dynamical diffraction: theory and implementation," *Acta Crystallogr. A*, vol. 71, no. 2, Art. no. 2, Mar. 2015, doi: 10.1107/S2053273315001266.

[130] L. Palatinus *et al.*, "Structure refinement using precession electron diffraction tomography and dynamical diffraction: tests on experimental data," *Acta Crystallogr. B*, vol. 71, no. 6, pp. 740–751, Dec. 2015, doi: 10.1107/S2052520615017023.

[131] L. Palatinus *et al.*, "Hydrogen positions in single nanocrystals revealed by electron diffraction," *Science*, vol. 355, no. 6321, pp. 166–169, Jan. 2017, doi: 10.1126/science.aak9652.

[132] A. Suresh *et al.*, "Ionisation of atoms determined by kappa refinement against 3D electron diffraction data," *Nat. Commun.*, vol. 15, no. 1, p. 9066, Oct. 2024, doi: 10.1038/s41467-024-53448-2.

[133] P. B. Klar *et al.*, "Accurate structure models and absolute configuration determination using dynamical effects in continuous-rotation 3D electron diffraction data," *Nat. Chem.*, vol. 15, no. 6, pp. 848–855, Jun. 2023, doi: 10.1038/s41557-023-01186-1.

[134] K.-N. Truong *et al.*, "Making the Most of 3D Electron Diffraction: Best Practices to Handle a New Tool," *Symmetry*, vol. 15, no. 8, Aug. 2023, doi: 10.3390/sym15081555.

[135] S. Smeets and W. Wan, "Serial electron crystallography: merging diffraction data through rank aggregation," *J. Appl. Crystallogr.*, vol. 50, no. 3, pp. 885–892, Jun. 2017, doi: 10.1107/S1600576717005854.

[136] C. G. Jones *et al.*, "Characterization of Reactive Organometallic Species via MicroED," *ACS Cent. Sci.*, vol. 5, no. 9, pp. 1507–1513, Sep. 2019, doi: 10.1021/acscentsci.9b00403.

[137] L. R. Doyle *et al.*, "MicroED characterization of a robust cationic σ-alkane complex stabilized by the $[B(3,5\text{-}(SF_5)_2C_6H_3)_4]^-$ anion, via on-grid solid/gas single-crystal to single-crystal reactivity," *Dalton Trans.*, vol. 51, no. 9, pp. 3661–3665, Mar. 2022, doi: 10.1039/D2DT00335J.

[138] R. J. Hemley, "Effects of High Pressure on Molecules," *Annu. Rev. Phys. Chem.*, vol. 51, no. Volume 51, 2000, pp. 763–800, Oct. 2000, doi: 10.1146/annurev.physchem.51.1.763.

[139] V. Iota, C. S. Yoo, and H. Cynn, "Quartzlike Carbon Dioxide: An Optically Nonlinear Extended Solid at High Pressures and Temperatures," *Science*, vol. 283, no. 5407, pp. 1510–1513, Mar. 1999, doi: 10.1126/science.283.5407.1510.

[140] M. I. Eremets, A. G. Gavriliuk, I. A. Trojan, D. A. Dzivenko, and R. Boehler, "Single-bonded cubic form of nitrogen," *Nat. Mater.*, vol. 3, no. 8, pp. 558–563, Aug. 2004, doi: 10.1038/nmat1146.

[141] M. Bykov *et al.*, "Fe-N system at high pressure reveals a compound featuring polymeric nitrogen chains," *Nat. Commun.*, vol. 9, no. 1, p. 2756, Jul. 2018, doi: 10.1038/s41467-018-05143-2.

[142] Y. Wang *et al.*, "Stabilization of hexazine rings in potassium polynitride at high pressure," *Nat. Chem.*, vol. 14, no. 7, pp. 794–800, Jul. 2022, doi: 10.1038/s41557-022-00925-0.

[143] A. P. Drozdov *et al.*, "Superconductivity at 250 K in lanthanum hydride under high pressures," *Nature*, vol. 569, no. 7757, pp. 528–531, May 2019, doi: 10.1038/s41586-019-1201-8.

[144] R. F. Smith *et al.*, "Ramp compression of diamond to five terapascals," *Nature*, vol. 511, no. 7509, pp. 330–333, Jul. 2014, doi: 10.1038/nature13526.

[145] V. Schettino and R. Bini, "Constraining molecules at the closest approach: chemistry at high pressure," *Chem. Soc. Rev.*, vol. 36, no. 6, pp. 869–880, May 2007, doi: 10.1039/B515964B.

[146] P. F. McMillan, "Chemistry of materials under extreme high pressure-high-temperature conditions," *Chem. Commun.*, no. 8, pp. 919–923, Apr. 2003, doi: 10.1039/B300963G.

[147] S. D. Kloß, M. L. Weidemann, and J. P. Attfield, "Preparation of Bulk-Phase Nitride Perovskite $LaReN_3$ and Topotactic Reduction to $LaNiO_2$-Type $LaReN_2$," *Angew. Chem. Int. Ed.*, vol. 60, no. 41, pp. 22260–22264, 2021, doi: 10.1002/anie.202108759.

[148] L. Dubrovinsky *et al.*, "Materials synthesis at terapascal static pressures," *Nature*, vol. 605, no. 7909, pp. 274–278, May 2022, doi: 10.1038/s41586-022-04550-2.

[149] C. E. Weir, E. R. Lippincott, A. Van Valkenburg, and E. N. Bunting, "Infrared Studies in the 1- to 15-Micron Region to 30,000 Atmospheres," *J. Res. Natl. Bur. Stand., Sect. A*, vol. 63A, no. 1, pp. 55–62, 1959, doi: 10.6028/jres.063A.003.

[150] J. C. Jamieson, A. W. Lawson, and N. D. Nachtrieb, "New Device for Obtaining X-Ray Diffraction Patterns from Substances Exposed to High Pressure," *Rev. Sci. Instrum.*, vol. 30, no. 11, pp. 1016–1019, Nov. 1959, doi: 10.1063/1.1716408.

[151] G. Shen and H. K. Mao, "High-pressure studies with x-rays using diamond anvil cells," *Rep. Prog. Phys.*, vol. 80, no. 1, p. 016101, Nov. 2016, doi: 10.1088/1361-6633/80/1/016101.

[152] G. J. Piermarini, S. Block, and J. D. Barnett, "Hydrostatic limits in liquids and solids to 100 kbar," *J. Appl. Phys.*, vol. 44, no. 12, pp. 5377–5382, Dec. 1973, doi: 10.1063/1.1662159.

[153] S. Klotz, J.-C. Chervin, P. Munsch, and G. L. Marchand, "Hydrostatic limits of 11 pressure transmitting media," *J. Phys. D: Appl. Phys.*, vol. 42, no. 7, p. 075413, Mar. 2009, doi: 10.1088/0022-3727/42/7/075413.

[154] K. Motaln, E. Uran, N. Giordano, S. Parsons, and M. Lozinšek, "Hydrostatic behaviour of highly inert Fomblin and Halocarbon fluids as pressure-transmitting media in high-pressure experiments," *J. Appl. Crystallogr.*, vol. 58, no. 1, pp. 221–226, Feb. 2025, doi: 10.1107/S1600576725000342.

[155] M. Virant, "Diamond anvil cell: models, figures, and animations." Zenodo, 2026. doi: 10.5281/zenodo.18874190.

[156] R. A. Forman, G. J. Piermarini, J. D. Barnett, and S. Block, "Pressure Measurement Made by the Utilization of Ruby Sharp-Line Luminescence," *Science*, vol. 176, no. 4032, pp. 284–285, Apr. 1972, doi: 10.1126/science.176.4032.284.

[157] G. Shen *et al.*, "Toward an international practical pressure scale: A proposal for an IPPS ruby gauge (IPPS-Ruby2020)," *High Pressure Res.*, vol. 40, no. 3, pp. 299–314, Jul. 2020, doi: 10.1080/08957959.2020.1791107.

[158] A. Katrusiak, "High-pressure crystallography," *Acta Crystallogr. A*, vol. 64, no. 1, pp. 135–148, Jan. 2008, doi: 10.1107/S0108767307061181.

[159] M. I. Eremets, V. S. Minkov, P. P. Kong, A. P. Drozdov, S. Chariton, and V. B. Prakapenka, "Universal diamond edge Raman scale to 0.5 terapascal and implications for the metallization of hydrogen," *Nat. Commun.*, vol. 14, no. 1, p. 907, Feb. 2023, doi: 10.1038/s41467-023-36429-9.

[160] W. A. Bassett, "Diamond anvil cell, 50th birthday," *High Pressure Res.*, vol. 29, no. 2, pp. 163–186, Jun. 2009, doi: 10.1080/08957950802597239.

[161] R. Boehler, "High-pressure experiments and the phase diagram of lower mantle and core materials," *Rev. Geophys.*, vol. 38, no. 2, pp. 221–245, 2000, doi: 10.1029/1998RG000053.

[162] I. Kupenko *et al.*, "Portable double-sided laser-heating system for Mössbauer spectroscopy and X-ray diffraction experiments at synchrotron facilities with diamond anvil cells," *Rev. Sci. Instrum.*, vol. 83, no. 12, p. 124501, Dec. 2012, doi: 10.1063/1.4772458.

[163] Z. Mazej, E. Goreshnik, and K. O. Christe, "Photochemical preparation of $Cs[MF_6]$ salts (M = Ru, Rh, Os, Ir, Pt); crystal structures and Raman spectra," *J. Fluorine Chem.*, vol. 268, p. 110128, May 2023, doi: 10.1016/j.jfluchem.2023.110128.

[164] Z. Mazej and B. Žemva, "Synthesis of arsenic pentafluoride by static fluorination of As_2O_3 in a closed system," *J. Fluorine Chem.*, vol. 126, no. 9, pp. 1432–1434, Oct. 2005, doi: 10.1016/j.jfluchem.2005.07.010.

[165] G. M. Lucier, S. H. Elder, L. Chacon, and N. Bartlett, "The room temperature oxidation of gold, ruthenium, osmium, iridium, platinum, or palladium with fluorine in anhydrous hydrogen fluoride," *Eur. J. Solid State Inorg. Chem.*, vol. 33, pp. 809–820, 1996.

[166] O. Graudejus, S. H. Elder, G. M. Lucier, C. Shen, and N. Bartlett, "Room Temperature Syntheses of AuF_6^- and PtF_6^- Salts, $Ag^+AuF_6^-$, $Ag^{2+}PtF_6^{2-}$, and $Ag^{2+}PdF_6^{2-}$, and an Estimate for $E(MF_6^-)$ [M = Pt, Pd]," *Inorg. Chem.*, vol. 38, no. 10, pp. 2503–2509, May 1999, doi: 10.1021/ic981397z.

[167] Z. Mazej, "Room temperature syntheses of MnF_3, MnF_4 and hexafluoromanganete(IV) salts of alkali cations," *J. Fluorine Chem.*, vol. 114, no. 1, pp. 75–80, Mar. 2002, doi: 10.1016/S0022-1139(01)00566-8.

[168] W. J. Casteel, D. H. Lohmann, and N. Bartlett, "Room temperature preparations of second and third transition series tetrafluorides and a possible novel structure type for OsF_4 and RhF_4," *J. Fluorine Chem.*, vol. 112, no. 2, pp. 165–171, Dec. 2001, doi: 10.1016/S0022-1139(01)00507-3.

[169] Z. Mazej, "Photochemical Syntheses of Fluorides in Liquid Anhydrous Hydrogen Fluoride," in *Modern Synthesis Processes and Reactivity of Fluorinated Compounds*, H. Groult, F. R. Leroux, and A. Tressaud, Eds., Elsevier, 2017, pp. 587–607. doi: 10.1016/B978-0-12-803740-9.00020-2.

[170] W. E. Falconer *et al.*, "Gas-phase structures and mass spectra of binary pentafluorides," *J. Fluorine Chem.*, vol. 4, no. 2, pp. 213–234, Jul. 1974, doi: 10.1016/S0022-1139(00)82515-4.

[171] L. Merrill and W. A. Bassett, "Miniature diamond anvil pressure cell for single crystal x-ray diffraction studies," *Rev. Sci. Instrum.*, vol. 45, no. 2, pp. 290–294, Feb. 1974, doi: 10.1063/1.1686607.

[172] R. Boehler and K. De Hantsetters, "New anvil designs in diamond-cells," *High Pressure Res.*, vol. 24, no. 3, pp. 391–396, Sep. 2004, doi: 10.1080/08957950412331323924.

[173] S. A. Moggach, D. R. Allan, S. Parsons, and J. E. Warren, "Incorporation of a new design of backing seat and anvil in a Merrill–Bassett diamond anvil cell," *J. Appl. Crystallogr.*, vol. 41, no. 2, pp. 249–251, Apr. 2008, doi: 10.1107/S0021889808000514.

[174] J. C. Chervin, B. Canny, and M. Mancinelli, "Ruby-spheres as pressure gauge for optically transparent high-pressure cells," *High Pressure Res.*, vol. 21, no. 6, pp. 305–314, Dec. 2001, doi: 10.1080/08957950108202589.

[175] M. Virant and M. Lozinšek, "CrimsonCalc: a software tool for pressure determination based on ruby fluorescence spectra," *J. Appl. Crystallogr.*, vol. 58, no. 5, pp. 1827–1833, Oct. 2025, doi: 10.1107/S1600576725007216.

[176] M. Veith and H. Bärnighausen, "Die Kristall- und Molekülstruktur von Bis(trimethylsilyl)diimin," *Acta Crystallogr. B*, vol. 30, no. 7, pp. 1806–1813, Jul. 1974, doi: 10.1107/S056774087400584X.

[177] M. Lozinšek, H. P. A. Mercier, and G. J. Schrobilgen, "Mixed Noble-Gas Compounds of Krypton(II) and Xenon(VI); $[F_5Xe(FKrF)AsF_6]$ and $[F_5Xe(FKrF)_2AsF_6]$," *Angew. Chem. Int. Ed.*, vol. 60, no. 15, pp. 8149–8156, 2021, doi: 10.1002/anie.202014682.

[178] Rigaku OD, *CrysAlisPro*. (2025). Rigaku Corporation, Wrocław, Poland.

[179] G. M. Sheldrick, "*SHELXT* – Integrated space-group and crystal-structure determination," *Acta Crystallogr. A*, vol. 71, no. 1, pp. 3–8, Jan. 2015, doi: 10.1107/S2053273314026370.

[180] L. Palatinus and G. Chapuis, "*SUPERFLIP* – a computer program for the solution of crystal structures by charge flipping in arbitrary dimensions," *J. Appl. Crystallogr.*, vol. 40, no. 4, Art. no. 4, Aug. 2007, doi: 10.1107/S0021889807029238.

[181] G. M. Sheldrick, "A short history of *SHELX*," *Acta Crystallogr. A*, vol. 64, no. 1, pp. 112–122, Jan. 2008, doi: 10.1107/S0108767307043930.

[182] G. M. Sheldrick, *SHELXS-2014, Program for structure solution*. (2014). Universität of Göttingen, Göttingen, Germany.

[183] G. M. Sheldrick, "Crystal structure refinement with *SHELXL*," *Acta Crystallogr. C*, vol. 71, no. 1, pp. 3–8, Jan. 2015, doi: 10.1107/S2053229614024218.

[184] O. V. Dolomanov, L. J. Bourhis, R. J. Gildea, J. a. K. Howard, and H. Puschmann, "*OLEX2*: a complete structure solution, refinement and analysis program," *J. Appl. Crystallogr.*, vol. 42, no. 2, Art. no. 2, Apr. 2009, doi: 10.1107/S0021889808042726.

[185] H. Putz and K. Brandenburg, *Diamond – Crystal and Molecular Structure Visualization*. (2025). Crystal Impact, Bonn, Germany.

[186] H. Putz and K. Brandenburg, *Match! - Phase Analysis using Powder Diffraction*. Crystal Impact, Bonn, Germany.

[187] M. Mezouar *et al.*, "The high flux nano-X-ray diffraction, fluorescence and imaging beamline ID27 for science under extreme conditions on the ESRF Extremely Brilliant Source," *High Pressure Res.*, vol. 44, no. 3, pp. 171–198, Jul. 2024, doi: 10.1080/08957959.2024.2363932.

[188] H.-P. Liermann *et al.*, "The Extreme Conditions Beamline P02.2 and the Extreme Conditions Science Infrastructure at PETRA III," *J. Synchrotron Radiat.*, vol. 22, no. 4, pp. 908–924, Jul. 2015, doi: 10.1107/S1600577515005937.

[189] E. Bykova *et al.*, "Single-crystal diffractometer coupled with double-sided laser heating system at the Extreme Conditions Beamline P02.2 at PETRAIII," *Rev. Sci. Instrum.*, vol. 90, no. 7, p. 073907, Jul. 2019, doi: 10.1063/1.5108881.

[190] A. Aslandukov, M. Aslandukov, N. Dubrovinskaia, and L. Dubrovinsky, "Domain Auto Finder (*DAFi*) program: the analysis of single-crystal X-ray diffraction data from polycrystalline samples," *J. Appl. Crystallogr.*, vol. 55, no. 5, pp. 1383–1391, Oct. 2022, doi: 10.1107/S1600576722008081.

[191] K. Motaln *et al.*, "Reactive Noble-Gas Compounds Explored by 3D Electron Diffraction: XeF_2–MnF_4 Adducts and a Facile Sample Handling Procedure," *ACS Cent. Sci.*, vol. 10, no. 9, pp. 1733–1741, Aug. 2024, doi: 10.1021/acscentsci.4c00815.

[192] K. Gurung *et al.*, "A simple cryotransfer method for 3D electron diffraction measurements of highly sensitive samples," *J. Appl. Crystallogr.*, vol. 58, no. 3, pp. 1079–1084, Jun. 2025, doi: 10.1107/S1600576725002456.

[193] L. Palatinus, P. Brázda, M. Jelínek, J. Hrdá, G. Steciuk, and M. Klementová, "Specifics of the data processing of precession electron diffraction tomography data and their implementation in the program *PETS2.0*," *Acta Crystallogr. B*, vol. 75, no. 4, Art. no. 4, Aug. 2019, doi: 10.1107/S2052520619007534.

[194] M. C. Burla *et al.*, "Crystal structure determination and refinement via *SIR2014*," *J. Appl. Crystallogr.*, vol. 48, no. 1, pp. 306–309, Feb. 2015, doi: 10.1107/S1600576715001132.

[195] V. Petříček, M. Dušek, and L. Palatinus, "Crystallographic Computing System *JANA2006*: General features," *Z. Kristallogr. Cryst. Mater.*, vol. 229, no. 5, pp. 345–352, May 2014, doi: 10.1515/zkri-2014-1737.

[196] M. Wojdyr, "*Fityk*: a general-purpose peak fitting program," *J. Appl. Crystallogr.*, vol. 43, no. 5, pp. 1126–1128, Oct. 2010, doi: 10.1107/S0021889810030499.

[197] K. Motaln, K. Gurung, M. Dragomir, D. Kurzydłowski, L. Palatinus, and M. Lozinšek, "Crystal Structures of $XeF_2 \cdot 2PtF_4$ and $XeF_2 \cdot 2PdF_4$ Determined by 3D Electron Diffraction and Structural Models of $XePtF_6$," *Inorg. Chem.*, vol. 64, no. 29, pp. 14968–14976, Jul. 2025, doi: 10.1021/acs.inorgchem.5c01740.

[198] J. Burgess, C. J. W. Fraser, V. M. McRae, R. D. Peacock, and D. R. Russell, "The adduct $XeF_2 \cdot 2SbF_5$: Its crystal structure and thermochemistry," *J. Inorg. Nucl. Chem.*, vol. 28, pp. 183–188, Jan. 1976, doi: 10.1016/0022-1902(76)80624-0.

[199] K. Motaln, M. Virant, and M. Lozinšek, "Coordination of XeF_2 to fluoridometal cations: The Adduct Cations $[PtF_3(XeF_2)_3]^+$ and $[PdF_3(XeF_2)_3]^+$," *Inorg. Chem.*, vol. 65, no. 10, pp. 5668–5677, 2026, doi: 10.1021/acs.inorgchem.5c05940.

[200] K. Motaln and M. Lozinšek, "Structural investigations of the XeF_2–PtF_5 system: crystal structures of $[Xe_2F_3][PtF_6] \cdot XeF_2$, $[Xe_2F_3][PtF_6]$, and $[XeF][PtF_6]$," *Acta Chim. Slov.*, vol. 73, no. 1, pp. 62–69, Mar. 2026, doi: 10.17344/acsi.2026.9768.

[201] M. Tramšek, E. Goreshnik, and G. Tavčar, "Oxidation of ruthenium and iridium metal by XeF_2 and crystal structure determination of $[Xe_2F_3][RuF_6]\cdot XeF_2$ and $[Xe_2F_3][MF_6]$ (M = Ru, Ir)," *Acta Chim. Slov.*, vol. 63, no. 2, Art. no. 2, 2016, doi: 10.17344/acsi.2016.2373.

[202] F. Tamadon, S. Seidel, and K. Seppelt, "Reactions of Xenon with Iridium- and Osmiumhexafluoride," *Acta Chim. Slov.*, vol. 60, no. 3, pp. 491–494, 2013.

[203] N. Bartlett, M. Gennis, D. D. Gibler, B. K. Morrell, and A. Zalkin, "Crystal structures of $[XeF^+][RuF_6^-]$ and $[XeF_5^+][RuF_6^-]$," *Inorg. Chem.*, vol. 12, no. 8, pp. 1717–1721, Aug. 1973, doi: 10.1021/ic50126a002.

[204] R. Hagiwara, F. Hollander, C. Maines, and N. Bartlett, "The crystal structure of $[Ag(XeF_2)_2]AsF_6$ formed in the oxidation of Xe by $AgFAsF_6$," *Eur. J. Solid State Inorg. Chem.*, vol. 28, no. 5, pp. 855–866, 1991.

[205] K. Matsumoto, R. Hagiwara, Y. Ito, and O. Tamada, "Synthetic, structural and thermal studies of Ag(I)–XeF_2 complex salts," *Solid State Sci.*, vol. 4, no. 11, pp. 1465–1469, Nov. 2002, doi: 10.1016/S1293-2558(02)00037-7.

[206] M. Tramšek, P. Benkič, and B. Žemva, "$[M(XeF_2)_3](AsF_6)_2$ (M=Pb, Sr): the first coordination compounds of M^{2+} with XeF_2 ligand," *Solid State Sci.*, vol. 4, no. 1, pp. 9–14, 2002, doi: 10.1016/S1293-2558(01)01206-7.

[207] A. Turičnik, P. Benkič, and B. Žemva, "$Ba(SbF_6)_2 \cdot 5XeF_2$: First Xenon(II) Compound with Barium. Synthesis, Vibrational Spectra, and Crystal Structure," *Inorg. Chem.*, vol. 41, no. 21, pp. 5521–5524, Oct. 2002, doi: 10.1021/ic025670f.

[208] T. Mrzljak, E. Goreshnik, G. Tavčar, and M. Tramšek, "Coordination Chemistry of Copper and Nickel with Xenon Difluoride and the Hexafluororuthenate(V) Anion: Synthesis and Structural Studies," *Eur. J. Inorg. Chem.*, vol. 28, no. 24, p. e202500275, 2025, doi: 10.1002/ejic.202500275.

[209] K. Lutar, H. Borrmann, Z. Mazej, M. Tramšek, P. Benkič, and B. Žemva, "Novel lanthanoid fluoroarsenates," *J. Fluorine Chem.*, vol. 101, no. 2, pp. 155–160, Feb. 2000, doi: 10.1016/S0022-1139(99)00152-9.

[210] M. Tramšek, E. Lork, R. Mews, and B. Žemva, "Synthesis and Raman Spectra of $[Nd(XeF_2)_n](AsF_6)_3$ (n=3, 2.5) and Crystal Structure of $[Nd(XeF_2)_{2.5}](AsF_6)_3$," *J. Solid State Chem.*, vol. 162, no. 2, pp. 243–249, Dec. 2001, doi: 10.1006/jssc.2001.9280.

[211] Z. Mazej and E. Goreshnik, "XeF_2 Coordination to La, Ce, Pr, Nd, Sm, Eu, Gd, Tb, Dy and Y in Rare-Earth Metal(III) Tetrafluoridoborates," *Eur. J. Inorg. Chem.*, vol. 2021, no. 26, pp. 2669–2681, 2021, doi: 10.1002/ejic.202100353.

[212] G. Tavčar and B. Žemva, "XeF_4 as a Ligand for a Metal Ion," *Angew. Chem. Int. Ed.*, vol. 48, no. 8, pp. 1432–1434, 2009, doi: 10.1002/anie.200803365.

[213] M. Lozinšek, H. P. A. Mercier, D. S. Brock, B. Žemva, and G. J. Schrobilgen, "Coordination of KrF_2 to a Naked Metal Cation, Mg^{2+}," *Angew. Chem Int. Ed.*, vol. 56, no. 22, pp. 6251–6254, 2017, doi: 10.1002/anie.201611534.

[214] G. Bergerhoff, R. Hundt, R. Sievers, and I. D. Brown, "The inorganic crystal structure data base," *J. Chem. Inf. Comput. Sci.*, vol. 23, no. 2, pp. 66–69, May 1983, doi: 10.1021/ci00038a003.

[215] D. Zagorac, H. Müller, S. Ruehl, J. Zagorac, and S. Rehme, "Recent developments in the Inorganic Crystal Structure Database: theoretical crystal structure data and related features," *J. Appl. Crystallogr.*, vol. 52, no. 5, pp. 918–925, Oct. 2019, doi: 10.1107/S160057671900997X.

[216] G. Tavčar and B. Žemva, "$[Li(XeF_2)_n](AF_6)$ (A = P, As, Ru, Ir), the First Xenon(II) Compounds of Lithium. Synthesis, Raman Spectrum, and Crystal Structure of $[Li(XeF_2)_3](AsF_6)$," *Inorg. Chem.*, vol. 52, no. 8, pp. 4319–4323, Apr. 2013, doi: 10.1021/ic302323j.

[217] M. Lozinšek and K. Radan, "Alkali-Metal Fluoridooxidovanadates(V)," in *Solid-State Science & Research Meeting, Book of abstracts and programme*, Zagreb, 2023, p. 70.

[218] G. Tavčar, E. Goreshnik, and Z. Mazej, "Homoleptic $[M(XeF_2)_6]^{2+}$ cations of copper(II) and zinc(II)—Syntheses and crystal structures of $[M(XeF_2)_6](SbF_6)_2$ (M = Cu, Zn)," *J. Fluorine Chem.*, vol. 127, no. 10, pp. 1368–1373, Oct. 2006, doi: 10.1016/j.jfluchem.2006.04.007.

[219] N. Bartlett and D. H. Lohmann, "Fluorides of the noble metals. Part III. The fluorides of platinum," *J. Chem. Soc.*, pp. 619–626, Jan. 1964, doi: 10.1039/JR9640000619.

[220] O. Graudejus, A. P. Wilkinson, L. C. Chacón, and N. Bartlett, "M−F Interatomic Distances and Effective Volumes of Second and Third Transition Series MF_6^- and MF_6^{2-} Anions," *Inorg. Chem.*, vol. 39, no. 13, pp. 2794–2800, Jun. 2000, doi: 10.1021/ic000041w.

[221] J. H. Burns, "The crystal structure of lithium fluoroantimonate(V)," *Acta Crystallogr.*, vol. 15, no. 11, pp. 1098–1101, 1962, doi: 10.1107/S0365110X62002935.

[222] R. B. Roof, "The crystal structure of $KAsF_6$," *Acta Crystallogr.*, vol. 8, no. 11, pp. 739–739, 1955, doi: 10.1107/S0365110X55002302.

[223] J. A. Ibers, "A note on the least-squares method: the refinement of the structure of $KAsF_6$," *Acta Crystallogr.*, vol. 9, no. 11, pp. 967–969, 1956, doi: 10.1107/S0365110X56002710.

[224] G. Gafner and G. J. Kruger, "Potassium arsenic hexafluorine: a redetermination," *Acta Crystallogr. B*, vol. 30, no. 1, pp. 250–251, Jan. 1974, doi: 10.1107/S0567740874002597.

[225] P. A. Agron, G. M. Begun, H. A. Levy, A. A. Mason, C. G. Jones, and D. F. Smith, "Xenon Difluoride and the Nature of the Xenon-Fluorine Bond," *Science*, vol. 139, no. 3557, pp. 842–844, Mar. 1963, doi: 10.1126/science.139.3557.842.

[226] M. Tramšek, P. Benkič, and B. Žemva, "$[Mg(XeF_2)_n](AsF_6)_2$ (n = 4, 2): First Compounds of Magnesium with XeF_2," *Inorg. Chem.*, vol. 43, no. 2, pp. 699–703, Jan. 2004, doi: 10.1021/ic034826o.

[227] Z. Mazej and E. Goreshnik, "Synthesis, Raman Spectra and Crystal Structures of $[Cu(XeF_2)_n](SbF_6)_2$ (n = 2, 4)," *Inorg. Chem.*, vol. 47, no. 10, pp. 4209–4214, May 2008, doi: 10.1021/ic702249u.

[228] R. E. Stene, B. Scheibe, W. Petry, and F. Kraus, "Synthesis and Characterization of the Hexafluoridomolybdates(V) A[MoF_6] (A = Li – Cs)," *Eur. J. Inorg. Chem.*, vol. 2020, no. 19, pp. 1834–1843, May 2020, doi: 10.1002/ejic.202000141.

[229] U. Schwarz and K. Syassen, "The behaviour of solid XeF_2 under pressure," *High Pressure Res.*, vol. 9, no. 1–6, pp. 47–50, May 1992, doi: 10.1080/08957959208245611.

[230] M. Kim, M. Debessai, and C.-S. Yoo, "Two- and three-dimensional extended solids and metallization of compressed XeF_2," *Nat. Chem.*, vol. 2, no. 9, pp. 784–788, Sep. 2010, doi: 10.1038/nchem.724.

[231] G. Wu *et al.*, "Confirmation of the Structural Phase Transitions in XeF_2 under High Pressure," *J. Phys. Chem. C*, vol. 121, no. 11, pp. 6264–6271, Mar. 2017, doi: 10.1021/acs.jpcc.6b11558.

[232] J. Liu *et al.*, "Structural Phase Transition and Decomposition of XeF_2 under High Pressure and Its Formation of Xe–Xe Covalent Bonds," *Inorg. Chem.*, vol. 63, no. 26, pp. 12248–12254, Jul. 2024, doi: 10.1021/acs.inorgchem.4c01599.

[233] B. G. Müller and M. Serafin, "Single-crystal investigations on PtF_4 and PtF_5," *Eur. J. Solid State Inorg. Chem.*, vol. 29, pp. 625–633, 1992.

[234] S. Alvarez, "A cartography of the van der Waals territories," *Dalton Trans.*, vol. 42, no. 24, pp. 8617–8636, 2013, doi: 10.1039/C3DT50599E.

[235] J. Vogt and S. Alvarez, "van der Waals Radii of Noble Gases," *Inorg. Chem.*, vol. 53, no. 17, pp. 9260–9266, Sep. 2014, doi: 10.1021/ic501364h.

[236] T. Drews and K. Seppelt, "The Xe_2^+ Ion—Preparation and Structure," *Angew. Chem. Int. Ed.*, vol. 36, no. 3, pp. 273–274, 1997, doi: 10.1002/anie.199702731.

[237] S. Seidel and K. Seppelt, "Xenon as a Complex Ligand: The Tetra Xenono Gold(II) Cation in $AuXe_4^{2+}(Sb_2F_{11}^-)_2$," *Science*, vol. 290, no. 5489, pp. 117–118, Oct. 2000, doi: 10.1126/science.290.5489.117.

[238] T. Drews, S. Seidel, and K. Seppelt, "Gold–Xenon Complexes," *Angew. Chem Int. Ed.*, vol. 41, no. 3, pp. 454–456, 2002, doi: 10.1002/1521-3773(20020201)41:3%3C454::AID-ANIE454%3E3.0.CO;2-7.

Bibliography

Publications Related to the Thesis

Journal Articles

K. Motaln, K. Gurung, P. Brázda, A. Kokalj, K. Radan, M. Dragomir, B. Žemva, L. Palatinus, and M. Lozinšek, "Reactive Noble-Gas Compounds Explored by 3D Electron Diffraction: XeF_2–MnF_4 Adducts and a Facile Sample Handling Procedure", *ACS Central Science*, vol. 10, no. 9, pp. 1733–1741, 2024.

K. Motaln, K. Gurung, M. Dragomir, D. Kurzydłowski, L. Palatinus, and M. Lozinšek, "Crystal Structures of $XeF_2 \cdot 2PtF_4$ and $XeF_2 \cdot 2PdF_4$ Determined by 3D Electron Diffraction and Structural Models of $XePtF_6$", *Inorganic Chemistry*, vol. 64, no. 29, pp. 14968–14976, 2025.

K. Motaln, M. Virant, and M. Lozinšek, "Coordination of XeF_2 to fluoridometal cations: Synthesis and Structure of Salts Containing the $[MF_3(XeF_2)_3]^+$ (M = Pd, Pt) Adduct Cations", *Inorganic Chemistry*, vol. 65, no. 10, pp. 5668–5677, 2026.

K. Motaln and M. Lozinšek, "Structural investigations of the XeF_2–PtF_5 system: crystal structures of $[Xe_2F_3][PtF_6] \cdot XeF_2$, $[Xe_2F_3][PtF_6]$, and $[XeF][PtF_6]$", *Acta Chimica Slovenica*, vol. 73, no. 1, pp. 62–69, 2026.

Conference Contributions – Abstracts

K. Motaln, K. Radan, M. Lozinšek, "Structural reinvestigation of the XeF_2—MnF_4 system", 27th Annual Meeting of the Slovenian Chemical Society, Portorož, Slovenia, 2021.

K. Motaln, K. Radan, M. Lozinšek, "Crystallographically characterised compounds from the XeF_2—MnF_4 system", 20th European Symposium on Fluorine Chemistry – ESFC, Berlin, Germany, 2022.

K. Motaln, K. Radan, M. Lozinšek, "Structures of the XeF_2—MnF_4 adducts", The Twenty-eighth Croatian-Slovenian Crystallographic Meeting, CSCM28, Poreč, Croatia, 2022.

K. Motaln, K. Radan, M. Lozinšek, "Synthesis and crystal structures of $a XeF_2 \cdot b MnF_4$ compounds", 14th Jožef Stefan International Postgraduate School Students' Conference, Kamnik, Slovenia, 2022.

K. Gurung, K. Motaln, P. Brázda, K. Radan, M. Lozinšek, L. Palatinus, "Structural determination of XeF_2/MF_4 (M = Mn, Pd) compounds by 3D electron diffraction", IUCr 2023: 26th Congress and General Assembly of the International Union of Crystallography, Melbourne, Australia, 2023.

K. Motaln, M. Lozinšek, "On the synthesis and structure of salts containing the peculiar $[M^{IV}F_3(XeF_2)_3]^+$ (M = Pd, Pt) cations", Thirtieth Croatian-Slovenian Crystallographic Meeting, Veli Lošinj, Croatia, 2024.

K. Motaln, M. Lozinšek, "Synthesis and structural characterization of the novel salts containing unique $[M^{IV}F_3(XeF_2)_3]^+$ (M = Pd, Pt) cations", 29th Conference of the Serbian Crystallographic Society, Ruma, Serbia, 2024.

K. Motaln, M. Lozinšek, "Preparation and structural characterisation of salts containing the unique $[MF_3(XeF_2)_3]^+$ (M = Pd, Pt) adduct cations", Fluorine Frontiers: A Symposium Honoring the Legacy of Boris Žemva, Ljubljana, Slovenia, 2024.

K. Motaln, K. Gurung, P. Brázda, L. Palatinus, M. Lozinšek, "Structural investigation of fluoridopalladates(IV) by 3D ED", 34th European Crystallography Meeting, Padova, Italy, 2024.

K. Motaln, K. Gurung, P. Brázda, L. Palatinus, M. Lozinšek, "Crystal structures of fluoridopalladates(IV) explored by 3D electron diffraction", 30th Annual Meeting of the Slovenian Chemical Society, Portorož, Slovenia, 2024.

M. Lozinšek, K. Motaln, K. Gurung, P. Brázda, K. Radan, M. Dragomir, L. Palatinus, "Crystal structures of reactive air-sensitive compounds by 3D electron diffraction on nm-sized crystallites", 30th Annual Meeting of the Slovenian Chemical Society, Portorož, Slovenia, 2024.

K. Motaln, M. Lozinšek, "Coordination of xenon(II) fluorides to alkali metal cations", Thirty-first Slovenian-Croatian Crystallographic Meeting, Rogla, Slovenia, 2025.

M. Lozinšek, K. Motaln, K. Gurung, P. Brázda, E. Uran, K. Radan, M. Dragomir, L. Palatinus, "Crystal structure determination of reactive compounds by 3D electron diffraction", Thirty-first Slovenian-Croatian Crystallographic Meeting, Rogla, Slovenia, 2025.

M. Lozinšek, K. Motaln, K. Gurung, P. Brázda, K. Radan, M. Dragomir, D. Kurzydłowski, L. Palatinus, "New Insights into the Structure of $XePtF_6$", Solid-State Science & Research Meeting, Zagreb, Croatia, 2025.

M. Lozinšek, K. Motaln, K. Gurung, P. Brázda, E. Uran, K. Radan, M. Dragomir, L. Palatinus, "Crystal structure elucidation of xenon compounds by 3D electron diffraction on nanometer-sized crystallites", 21st European Symposium on Fluorine Chemistry – ESFC, Lisbon, Portugal, 2025.

M. Lozinšek, K. Motaln, K. Gurung, P. Brázda, E. Uran, K. Radan, M. Dragomir, D. Kurzydłowski, L. Palatinus, "3D electron diffraction studies of reactive xenon compounds", 19th European Conference on Solid State Chemistry, Malaga, Spain, 2025.

K. Motaln, S. Olszewska, M. Virant, E. Uran, O. Sanko, K. Radan, M. Dragomir, N. Giordano, B. Wehinger, D. Kurzydłowski, M. Lozinšek, "Structural investigations of the XeF_2–PtF_4 system under extreme conditions", 31st Annual Meeting of the Slovenian Chemical Society, Portorož, Slovenia, 2025.

M. Lozinšek, K. Motaln, K. Gurung, P. Brázda, E. Uran, K. Radan, M. Dragomir, D. Kurzydłowski, L. Palatinus, "Reactive compounds explored by 3D electron diffraction", 3-day International Conference on Materials Science, Verona, Italy, 2025.

Other Publications

Journal Articles

K. Motaln, A. E. Cotman, M. Lozinšek, "(*S*)-2-[(*S*)-2,2,2-Trifluoro-1-hydroxyethyl]-1-tetralone" *IUCrData*, vol. 8, no. 1, p. x221209, 2023.

K. Motaln, M. Lozinšek, "Crystal structure of $CaSiF_6 \cdot 2H_2O$(*mP*2) and reevaluation of the Si^{IV}–F bond-valence parameter R_0", *Acta Crystallographica Section E, Crystallographic Communications*, vol. 79, no. 12, pp. 1121–1126, 2024.

K. Motaln, E. Uran, N. Giordano, S. Parsons, M. Lozinšek, "Hydrostatic behaviour of highly inert Fomblin and Halocarbon fluids as pressure-transmitting media in high-

pressure experiments", *Journal of Applied Crystallography*, vol. 58, no. 1, pp. 221–226, 2025.

S. Olszewska, S. B. Pillai, D. Upadhyay, K. Zdun, J. Drapała, K. Motaln, M. Dragomir, M. Lozinšek, D. Kurzydłowski, "Pressure-Induced Comproportionation in Palladium Trifluoride", *Inorganic Chemistry*, vol. 64, no. 18, pp. 9026–9034, 2025.

K. Gurung, E. Uran, K. Motaln, P. Brázda, K. Radan, M. Lozinšek, L. Palatinus, "A simple cryotransfer method for 3D electron diffraction measurements of highly sensitive samples", *Journal of Applied Crystallography*, vol. 58, no. 3, pp. 1079–1084, 2025.

Conference Contributions – Abstracts

K. Radan, K. Motaln, M. Lozinšek, "Xenon(II) polyfluoridostannates(IV)", 27th Annual Meeting of the Slovenian Chemical Society, Portorož, Slovenija, 2021.

K. Motaln, M. Lozinšek, "Crystal structure determination of novel salts containing poly(hydrogen fluoride) anions", 28th Annual Meeting of the Slovenian Chemical Society, Portorož, Slovenija, 2022.

E. Uran, K. Motaln, M. Lozinšek, "Inert pressure transmitting media for high-pressure structural investigation of noble-gas compounds", International School of Crystallography, 56th course, Crystallography under extreme conditions: the future is bright and verry compressed, Erice, Italy, 2022.

K. Radan, K. Motaln, M. Lozinšek, "Recent advances in the field of Xenon(II) compounds with polymeric fluoroanions", 4th International Congress of Chemists and Chemical Engineers of Bosnia and Herzegovina, Sarajevo, Bosnia and Herzegovina, 2022.

K. Motaln, K. Gurung, P. Brázda, L. Palatinus, M. Lozinšek, "Crystal structure elucidation of silver(II) sulfates by 3D electron diffraction", 15th Jožef Stefan International Postgraduate School Students' Conference, Kamnik, Slovenia, 2023.

K. Motaln, M. Lozinšek, "The elusive crystal structure of $XeOF_2$", Twenty-ninth Slovenian-Croatian Crystallographic Meeting, Topolšica, Slovenia, 2023.

K. Motaln, K. Gurung, P. Brázda, L. Palatinus, M. Lozinšek, "Structural investigation of silver(II) sulfates by 3D ED", Solid-State Science & Research Meeting, Zagreb, Croatia, 2023.

E. Uran, K. Motaln, M. Lozinšek, "Hydrostatic behaviour of selected chemically inert pressure-transmitting media", 28th AIRAPT and 60th EHPRG International Conference 2023, Edinburgh, UK, 2023.

D. Kurzydłowski, D. Upadhyay, K. Zdun, J. Drapała, K. Motaln, M. Lozinšek, "Phase transitions in compressed palladium trifluoride: how $Pd(II)Pd(IV)F_6$ becomes $Pd(III)F_3$", 28th AIRAPT and 60th EHPRG International Conference 2023, Edinburgh, UK, 2023.

K. Motaln, M. Lozinšek, "Crystal structure elucidation of $XeOF_2$", 29th Annual Meeting of the Slovenian Chemical Society, Portorož, Slovenia, 2023.

K. Motaln, E. Uran, M. Lozinšek, "Evaluation of hydrostatic properties of selected halogenated fluids under high pressure", 16th Jožef Stefan International Postgraduate School Students' Conference: Two decades of discovery: advancing science and solutions, Piran, Slovenia, 2024.

M. Lozinšek, K. Motaln, E. Uran, "Exploring novel highly chemically resistant hydrostatic media" presentation at The 2nd High-Pressure Single-Crystal X-Ray Diffraction Summer School, Edinburgh, UK, 2024.

K. Gurung, K. Motaln, M. Belak Vivod, P. Brázda, G. King, M. Lozinšek, M. Dragomir, L. Palatinus, "Solving ambiguities: redetermining the crystal structures of rare Ag(II)

compound using 3D ED", 34th European Crystallography Meeting, Padova, Italy, 2024.

S. Olszewska, D. Upadhyay, S. B. Pillai, K. Zdun, J. Drapała, K. Motaln, M. Lozinšek, D. Kurzydłowski, "Phase transitions in compressed palladium trifluoride", Fluorine Frontiers: A Symposium Honoring the Legacy of Boris Žemva, Ljubljana, Slovenia, 2024.

M. Virant, E. Uran, K. Radan, O. Sanko, K. Motaln, M. Dragomir, S. Olszewska, D. Kurzydłowski, N. Giordano, M. Lozinšek, "High-pressure structural study of XeF_6", 31st Annual Meeting of the Slovenian Chemical Society, Portorož, Slovenia, 2025.

Biography

The author of this dissertation was born on August 31, 1996 in Maribor, Slovenia. In the early stages of education, he developed a great interest in natural sciences, which eventually led him to enroll in the Faculty of Chemistry and Chemical Technology at the University of Ljubljana. There, he obtained bachelor's and master's degree in chemical engineering, finishing his studies in 2021 after successfully defending master's thesis titled "Enzyme microkinetics in a microchannel with immobilized enzyme in gel film". In the same year he started working at the Extreme Conditions Chemistry Laboratory at the Jožef Stefan Institute and enrolled in the Ph.D. program Nanosciences and Nanotechnologies at the Jožef Stefan International Postgraduate School.

In the course of employment at Jožef Stefan Institute, he has specialized in the field of inorganic fluorine chemistry. His research primarily encompassed the synthesis, structural, and vibrational characterization of noble-gas compounds and high-valent fluorides, as well as high-pressure diamond anvil cell experiments. His synthetic work focused on thermal reactions utilizing melts of xenon difluoride or reactions involving the use anhydrous HF solvent, whereas the structural characterization was mainly accomplished through single-crystal X-ray diffraction and 3D electron diffraction as well as Raman and infrared spectroscopy. During his doctoral studies, he further expanded his expertise in diffraction methods by attending the 2022 Zurich School of Crystallography and the AIC 2023 International School on Electron Crystallography. He also presented the results of his research at 17 conferences in Slovenia and abroad, receiving a total of five awards for these contributions.